Resistance and Ultrasonic Spot Welding of Light-Weight Metals

DISSERTATION

Presented in Partial Fulfillment of the Requirements for the Degree Doctor of Philosophy in the Graduate School of The Ohio State University

By

Ying Lu

Graduate Program in Welding Engineering

The Ohio State University

2018

Dissertation Committee

Dr. Wei Zhang, Advisor

Dr. Carolin Fink

Dr. Xun Liu

Abstract

Multi-materials vehicle structures, employing light-weight metals such as advanced high strength steels (AHSS), aluminum alloys, and magnesium alloys, can satisfy the ever-increasing requirement of light-weighting and fuel efficiency, as well as maintaining or improving the crash resistance of vehicles. Resistance spot welding (RSW) is one of the most widely used joining methods and ultrasonic spot welding (USW) is one of the promising solid-state joining techniques in automotive industries. The present research provides a fundamental understanding of the process-microstructure-mechanical properties of resistance and ultrasonic spot welding of light-weight metals. Such understanding is essential for achieving both sound weld quality and accurate prediction of deformation and failure behaviors of spot welds.

The dissertation consists of three main parts: (1) study of the relationship of process-microstructure-mechanical properties for resistance spot welded two sheets (2T) and complex stack-ups of ultra-high strength grade of AHSS, (2) development of a novel technique, namely Ultrasonic Plus Resistance Spot Welding, for dissimilar metal joining of Al to steel, and (3) investigation of the bonding mechanism of USW of Al by in-situ relative vibration measurement.

The light-weight metal studied in the first part of the dissertation is hot-stamped boron steel Usibor® 1500, an ultra-high strength grade of UHSS, which has been increasingly used in automotive industries for light-weighting and improvement of crash resistance of vehicle. However, highly non-uniform temperature gradients experienced by workpieces during RSW can lead to the formation of the subcritical and coarse-grained heat affected zone (SCHAZ and CGHAZ, respectively), regions prone to "premature" failure for the ultra-high strength steels. CGHAZ consists of fully martensitic microstructure with high strength but low ductility, while the microstructure of the SCHAZ is tempered martensite with low strength but high ductility.

Accurate prediction of spot weld properties, such as surface electrode indentation and local hardness, is essential for computer-aided engineering (CAE) based design of light-weight and impact-resistant structures. In this study, a 3D fully coupled electro-thermo-mechanical model incorporating an improved electrical contact resistance formula from the literature is developed for resistance spot welding of aluminum-silicon coated hot-stamped boron steel. The temperature profiles, contact pressure distribution, nugget formation, and electrode indentation during RSW are numerically investigated. Tempering kinetics of base metal martensite is experimentally measured by isothermal tempering tests and used to extract kinetics parameters for a Johnson-Mehl-Avrami-Kolmogorov (JMAK) equation. The non-isothermal JMAK equation coupled with the process model is shown to accurately predict local SCHAZ softening.

Currently, there is a lack of local constitutive (stress-strain) behaviors of the CGHAZ and SCHAZ, which are essential for accurate prediction of deformation and fracture of resistance spot welds. Two approaches are used to generate the local constitutive behaviors for the SCHAZ and CGHAZ of hot stamped steel welds. In the first approach, CGHAZ and SCHAZ microstructure are simulated by Gleeble. Such Gleeble samples are loaded in quasi-static tensile testing aided with digital image correlation (DIC) for surface strain mapping. In the second approach, nanoindentation of the actual weld is used to extract the stress-strain curves of base metal, CGHAZ and SCHAZ. The yield strength extracted by nanoindentation are found to be comparable to those extracted by tensile testing of Gleeble simulated sample.

Besides 2T stack-ups of similar steels, complex stack-ups, such as 3T and 4T stack-ups of low carbon steel and AHSS, are increasingly used for smart design and light-weighting of vehicles. A major challenge for RSW of complex stack-ups with large thickness ratio is the limited nugget penetration into thin sheet at the outside of the stack-up. The effect of welding current, electrode force, electrode material/size on weld geometry is investigated for (i) a 3T stack-up of 0.75mm JAC270/1.4mm JSC 980/1.4mm JSC 590, and (ii) a 4T stack-up of 0.75 mm JAC270/1.4 mm JSC 980/1.4 mm JSC 590/1.5 mm Usibor® 1500. For 4T, a welding procedure involving pulsation is developed to achieve a sound joint. The procedure has 3 pulses with high welding current and short welding time for the 1st and 3rd pulse and lower welding current and longer welding time for the 2nd pulse. The 3D fully coupled electro-thermo-mechanical simulation is extended to investigate nugget formation in these complex stack-ups.

The second part of the dissertation is focused on the development of a new dissimilar metal joining method, namely ultrasonic plus resistance spot welding (abbreviated as U+RSW). In this part, the U+RSW method is applied to join Al to steel where an Al insert is first joined to a steel sheet using USW. Next, the Al insert side of the steel sheet is welded to an Al sheet by the standard RSW. No expulsion is observed up until welding current of 16.5 kA. Al/steel welds created by U+RSW show a brazing feature with liquid aluminum wetting and spreading on the solid steel surface. A less than 2 μm thick intermetallics layer is observed at Al insert/steel interface with a high joint strength of 3.2 kN at the welding current of 16.5 kA. The formation of such a thin layer of intermetallics is attributed to the metallurgical bond formed at Al/steel interface by USW, which in turn reduces the electrical resistance and temperature at this interface during subsequent RSW.

In lap shear tensile testing, four different failure modes take place depending on the welding current. As the current is higher than 15.2 kA, a nugget pull-out failure mode is observed. Moreover, the final strength of the Al/steel weld is only negligibly affected by the joint quality of the insert/steel joint as long as the USW energy is higher than 150 J. In addition to the conventional tensile shear testing, a wedge testing was applied to observe the deformation, strain distribution, and crack initiation and propagation of dissimilar Al to steel weld joined by U+RSW.

The third and last part of the dissertation is to understand the bonding mechanism in USW. Particularly, the relative motion of the sonotrode, aluminum specimens, and anvil in USW is investigated using an in-situ velocity measurement technique, Photonic Doppler

Velocimetry (PDV). The relative motion analysis is correlated to destructive testing results, including lap-shear tensile testing and weld microstructure characterization, to understand and quantify bond formation during USW. The results indicate that four bonding stages are present: a slip stage, slip-stick transition stage, stick stage, and over-welding stage. In particular, the end of the stick stage, marked by the sonotrode tip and foils vibrating at the same velocity, is essential to achieve peak bond strength as well as a fracture mode change from “interfacial failure” to “nugget pull-out”.

In summary, the present research studies the process-microstructure-property relationships of resistance spot welding of AHSS, dissimilar metal welding of Al to steel, and ultrasonic spot welding of Al. An improved fundamental understanding is developed for (1) heat conduction, electric current flow, mechanical stress and deformation, and nugget formation in 2T and complex stack-ups of resistance spot welded ultra-high strength steel, (2) tempering kinetics of martensite and SCHAZ softening, (3) microstructure-specific constitutive behaviors, (4) weldability, intermetallics, and strength of dissimilar metal joint between Al and steel in U+RSW, and (5) bonding mechanism in USW. Such new knowledge is essential to ensure sound multi-materials vehicle structures employing various light-weight metals to satisfy the ever-increasing demand for fuel efficiency and crash resistance.

Dedication

To my parents, aunt and my husband

for their inspiration, encouragement and love

Acknowledgments

I would like to express my deep appreciation to my advisor Dr. Wei Zhang for his inspiration and guidance. Thanks for taking me as a PhD student in our group and your suggestions and mentorship in my research and life are greatly appreciated.

I wish to thank Honda R&D Inc. and Simulation Innovation and Modeling Center (SIMCenter) for the financial support. Special thanks to Tim Abke and Skye Malcolm for the helpful discussion of the project and enable our research results to have practical impact on industries.

I would like to thank Menachem Kimchi for sharing his knowledges in resistance spot welding. Special thanks to Dr. Xun Liu and Dr. Carolin Fink for participating in my dissertation committee. Thank you to our group members, Andrea Peer, Tyler Borchers, Dan Tang, Hyeyun Song, Yousub Lee, Kaiwen Zhang, Alexey Kuprienko and other colleagues for sharing their ideas and knowledge. Additional thanks to my mentees, Ellis Mayton, Jolene Tran and Luke Walker for their hardworking. Thanks also go to Ed Pfeifer for helping in Gleeble and Geoff Taber for training on PDV. Lastly, I would like to thank my parents, aunt and my husband for their unconditional support and love. Thank you for your understanding, helping and always believing in me.

Vita

2005 – 2009 B.S. in Metallurgical Engineering, USTB

2009 – 2012 M.S. in Materials Science and Engineering, Beihang University

2012 – 2014 Graduate Research Assistant, Carnegie Mellon University

2014 – 2017 M.S. in Welding Engineering, The Ohio State University

2017 – present Graduate Research Assistant, The Ohio State University

Publications

Y. Lu, A. Peer, T. Abke, M. Kimchi, and W. Zhang, Subcritical heat affected zone softening in hot-stamped boron steel during resistance spot welding, Materials & Design, Vol. 155, pp. 170-184 (2018).

Y. Lu, A. Peer, T. Abke, M. Kimchi, W. Zhang, Heat-Affected Zone Microstructure and Local Constitutive Behaviors of Resistance Spot Welded Hot-Stamped Steel, in: Sheet Met. Weld. Conf. XVII, Livonia, MI, 2016: pp. 1–17.

Y. Lu, H. Song, G.A. Taber, D.R. Foster, G.S. Daehn, W. Zhang, In-situ measurement of relative motion during ultrasonic spot welding of aluminum alloy using Photonic Doppler Velocimetry, J. Mater. Process. Technol. 231 (2016) 431–440

A. Peer, Y. Lu, T. Abke, M. Kimchi, Deformation Behaviors of Subcritical Heat-affected Zone of Ultra-high Strength Steel Resistance Spot Welds, in 9th International Seminar & Conference on Advances in Resistance Spot Welding, Miami, FL, 2016: pp. 1–15.

W. Zhang, Y. Lu, E. Mayton and M. Kimchi, "Welding methods including formation of an intermediate joint using a solid state welding process", Patent Application No. 16/006,903, Jun. 13, 2018.

Fields of Study

Major Field: Welding Engineering

Table of Contents

Abstract ii

Dedication vii

Acknowledgments viii

Vita ix

List of Tables xv

List of Figures xvii

Chapter 1 Introduction 1

1.1 Background and motivation 1
1.2 Research objective 4
1.3 Thesis outline 5

Chapter 2 Literature review 7

2.1 Introduction to AHSS 7
2.1.1 Dual-phase steel 8
2.1.2 Hot stamped boron steel 9
2.1.3 Phase transformation 15
2.1.4 Tempering of martensite 17
2.2 Resistance spot welding 26
2.2.1 Resistance spot welding fundamentals 26
2.2.2 Resistance spot welding of AHSS 35
2.3 Resistance spot welding process modeling 38
2.3.1 Process models 38
2.3.2 Model for contact resistance 40
2.3.3 Metallurgical model 42

2.4 Mechanical testing of resistance spot welds 42
2.4.1 Mechanical testing 42
2.4.2 Fracture modes 47
2.4.3 Key factors for fracture 48
2.4.4 Failure prediction of spot welds 52
2.5 Resistance spot welding of complex stack-ups 61
2.6 Resistance spot welding of Al/steel 66
2.6.1 Direct RSW of Al alloys to steel 66
2.6.2 RSW of Al/steel using cover plates 68
2.6.3 RSW of Al/steel using interlayer 69
2.7 Important unanswered questions 73
Chapter 3 Resistance spot welding of 2T stack-up of hot-stamped steel 76
3.1 Approaches 76
3.1.1 Resistance spot welding experiment 76
3.1.2 Softening kinetics for the SCHAZ 78
3.1.3 RSW process modelling 83
3.1.4 Stress-strain curve of local HAZ for post weld simulation 93
3.2 Model validation 97
3.3 Temperature evolution and nugget formation 100
3.4 Evolution of contact pressure during RSW 103
3.5 Weld microstructure and hardness 106
3.5.1 Experimental characterization of weld microstructure 106
3.5.2 Nanoindentation 112
3.5.3 Isothermal tempering tests for simulated SCHAZ 115
3.5.4 Hardness map of resistance spot weld 117
3.6 Local constitutive behavior for post weld simulation 124
3.6.1 Gleeble simulation of CGHAZ and SCHAZ 124
3.6.2 Stress-strain curves of Gleeble simulated samples 128
3.6.3 Stress-strain curves extracted from nanoindentation 131
3.7 Summary and conclusions 134
Chapter 4 Resistance spot welding of complex stack-ups 138

4.1 Resistance spot welding of 3T stack-up 138
4.1.1 Approach 138
4.1.2 RSW process simulation 142
4.1.3 Effect of welding current on nugget formation 146
4.1.4 Effect of electrode force 150
4.1.5 Effect of electrode material 151
4.1.6 Microhardness distribution 152
4.1.7 Model validation 153
4.1.8 Nugget formation and Bonding mechanism 156
4.1.9 Tempering kinetics of JSC980 161
4.1.10 Local stress-strain curve of JSC980 for post-weld simulation 168
4.2 Resistance spot welding of 4T stack-up 169
4.2.1 Experiment 169
4.2.2 Effect of pulsation on nugget formation 173
4.2.3 Nugget formation kinetics 181
4.2.4 Microstructure and microhardness 186
4.2.5 Failure behavior 190
4.2.6 RSW process simulation of 4T stack-ups 191
4.3 Conclusions 194
Chapter 5 Ultrasonic + resistance spot welding of Al to steel 198
5.1 Introduction 198
5.2 Feasibility study 199
5.2.1 Experiment 199
5.2.2 Microstructure and mechanical properties of the intermediate joint 203
5.2.3 Microstructure of U+RSW welds 205
5.2.4 Bond formation in U+RSW 210
5.2.5 Mechanical properties of U+RSW joints 213
5.2.6 Fracture mechanism in U+RSW 215
5.2.7 Effect of intermediate joint on mechanical properties of primary joints 223
5.3 Insert material 224
5.3.1 Experiment 224
5.3.2 Effect of AC and DC machine on mechanical properties 225

5.3.3 Effect of the insert on mechanical properties 228
5.3.4 Effect of electrode geometry on mechanical properties 229
5.3.5 Effect of welding time on mechanical properties 232
5.3.6 Effect of the intermediate joint on strength of the final joint 235
5.4 Wedge testing of U+RSW welds 237
5.4.1 Experiment 237
5.4.2 Effect of welding current on half weld 238
5.4.3 Comparison of full weld with half weld 243
5.5 Conclusions 247
Chapter 6 In-situ relative motion measurement during ultrasonic spot Introduction 251
6.1 Introduction 251
6.2 Experiment 255
6.2.1 Ultrasonic spot welding 255
6.2.2 Velocity measurement using PDV 256
6.2.3 Bond quality characterization 257
6.3 Results 258
6.3.1 Motion of sonotrode tip and specimens 258
6.3.2 Lap shear strength and fracture mode 262
6.3.3 Weld interface microstructure 264
6.4 Discussion 267
6.4.1 Bond evolution 267
6.4.2 Peak temperature experienced at bond interface 275
6.4.3 Comparison with bonding mechanisms from literature 276
6.4.4 Effect of welding parameters 278
6.5 Summary and Conclusions 280
Chapter 7 Conclusions and future work 282
7.1 Conclusions 282
7.1.1 Resistance spot welding of 2T stack-ups of Usibor 1500 282
7.1.2 Resistance spot welding of complex stack-ups 284
7.1.3 U+RSW of Al to steel 286
7.1.4 In-situ relative motion measurement in USW 289

7.2 Future work 290
7.2.1 Resistance spot welding of 4T stack-ups 290
7.2.2 U+RSW of Al to steel 291
Bibliography 292

List of Tables

Table 2.1 Chemical composition of 22MnB5 (wt. %)[25] 11

Table 2.2 Hardness, failure mode and predicted critical weld size for different steels [83] 52

Table 2.3 Comparison of peak strength and joint efficiency in the literature for Al/steel resistance spot welding 73

Table 3.1 Chemical composition of Usibor 1500 (wt. %) [111] 77

Table 3.2 Parameters used for resistance spot welding of 1.5-mm-thick Usibor steel sheets. During RSW, a current waveform consisted of 3 impulses of 11 cycles of current-on followed by 2 cycles of current-off. 1 cycle = 1/60 of a second. 78

Table 3.3 Phase transformation temperatures of Usibor 1500 measured by dilatometry in Gleeble. M_s and M_f are the martensite start and finish temperatures, respectively 81

Table 3.4 Summary of testing conditions for isothermal tempering experiments 82

Table 3.5 Electric contact resistance parameters for E/S and S/S interfaces [69] 88

Table 3.6 Surface roughness of spot welded Usibor 1500 after vibratory polishing and etching in 2% Nital 96

Table 3.7 Strength coefficient (K, MPa) and strain hardening exponent (n) of BM, CGHAZ and SCHAZ 133

Table 4.1 Nominal composition of materials 141

Table 4.2 Welding parameters for resistance spot welding of 3T stack-up of steel sheets 142

Table 4.3 Chemical compositions of steels (wt%) used in 4T RSW 170

List of Figures

Figure 2.1 Net weight of AHSS and UHSS per NA light vehicle (2012 – 2025) [1]..... 7

Figure 2.2 Tensile strength as a function of martensite volume fraction and carbon content [20] 9

Figure 2.3 Example of hot stamped components in a vehicle[21]..... 10

Figure 2.4 Schematics of hot stamping processes : (a) direct hot stamping, and (b) indirect hot stamping [21]..... 11

Figure 2.5 Effect of alloying elements on hardenability of medium carbon steels [22]... 12

Figure 2.6 Binary phase diagram of Al-Si [28] 13

Figure 2.7 Cross-sectional SEM micrographs of aluminized coating heated at 930 ^{o}C for 5 min with (a) the heating rate of 10 ^{o}C/s in air, and (b) the heating rate of 30 ^{o}C/s in vacuum[23] 15

Figure 2.8 A schematic diagram showing various HAZs sub-regions with in a typical steel weld with 0.15 wt. % C [29]..... 16

Figure 2.9 Schematics of metallurgical reaction during 1 hour tempering of carbon steels [32]..... 19

Figure 2.10 Effect of Mo on tempering of quenched steel (0.1 wt% C) [34]..... 20

Figure 2.11 Schematic TTP curve showing the effect of heating rate on cementite nucleation [35] 21

Figure 2.12 Steady state cementite nucleation rate in ferrite at grain boundaries and dislocation [35] 22
Figure 2.13 SEM micrographs of (a) DP steel isothermally tempered at 650 ^{o}C for 5400 s with heating rate of 0.5 K/s and cooled to room temperature in 10 seconds by air cooling, and (b) non-isothermally tempered martensite by resistance spot welding with high heating rate (> 2000 K/s), negligible holding time [37] 22
Figure 2.14 General shape of JMAK equation [41]..... 26
Figure 2.15 Schematics of simple weld schedule [44] 27
Figure 2.16 Effect of electrode force on contact resistance [44] 30
Figure 2.17 Resistances in resistance spot welding [44] 32
Figure 2.18 Effect of temperature on resistivity of several metals (Cu, Al, and a mild steel) [49] 32
Figure 2.19 Generalized dynamic resistance curves [51] 34
Figure 2.20 Dynamic resistance curve for Al-Si-coated hot-stamped boron steel [52].... 34
Figure 2.21 Initial peak resistance variation with welding current for (a) Al-Si-coated hot stamped steel, and (b) GA coated hot stamped steel [52]..... 35
Figure 2.22 Microhardness distribution of resistance spot welded hot-stamped 22MnB5: (a) as-received (thus softened) condition, and (b) hot-stamped (thus hardened) condition [2]..... 36
Figure 2.23 Comparison of weldable current range of Al-Si coated and zinc coated hot-stamped boron steel[55]..... 37

Figure 2.24 Coating at the periphery of the resistance spot welds in Al-Si coated hot-stamped boron steel[55] 37
Figure 2.25 Schematics of loading condition in (a) tensile shear test (TST), (b) coach-peel test (CP), and (c) cross-tension test (CTT) [76] 43
Figure 2.26 Typical load-displacement curve in TST [77] 44
Figure 2.27 Set-up for wedge test in SEM [78] 46
Figure 2.28 Geometry of the wedge with the wedge angle of 73.7º[80] 46
Figure 2.29 Schematics of single-sided wedge test with one side clamped and wedge inserted on the other side [80] 47
Figure 2.30 Effect of weld nugget size on failure modes of resistance spot welded hot-stamped boron steel [80] 47
Figure 2.31 Typical types of failure modes during tensile shear testing: (a) interfacial fracture, (b) button pull-out failure, (c) partial interfacial fracture, and (d) partial thickness-partial pullout [75] 48
Figure 2.32 (a) Pull-out failure in SCHAZ of 22MnB5 in tensile shear test (TST), and (b) pull-out failure in CGHAZ of 22MnB5 in KS2-90º in resistance spot welded 22MnB5/ HC340LAD [3] 51
Figure 2.33 Effect of peak load and failure modes on FZ size [83] 52
Figure 2.34 Load displacement curves of tensile sample with and without spot weld [4] 53
Figure 2.35 Strain distribution of tensile specimen with spot weld at 1100 MPa, 1250 MPa, 1300 MPa, 1320 MPa (just before crack initiation) and after crack initiation [4] .. 54

Figure 2.36 Constitutive behaviors (true stress vs. true strain) in tension of SCHAZ and CGHAZ of resistance spot welded (a) DP 450, and (b) DP 980 steels [6]..... 55
Figure 2.37 Comparison of stress-strain curve generated by IIT and tensile testing [87] 56
Figure 2.38 Clamping conditions for KS2-coupons with different loading angles [3] 57
Figure 2.39 Comparison of fracture locations predicted by FEM and experimental data (a) calculated tensile shear fracture in SCHAZ of hot-stamped 22MnB5, and (b) calculated pull-out button in CGHAZ of hot-stamped 22MnB5 under KS2-90^{o} loading condition [3]..... 58
Figure 2.40 Measured and predicted stress-strain curve of tensile test with spot welds and the comparison of measured and predicted axial strain distribution immediately before and after crack initiation in the softened HAZ [4]..... 59
Figure 2.41 FE modeling of tensile tests with spot welds with the mesh size of 0.75 mm, 1.5 mm and 3 mm [4]..... 60
Figure 2.42 Comparison of the measured and predicted stress-strain curves with different mesh sizes [4]..... 61
Figure 2.43 Welding current and force used for resistance spot welding of thin/thick/thick 3T stack-ups [7] 64
Figure 2.44 Effect of bottom sheet thickness on (a) nugget size at each interface and (b) penetration into top and bottom sheet [92] 65
Figure 2.45 Cross-sectional macrostructure of typical Al/Steel resistance spot welds and SEM images of Al/Steel interface regions: (a) – (d) correspond to region A-D respectively [102]..... 68

Figure 2.46 Schematic diagram showing resistance spot welding with a cover plate [108] 69
Figure 2.47 Fracture modes of H220YD high strength steel/6008-T66 resistance spot weld joints (a) interfacial fracture without interlayer and (b) pull-out failure with 4047 AlSi12 interlayer thickness of 300 μm [110]..... 72
Figure 3.1 Base metal microstructure of hot-stamped Usibor 1500 in the press-hardened state. 77
Figure 3.2 Typical thermal cycle used for isothermal tempering test in Gleeble 3800. For this case, the tempering condition was 650 ºC (923 K) for 5 s. P_Temp is the programmed temperature profile, while M_Temp is the actual temperature profile experienced by the steel coupon. 82
Figure 3.3 Geometry and mesh of the quarter process model for resistance spot welding of Usibor 1500 steel sheets. 85
Figure 3.4 Representative curves of temperature- and pressure-dependent electrical contact resistance (ECR) at electrode/steel (E/S) and steel/steel (S/S) interfaces. 89
Figure 3.5 Temperature-dependent thermo-physical properties of Usibor 1500 steel and the copper electrode. 90
Figure 3.6 Temperature-dependent mechanical properties of Usibor 1500 steel and the copper electrode. 91
Figure 3.7 Schematic illustration of (a) mechanical boundary conditions, and (b) thermo-electrical boundary conditions applied in the process model. 92
Figure 3.8 Tensile test sample geometry (dimension in inches)..... 95

Figure 3.9 Comparison between the simulated nugget dimensions (i.e., nugget diameter and thickness) and experimental measurements. Calculated temperature is given in Celsius in (a). Welding current in (b) and (c) corresponds to the equivalent DC..... 98
Figure 3.10 Comparison between the simulated and experimentally-measured surface electrode indentation as a function of welding current. OM is the indentation measured via optical microscope, and caliper is that measured using a caliper. 100
Figure 3.11 Calculated temperature field showing (a) initial nugget formation at the sixth cycle of the first impulse (t = 100 ms), and (b) fully-grown nugget at the end of the third impulse (t = 617 ms). The welding current was 6.7 kA..... 101
Figure 3.12 Temperature profiles at the centre of the weld nugget and four other locations in the HAZ (welding current = 6.7 kA). 103
Figure 3.13 Evolution of contact pressure distribution at (a) electrode/steel and (b) steel/steel interfaces 105
Figure 3.14 (a) macrograph of the spot weld cross section, and SEM images of (b) weld metal, (c) CGHAZ, (d) FGHAZ, and (e) ICHAZ. The locations of observation in (b) through (e) are marked in (a) 108
Figure 3.15 SEM images of tempered martensite in the SCHAZ at (a) 10 μm, (b) 100 μm, (c) 300 μm, (d) 500 μm, (e) zoomed-in view of (d), and (f) 800 μm away from A_{C1} boundary 111
Figure 3.16 Load-displacement curves for base metal (BM) and tempered martensite with the distance of 10 μm (TM10), 200 μm (TM200), 500 μm (TM500), 800 μm (TM800) to A_{C1} line..... 113

Figure 3.17 Transverse nanohardness profile of spot welded Usibor® 1500..... 114
Figure 3.18 Linearized JMAK equation to extract tempering kinetics parameters. 115
Figure 3.19 Comparison of measured softening (plotted as discrete points) to the calculated softening (plotted as curves) showing the goodness of fit for the extracted kinetics parameters..... 117
Figure 3.20 A composite picture of predicted temperature distribution (left) and hardness map (right) in resistance spot welded Usibor 1500 for welding current of 6.7 kA. Temperature is given in Celsius and hardness in Vickers. 119
Figure 3.21 Predicted and measured hardness profiles along (a) one path parallel to faying surfaced, (b) another path on cross section of spot weld. The measurement locations in (a) and (b) are schematically shown in (c) and (d), respectively. 120
Figure 3.22 Tempering kinetics extracted by peak temperature with tempering time of 1 s 122
Figure 3.23 Comparison of predicted hardness using JMAK and peak temperature to the experimental results 122
Figure 3.24 Effect of welding current on the width of HAZ sub-regions and weld nugget diameter..... 124
Figure 3.25 Temperature profiles of physically-simulated (a) CGHAZ and (b) SCHAZ by Gleeble® 3800 125
Figure 3.26 Comparison of microstructure of CGHAZ (a and b) and SCHAZ (c and d). (a) and (c) are for actual spot welds, and (b) and (d) are for Gleeble simulated samples 127

Figure 3.27 Nanohardness of CGHAZ and SCHAZ in spot welds and physically-simulated samples. 1300WQ and 700WQ are simulated CGHAZ and SCHAZ, respectively 128
Figure 3.28 Distribution of normal strain in the vertical direction for (a) Gleeble simulated CGHAZ and (b) SCHAZ..... 130
Figure 3.29 Comparison of engineering stress-strain curves extracted with varying length of the virtual extensometer..... 130
Figure 3.30 True Stress-strain curves for Usibor® 1500 base metal and Gleeble simulated CGHAZ and SCHAZ..... 131
Figure 3.31 True stress-strain curves of (a) BM by tensile testing and nanoindentation extraction, (b) CGHAZ and (c) SCHAZ by tensile testing of Gleeble simulated sample and nanoindentation extraction on actual welds and Gleeble simulated sample..... 134
Figure 4.1 Schematics of the 3T stack of 0.75 mm JAC270/1.4 mm JSC980/1.4 mm JSC590 steels 139
Figure 4.2 Base metal microstructure of (a) JAC 270, (b) JSC 980 and (c) JSC 590 140
Figure 4.3 Geometry and mesh of the quarter process model for resistance spot welding of the 3T stack of 0.75 mm JAC270/1.4 mm JSC980/1.4 mm JSC590 144
Figure 4.4 Temperature-dependent electrical contact resistance (ECR) at electrode/sheet (E/S) interface and sheet/sheet (S/S) interface for GA coated steel and uncoated steel [92] 144
Figure 4.5 Temperature-dependent thermo-physical properties of steels and copper electrode[91] 145

Figure 4.6 Temperature-dependent mechanical properties of steels and copper electrode[91] 146
Figure 4.7 Optical micrograph of resistance spot welded 3T stack-up at welding current of (a) 5 kA, (b) 6 kA, and (c) 9.5 kA. Other welding parameters are electrode force: 3.4 kN, and welding time: 300 ms 148
Figure 4.8 Effect of welding current on nugget size for 3T stack-up of 0.75 mm JAC270/1.4 mm JSC980/1.4 mm JSC590 149
Figure 4.9 (a) Penetration into thin sheet, and (b) electrode indentation into top and bottom sheets for 3T stack-up 149
Figure 4.10 Effect of electrode force on (a) nugget diameter, and (b) penetration into thin sheet 151
Figure 4.11 Macrostructure of resistance spot welding of 3T stack-up with (a) 6 mm Class 1 electrodes, and (b) 6 mm Class 3 electrode and 8 mm Class 1 electrode on thin and thick sheet side respectively. Other welding parameters are welding current = 9.5 kA, and electrode force = 4.4 kN 152
Figure 4.12 (a) Microhardness mapping of resistance spot welded 3T stack-up, and (b) microhardness profile across a half of the spot welds. Welding parameters are 6 mm-surface diameter Class 3 electrode on thin sheet side, and 8 mm-surface diameter Class 1 electrode on thick sheet side, welding current = 9.5 kA, and electrode force = 4.4 kN . 153
Figure 4.13 Predicted dynamic resistance curves versus experimentally measured dynamic resistance as a function of welding time for 8 kA 155

Figure 4.14 Comparison between simulated nugget sizes and experimental measurements for welding current of 8 kA 156
Figure 4.15 Contact pressure distribution at interface A and B with welding time of 5 ms, current of 8 kA and electrode force of 3.4 kN 158
Figure 4.16 Nugget formation in resistance spot welding of 3T stack-up with welding current of 8 kA, electrode force of 3.4 kN and welding time of (a) 5 ms, and (b) 102 ms 159
Figure 4.17 Current density distribution at interface A and B with welding time of 5 ms, 200 ms and 300 ms 159
Figure 4.18 Effect of welding current on nugget initiation 161
Figure 4.19 Hardness as a function of H-J parameter for JSC980..... 163
Figure 4.20 Linearization of JSC980 softening data obtained from isothermal tempering tests 165
Figure 4.21 Linearized JMAK equation to extract tempering kinetics parameters for JSC980 166
Figure 4.22 Comparison of the measured softening extent with the JMAK calculation using extracted kinetic parameters for JSC980..... 167
Figure 4.23 Comparison of measured hardness with JMAK calculation using extracted kinetic parameters for JSC980 168
Figure 4.24 Local stress-strain curves of BM and Gleeble simulated CGHAZ and SCHAZ for JSC980 169

Figure 4.25 Base metal microstructure of (a) JSC 270, (b) JSC980, (c) JSC590, (d) Usibor1500 171
Figure 4.26 Schematics of welding schedule of resistance spot welding of 4T stack-up comprising 0.75 mm thick JAC270 / 1.4 mmt thick DP980 / 1.4 mm thick DP590 / 1.5 mm thick Usibor® 1500 172
Figure 4.27 Schematics of mechanical testing for resistance spot welded 4T stack-ups 173
Figure 4.28 Macrostructure of the resistance spot welded JAC270/JSC980/JSC590/Usibor 1500 with different welding schedules (the format of the label is 1st impulse current_1st impulse time_2nd impulse current_2nd impulse time_3rd impulse current_3rd impulse time; cool time between the impulses = 33 ms). 175
Figure 4.29 Effect of the welding current of the 1st impulse on nugget diameter 176
Figure 4.30 Effect of the welding current of the 1st impulse on nugget penetration into thin sheet 177
Figure 4.31 Effect of the welding current of the 2nd impulse on nugget diameter 178
Figure 4.32 Effect of the welding current of the 2nd pulse on nugget penetration into thin sheet 179
Figure 4.33 Effect of the welding current of the 3rd pulse on nugget diameter 180
Figure 4.34 Effect of the welding current of the 3rd impulse on nugget penetration into thin sheet 181
Figure 4.35 Welding current and corresponding resistance curves for the 4T stack-up welds with the welding schedule of 11kA and 50ms in the 1st impulse, 9kA and 367ms in the 2nd impulse, and 11kA and 50 ms in the 3rd impulse 184

Figure 4.36 Optical macrographs showing the coating removal at JAC270 and Usibor 1500 during the initial stage of welding. The left and middle columns had only the 1st impulse, and the right column had the 1st and 2nd impulses..... 185
Figure 4.37 Optical images showing (a) bond creation at JSC590/Usibor 1500 interface, and (b) zoomed-in image of the IMCs formed at this interface after the welding time of 2nd impulse = 50 ms 185
Figure 4.38 Nugget formation kinetics for the 4T stack-up welds observed by interrupted tests: (a) and (b) had only two impulses, and (c) included all three impulses 186
Figure 4.39 Microhardness map on the cross-section of the 4T stack-up (the welding currents for the 1st, 2nd and 3rd impulses are 13kA, 9kA and 11kA respectively) 188
Figure 4.40 Hardness profile along the center of each steel sheet..... 189
Figure 4.41 Button pull-out on JAC270 during peel test and button pull-out from JSC 590 during lap-shear tensile testing 190
Figure 4.42 Load-displacement curve of resistance spot welded 4T stack-up at the JSC590/Usibor 1500 interface 191
Figure 4.43 Calculated temperature distribution at the end of the 1st impulse (welding schedule: 14kA/33 ms in the 1st impulse, 9kA/367ms in the 2nd impulse, and 11kA/50ms in the 3rd impulse) 192
Figure 4.44 Nugget initiation in the 4T stack-ups during the 2nd impulse..... 193
Figure 4.45 Nugget formed in the 4T stack-ups at the end of the 3rd impulse..... 193

Figure 4.46 Comparison of predicted and measured dynamic resistance curves (welding schedule: 14kA/33 ms in the 1st pulse, 9kA/367ms in the 2nd pulse, and 11kA/50ms in the 3rd pulse)..... 194
Figure 5.1 Schematic diagram of U+RSW welding procedure 200
Figure 5.2 Sample geometry for lap-shear tensile testing (mm)..... 203
Figure 5.3 Cross-sectional microstructure of the intermediate joint by ultrasonic spot welding of 6061 aluminum alloy with 1008 steel (welding parameters: vibration amplitude = 50 μm, normal force = 1.75 kN, and welding energy of 255 J) 204
Figure 5.4 Load-displacement curves for intermediate joint welded by ultrasonic spot welding of 0.4 mm-thick AA6061 with 0.9 mm-thick uncoated low carbon steel AISI 1008..... 205
Figure 5.5 Cross-sectional macrostructure of dissimilar metal joints of aluminum alloy 6061 to 1008 steel by (a) direct RSW (13 kA – 5 cycles – 3.56 kN), and (b) U+RSW low current (13.3 kA – 5 cycles – 3.56 kN electrode force), and (c) U+RSW high current (16.1 kA - 5 cycles – 3.56 kN electrode force)..... 207
Figure 5.6 Effect of welding current on nugget diameter with welding time of 5 cycles and electrode force of 3.56 kN..... 208
Figure 5.7 IMC morphology at the center of the weld and EDX line scan data at insert/steel interface (16.5 kA-5 cycles - 3.56 kN) 209
Figure 5.8 IMCs thickness across the insert/steel interface as a function of distance to the weld center (16.5 kA-5 cycles - 3.56 kN)..... 210

Figure 5.9 Nugget of Al-Steel RSW joint at welding current of 13 kA: simulation (left) versus experiment (right). Temperatures are in °C. 654 is the liquidus temperature of Al, and 1535 is that of the steel..... 213
Figure 5.10 Temperature profile (a) at Al/steel interface during direct RSW and U+RSW (welding current: 13 kA, and welding time: 5 cycles), and (b) at center of the weld, 1 mm and 2.5 mm away from the weld center for U+RSW weld..... 213
Figure 5.11 Effect of welding current on tensile shear strength and fracture energy of welded joints of aluminum alloy 6061 and AISI 1008 steel..... 215
Figure 5.12 Fracture modes in lap shear tensile testing of U+RSW welded Al/steel joints 216
Figure 5.13 Representative fracture surface for four types of fracture modes at aluminum side (left) and steel side (right): (a) Type 1 (shear fracture at Al/insert interface; (b) Type 2 (partial/full nugget pull-out from insert); (c) Type 3 (button pull-out from Al sheet); and (d) Type 4 (interfacial fracture through insert/steel interface)..... 217
Figure 5.14 SEM images of fracture surface on steel side for Type 2 (partial/full nugget pull-out from insert): (a) Overall view, (b) Zoomed in morphology of Region 1, and (c) Zoomed in morphology of Region 2..... 219
Figure 5.15 SEM images of fracture surface on steel side for Type 3 (nugget pull-out from Al sheet): (a) Overall view, and (b) Zoomed in morphology of Region 1..... 219
Figure 5.16 SEM images of fracture surface on steel side for Type 4 (interfacial fracture): (a) Overall view, (b) Zoomed in morphology of Region 1, and (c) Zoomed in morphology of Region 2..... 220

Figure 5.17 (a) Effect of welding current on fracture mode, and (b) typical load-displacement curves for the four types of failure modes in lap shear tensile testing of direct RSW and U+RSW welded AA6061/1008 steel 222
Figure 5.18 Effect of the bond quality of the intermediate joint on tensile shear strength of primary joints in U+RSW spot welded AA6061/1008 steel joints 224
Figure 5.19 Effect of power source (AC/MFDC) on nugget diameter (electrode force: 3.56 kN, and welding time: 200 ms)..... 227
Figure 5.20 Effect of power source (AC/MFDC) on lap-shear strength of U+RSW welds 227
Figure 5.21 Effect of welding insert on the peak strength..... 229
Figure 5.22 Macrostructure of Al/steel welds using U+RSW with a dome-shaped electrode on the steel side (welding current of 19 kA, welding time of 67 ms, and MFDC machine)..... 230
Figure 5.23 Effect of welding current on nugget diameter for the dome-shaped versus flat electrodes 231
Figure 5.24 Effect of welding current on peak strength and failure modes for dome-shaped versus F-type electrodes..... 232
Figure 5.25 (a) macrostructure, and (b) zoomed-in image of the IMCs formed on the top surface of aluminum sheet due to over-melting when long welding time of 200 ms was used 233
Figure 5.26 Effect of welding time on nugget diameter with 0.3 mm-thick AA3003 as an insert using the MFDC welder..... 234

Figure 5.27 Effect of welding time on peak strength with 0.3 mm-thick AA3003 as an insert using the MFDC welder 235
Figure 5.28 Effect of intermediate joint quality on peak strength of the U+RSW welds for AA3003 as an insert with dome-shaped electrodes 236
Figure 5.29 Dimensions of the wedge and sample in single-sided wedge test 238
Figure 5.30 Load displacement curves of different failure modes occurring at different welding currents. Tested by single-sided wedge test 239
Figure 5.31 Strain (ε_{xx}) distribution for Type 2 failure. The left leg is the Al sheet, and the right leg is the insert and steel 241
Figure 5.32 Strain distribution for button pull-out failure mode (Type 3) with welding current of 19 kA 242
Figure 5.33 Strain distribution for button pull-out failure mode (Type 3) with welding current of 20 kA 243
Figure 5.34 Load displacement curves of full weld and half weld (welding current: 19 kA) for single-sided wedge testing 246
Figure 5.35 Comparison of peak strength of full weld versus half weld tested by single-sided wedge testing 247
Figure 6.1 Schematics of ultrasonic spot welding setup 258
Figure 6.2 In-situ PDV velocity measurement setup with a zoomed-in view showing the focus of laser spots (0.09 mm in diameter) on sonotrode tip, top and bottom foils 258

Figure 6.3 Example showing the average of the maximum velocity obtained for four contiguous cycles of velocity profiles. The welding parameters: vibration frequency = 20 kHz, peak-to-peak vibration amplitude = 50 µm, and normal force = 1754 N 259
Figure 6.4 Maximum velocity profiles of the sonotrode, top foil, and bottom foil for welding energies of (a) 10 J, (b) 20 J, (c) 100 J, (d) 250 J, and (e) 300 J. Measurement was done on five different samples..... 261
Figure 6.5 Load-displacement curves for “interfacial failure” mode and “nugget pull-out” mode..... 263
Figure 6.6 Effect of welding energy on (a) the average tensile shear strength, and (b) fracture energy 264
Figure 6.7 SEM images of an AA 6061 sample welded with an energy of 100 J, showing (a) partially bonded region near the weld line marked in the dashed oval, and (b) unbonded region..... 266
Figure 6.8 EBSD inverse pole plot of an AA 6061 sample welded with an energy of 275 J, showing (a) bonded region near the weld line, (b) higher magnification view of fine grains marked in the dashed box in (a), and (c) partially bonded region at a different location from (a) 267
Figure 6.9 (a) Maximum velocity profiles of the sonotrode, two foils, and anvil for an over-welded sample with a welding energy of 300 J, and (b) the relative motion 268
Figure 6.10 Optical images showing the imprint on the bottom foil by the anvil tip at welding energies of (a) 20 J, (b) 100 J and (c) 250 J with inset optical topographical images. (d) plots the typical depth profile across an indent at the three welding energies

and the “tooth” profile of anvil. (e) is an optical image of the anvil knurl pattern with inset optical topographical image, and (f) the typical surface profile of the anvil knurl pattern 274

Chapter 1 Introduction

1.1 Background and motivation

With rising concerns of environmental issues caused by greenhouse gas emission and growing concern of passenger safety, there is an increasing demand for light weighting of vehicles. Advanced high strength steels (AHSS), such as Dual Phase (DP) steels and hot-stamped boron steels, have been increasingly used in automotive industries to reduce vehicle weight by gauge reduction and increasing crash resistance of the anti-intrusion components due to their high strength [1]. Resistance spot welding (RSW) is one of the prominent joining methods in automotive industries. However, highly non-uniform temperature gradients experienced by workpieces during RSW can lead to the formation of sub-critical heat affected zone (SCHAZ) and coarse-grained heat affected zone (CGHAZ), regions prone to "premature" failure for ultra-high strength steels. Specifically, in resistance spot welding of hot-stamped boron steel, the SCHAZ has approximately 40% of hardness/strength reduction compared to the base metal [2]. A pull-out failure takes place at SCHAZ under shear loading, while CGHAZ could be a potential failure location under tensile load in resistance spot welded 22MnB5 due to its low ductility[3,4].

As SCHAZ softening has a significant effect on the load-bearing capacity and failure mode, an ability to quantitatively predict the HAZ softening is essential to control and

optimize resistance spot welds. While an integrated thermal-microstructure model was developed by Babu et al. [5] for resistance spot welded low carbon steel, there is a lack of microstructure model for spot welded hot-stamped boron steels. In addition, severe electrode indentation can lead to premature pull-out failure due to excess stress concentration, reducing the load-bearing capacity of resistance spot welds. Hence, knowledge of electrode indentation as a function of welding processing parameters (e.g., heat input and electrode force) is important to the study of deformation and failure behaviors of the spot welds. Therefore, it is essential to create a finite element model with an improved electrical contact resistance to simulate resistance spot welding of Usibor®1500, an AlSi coated hot-stamped boron steel.

Accurate prediction of fracture behavior of spot welded Usibor® 1500 can reduce the amount of destructive testing, thus important for vehicle design. A prerequisite for such accurate prediction of fracture behavior is the knowledge of local (microstructure-specific) constitutive behavior. Due to the small dimension as well as steep microstructure gradient in HAZ of spot welds, obtaining the local stress-strain curves of different HAZ sub-regions via conventional tensile testing is challenging. Methods such as micro-tensile testing need significant effort on sample preparation and may be further limited by the resolution of strain measurement during tensile loading. An “indirect” method can be used to extract the local constitutive behavior is to recreate HAZ microstructure by Gleeble [6].

Complex stack-ups of steels with innovative design can efficiently reduce vehicle weight. Complex stack-ups is usually defined as more than two sheets with similar/dissimilar materials and non-equal sheet thickness [7]. Resistance spot welding of complex stack-ups is challenging, especially when there exists a thin sheet of low carbon steel that is attached to multiple AHSS with high thickness ratio (thickness ratio = total thickness of the stack-up / thickness of the thinnest sheet). To solve the heat balance problem and increase the nugget penetration into the thin sheet, cover sheet can be used on the thin sheet side [8] or weld using electrodes with different geometry/materials and complex welding schedules to reduce heat loss through the water-cooled electrode or increase heat generation on the thin sheet side [7]. However, there is still lack of a fundamental understanding of the factors affecting nugget formation in complex stack-ups.

To further reduce vehicle weight, light-weighting materials, such as aluminum alloys, magnesium alloys and carbon fiber reinforced plastic (CFRP), are increasing utilized in automotive industries for multi-materials design of the vehicle[9]. Among them, aluminum alloys are the most promising materials considering about their properties and the cost. However, aluminum has been so far used in the components that don't require extremely high strength, such as the hood, doors and roof. The issue coming out will be joining of aluminum to steels. Considering that RSW is still the most widely used joining method in automotive assembly line, researchers have been conducted on direct resistance spot welding [10–12], resistance spot welding with an insert [13–16] and resistance element welding of Al to steel [17,18]. However, expulsion may occur with

the formation of thick intermetallic compounds (IMCs) at Al/steel interface by direct resistance spot welding or resistance spot welding with an insert, which results in the deterioration of the mechanical property of the spot welds. In this study, a new joining technique combined resistance spot welding with ultrasonic spot welding has been developed and the mechanical properties of the welds have been tested.

1.2 Research objective

The overarching objective of this research is to develop a fundamental understating of the process-microstructure-property relation for resistance and ultrasonic spot-welded light-weight metals. The specific objectives are summarized as follows:

(1) Investigation of softening in subcritical heat affected zone of resistance spot welded hot-stamped boron steels by weld microstructure characterization and tempering kinetics of martensite. The local constitutive behavior of the potential failure locations, such as SCHAZ and CGHAZ, are extracted and incorporated into performance model to investigate its effect on the accuracy of deformation and failure behavior prediction.

(2) Investigate the nugget formation mechanisms and the key factors for nugget penetration into thin sheet in complex stack-ups of steels with varying sheet thickness and coatings and high thickness ratio.

(3) Improve resistance spot welding of dissimilar metal joining of Al to steel using a new technique, Ultrasonic Plus Resistance Spot Welding (U+RSW). Feasibility study is conducted based on the concept developed with further optimization on

the process parameters. The bonding mechanisms are investigated through numerical simulation to validate the concept.

(4) Relative motion and bonding mechanism study of ultrasonic spot welding of aluminum alloys using Photonic Doppler Velocimetry (PDV) to better understand the factors that affect the joint quality of the intermediate joint and the final joint in U+RSW technique.

1.3 Thesis outline

This dissertation is organized as follows.

Chapter 1 provides the introduction and motivation of the research.

Chapter 2 is the literature review on resistance spot welding of AHSS and dissimilar metal welding of Al/steel.

Chapter 3 is to investigate the relationship of process, microstructure and failure behavior of resistance spot welded 2T stack-ups of AlSi coated hot-stamped boron steel. Particularly, it is developed an improved understanding of weld microstructure, tempering kinetics of martensite, and local, microstructure-specific constitutive behavior.

Chapter 4 is to investigate the heat balance and nugget formation mechanicms in resistance spot welding of complex stack-ups, inculding thin/thick/thick 3T stack-ups and thin/thick/thick/thick 4T stack-ups, by both experiment and numerical simulation.

Chapter 5 discusses a new technique for joining aluminum alloy to steel, namely Ultrasonic Plus Resistance Spot Welding (U+RSW). The feasiblity of U+RSW is studied for joining aluminum alloy (AA) 6061 to AISI 1008 steel, involving optimizing electrode geometry, mechanical testing (lap-shear tensile and wedge testing), and characterization of interfacial microstructure.

Chapter 6 investigates the relative motion and bonding mechanism of ultrasonic spot welding using Photonic Doppler Velocimetry (PDV), which is the welding process used in Chapter 5 for the intermediate joints.

Chapter 7 summarizes the major conclusions of the dissertation and identifies the future work.

Chapter 2 Literature review

2.1 Introduction to AHSS

With the rising demand of light weighting thereby reducing the greenhouse gas emission and improvement of crash-resistance of a vehicle, advanced high strength steels (AHSS) has been extensively used in automotive industries. For example, 72% of GM's Chevrolet Cruze's body consists of AHSS. Combining with clean sheet redesign, a 52 kg mass reduction in body-in-white (BIW) is achieved. Figure 2.1 shows the projected amount of AHSS (ultimate tensile strength (UTS) > 500 MPa) and ultra-high strength steels (UHSS) (UTS > 800 MPa) utilized in North American (NA) light vehicles from 2012. In particular, it is expected to be 483 pounds of AHSS utilized per vehicle in 2025, which is about twice of what has been used in 2014.

Figure 2.1 Net weight of AHSS and UHSS per NA light vehicle (2012 – 2025) [1]

2.1.1 Dual-phase steel

Dual-phase (DP) steels consist of islands of martensite in soft ferrite matrix; such microstructure provides high strength and ductility. DP steel is inter-critically annealed at temperatures between A_{C1} and A_{C3} and quenched to room temperature to form a composite of martensite and ferrite [19]. The flow stress of DP steel depends on both the volume fraction of martensite (V_m) and the tensile strength/carbon content of martensite as shown in Figure 2.2 [20]. The strength of dual phase steels can be predicted by:

$$S_d(MPa) = 497 + 2289 \times V_m[\frac{C_d - C_f}{V_m} + C_f]^{1/2} + 111V_m - 67{V_m}^2$$

where V_m is the volume fraction of martensite phase, C_f is the carbon content of ferrite, C_d is the carbon content of dual phase steels which can be expressed by:

$$C_d = C_m V_m + C_f(1 - V_m)$$

where C_m is the carbon content of martensite.

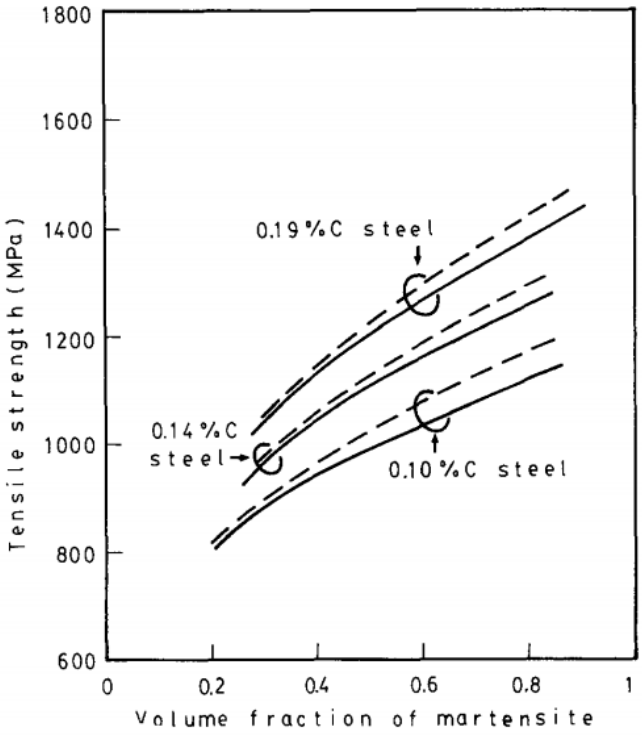

Figure 2.2 Tensile strength as a function of martensite volume fraction and carbon content [20]

2.1.2 Hot stamped boron steel

Hot-stamped boron steels, a class of UHSS, exhibits high ultimate tensile strength (~1500 MPa) and thus are increasingly used in crash resistant components, e.g., A-pillar, B-pillar and bumper, in a vehicle's body-in-white structure as shown in Figure 2.3 [21]. In 2012, more than 20 % of the body-in-white by mass has been manufactured by hot-stamped steels in some European car models, such as Audi A3, Volvo V40 [22].

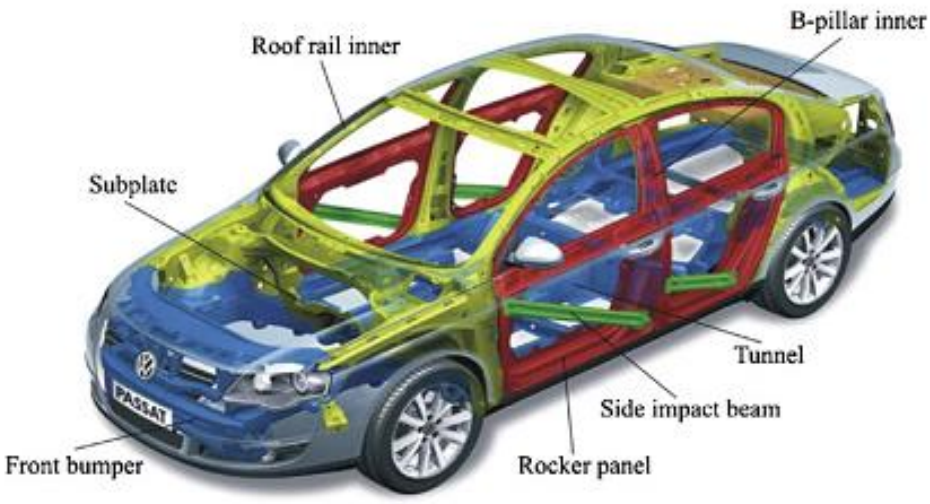

Figure 2.3 Example of hot stamped components in a vehicle[21]

There are two types of hot-stamping processes, i.e. direct hot stamping and indirect hot stamping. Schematics of two hot stamping processes is shown in Figure 2.4. Before hot stamping, microstructure of 22MnB5 consists of ferrite and pearlite, which results in strength of 600 MPa with high ductility of 25% [23]. In direct hot stamping, the blank plate is heated up to austenization temperature (900 – 950 ^{o}C) in furnace for 3 – 10 min. Then it is quickly transferred to the die to be formed into the desired shape and quenched at the same time with cooling rate higher than 25 ^{o}C/s. In indirect hot-stamping process, the blank plate is cold formed to be 90 – 95% of the final shape before heating, and then quenched and formed to the final shape. Indirect hot stamping is applicable to large and complicate shaped components. For uncoated hot stamped boron steel, shot blasting is required after hot stamping to remove scales. AlSi coated Usibor 1500-AS (developed by Arcelor Mittal) can be directly hot-stamped since the AlSi coating can prevent surface oxidation, scale formation and decarburization of 22MnB5 base metal [24].

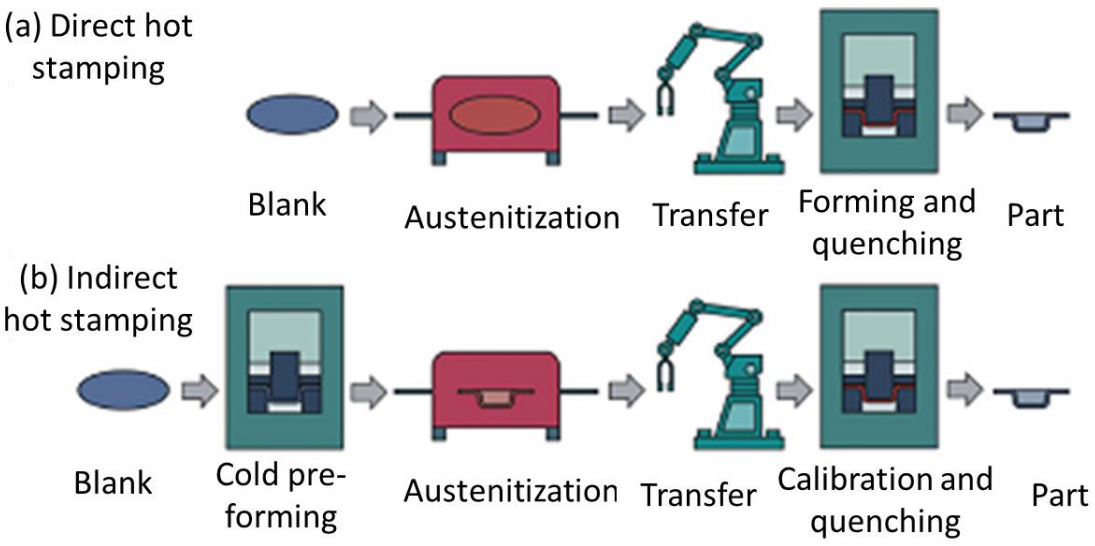

Figure 2.4 Schematics of hot stamping processes : (a) direct hot stamping, and (b) indirect hot stamping [21]

2.1.2.1 *Metallurgical consideration of boron steel*

Typical composition of 22MnB5 boron steel is displayed in Table 2.1. As shown in Figure 2.5, alloying of carbon, manganese, chromium can reduce the bainite formation temperature and shift the "nose" of the CCT curve to longer times [22]. Carbon is a strong austenite stabilizer and the high strength of martensite is obtained by interstitial solution strengthening of carbon. Mn is added to increase the hardenability by retarding the decomposition of austenite.

Table 2.1 Chemical composition of 22MnB5 (wt. %)[25]

C	**Mn**	**P**	**S**	**Si**	**Al**	**Ti**	**B**
0.2-0.25	1.1-1.4	≤0.025	≤0.008	0.15-0.35	≤0.015	0.02-0.05	0.002-0.005

Boron is an interstitial element that is added in boron steel to effectively improve the hardenability by retarding the nucleation rate of ferrite and carbide when it is in the solution of austenite [26]. However, boron has high affinity for oxygen and it is a nitride former. Thus, the steels need to be fully killed and de-oxidized. Titanium and aluminum are added to tie up nitrogen by the formation of AlN and TiN [23]. The critical cooling rate of phase transformation to martensite in 22MnB5 boron steel is 27 K/s.

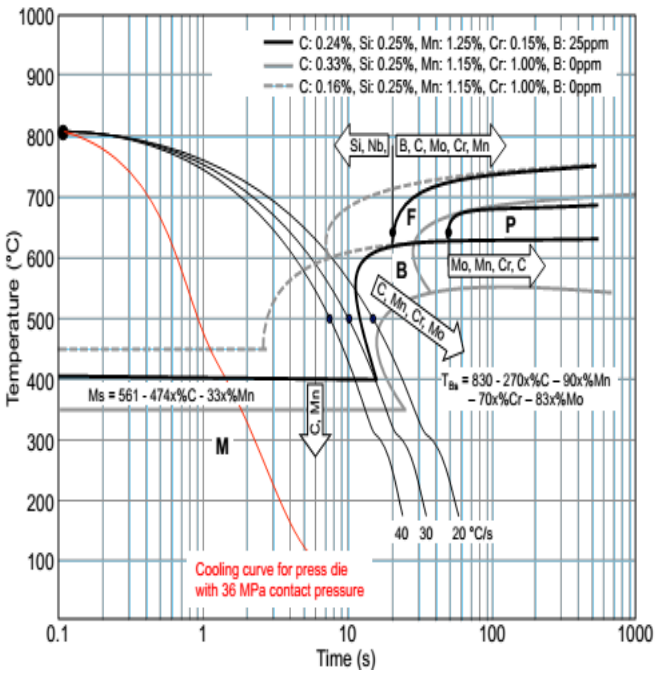

Figure 2.5 Effect of alloying elements on hardenability of medium carbon steels [22]

2.1.2.2 ***Coatings on boron steel***

Al-Si and galvannealed coating are the common coatings used on hot-stamped boron steel to improve the corrosion resistance.

There are two types of hot-dipped aluminized coatings. One type of aluminized coatings consist of pure aluminum, which is usually used for making reflective surface, such as building cladding panels [27]. The other is Al-Si alloy with 7-11 wt.% Si, which is near to the eutectic composition based on Al-Si phase diagram as shown in Figure 2.6. This type of coating is widely used in sheet steels in automotive industries since it has excellent corrosion resistance and high temperature oxidation resistance. Usually a 25-30 μm thick layer is coated onto 22MnB5 by hot dipping it into a molten Al alloy with the composition of 88 wt. % Al, 9 wt. % Si, and 3 wt. % Fe with the dipping temperature of 675 ^{o}C. Adding Si in the molten Al alloy is to form an inhibition layer of Fe_2SiAl_7 to prevent the rapid formation of hard and brittle Fe_2Al_5. The as-produced Al-Si coating consists of Al-Si eutectic matrix, a 5 μm thick Fe_2SiAl_7 and less than 1 μm thick Fe_2Al_5 and $FeAl_3$.

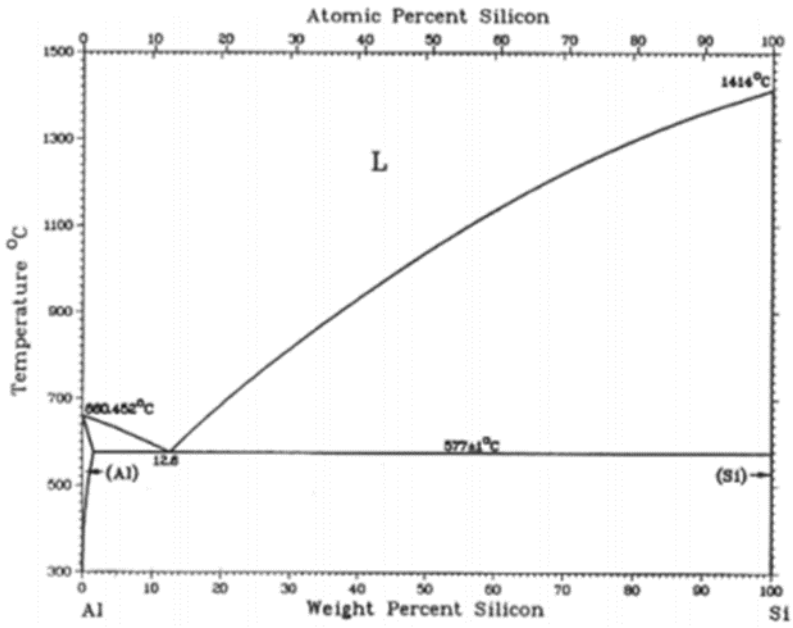

Figure 2.6 Binary phase diagram of Al-Si [28]

During hot-stamping, the heating temperature is above 900 ^{o}C, which is higher than the melting temperature of Al-Si eutectic (577 ^{o}C). The molten coating can adhere to the furnace equipment and multi-layer coatings with different intermetallics are shown in the Figure 2.7. The top layer is a thin layer of Al_2O_3, which behaves as a barrier for further oxidation of the coating. The phase transformation under the aluminum oxide layer is complex. In general, the Al-Si coatings after hot-stamping process usually consist of multi-layers of $FeAl_2$ and Fe_2SiAl_2 and a diffusion layer being identified as Fe_3Al at room temperature. At high temperature, the diffusion layer transforms to α-Fe with Al and Si in the solid solution, which is ductile and can arrest microcracks. The phase transformation of the coating is sensitive to the heat treatment parameters, such as heating rate, soaking time and initial coating thickness. With low heating rate of 10 ^{o}C/s in air, the Fe_2SiAl_2 layer is continuous with only a few Fe_2SiAl_2 island near to the coating surface. However, with high heating rate of 30 ^{o}C/s, island type Fe_2SiAl_2 forms with a higher Si content of 11 – 12 wt. %. The Al-Si coating has reasonable weldability, paintability and corrosion resistance.

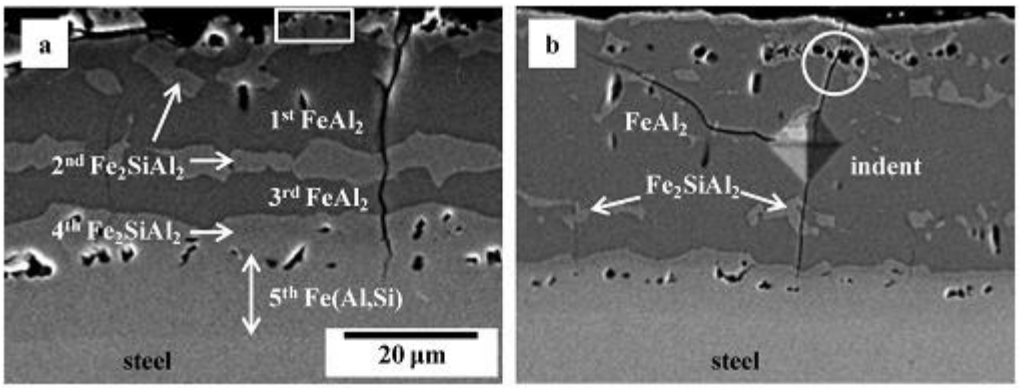

Figure 2.7 Cross-sectional SEM micrographs of aluminized coating heated at 930 ^{o}C for 5 min with (a) the heating rate of 10 ^{o}C/s in air, and (b) the heating rate of 30 ^{o}C/s in vacuum[23]

2.1.3 Phase transformation

The base metal of hot-stamped boron steel consists of martensite. Martensite transformation is diffusionless by atoms changing their positions in a coordinated manner, and martensite plates grow with a high speed approaching the speed of sound in metals.

In steel welding, the fusion zone is completely melted. Solid state phase transformation takes place in heat affected zones (HAZs). Figure 2.8 shows phase transformation in the HAZs in a typical steel weld. The following discussion considers a base metal with fully martensitic microstructure. The base metal heated up to a peak temperature between 200 ^{o}C to A_{C1} is tempered, which is called sub-critical heat affected zone (SCHAZ). Depending on the extent of martensite in the base metal, the tempering effect on mechanical property varies. When the temperature is between A_{C1} and A_{C3}, the base metal transforms to austenite and ferrite. Upon cooling, the newly formed austenite

transforms to stable low temperature phases, i.e. ferrite and pearlite, or metastable phase, i.e. bainite and martensite, depending on the cooling rate. The corresponding heat affect zone sub-region is called inter-critical heat affected zone (ICHAZ). When the temperature is just above A_{c3}, base metal is completely transformed to austenite. However, with low peak temperature, refined austenite grains form in the recrystallized zone/fine-grained heat affected zone (FGHAZ). Region near to the fusion zone, with rapid austenite grains growth due to high temperature, is referred to as the coarse-grained heat affected zone (CGHAZ).

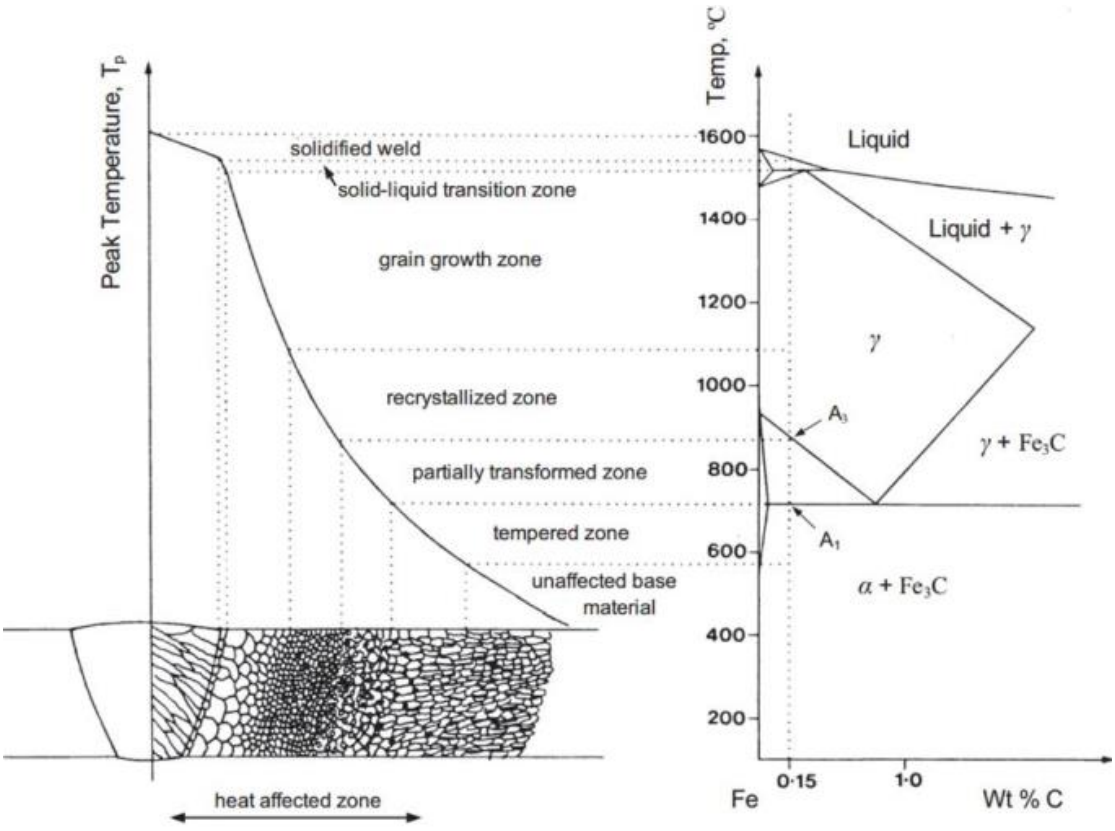

Figure 2.8 A schematic diagram showing various HAZs sub-regions with in a typical steel weld with 0.15 wt. % C [29]

When austenite is rapidly cooled down, the diffusional phase transformation to ferrite, pearlite and bainite is prohibited and the diffusionless phase transformation to martensite takes place. Since martensite transformation is diffusionless, martensite is supersaturated with carbon with a body centered tetragonal (BCT) structure. The extent of tetragonality (c/a ratio) of the unit cell in martensite depends on its carbon content [30]. In steel with high carbon concentration, untempered martensite possesses high strength but low ductility.

2.1.4 Tempering of martensite

2.1.4.1 *Tempering stages*

When steels with the microstructure consisting of a certain amount of martensite, i.e. DP steels and martensitic steels, are heated below A_{c1}, carbon diffuses from martensite to form ferrite and cementite. The process of martensite tempering consists of several stages, such as carbon segregation, ε-carbide formation, cementite formation, retained austenite decomposition and recovery and recrystallization of martensite microstructure as shown in Figure 2.9 [31]. The tempering process starts by carbon diffusion and segregation at the defects to form carbides. The details of each tempering stage are listed as follows.

Tempering stage 0: This stage occurs at temperatures below 150 ^{o}C. Carbon segregates at dislocations and lath boundaries in lath martensite [32].

Tempering stage 1: This stage occurs at temperatures ranging from 150 ^{o}C to 250 ^{o}C. Transition carbides, ε-carbides ($Fe_{2.4}C$) with closed packed hexagonal structure (HCP), form when the carbon content is higher than 0.2 wt.% (no carbide precipitation with carbon content less than 0.2 wt.%) [33].

Tempering stage 2: This stage occurs at temperatures ranging from 200 ^{o}C to 300 ^{o}C during which retained austenite decomposes into ferrite and cementite [33].

Tempering stage 3: This stage occurs at temperatures ranging from 200 ^{o}C to 350 ^{o}C, during which the segregated carbon and ε-carbides transform into cementite (Fe_3C). At lower temperatures, i.e. 200 ^{o}C, rod-like shaped cementite precipitates at the phase boundary of ε-carbide and the matrix. Other nucleation sites for cementite can be prior austenite grain boundaries and lath boundaries. At the same time, martensite with body centered tetragonal (BCT) structure changes to body centered cubic (BCC) with c/a ratio of 1 [32]. Thus, the strengthening mechanism transfers from the solid solution strengthening and dislocation strengthening in as-quenched martensite to precipitation strengthening due to carbide formation in tempered martensite.

Tempering stage 4: Carbides coarsening takes place when the temperature is between 400 ^{o}C to 600 ^{o}C. Carbides spheroidisation and recrystallization of ferrite occur when the temperature is above 600 ^{o}C [33]. The strength of tempered martensite depends on the size and distribution of carbides formed during tempering process.

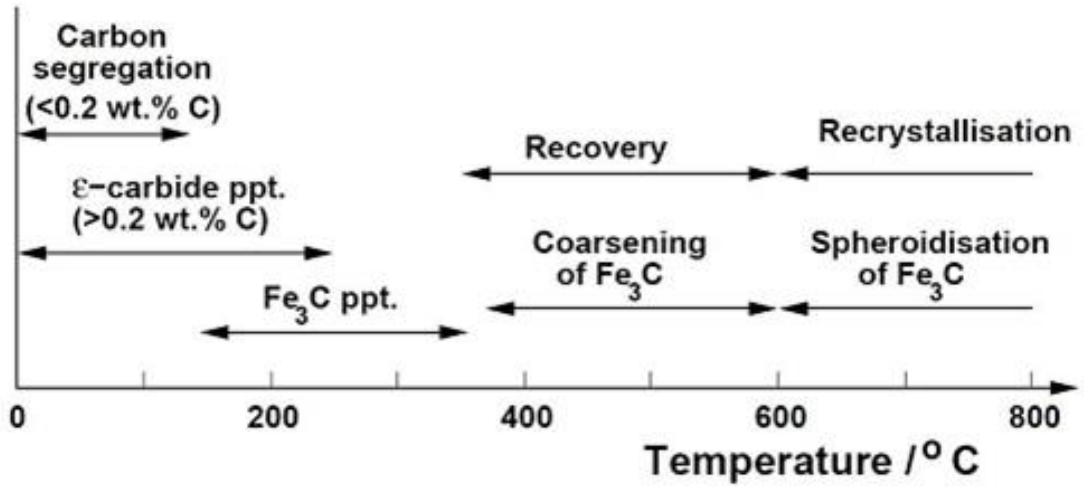

Figure 2.9 Schematics of metallurgical reaction during 1 hour tempering of carbon steels [32]

Tempering stage 5: In steels alloying with strong carbide-forming elements, such as Cr, Mo, W, V, Ti, alloy carbides, which are thermodynamically more stable compared to cementite, form at higher tempering temperature (500 ^{o}C – A_{C1}). Fine alloy carbides replace coarse cementite and it results in hardness/strength increase which is referred to as secondary hardening. Figure 2.10 is a plot of hardness as a function of Holloman-Jaffe parameter, showing the effect of Mo on hardness of tempered steel. Secondary hardening can often result in high hardness that exceeds as-quenched martensite. In general, steels with no/limited amounts of carbide-forming elements shows continuous decreasing of hardness at high temperature. In steel with a smaller amount of carbide-forming elements, such as 0.47 wt. % Mo in Figure 2.10, secondary hardening effect is not notable. Hardness is higher than the as-quenched martensite when the steels alloy with sufficient amount of carbide-forming element, i.e. 3.07 wt. % Mo, are tempered at high tempering temperature of 600 ^{o}C.

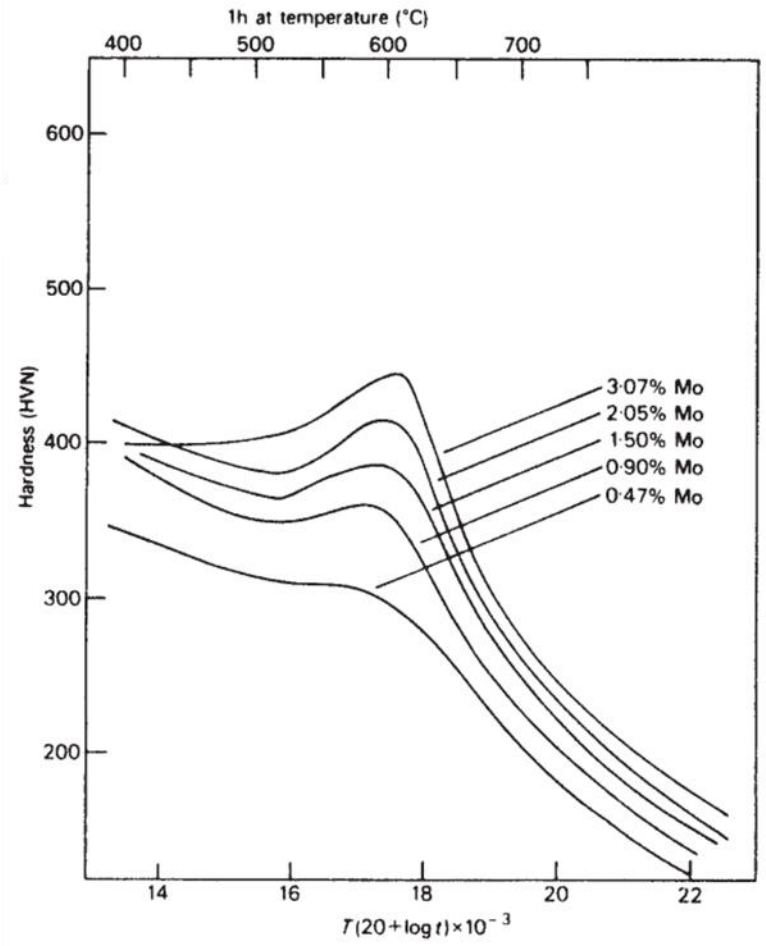

Figure 2.10 Effect of Mo on tempering of quenched steel (0.1 wt% C) [34]

2.1.4.2 ***Effect of heating rate on tempering***

Non-isothermal tempering of martensite commonly takes place in welding process with rapid heating rate, i.e. resistance spot welding, laser welding, electron beam welding et al. Furuhara et al. [35] reported that heating rate significantly affects the softening behavior when holding time is negligible during non-isothermal tempering.

Figure 2.11 schematically shows the effect of heating rate on the cementite nucleation temperature. Rapid heating leads to the increase of the temperature at which cementite

precipitation starts as shown by the open circle on the TTP curve. Based on the nucleation kinetics shown in Figure 2.12, the nucleation rate at high-angle grain boundaries generally increases with tempering temperature. Thus, dense and refined cementite nucleates at higher tempering temperature. Moreover, the time for cementite growth reduces with rapid heating rate. Cementite spheroidization temperature delays from 500 ^{o}C during slow heating to 600 ^{o}C during rapid heating [36]. Baltazar et al. [37] compared the non-isothermal tempering of martensite to isothermal tempering of martensite. As is shown in Figure 2.13, during isothermal tempering, coarse and spherical cementite with the size of ~ 225 nm precipitates at the prior austenite grain boundaries and block boundaries. Non-isothermal tempering results in fine intralath/interlath cementite with the size of 22 nm and block/prior austenite boundaries with the size of 45 nm.

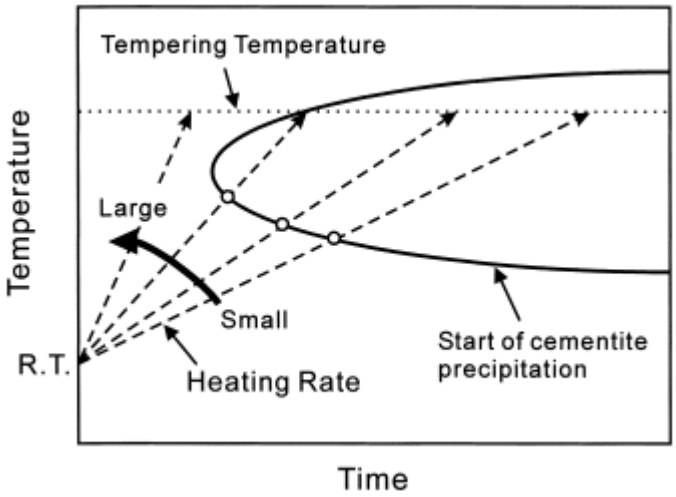

Figure 2.11 Schematic TTP curve showing the effect of heating rate on cementite nucleation [35]

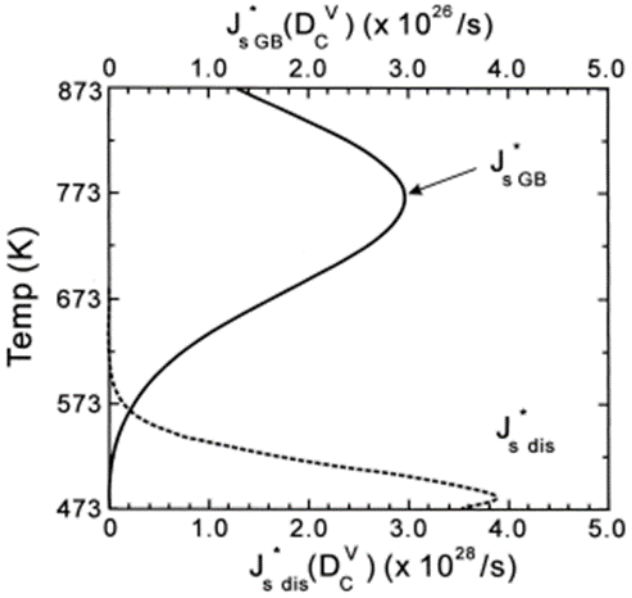

Figure 2.12 Steady state cementite nucleation rate in ferrite at grain boundaries and dislocation [35]

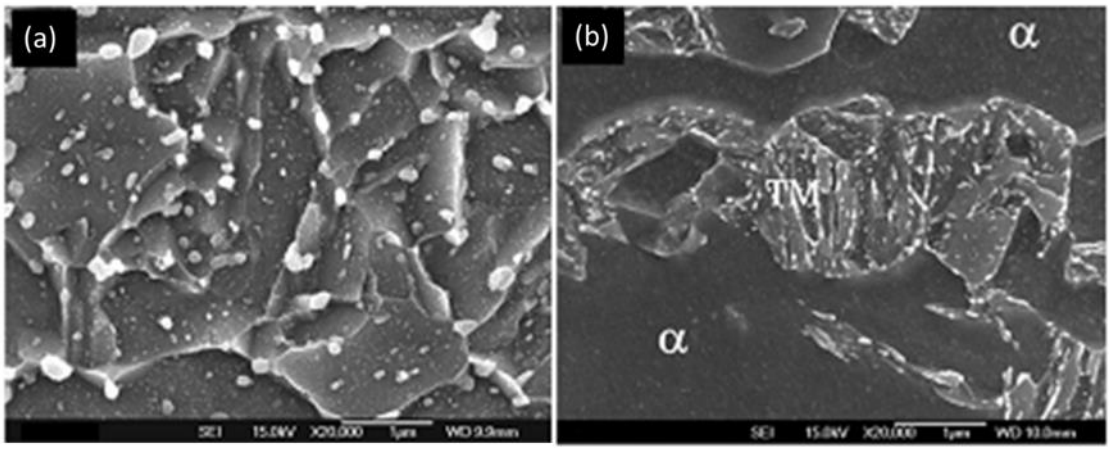

Figure 2.13 SEM micrographs of (a) DP steel isothermally tempered at 650 ºC for 5400 s with heating rate of 0.5 K/s and cooled to room temperature in 10 seconds by air cooling, and (b) non-isothermally tempered martensite by resistance spot welding with high heating rate (> 2000 K/s), negligible holding time [37]

2.1.4.3 ***Hollomon-Jaffe tempering parameter***

To predict the local hardness in SCHAZ of JSC980, Hollomon and Jaffe developed a semi-empirical equation to describe the effect of tempering time and temperature on hardness. The Hollomon-Jaffe (H-J) tempering parameter was defined as:

$$TP_{H-J} = T[c + \log(t)] \qquad \text{Equation 2.1}$$

In which, $TP_{H\text{-}J}$ is the H-J tempering parameter, T is the tempering temperature in Kelvin, t is the tempering time in second, c is a constant which is correlated to martensite carbon content.

C = 17.7 – 5.8 × (percent carbon) for time in seconds

C = 21.3 – 5.8 × (percent carbon) for time in hours

Jaffe et al. [38] tempered 6 different steels at temperatures of 100 ºC to 700 ºC for the times varying from 10 seconds to 24 hours. The hardness was plotted as a function of tempering parameters. The tempering curves can be generated for a specific steel and the hardness in a specific tempering condition can be predicted as long as the tempering parameter is given. The tempering parameter has no physical meaning rather than based on fitting of experimental results. However, the H-J parameter can be used for hardness prediction of steels with secondary hardening during tempering.

2.1.4.4 ***Johnson-Mehl-Avrami-Kolmogorov equation***

The other way to model tempering kinetics of martensite is a semi-empirical model that is developed by Johnson, Mehl, Avrami and Kolmogorov [39,40]. The model is based on the phase transformation model that is used to describe the time dependent transformation of parent phase into daughter phase. Three stages are proposed in a nucleation-growth-type phase transformation process. Nucleation of a daughter phase takes place initially. The phase transformation rate is slow at the first stage since the transformation occurs by nucleation only. With time increase, nucleation continues while the previous nucleated daughter phase grows, showing rapid increase in volume fraction of new phase. Finally, the phase transformation rate slows down again since limited parent phase has been left and the daughter phases impinge on each other. At a constant temperature, the JMAK equation is as follows[41]

$$\phi = 1 - \exp(-(kt)^n) \qquad \text{Equation 2.2}$$

$$\mathrm{k} = k_0 \exp(-\frac{Q}{RT}) \qquad \text{Equation 2.3}$$

where, Φ is the volume fraction of the new phase, t is the time (s), n is the JMAK exponent, k is a rate parameter (s^{-1}), which is described in the formation of Arrhenius equation. *T* is the tempering temperature (K), k_0 is the pre-exponent constant (s^{-1}), *Q* is the activation energy (J/mol), and *R* is the universal gas constant (8.314 J/mol-K) The JMAK equation leads to a sigmoidal curve, as shown in Figure 2.14.

The JMAK equation shown above describes the phase transformation during isothermal tempering. However, the thermal history experienced by the base metal in welding process is non-isothermal. Therefore, additive rule should be combined with JMAK equation to describe the transformation kinetics in non-isothermal condition, as shown below [42]

$$\phi_i = 1 - \exp\left\{-\{k_0 \times \exp\left(-\frac{Q}{RT_i}\right) \times (\Delta t + \tau_i)\}^n\right\} (1 \leq \mathrm{i} \leq \mathrm{m}) \qquad \text{Equation 2.4}$$

$$\tau_i = \frac{\sqrt[n]{-\ln[1 - \phi_{i-1}]}}{k_i} \qquad \text{Equation 2.5}$$

Where ϕ_i is the volume fraction of tempered martensite at the end of ith step, τ_i is a time constant by determined by the continuity relation that the volume fraction of tempered martensite calculated at the end of i-1th step is equal to that at the beginning of the ith step. Δt is the time step.

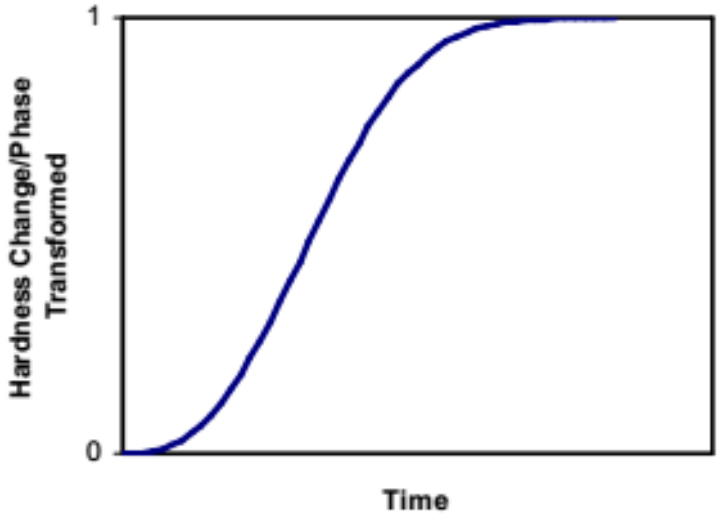

Figure 2.14 General shape of JMAK equation [41]

2.2 Resistance spot welding

2.2.1 Resistance spot welding fundamentals

Resistance spot welding is one of the most widely used sheet metal joining techniques in automotive industries since 1933. There are 3000 – 6000 resistance spot welds in a single car [43]. This joining technique has many advantages, such as, relatively low cost, ideal for high speed production due to short welding time, self-clamped, no filler metals required and easy to automate.

A typical welding cycle consists of 4 stages (Figure 2.15):

Squeeze time: the time between timer initiation and passing current. This time is to assure good contact at sheet interface by applying electrode force before the welding current is applied.

Weld time: the time that welding current is applied to the workpieces.

Hold time: the time during which the welding current is turned off while the electrode force is maintained. Thus, the molten metal solidifies during this time.

Off time: the time during which the electrode force is off, and the coupon is moved to another welding location. This is generally used when the welding cycle is repetitive. More features can be added into the welding schedules, such as preheat, upslope/downslope time, tempering time etc. [44].

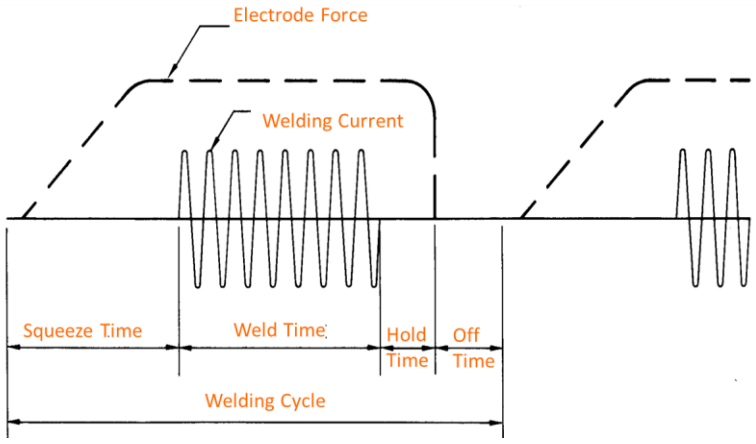

Figure 2.15 Schematics of simple weld schedule [44]

Nugget initiation and growth are controlled by the heat generation at faying surface/bulk sheets and the heat dissipation through the water-cooled electrode and the surrounding materials. The key factors for nugget growth are welding current, welding time, electrode force, electrode/sheet materials, electrode/sheet geometry and surface conditions of the sheets.

2.2.1.1 ***Welding current and time***

The heat generated during resistance spot welding is based on Joule's heating expressed by

$$Q = I^2Rt \qquad \text{Equation 2.6}$$

where Q is the total heat generated, I is the welding current, R is the total resistance, t is the welding time.

Welding current has the greatest effect on weld nugget growth. Welding current can be a single pulse, pulsation with several impulses and pulsation with different current/time in each pulse. Pulsation is used in welding thick sheets or complex stack-ups with varying sheet thickness/coatings/materials. In resistance spot welding of thin/thick/thick 3T stack-up, Gould et al. used a lower electrode force/a lower primary current for nugget formation at thin/thick sheet interface and a higher electrode force/higher secondary current for nugget generation at thick/thick sheet interface [7]. In resistance spot welding of thick sheets, compared to a single pulse with long welding time, using pulsation with cool time between pulses can reduce temperature at electrode/sheet interface and effectively increase electrode life.

Single phase alternating current (AC) and medium frequency direct current (MFDC) machine are most widely used in automotive industries. Hofman et al. [45] found that there is no major difference of the weld quality for AC and DC machine when welding 1 mm-thick DP600. On the other hand, tensile and cross-tension load increases when

welding 1.5 mm-thick DP600 with MFDC machine. Li et al. [46] showed that nugget diameter is larger for MFDC at low welding current compared to AC, while the effect of power source on nugget diameter is decreasing as welding current increases. Thus, a larger welding current range can be obtained with MFDC inverter. The possible reason is that dynamic resistance is higher at the first few cycles for DC welding processes due to a lack of current peaks and less contact interfaces breakdown.

Welding time is also a key factor for nugget growth. The welding time should be selected so that it is long enough to prevent insufficient nugget growth, but not overly long to cause expulsion. Moreover, with excess welding time, a steady state can be achieved at which there is no further nugget growth with increasing welding time. With the prerequisite of sufficient nugget growth, the welding time should be kept as short as possible to reduce the cost and cycle time of production.

2.2.1.2 ***Electrode force***

Coupons are squeezed with a certain electrode force before welding current is applied to make sure that the workpieces are in good contact at the faying surfaces. The localized forging force can be applied by traditional pneumatic driven welding gun and electric motor driven servo guns. With pneumatic driven welding gun, the squeeze time should be more than 0.6 seconds to achieve the set value. However, only 0.16 seconds is required to stabilize the clamping force by electric servo gun with more accurate control on position and velocity of the electrodes [47]. Moreover, in resistance spot welding of complex

stack-ups with thin sheet as the outer panel, a two-step force can be applied to facilitate nugget formation at thin/thick sheet interface[7] [48].

The effect of electrode force on contact resistance is shown in Figure 2.16. With high electrode force, contact resistance is almost independent of electrode force, which increases the consistency of weld quality. However, excessive electrode force may lead to large indentation and unnecessary electrode wear. With small electrode force, contact resistance is highly dependent on electrode force, which results in part-to-part variation in production even though the same welding schedule is applied. Moreover, early expulsion may occur with low electrode force, especially in resistance spot welding of coated AHSS.

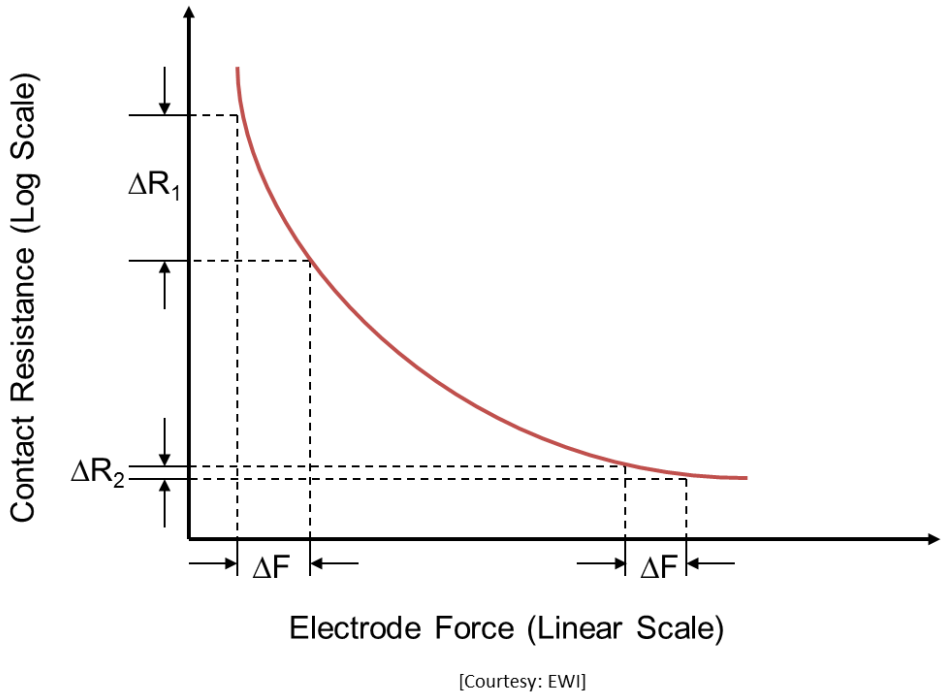

Figure 2.16 Effect of electrode force on contact resistance [44]

2.2.1.3 ***Resistances in spot welding***

The system consisting of workpieces and electrodes is the secondary circuit of the resistance welding machine. There are seven resistors connected in series in the secondary circuit of resistance spot welding of 2T stack-ups, which are bulk resistances of the workpieces, bulk resistances of the copper electrodes, contact resistance at the workpieces interface and contact resistance at the workpiece/electrode interface (Figure 2.17).

Bulk resistivities of various metals have been extensively studied, and the effect of temperature on resistivity of steel, aluminum and copper, is shown in Figure 2.18. In general, the resistivity of metals increases with increasing temperature. The resistivity of steel is about 20 times that of the copper electrode, even at elevated temperatures. Therefore, the heat generation is mainly at the sheet/sheet interface and bulk of the sheets due to high contact resistance at sheet/sheet (S/S) interface and bulk resistivity of the workpieces.

Contact resistance is highly depending on temperature, electrode force and the surface conditions of the materials, such as the coatings, surface roughness, oxide layer and contaminations. Oxide layer can have a great effect on contact resistance since it is non-conductive. However, an extremely thin layer of oxide has no obvious effect on the contact resistance [23]. Due to the complicated feature of contact resistance at sheet/sheet and sheet/electrode interface, it remains a challenging task to accurately measure temperature and pressure dependent contact resistance.

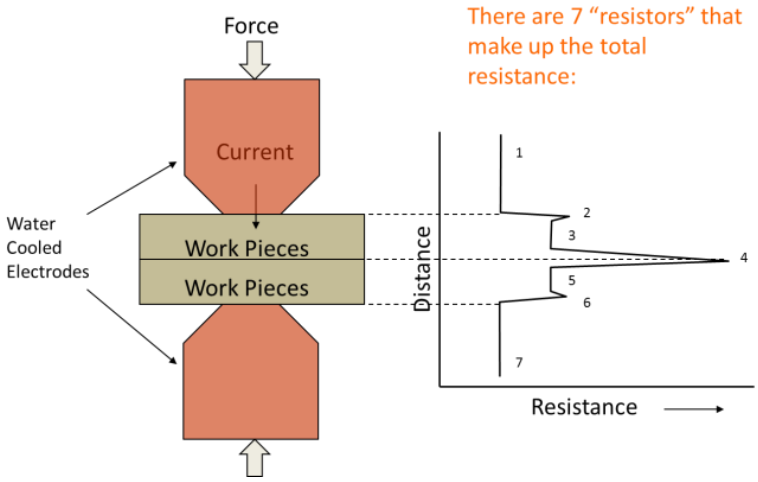

Figure 2.17 Resistances in resistance spot welding [44]

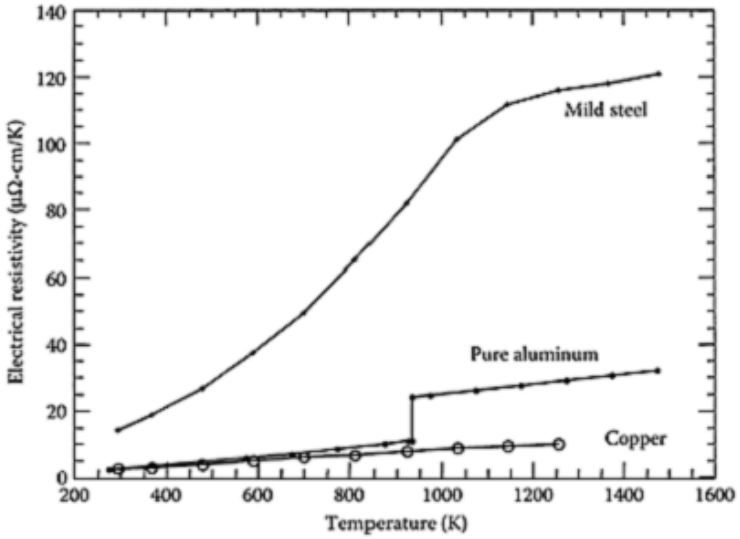

Figure 2.18 Effect of temperature on resistivity of several metals (Cu, Al, and a mild steel) [49]

Dynamic resistance is a measure of total electrical resistance change during welding. It can be calculated based on tip voltage and welding current. Dynamic resistance has been one of the signals that is commonly monitored during welding process since it is found to have good correlation with weld quality [49]. Gedeon and Eager [50] [51] identified different stages in the dynamic resistance curves of uncoated steel, galvannealed (GA)

steel and galvanized (GI) steel. Figure 2.19Figure 2.19 shows the generalized dynamic resistance curve. The sudden drop in Region 1 is due to the breakdown of the insulating films. Slight resistance increase in Region 2 is caused by bulk heating of coatings at electrode/sheet interfaces. Region 3 is due to completely melting of zinc coating, which reduces the contact resistance to be near to zero, while the temperature of sheets is not high enough to increase the bulk resistivity of the sheets. Region 4 is due to bulk heating of sheets. Soft zinc is pushed to the periphery of the nugget, which creates extra current paths and results in slight resistance reduction in Region 5. Region 6 is a continuous increasing in bulk resistivity due to the heating of the sheets. Region 7 is due to plastic deformation of the sheets, which increases the contact area. The sudden drop of resistance in Region 8 is due to expulsion. Among these stages, GI coatings exhibit all eight stages, GA coatings exhibit all stages except for 4 and 5, while uncoated steel exhibits only Stages 1, 6, 7, and 8.

In comparison, the dynamic resistance curve of Al-Si-coated hot stamped boron steels consists of seven stages, which is comparable to that of GA steel as shown in Figure 2.20. The unique stage is Stage 0, at which resistance increases rapidly till peak. The resistance increase is due to voltage build-up as current flows until it reaches the breakdown voltage of the insulating film, where the resistance achieves its peak value. Therefore, the peak of the dynamic resistance is different from the static resistance and it is significantly affected by the welding current as shown in Figure 2.21. As welding current increase, the peak resistance decreases. The possible reasons are as follows. Firstly, high welding current leads to low resistance since the breakdown voltage of the film is constant.

Secondly, high heating rate can effectively soften the asperities, which results in lower resistance [52].

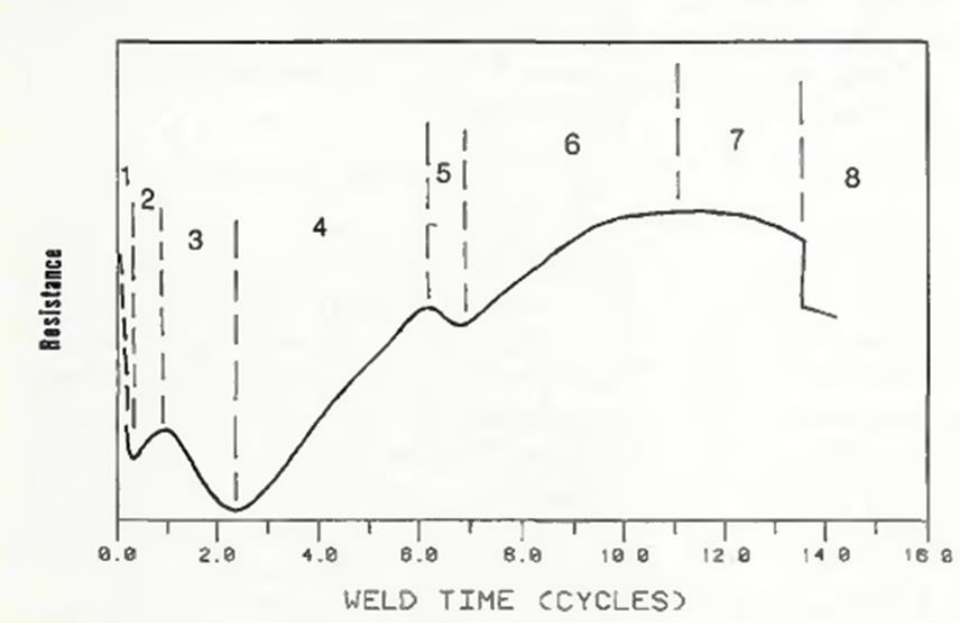

Figure 2.19 Generalized dynamic resistance curves [51]

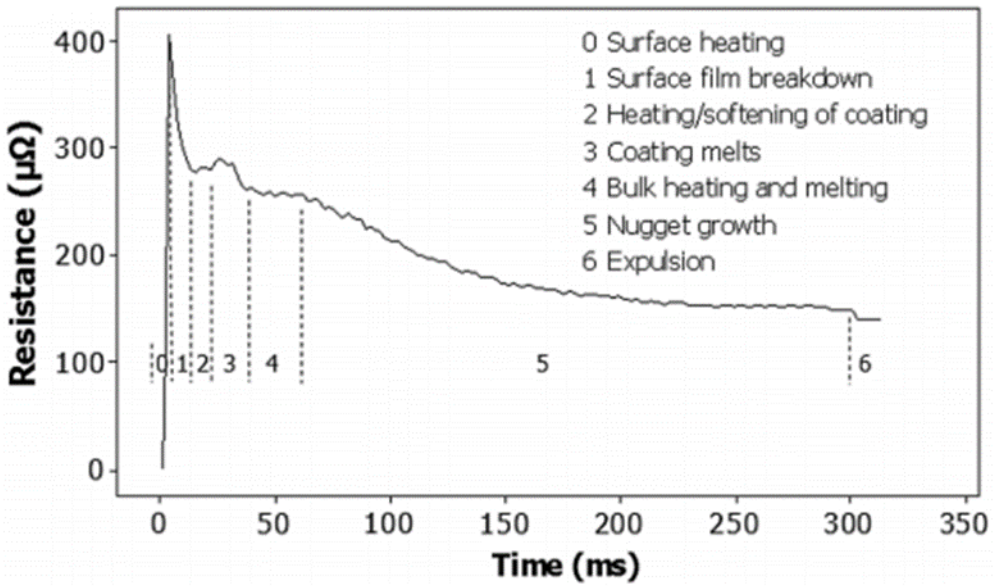

Figure 2.20 Dynamic resistance curve for Al-Si-coated hot-stamped boron steel [52]

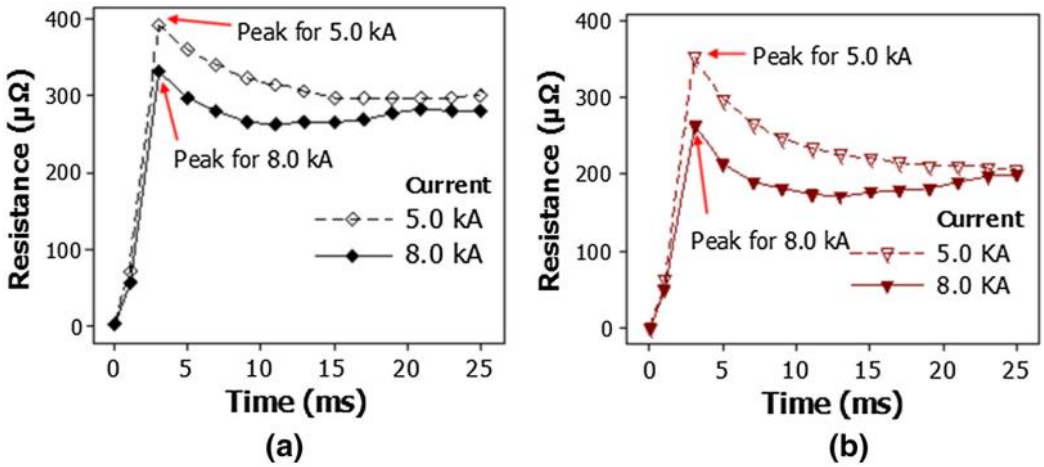

Figure 2.21 Initial peak resistance variation with welding current for (a) Al-Si-coated hot stamped steel, and (b) GA coated hot stamped steel [52]

2.2.2 Resistance spot welding of AHSS

The main issue in resistance spot welding of coated hot-stamped boron steel is the coatings and oxides. Therefore, the coatings need to be melted and squeezed to the periphery of the nugget. Jong et al. [53], Yu et al. [54] and Ighodaro et al. [2] studied microstructure and mechanical properties of resistance spot welded Al-Si and GA coated Usibor® 1500. Figure 2.22 shows the hardness distribution of resistance spot welded boron steel with different coatings in both as-received condition and after hot-stamping. A sub-critical heat affected zone (tempered zone) is shown in the region near to base metal with about 40% of hardness reduction for hot-stamped boron steel; this region is one of the potential failure locations in mechanical testing. There is negligible difference on the hardness distribution for hot-stamped boron steel with different coatings.

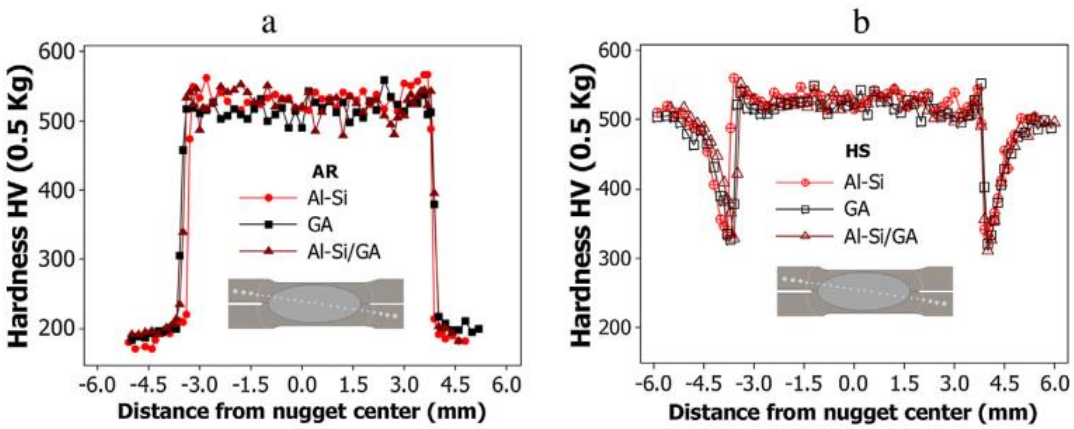

Figure 2.22 Microhardness distribution of resistance spot welded hot-stamped 22MnB5: (a) as-received (thus softened) condition, and (b) hot-stamped (thus hardened) condition [2]

Ji et al. [55] and Saha et al. [56] studied the effect of coatings on weldability of hot-stamped boron steel. For Al-Si-coated hot-stamped boron steel with the coating thickness of 43 μm, the weldable current range is 2.0 kA, while no weldable current range can be obtained for zinc-coated hot-stamped boron steel (Figure 2.23). For Al-Si-coated hot-stamped boron steel, the contact resistance is 1860 μΩ, which is comparable to that of the bare steel (1750 μΩ). This indicates that the oxide layer formed during hot-stamping process is so thin that it has little to no effect on the contact resistance. The coating of Al-Si coated hot-stamped boron steel consists of $FeAl_2$, Fe_2SiAl_2, and Fe (Al, Si) diffusion layer with thin layer of aluminum oxide at the top most surface. At the welding time of 2 cycles, a solid solution of Al and Si in α-Fe (Fe (Al,Si)) still exists at the interface with the other intermetallic layers melted and pushed away by the electrode force. With increasing welding time to 3 cycles, the solid solution of Fe (Al,.Si) is melted and squeezed out. The resolidified coating near to the notch of the spot welds (along the faying surfaces) is shown in Figure 2.24. The liquid coatings pushed to the periphery of

the weld zone create an additional current path, resulting in a better controlled weld nugget growth.

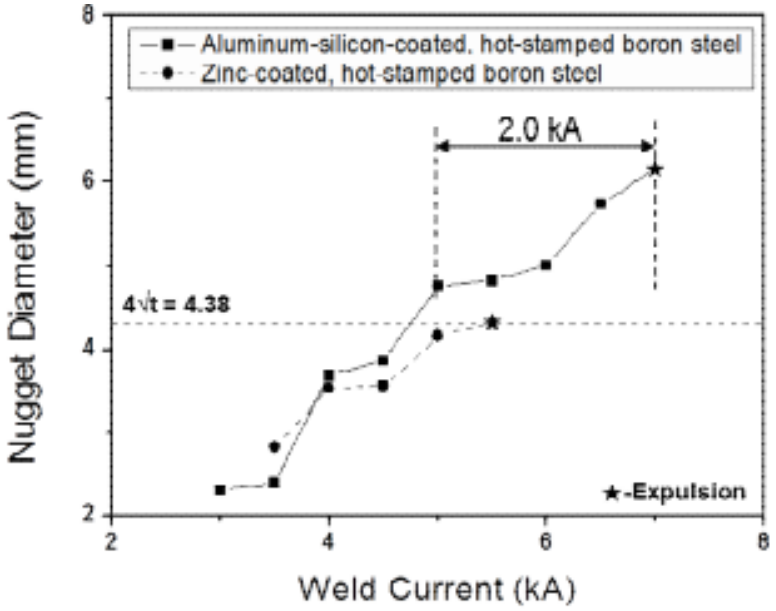

Figure 2.23 Comparison of weldable current range of Al-Si coated and zinc coated hot-stamped boron steel[55]

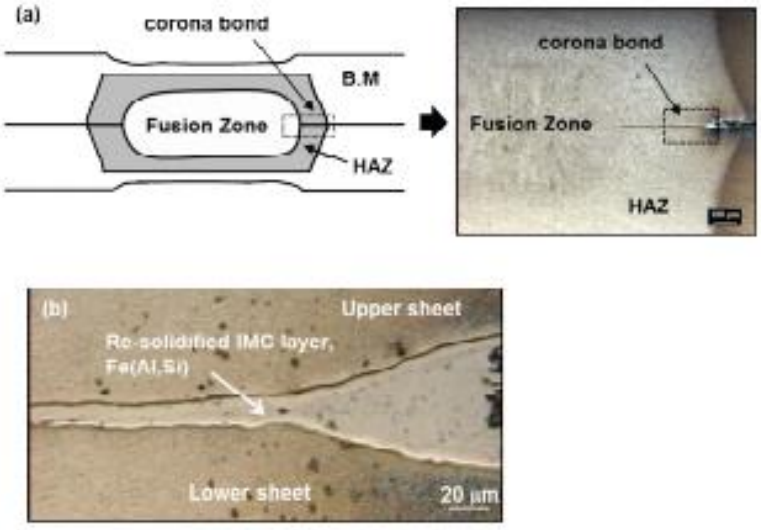

Figure 2.24 Coating at the periphery of the resistance spot welds in Al-Si coated hot-stamped boron steel[55]

2.3 Resistance spot welding process modeling

2.3.1 Process models

Between 1960s to 1970s, many analytical models were used by Greenwood [57], and Gould. et al. [58] to analyze the temperature distribution and nugget development of the spot welding process. However, no thermal-mechanical coupling was included in those early models to analyze stress distribution and its effect on current and temperature distribution.

In 1984, Nied et al. [59] created a 2D axisymmetric FEA model in commercially available software ANSYS to predict stress distribution, temperature profiles, nugget size and thermal expansion of electrodes, and the model was validated by experimental results of spot welding of 321 pickled stainless steel. Although temperature dependent thermal properties were used and latent of fusion was taken into account in the thermal calculation, the temperature dependent flow stress and electrical and thermal contact resistance of the surface element used was not clearly illustrated. Tsai et al. [60] used an axisymmetric thermomechanical coupled FE model to predict the stress distribution at electrode/workpiece and workpiece/workpiece interfaces and nugget evolution. Stress concentration can be observed at the edge of the electrode at both electrode/sheet and sheet/sheet interfaces at squeeze cycle. A ring-like weld nugget was formed at an offset distance away for the center axis of the electrode, and the molten metal subsequently expands inward to engulf the center of the nugget during the welding cycles. Nugget growth at stack-ups with unequal thickness and dissimilar materials were investigated.

However, several factors, e.g., contact resistance, and coefficient of friction, were not investigated.

Hou et al. [61] developed a 2D axisymmetric thermo-elastic-plastic model in ANSYS to analyze the contact pressure distribution, residual stress and displacement of the electrode. The temperature field from thermal-electrical analysis was applied as load in each node. The temperature dependent plastic properties of the workpieces and electrodes were considered in the model. Nodeh et al. [62] used a 2D axisymmetric model to predict residual stresses in resistance spot welds and compared with the experimental data measured by X-ray diffraction. Tensile residual stress existed at the weld center and they reduced in radial direction with compressive stress located at the edge of the weld. Eisazadeh et al. [63] also developed a coupled thermo-electro-structural finite element model to predict temperature distribution and nugget size in spot welded steel. The highest temperature is always at the center of the faying surfaces. The effect of contact resistance and electrode force on nugget formation at the faying surfaces was discussed. With increasing contact resistance caused by surface condition variation, nugget size increased. With high electrode force, nugget size decreased due to increase in contact area and decrease in contact resistance. However, the contact resistance was not temperature/pressure dependent. Moshayedi et al. [64] developed a fully coupled 2D electro-thermo-mechanical finite element model to study the effect of welding time and current on nugget development of AISI 304L stainless steels using ANSYS.

The aforementioned modeling method for RSW of steels has also been used for RSW of dissimilar metals. For example, Wang et al. [65] and Wan et al. [66] developed a fully coupled multi-physics model for resistance spot welding process simulation of Al to steel. The nugget size, shape, dynamic current flow and deformation was accurately predicted. The temperature profile at Al/steel interface and parabolic growth kinetics were used in prediction of intermetallic compound thickness [65][66].

2.3.2 Model for contact resistance

Contact resistance is a crucial factor that effects nugget formation at the first few cycles. To accurately measure the electrical and thermal contact resistance changing with temperature and pressure is indispensable for accurate prediction of nugget size and indentation in finite element simulation of resistance spot welding process. Babu et al. [67] developed an empirical model for prediction of electrical contact resistance of steel/steel and steel/copper interface. The contact resistance depends on the bulk resistivity, yield strength and the number of contact asperity at the interface. The model agrees well with the experimental results of pressure-dependent contact resistance at low contact pressure. The discrepancy with experimental results at high contact pressure is due to neglecting work hardening of asperities.

$$R_{CA} = (\rho_1 + \rho_2)\left[\frac{1}{4}\left(\frac{\pi\sigma_{YS}}{\eta P}\right)^{1/2} + \frac{3\pi}{16\eta^{1/2}}\right] \qquad \text{Equation 2.7}$$

where $\rho_1 \; and \; \rho_2$ are the bulk resistivities of the two workpieces, η is number density of asperities that are in real contact, σ_{YS} is the yield strength of the sheet, and P is the pressure.

Coatings, i.e. galvanized coating (GI), galvannealed coating (GA), and aluminium-silicon coating, have significant effect on contact resistance. Rogeon et al. [68] measured electrical contact resistance (ECR) at electrode/sheet and sheet/sheet interfaces of galvanized DP600 and XSG steels and uncoated XEG steels. A special device was used to measure the temperature and pressure dependent ECR. Kaars et al. [69] developed an improved formula for electrical contact resistance of Al-Si coated hot-stamped boron steel which considered both temperature and pressure effects. It was shown that the contact resistance was a strong function of the local temperature, and the electrical contact resistance was up to 10 times higher at steel/steel interface than electrode/steel interface. It is thus essential to utilize the electrical contact resistance formula that takes into account the effect of Al-Si coating (such as the one developed by Kaars et al. [69]) in the RSW process modelling.

$$r_g(T,P) = r_0 \cdot \left(\frac{P - P_k}{P_0 - P_k}\right)^{\varepsilon_P} \cdot \left(\frac{T - T_{lim} + (T_0 - T) \cdot 2^{-\frac{1}{\varepsilon_T}}}{T_0 - T_{lim}}\right)^{\varepsilon_T} \qquad \text{Equation 2.8}$$

where r_0 is the base resistance value, P is the contact pressure, P_k is the corrective pressure (kept at -5 MPa in this model), P_0 is the reference pressure, ε_P and ε_T are the pressure and temperature exponents, respectively, T is the local interface temperature,

T_{lim} is a so-called half-resistance temperature at which the value of base resistance r_0 is halved, and T_0 is room temperature (293.15 K).

2.3.3 Metallurgical model

Hot-stamped boron steels in the press-hardened state possess fully martensitic microstructure which can be severely softened by the formation of SCHAZ during RSW, with about 40% reduction in hardness compared to base metal (BM) [55,70–72]. Such severe HAZ softening is not typically observed in resistance spot welded low carbon steels, e.g., dual phase (DP) 590 or lower strength steels. The cause for the HAZ softening is the over-tempering of BM martensite due to exposure to elevated temperature, resulting in the formation of fine quasi-spherical/plate-like interlath cementite. As such softening has a significant effect on the load bearing capacity and failure mode [16,19], ability to quantitatively predict the HAZ softening is essential to control and optimise resistance spot welds. While an integrated thermal-microstructure model was developed by Babu et al. for resistance spot welded low carbon steel [74], there is a lack of microstructure model for spot welded hot-stamped boron steels.

2.4 Mechanical testing of resistance spot welds

2.4.1 Mechanical testing

2.4.1.1 *General mechanical testing*

During service, the resistance spot welds can experience both shear loading due to the relative motion between sheets and tensile loading due to the separating force applied

normal to the sheets [75]. Except for quasi-static testing, fatigue and impact loading condition are considered. Moreover, rough road/driving may lead to overloading of the vehicle. Tensile shear test (TST), coach-peel test (CP) and cross-tension/U-tension test have been used to represent the shear loading, tensile loading due to bending moment, and pure tensile loading condition, respectively. The schematics of each testing methods are shown in Figure 2.25.

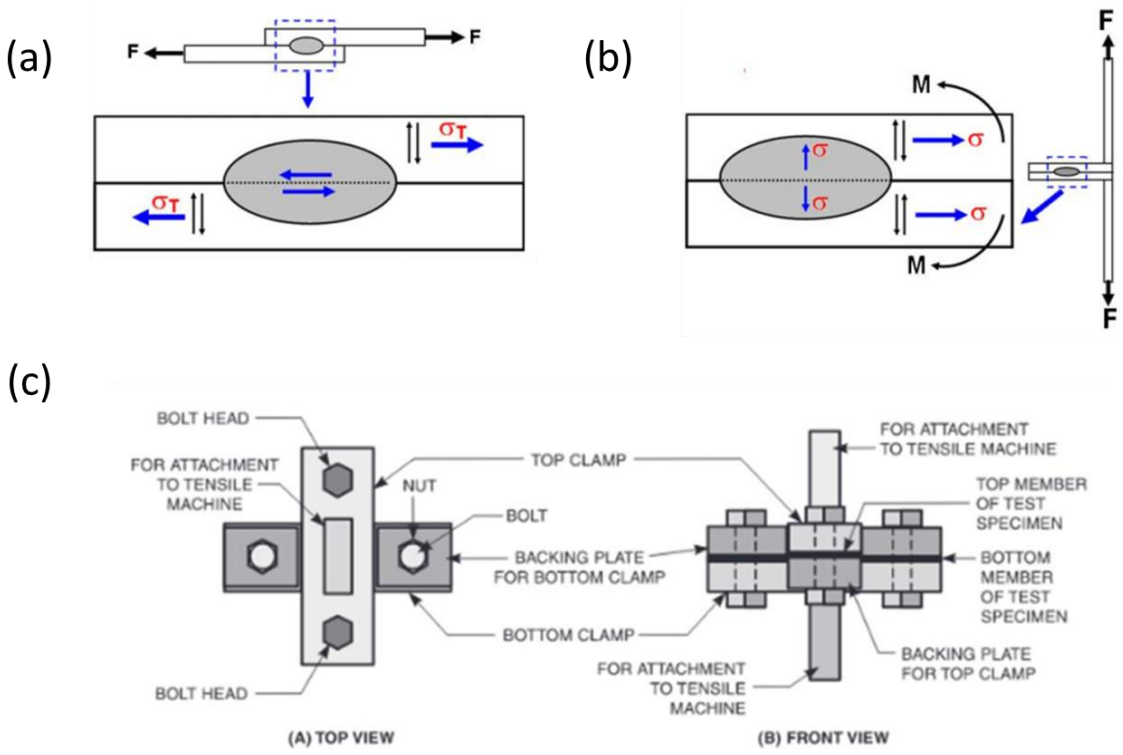

Figure 2.25 Schematics of loading condition in (a) tensile shear test (TST), (b) coach-peel test (CP), and (c) cross-tension test (CTT) [76]

The typical load-displacement curve during TST test is shown in Figure 2.26Figure 2.26. The key parameters that can be used to describe the mechanical behavior of the spot welds are the peak load, elongation at the peak load and the failure energy which is

defined by the area under the load-displacement curve until peak load. High fracture energy requires both high peak load and elongation.

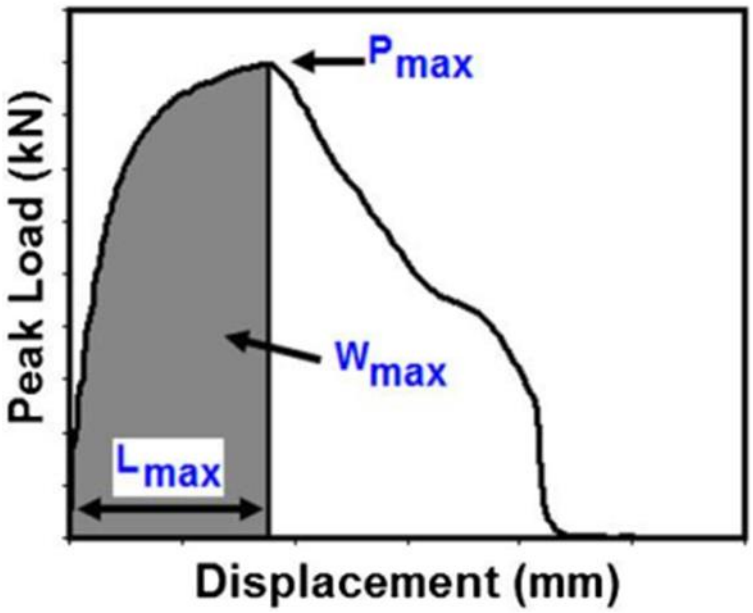

Figure 2.26 Typical load-displacement curve in TST [77]

2.4.1.2 ***Wedge testing***

Wedge testing is a novel *in-situ* mechanical testing method for resistance spot welds developed by Payen [78] and Lacroix et al [79]. CTT is commonly used in automotive industries to measure the strength of resistance spot welds. However, the failure criteria derived from CTT are based on empirical consideration of different failure modes observed, which is inconsistent especially for advanced high strength steels. Wedge test is developed to simulate CTT, therefore, the loading mode is mode I. Meanwhile, to observe the crack initiation and propagation during loading, the sample is cross-sectioned

in half. Moreover, compared to other testing methods, the observed surface in wedge test moves/deforms as little as possible for improved imaging.

In Payen's wedge test, the angle of the wedge is 73.7^{o}. The free surface is fine polished and etched. The whole setup is placed in a SEM chamber as shown in Figure 2.27. As the spot weld is made with welding current just below expulsion current to ensure maximum strength, different notch shapes can be created with "bi-notch" on one side and sharp notch on the other side in DP780. Two wedges on both sides of the nugget and one wedge on sharp notch side of the nugget were tested separately. Upper critical heat affected zone/inter-critical heat affected zone failure can be observed on bi-notch side. In single wedge testing, crack propagates through the fusion zone, which results in an interfacial fracture.

Peer et al. [80] painted black and while speckle patterns on the cross-section surface and measured the strain distribution during loading using digital image correlation (DIC) in resistance spot welded 2T hot stamped boron steels. The dimension of the wedge and the schematics of the single-sided wedge testing are shown in Figure 2.28 and Figure 2.29, respectively. The effect of weld nugget size on failure modes was studied. It shows that failure modes change from interfacial fracture to weld metal, then to SCHAZ. When nugget size is smaller than 5.8 mm, interfacial fracture occurs. When nugget size is above 5.8 mm, crack deviates through weld nugget/CGHAZ/SCHAZ, as shown in Figure 2.30. Therefore, the failure criterion is closer to $5\sqrt{t}$, where t is the thickness of the sheets, to avoid an interfacial failure.

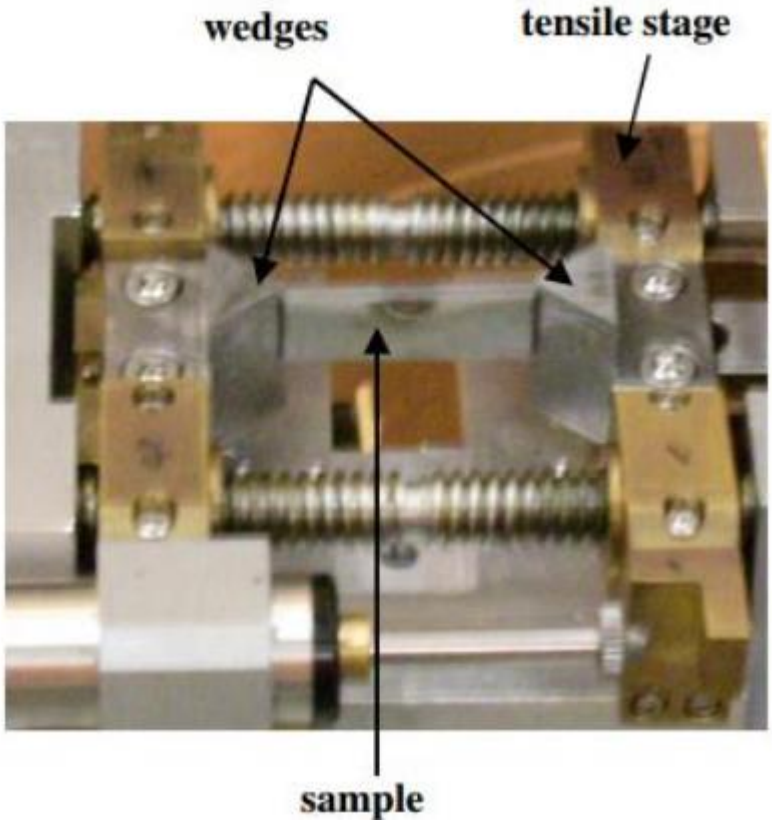

Figure 2.27 Set-up for wedge test in SEM [78]

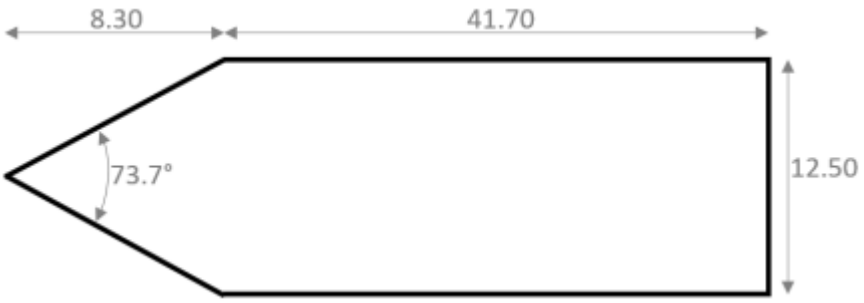

Figure 2.28 Geometry of the wedge with the wedge angle of 73.7^{o} [80]

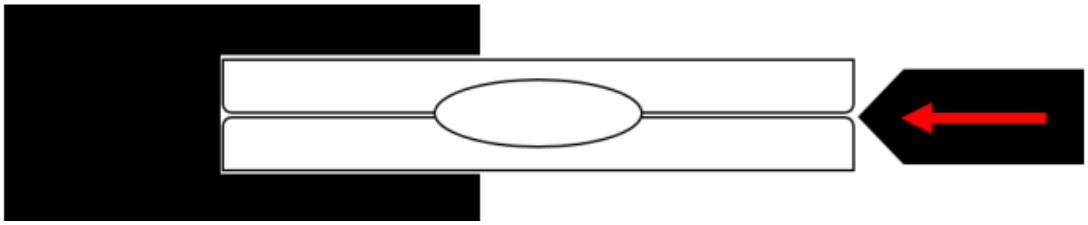

Figure 2.29 Schematics of single-sided wedge test with one side clamped and wedge inserted on the other side [80]

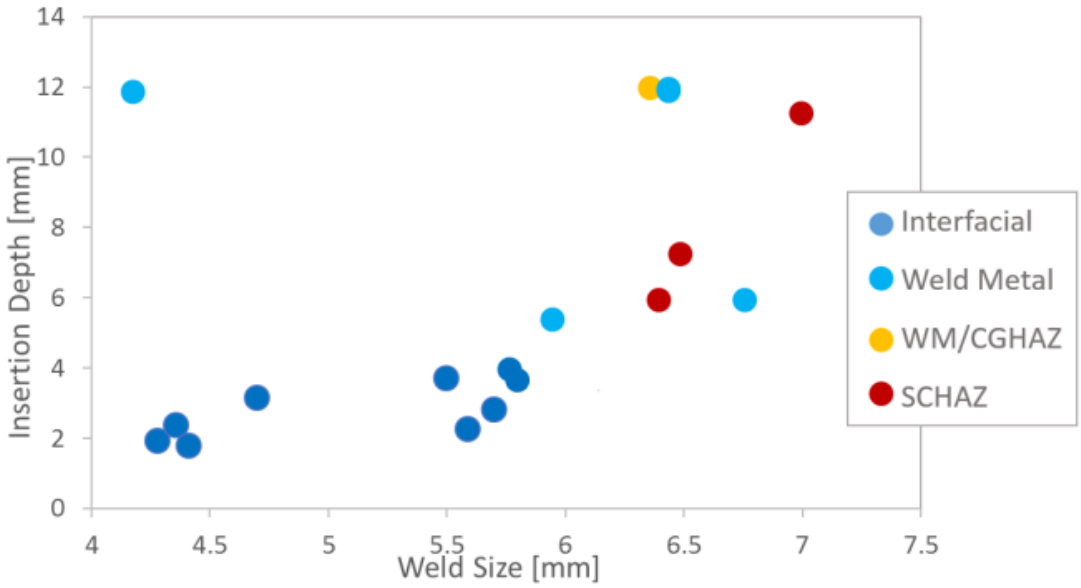

Figure 2.30 Effect of weld nugget size on failure modes of resistance spot welded hot-stamped boron steel [80]

2.4.2 Fracture modes

8 different failure modes have been utilized in automotive industries to describe failure. They can be further summarized into 4 categories: interfacial fracture (IF), pull-out failure (PF), partial interfacial fracture (PIF), and partial thickness-partial pullout (PT-PP) as shown in Figure 2.31.

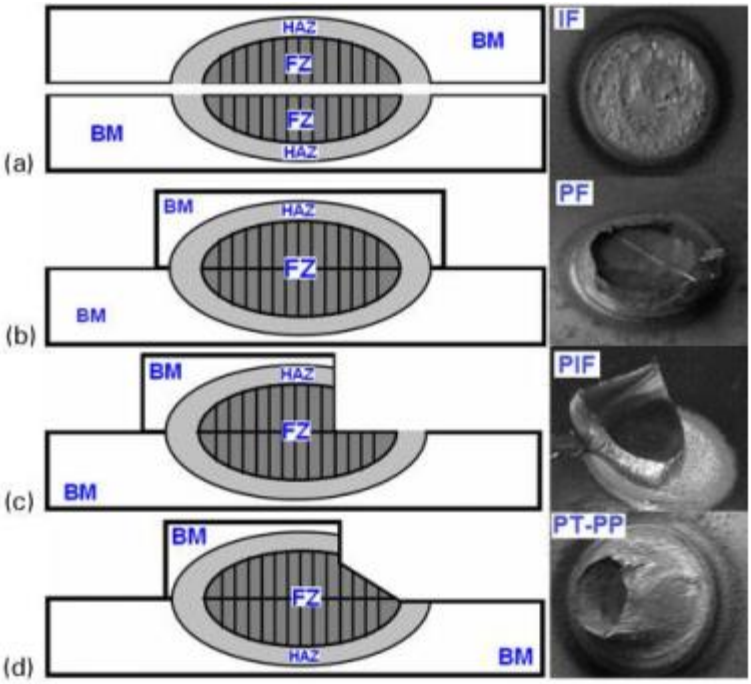

Figure 2.31 Typical types of failure modes during tensile shear testing: (a) interfacial fracture, (b) button pull-out failure, (c) partial interfacial fracture, and (d) partial thickness-partial pullout [75]

2.4.3 Key factors for fracture

There are numerous factors that may affect fracture behavior of spot welds. Dancette [81] classified them into three categories: geometrical factors (weld size, coupon thickness, etc.), loading modes (lap-shear tensile, cross tension or mixed), and metallurgical factors (HAZ softening, microstructure brittleness, porosity in weld nugget, etc.).

The effect of each factor on failure behavior of AHSS resistance spot welds was explained in detail by Pouranvari et al. [75] [82][83].

2.4.3.1 ***Geometrical factors***

(i) Weld nugget size

Weld nugget size is the width of the fusion zone, which is the most important factor for fracture behavior of spot welds. Larger nugget size reduces the stress of the weld nugget compared to the small one with same load. Thus, it is more resistant to interfacial fracture. The minimum weld nugget size for a specific sheet thickness based on many industrial standards for button pull-out is

$$D = K\, t^{0.5} \qquad \text{Equation 2.9}$$

where D is the weld nugget size, t is sheet thickness, and K is a constant varying from 3 to 6. In automotive industries, $D = 4\, t^{0.5}$ is used to specify the minimum weld size [84].

(ii) Sheet thickness

Thicker sheets require larger nugget size to promote button pull-out failure. Thicker sheet increases sheet stiffness, which prevents rotation during tensile shear test. Thus, higher force is required for necking and interfacial fracture mode (IF) is promoted [85]. Moreover, the cooling rate in thicker sheets is lower than that in thinner sheets, which may change the microstructure and hardness of weld nugget and HAZ [82].

(iii) Electrode indentation

Large electrode indentation reduces sheet thickness and results in stress concentration at the root of the indentation, which promotes button pull-out failure (PF). However, the load bearing capacity and the fracture energy absorption would be reduced [86].

(iv) Notch shape

The shape of the notch, e.g., sharp, square, and bi-notch, can affect the failure modes of the spot welds due to different stress concentration factors. The shape of the notch is significantly affected by welding parameters and asymmetric notch can be created if there is electrode misalignment.

2.4.3.2 ***Loading modes***

Resistance spot welds can experience tensile shear load, cross-tension load and mixed loads. Failure behavior of spot welds depends on loading condition as well. In quasi-static tensile shear test, pull-out failure occurs in the softened HAZ in 22MnB5 in dissimilar resistance spot welded joints of a high strength low alloy steel HC340LAD and a hot-stamped boron steel 22MnB5 (Figure 2.32). On the other hand, the pull-out failure takes place through CGHAZ when the weld is subjected to KS2-90° test.

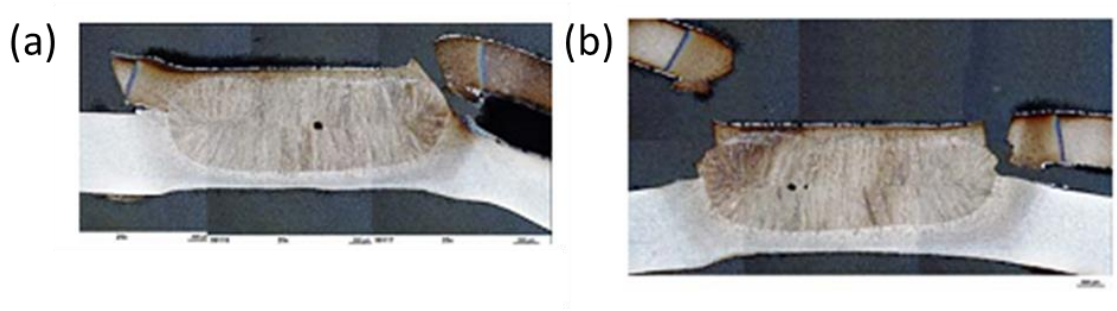

Figure 2.32 (a) Pull-out failure in SCHAZ of 22MnB5 in tensile shear test (TST), and (b) pull-out failure in CGHAZ of 22MnB5 in KS2-90^{o} in resistance spot welded 22MnB5/ HC340LAD [3]

2.4.3.3 ***Metallurgical factors***

(i) Porosity and shrinkage voids in the weld nugget

The effect of porosity or shrinkage voids on the failure behavior depends on the location of the voids. In addition, the extent of such effect is complicated by the failure mode of the welds. It has been reported that the shrinkage voids tend to form at the center of the weld. In button pull-out failure mode (PF), the shrinkage voids would not have an obvious effect on the loading bearing capacity. However, in interfacial failure mode, the weld area is reduced due to the existence of the porosities, thus the load bearing capacity and absorbed fracture energy are also reduced.

(ii) Hardness ratio of fusion zone and pull-out failure location (H_{FZ}/H_{PFL})

With increasing H_{FZ}/H_{PFL} (either increasing the fusion zone hardness or decreasing the pull-out failure location hardness, such as HAZ softening), the critical weld size for pull-out failure decreases, and PF takes place at lower peak load. Thus, another reason that

AHSS tends to have interfacial fracture is that the base metal of AHSS has high hardness and thus low H_{FZ}/H_{PFL} (Figure 2.33).

Table 2.2 Hardness, failure mode and predicted critical weld size for different steels [83]

Material	H_{BM}	H_{PFL}	H_{FZ}	H_{FZ}/H_{PFL}	P	Failure mode		Predicted D_C (mm)	$4t^{0.5}$
						IF	PF		
DP600	201.1 ± 2.09	201.1 ± 2.09	418.6 ± 3.78	2.09 ± 0.01	0.9	D < 6.3	D > 6.3	6.37 ± 0.05	4.89
DP780	254.2 ± 3.08	243.6 ± 8.5	399.2 ± 4.49	1.64 ± 0.04	0.9	D < 7.7	D > 8	8.13 ± 0.23	4.89
DP980	301.3 ± 2.23	253.2 ± 17.31	483.8 ± 3.03	1.91 ± 0.12	0.9	D < 6.9	D > 7.1	6.97 ± 0.44	4.89
DQSK	119.3 ± 2.22	119.3 ± 2.22	290.2 ± 7.66	2.41 ± 0.06	1	D < 4.9	D > 5	4.96 ± 0.13	4.89
AISI304	220.5 ± 1.56	199 ± 12.94	208.6 ± 6.38	1.05 ± 0.06	1	D < 8.5	-	11.41 ± 0.7	4.89

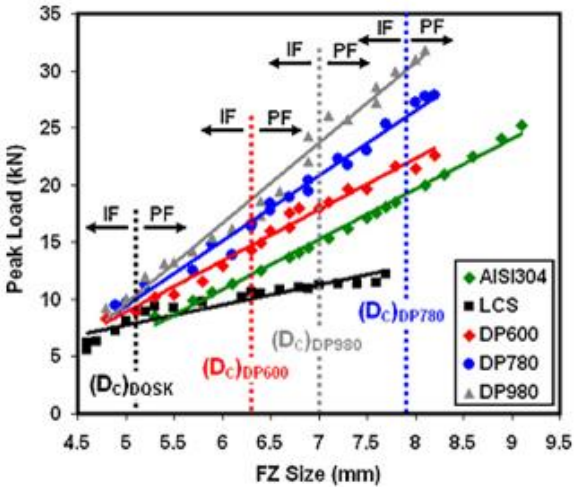

Figure 2.33 Effect of peak load and failure modes on FZ size [83]

2.4.4 Failure prediction of spot welds

Since resistance spot welded AHSS possesses complex microstructure with HAZ sub-regions consisted of varying mechanical properties, it is difficult to accurately predict the failure behavior based on simplified crash model.

Sommer et al. [4] investigated the effect of tempered zone on mechanical properties of resistance spot welded hot-stamped 22MnB5. The separated spot welded 22MnB5 sheets by electrical discharge machining (EDM) are tensile tested and the load displacement curve is compared to 22MnB5 base metal. The ultimate tensile strength of the sample with spot weld is 260 MPa lower than that of the base metal. The uniform elongation of the sample with spot weld is between 0.0175 and 0.02, which is lower than that of base metal (0.05) as shown in Figure 2.34. Figure 2.35 shows the strain distribution of tensile sample with spot weld under axial loading. Strain localizes at the softened HAZ with increasing load, resulting in crack initiation in the soften HAZ. Therefore, to accurately predict the failure behavior in resistance spot welded AHSS, it is indispensable to characterize the weld microstructure including weld nugget, HAZ sub-regions especially the softened HAZ and base metal and extract their constitutive behaviors.

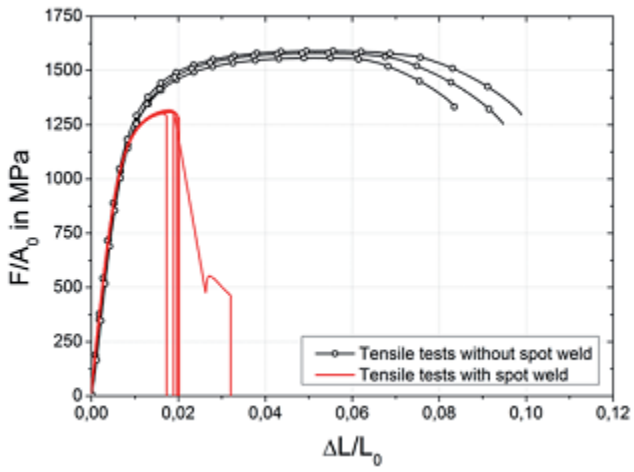

Figure 2.34 Load displacement curves of tensile sample with and without spot weld [4]

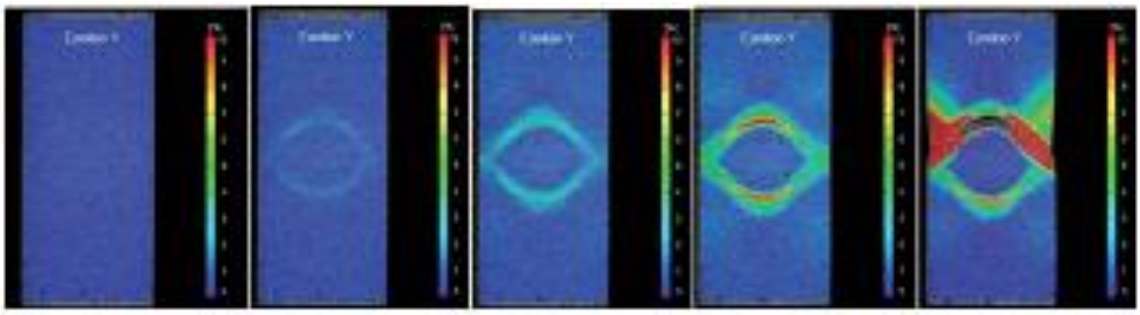

Figure 2.35 Strain distribution of tensile specimen with spot weld at 1100 MPa, 1250 MPa, 1300 MPa, 1320 MPa (just before crack initiation) and after crack initiation [4]

2.4.4.1 ***Local constitutive behavior extraction***

Dancette et al. [6] extracted the local mechanical properties of the SCHAZ and CGHAZ, the two potential failure locations, of resistance spot welded DP steels using thermo-mechanical simulator Gleeble® 3500. The thermal histories of SCHAZ and CGHAZ were simulated by process modeling using a commercially available FEA software SORPAS. Then, the predicted thermal profiles were used as inputs for physical simulation by Gleeble. The peak temperatures of the physical simulation were targeted at 700 ^{o}C and 1200 ^{o}C for SCHAZ and CGHAZ respectively. To accurately simulate the rapid heating and cooling rate, the heating rate was set to be 2000 ^{o}C/s. Cooling rate of a few hundreds of ^{o}C/s was obtained by a helium-gas-cooling device. Water quenching was also used to achieve the highest cooling rate. The cooling rate simulated by SORPAS was 3000 ^{o}C/s at 700 ^{o}C for 1 mm-thick DP sheets, which was between the cooling rate of water quenching (6700 ^{o}C/s at 700 ^{o}C) and the fastest He-quenching (600 ^{o}C/s at 700 ^{o}C). The Gleeble simulated samples with recreated microstructure were machined into dog-

bone shape and the constitutive behaviors of SCHAZ and CGHAZ were measured by quasi-static tensile testing, which is shown in Figure 2.36.

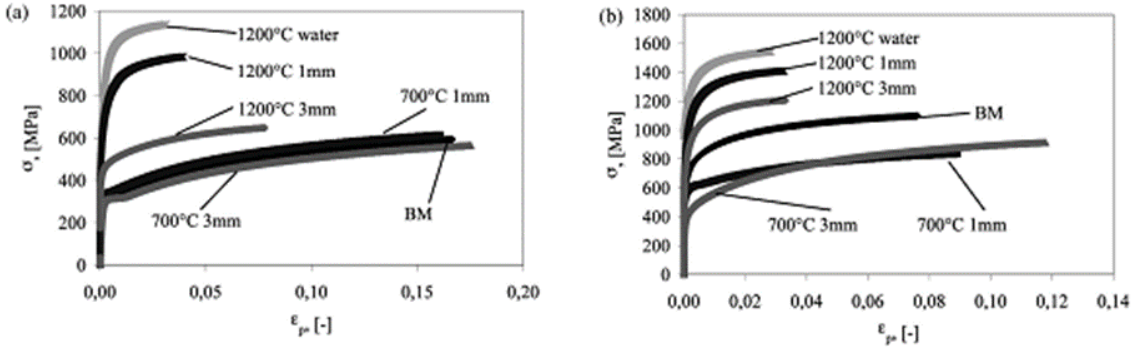

Figure 2.36 Constitutive behaviors (true stress vs. true strain) in tension of SCHAZ and CGHAZ of resistance spot welded (a) DP 450, and (b) DP 980 steels [6]

Ullner et al. [87] predicted the local stress-strain of resistance spot welded AHSS, i.e. TRIP steel (HCT690T) and a martensitic steel (HDT 1200 M), by instrumented indentation test with representative stress-strain (RS) method and artificial neural networks (NNs) method. They used a spherical indenter. For RS method, based on cyclic indentation, the yield strength and strain hardening coefficient are calculated. The elastic-plastic properties of steel are then estimated by a power law. An example of calculated true stress and true strain is shown in Figure 2.37.

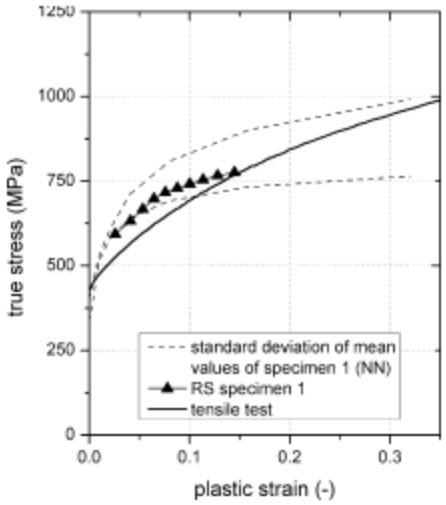

Figure 2.37 Comparison of stress-strain curve generated by IIT and tensile testing [87]

2.4.4.2 ***Failure prediction by FEA***

Burget et al. [3] simulated the deformation and fracture behaviors, e.g. load-displacement curves, peak load, fracture locations, of resistance spot welded 1mm-thick hot-stamped 22MnB5 and 1.5 mm-thick microalloyed high strength low alloy steel HC340LAD under different loading conditions, such as pure shear, pure axial loading and mixed loading conditions (Figure 2.38). The parameters of Gologanu material model and Thomason fracture criteria were determined by inverse simulation of smooth and notched sample of BM, HAZ and the weld nugget of the two steels. Then the parameters were used for prediction of fracture behavior of dissimilar resistance spot welds by Abaqus/Explicit. Base metal, weld metal and supercritical HAZ (including CGHAZ, FGHAZ and ICHAZ) were assigned same constitutive behaviors based on tensile testing of base metal. Constitutive behavior of nugget was measured by reduced tensile sample, while stress strain curve of SCHAZ was generated by quasi-static tensile testing of

Gleeble simulated sample with identical microstructure. The stress-strain curve up to necking was generated. The calculated stress-strain curve under shear, axial and mixed shear and axial loading conditions corresponded well with the respectively experimental results. Moreover, the simulated fracture locations under tensile shear loading was at SCHAZ of hot-stamped 22MnB5, while button pull-out took place at CGHAZ of hot-stamped 22MnB5 under axial loading, KS2-30º and KS2-60º (Figure 2.39).

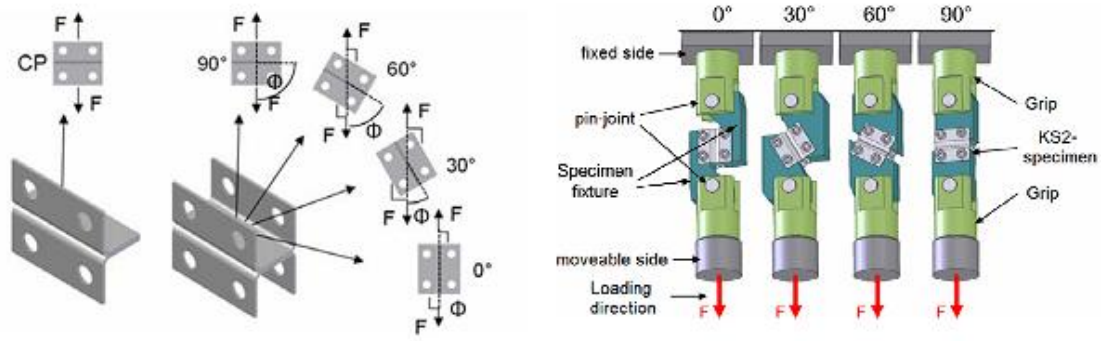

Figure 2.38 Clamping conditions for KS2-coupons with different loading angles [3]

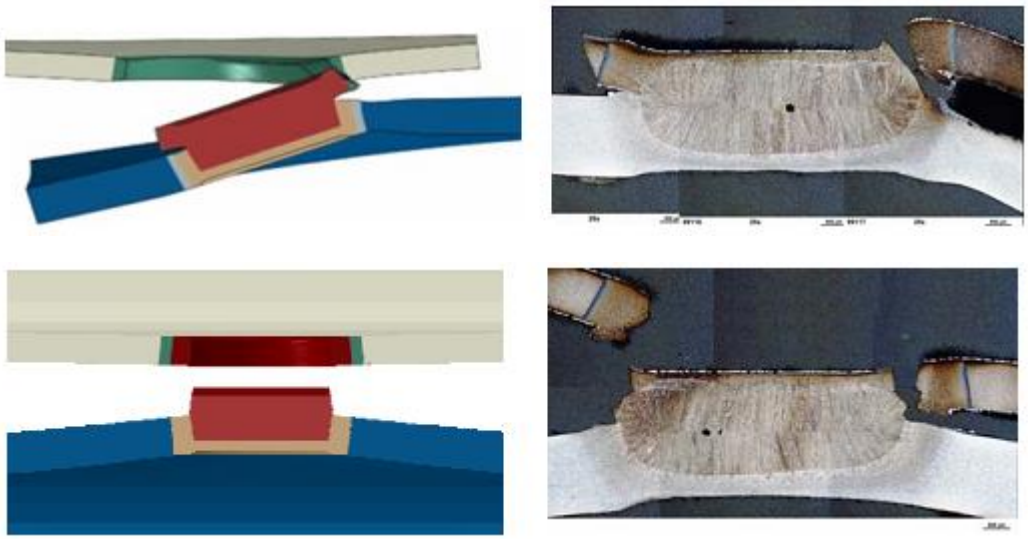

Figure 2.39 Comparison of fracture locations predicted by FEM and experimental data (a) calculated tensile shear fracture in SCHAZ of hot-stamped 22MnB5, and (b) calculated pull-out button in CGHAZ of hot-stamped 22MnB5 under KS2-90^{o} loading condition [3]

Sommer et al. [4] extracted the local stress-strain curves of the weld metal, SCHAZ and base metal based on simulated welding of hot-stamped 22MnB5 using Gleeble. The failure curves, defined as equivalent plastic strain as a function of stress triaxiality, for each region were obtained by inverse simulation of the tensile and shear tests. To validate the materials model, a tensile test with SCHAZ created by spot welding and a three-point bending test on components were simulated. A half of the tensile sample was simulated with eight-node solid element using LS-DYNA. Three regions, i.e. fusion zone (FZ), SCHAZ, and BM, were defined. The calculated reduction in load-bearing capacity of the specimen due to the existence of the softened HAZ correlated well with the experiment results as shown in Figure 2.40.

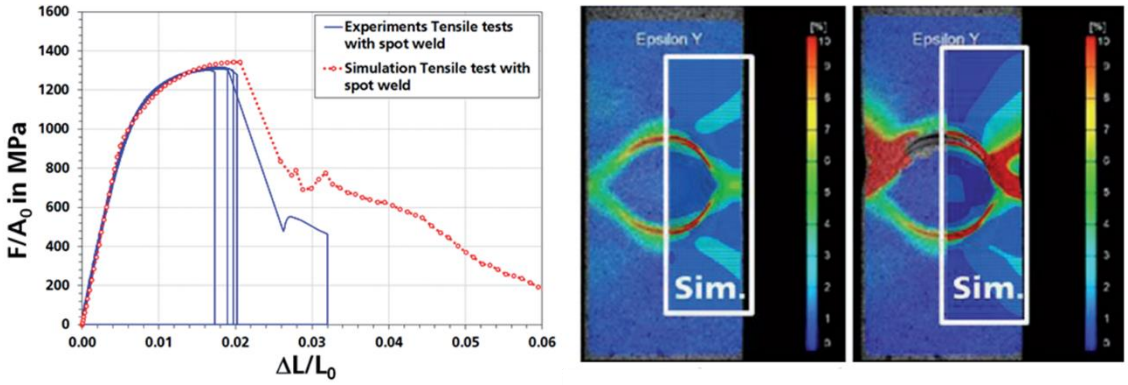

Figure 2.40 Measured and predicted stress-strain curve of tensile test with spot welds and the comparison of measured and predicted axial strain distribution immediately before and after crack initiation in the softened HAZ [4]

Due to the complexity of the crash model, simplified model is required while the crack initiation in the softened HAZ and propagation into the base metal needs to be taken into account in UHSS spot welds. For a simplified model, shell elements with coarse mesh have been used. To minimize the mesh size dependency, the failure curves were scaled for different mesh size. To validate the model, the tensile test with spot welds has been simulated with different mesh size of 0.75 mm, 1.5 mm and 3 mm as shown in Figure 2.41. The width of the SCHAZ is affected by the mesh size since the SCHAZ is modelled by one single row of shell element. The measured and predicted stress-strain curves are shown in Figure 2.42. The predicted stress-strain curve with small mesh size of 0.75 mm shows good agreement with the experimental results. On the other hand, the stress is underestimated for the large mesh size of 3 mm, which is due to the unrealistically large SCHAZ. To better fit the experimental results with the model using coarse mesh, the yield and failure curves of the SCHAZ were adjusted. However, this method is purely

phenomenological. Thus, to apply the materials model extracted for fine mesh solid element into the crash model with coarse mesh shell element is still challenging.

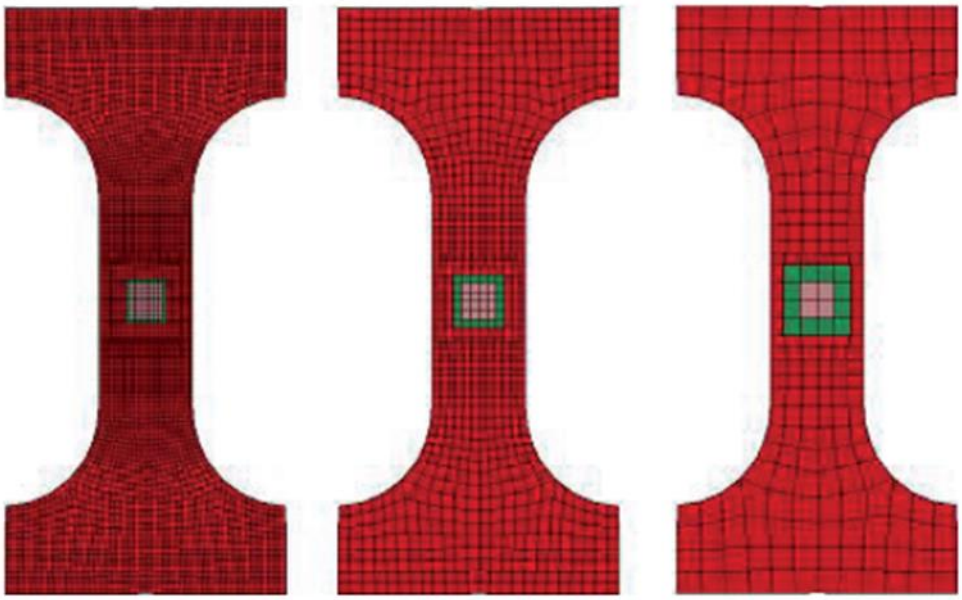

Figure 2.41 FE modeling of tensile tests with spot welds with the mesh size of 0.75 mm, 1.5 mm and 3 mm [4]

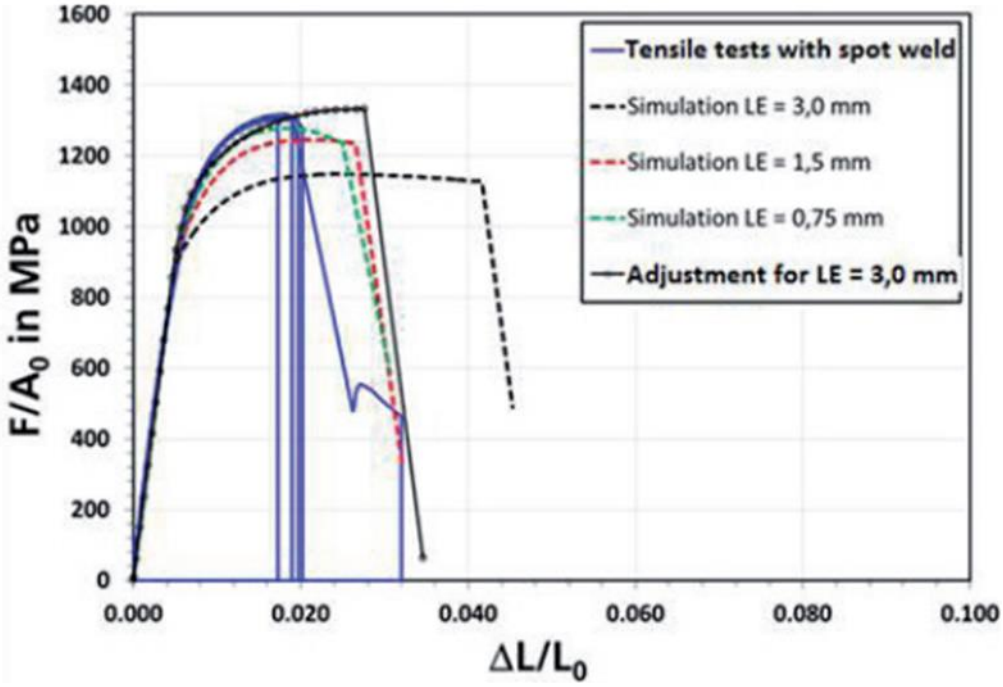

Figure 2.42 Comparison of the measured and predicted stress-strain curves with different mesh sizes [4]

2.5 Resistance spot welding of complex stack-ups

Smart structural design with complex stack-ups of AHSS offers additional opportunity to address the need for increasing fuel efficiency and improving the crashworthiness of a vehicle. Complex stack-ups is usually defined as more than two sheets with similar/dissimilar materials and equal/unequal sheet thickness [7].

Resistance spot welding of three sheet stack-up joints with equal sheet thickness is more difficult than 2T stack-ups since an extra interface is introduced and an insufficient nugget growth may occur depending on the nugget formation location which is strongly affected by the thickness of the sheet in the stack-up. For 3T stack-ups of uncoated low carbon steel, the critical sheet thickness is 1.5 mm at which the nugget diameter at

geometrical center and steel/steel interface is almost equal. Weld nugget growth rate is higher at geometrical center than steel/steel interface when the sheet is thinner than 1.5 mm. On the other hand, the nugget formation location shifts from geometrical center to steel/steel interface when the sheet thickness is more than 1.5 mm [75].

Resistance spot welding of complex stack-ups with unequal thickness can be even more challenging, especially when a thin sheet of low carbon steel is attached to multiple AHSS sheets with the thickness ratio of 5 or higher (thickness ratio = total thickness of the stack-up / thickness of the thinnest sheet), since it is difficult to obtain reasonable penetration into thin sheet without expulsion on thick-sheet side. Some researchers have tried resistance spot welding of thin/thick/thick stack-up with conventional welding electrodes and welding schedules. Coon et al. [88] obtained a welding current range of more than 1 kA with dome-shaped electrode and AC power source for 0.8/1.9/1.9 mm thick hot-dipped GI coated dual phase 600 (DP600). Nielsen et al. [89] investigated nugget formation mechanism of resistance spot welding of 7 different stack-ups of thin low carbon steel with two thick AHSS by both experiment and numerical simulation using SORPAS®. It showed that solid-state bonding was the predominant bonding mechanism at thin/thick sheet interface while a fusion zone formed at thick/thick sheet interface. However, a fusion zone at thin/thick sheet interface is crucial for a consistent ductile failure mode at different loading conditions.

To solve the heat balance problem and obtain a reasonable nugget penetration into thin sheet for a complex stack-up, there are generally 3 ways. (1) Resistance spot welding

with cover sheet. Yu [8] inserted a 0.22 mm-thick PT3000 (consisted of CrNi) between electrode and thin low carbon steel during resistance spot welding of 0.7 mm-thick GA coated SGACEN/ 2 mm-thick GI coated DP980/ 1.6 mm-thick CP1180. The joints welded with cover sheet showed higher tensile shear strength and larger penetration into thin sheet due to additional heat generation and less amount of heat loss on thin sheet side. (2) Electrodes with different electrical conductivity/geometry were used on thin/thick sheet side for changing heat extraction capabilities of the electrode and moving the center of the stack-up, as described in both resistance welding manual and welding handbooks. Gould et al. [7] showed that the spot welding with varying electrodes, e.g. class 3 electrode on thin sheet or 8-mm electrode on thick sheet side, are the most effective method in increasing penetration into thin sheet. (3) Complex welding schedules with varying electrode force. Gould et al. [7] used two-stage welding with varying force, current and time to increase penetration into thin sheet for 0.7-mm 270-MPa steel/ 2-mm DP590/ 2-mm DP590 (Figure 2.43). The best penetration into thin sheet can be obtained with short overall welding time, moderate forge force/weld force ratios, and high forge current/weld current ratios. However, there is no information about nugget growth mechanism.

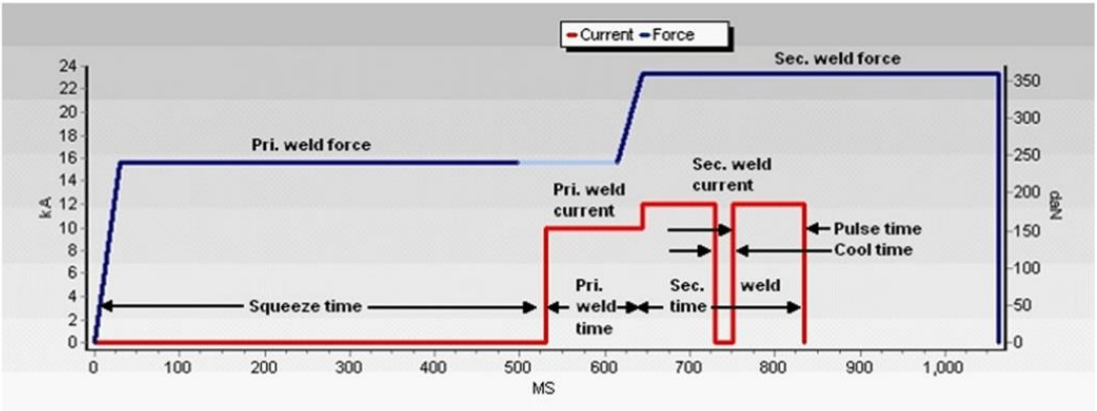

Figure 2.43 Welding current and force used for resistance spot welding of thin/thick/thick 3T stack-ups [7]

To better understand nugget development process in spot welding, numerical simulation can be utilized to study current/temperature distribution and contact pressure. There are various models on resistance spot welding of 2T stack-up on nugget size and microstructure prediction [60,64,66,90], as reviewed previously. However, limited researches have been reported on numerical simulation of 3T stack-ups with unequal sheet thicknesses. Nielsen et al. [89] simulated nugget formation process in complex 3T stack-ups. However, all the welds had limited penetration into thin sheet while there was no information about nugget development for an acceptable weld with at least 20% penetration into thin sheet. Ma et al. [91] generated the weld lobe curves for resistance spot welded 0.7-mm 270C / 1.4-mm 590Y / 1.8-mm 590Y using self-developed FEM software JWRIAN. However, there is no detailed analysis of nugget formation mechanism and no information about effect of welding parameters on nugget size at each faying interface and penetration into thin sheet. Shen [92] comprehensively studied the nugget formation process and effect of steel thickness combination on nugget diameter

and penetration at thin/thick sheet interface for resistance spot welded 3T stack-up of 0.6-mm SAE 1004/ 1.8-mm SAE 1004/ 1.4-mm DP600. It was shown that nugget initiated at 1.8-mm SAE 1004/ 1.4-mm DP600 interface earlier than the thin/thick sheet interface. To meet the minimum nugget diameter at thin/thick sheet interface and obtain at least 20% penetration into thin sheet, a critical ratio of sheet thickness between top and bottom sheets was 1:3 as shown in Figure 2.44.

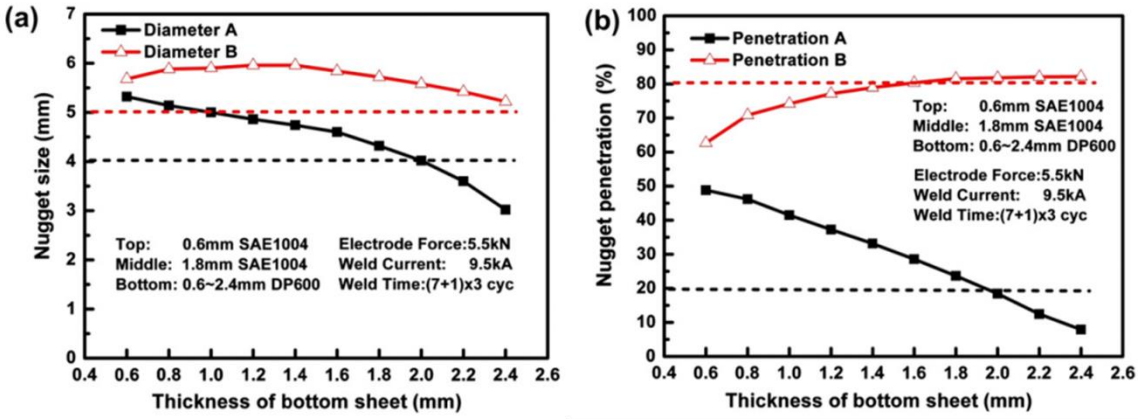

Figure 2.44 Effect of bottom sheet thickness on (a) nugget size at each interface and (b) penetration into top and bottom sheet [92]

Lastly, resistance spot welding of 4T stack-ups with high thickness ratio is challenging due to heat balance. Eizadi et al. [93] investigated resistance spot welding of four-sheet stack of unequal sheet thickness (0.7/1.2/1.2/0.9 mm). It is identified that nugget penetration into thin sheet is hindered due to rapid heat dissipation via water-cooled electrode. With increasing heat input, solid state bonding is changed into fusion bonding.

2.6 Resistance spot welding of Al/steel

To address an increasing demand on weight reduction of vehicle [94], multi-materials design has been developed utilizing advanced high strength steels as parts for crash performance and light metals, such as aluminum alloys, for further weight reduction and corrosion resistance. Dissimilar fusion welding of aluminum to steel is challenging. First, due to the low solubility of iron in aluminum, thick and brittle intermetallic compound (IMC) layer can form at weld interface, which deteriorates the load bearing capacity of the joints. Second, solidification related welding defects, such as shrinkage voids, solidification cracking, can form at weld interface [95]. Hence, in automotive industries, solid-state welding processes, such as ultrasonic spot welding [96], friction stir spot welding [97], vaporizing foil actuator welding (VFAW) [98], magnetic pulse welding (MPW) [99] and mechanical fastening (e.g., self-piercing riveting [100]), have been developed for dissimilar metal joining of aluminum alloys to steels to prevent the formation of IMCs and solidification related welding defects.

2.6.1 Direct RSW of Al alloys to steel

As one of the prominent joining methods in automotive industries, resistance spot welding of aluminum to steel have been studied recently for improvement on microstructure and mechanical properties of the joints. Zhang et al. [10,101,102] investigated the interfacial microstructure and its effect on mechanical properties of resistance spot welded joints of 1 mm-thick H220 Zn-coated high strength steel and 1.5 mm-thick 6008-T66 aluminum alloy. Dual-layer intermetallic compounds (IMCs), i.e.

lath-like/tongue-like η-Fe_2Al_5 on steel side and needle-like θ-$FeAl_3$ on aluminum alloy side, were observed at weld interface (Figure 2.45). IMCs have higher hardness compared to Al or steel base metal, with average hardness of approximately 8.7 GPa and 6.5 GPa for Fe_2Al_5 and Fe_4Al_{13} respectively, while the average hardness of Al and steel near to the interface were 1.1 and 2.1 GPa respectively [101]. A high peak load of 3.3 kN can be obtained at the optimized welding condition but exhibiting the interfacial fracture mode. The crack initiated at the brittle IMC, i.e. η-Fe_2Al_5 and propagated through the IMCs layer. Arghavani et al. [15] studied the effect of the zinc layer on the interfacial microstructure and joint strength of resistance spot welded aluminum alloy to galvanized steel. IMCs thickness was reduced in the Al/galvanized steel spot welded joints (GS-Al) compared to that in Al/low carbon steel joints (PS-Al). Both the tensile shear strength and cross-tension strength of Al/galvanized steel spot welded joints were higher than those of Al/low carbon steel joints when welding current was higher than 12 kA. A high tensile shear strength of approximately 6.5 kN and fracture energy of 3 J can be obtained at a current of 14 kA with lower IMCs thickness (< 5.5 μm). However, lower welding current resulted in inferior mechanical properties in GS-Al joints compared to PS-Al joints due to incomplete joining with residual Zn coating at the interface in GS-Al joints.

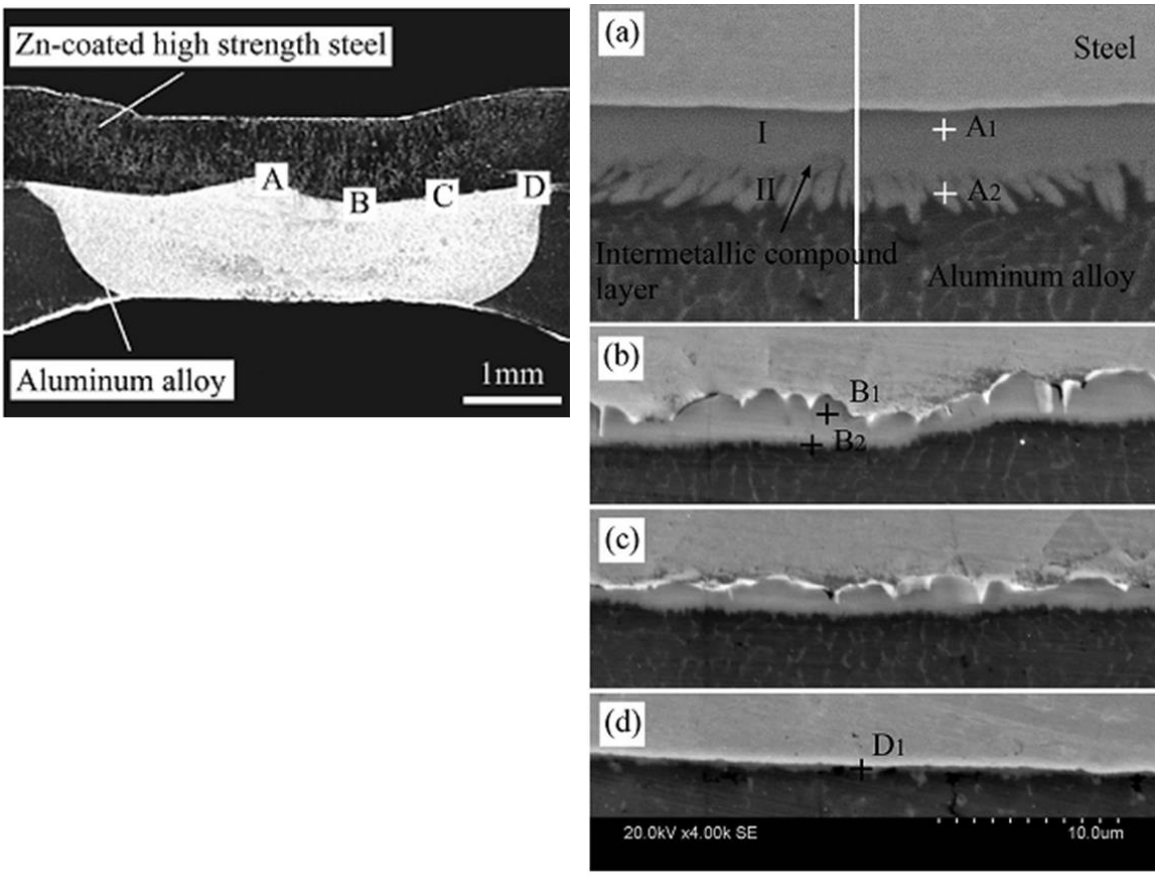

Figure 2.45 Cross-sectional macrostructure of typical Al/Steel resistance spot welds and SEM images of Al/Steel interface regions: (a) – (d) correspond to region A-D respectively [102]

2.6.2 RSW of Al/steel using cover plates

In order to improve the heat balance and reduce heat losses through water-cooled electrode while keeping a high temperature in the fusion zone in resistance spot welding of Al alloys to steel, Satonaka et al. [103] used a cover plate on the aluminum side in resistance spot welding of aluminum alloy to steels as shown in Figure 2.46. Qiu et al. [104–108] studied resistance spot welding of 1-mm-thick AA5052 aluminum alloy to a 1-mm-thick cold-rolled steel (SPCC) steel/austenitic stainless steel (SUS304) with SPCC

cover plate on the aluminum alloy side. The IMCs layer mainly consisted of tongue-like shaped Fe_2Al_5 on SPCC side and needle-like morphology of $FeAl_3$ on AA5052 side. However, at Al/SUS304 interfaces, the intermetallics were solid-solution of Cr and Ni in main phases (Fe_2Al_5 and $FeAl_3$), which can be expressed as (Fe, Cr, Ni)$_2Al_5$ and (Fe, Cr, Ni) Al_3, respectively. In general, thinner IMCs formed at Al/SUS304 interfaces compared to that at Al/SPCC interface. A peak tensile shear strength of 6.5 kN were obtained from Al/SUS304 joint at welding current of 12 kA with a pull-out failure mode due to thin IMCs of 2 μm. This tensile shear strength was about 0.5 kN higher than AA5052/AA5052 joints. However, a lower peak load of 4.68 kN were obtained for Al/SPCC joint with an interfacial fracture mode due to thick IMCs of 7 μm.

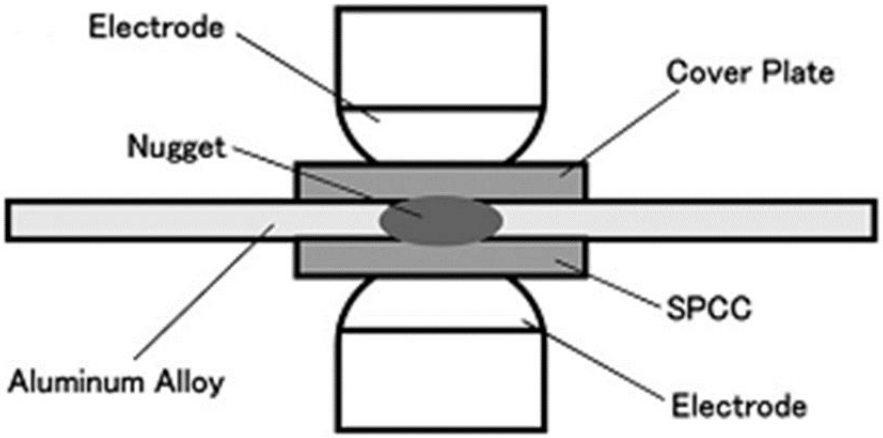

Figure 2.46 Schematic diagram showing resistance spot welding with a cover plate [108]

2.6.3 RSW of Al/steel using interlayer

Another way to improve weld strength of resistance spot welded Al/steel joints with the potential to reduce IMCs thickness was welding with an insert. Oikawa et al. [14]

utilized a 0.77-mm-thick cold-rolled aluminum clad steel sheet as an insert metal in resistance spot welding of 0.4-mm-thick cold rolled steel and 0.6-mm-thick pure aluminum. The IMCs thickness at the Al/Steel interface was about 5 μm. Tensile shear strength and cross-tension strength of 3.6 kN and 1.5 kN were obtained respectively, which were similar to Al/Al spot weld joints and much higher than those with direct resistance spot welding of 2.4 kN and 0.6 kN, respectively. Sun et al. [109] used a similar method to Oikawa et al. [14] for resistance spot welding of 1.4-mm-thick SAE 1008 mild steel and 2-mm-thick 5182-O aluminum alloy with 1 mm/1.5 mm – thick cold rolled Al cladded steel. The static and dynamic strength of RSW samples in cross-tension and coach peel test were comparable to those of the peak load of self-piercing rivets (SPR). Fatigue strength of RSW samples were lower than those of SPR samples due to stress concentration and tensile residual stress at notch tip. However, wide application of Al/steel resistance spot welding with aluminum cladded steel is still limited due to high cost and difficulties in hot/cold rolling process and weight increases by utilizing steel as an interlayer. Thus, more investigations have been done recently on improving the cladding method and using thinner and lighter metals as interlayers.

In order to reduce the intermetallic compound layer thickness, Zhang et al. [110] used 4047 AlSi12 as an interlayer to suppress the growth of intermetallic compound during resistance spot welding of 1 mm H22YD-Z100 Zn-coated high strength steel sheets with 1.5 mm EN AW 6008-T66 aluminum alloy sheets. The effect of interlayer thickness, i.e. 100 μm, 200 μm, 300 μm, 400 μm, on intermetallic compound (IMC) growth behavior and mechanical properties were investigated. IMC layer consisted of $Fe_2(Al,Si)_5$ and

$Fe_4(Al,Si)_{13}$ and the thickness of IMC layer reduced from 1.8 μm to 0.6 μm as the thickness of AlSi12 interlayer increasing from 100 μm to 400 μm. But all of them were much thinner compared to 4 μm for spot welds without an interlayer. Nugget diameter reduced with increasing interlayer thickness and maximum tensile shear strength of 6.2 kN and pull-out failure mode were obtained with an interlayer thickness of 300 μm. The fracture surfaces after lap-shear tensile testing is shown in Figure 2.47. Ibrahim et al. [16] investigated resistance spot welding of 2 mm AA6061-T6 and 2 mm type 304 austenitic stainless steel with 80 μm thick Al-Mg alloy (80 wt % Al and 20 wt% Mg). Under the same welding condition, lap shear tensile strength was higher for welds with Al-Mg interlayer than without the interlayer and a peak strength of 8.4 kN can be obtained with welding current of 16.1 kA and electrode force of 9.3 kN. A high tensile shear strength was caused by thin IMC layer (approximately 2 μm) formed at Al/steel weld interface. Fatigue strength of dissimilar RSW Al/steel samples was higher than friction stir spot welded (FSSW) samples. However, the failure mode depended on the load level. Pull-out failure occurred at high load (P_{max} > 3 kN), shear fracture at 2.25 kN < P_{max} <3 kN, and upper Al sheet fracture at P_{max} < 2.25 kN. It is noted that the aforementioned interlayers were directly placed between Al alloy and steel sheets without forming a metallurgical bond to any of the sheets prior to RSW.

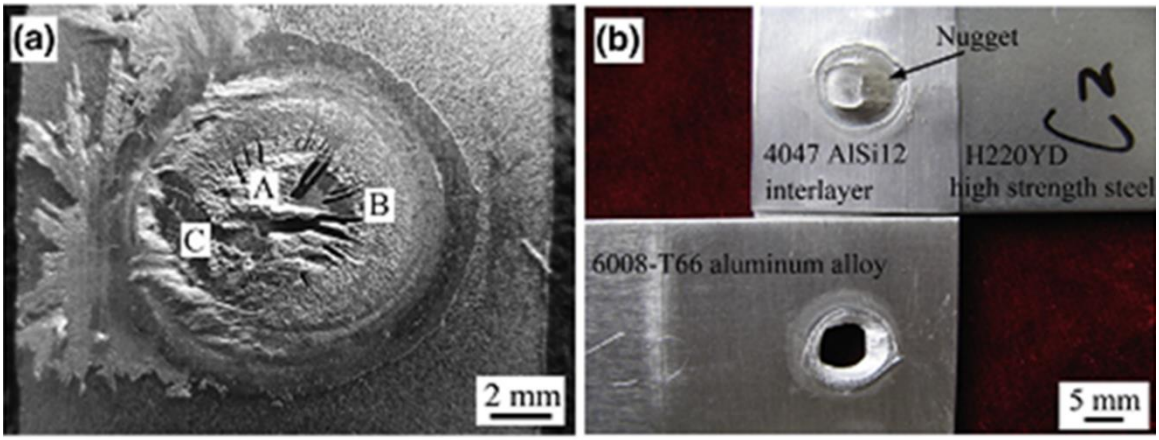

Figure 2.47 Fracture modes of H220YD high strength steel/6008-T66 resistance spot weld joints (a) interfacial fracture without interlayer and (b) pull-out failure with 4047 AlSi12 interlayer thickness of 300 μm [110]

Since the peak load is affected by both the nugget diameter and ultimate tensile strength of aluminum alloy, the strength and joint efficiency of the Al/Steel spot welds in the literature are calculated and summarized in Table 2.3. For interfacial failure mode, assuming a perfect cylindrical nugget (without welding defects, i.e. shrinkage voids) formed with radius of r, the shear strength of the fusion zone and joint efficiency can be expressed in Equation 2.10 and Equation 2.11:

$$\tau_{IF} = \frac{Peak\ load}{\pi r^2} \qquad \text{Equation 2.10[82]}$$

$$\text{joint efficiency (IF)} = \frac{\tau_{IF}}{UTS\ of\ aluminum\ alloy} \qquad \text{Equation 2.11}$$

For pull-out failure mode, the strength and joint efficiency can be expressed in Equation 2.12 and Equation 2.13 :

$$\sigma_{PFL} = \frac{Peak\ load}{2\pi rt} \qquad \text{Equation 2.12[82]}$$

$$\text{joint efficiency (BP)} = \frac{\sigma_{PFL}}{UTS\ of\ aluminum\ alloy} \qquad \text{Equation 2.13}$$

where t is the sheet thickness of aluminum alloy.

Table 2.3 Comparison of peak strength and joint efficiency in the literature for Al/steel resistance spot welding

Peak load(kN)	Nugget diameter (mm)	Strength (MPa)	Failure mode	Aluminum alloy UTS (MPa)	Joint efficiency (%)	Reference
3.309	5.787	125.8	IF	340	37	[101]
6.5	9.31	95.5	IF	250	38	[15]
4.68	9	73.6	IF	250	29	[106]
6.5	10	206.9	BP	250	83	[106]
6.2	9.62	205.1	BP	340	60	[110]

2.7 Important unanswered questions

To achieve a sound joint for resistance and ultrasonic spot welding of two sheets or complex stack-ups of AHSS and dissimilar metal welding of aluminum alloy to steels, it is important to investigate the process-microstructure-property relations. Below are the technical gaps that are addressed in this dissertation.

(a) SCHAZ softening and local constitutive behavior of potential failure locations

Failure behavior of resistance spot welded UHSS, such as hot-stamped boron steels, is difficult to be accurately predicted due to the heterogeneous microstructure created in RSW. It is important to investigate the following questions: (1) what is the softening mechanism in SCHAZ? (2) how to accurately predict the microstructure and microhardness of resistance spot welded hot-stamped boron steels, especially the SCHAZ? (3) how to accurately extract the local constitutive behaviors of the potential failure locations? (4) how do the deformation or failure behaviors make a difference when the local constitutive behaviors are applied in the performance model?

To address these questions, microstructure of resistance spot welded hot-stamped boron steels, especially the SCHAZ, has been characterized in detail. A 3D fully coupled electro-thermo-structural-metallurgical model has been developed to predict thermal profiles, nugget formation and microhardness during RSW. Local constitutive behaviors of SCHAZ and CGHAZ have been extracted to be used as input for performance model.

(b) Nugget formation mechanism in complex stack-ups of AHSS

To achieve a reasonable penetration into the thin sheet and a consistent joint quality in resistance spot welded complex stack-ups of AHSS, it'll be beneficial to understand the nugget formation mechanism, the key factors that affect the penetration into the thin sheets, the effect of coatings or stack-up sequence of the steels and the function of each pulse if pulsation is utilized.

Process simulation in this study has been combined with the experimental results for a better understanding of the factors mentioned above.

(c) IMCs reduction in Al to steels joining

A sound joint in resistance spot welding of Al to steels is challenging since the two materials are incompatible. In particular, severe expulsion may take place with thick IMCs formed at the faying interface. The upcoming questions will be: (a) what are the main causes for expulsion and the formation of thick IMCs at the faying interface? (b) how to effectively control these factors to avoid expulsion and reduce IMCs thickness?

To solve the problems mentioned above, a novel technique based on RSW, namely U+RSW, has been developed for IMCs thickness reduction and mechanical property improvement of Al to steel welded joints.

(d) Relative motion and bonding mechanism in USW

In USW of aluminum alloys, to achieve a sound joint, the following questions need to be addressed: (1) what is the vibration kinetics of the foils and the sonotrode during USW? (2) how can the vibration kinetics be correlated to the bond quality of the USW welds? A PDV system is used in this study for in-situ relative motion measurement at multiple locations, i.e. sonotrode, top foil, bottom foil and the anvil, during ultrasonic spot welding process.

Chapter 3 Resistance spot welding of 2T stack-up of hot-stamped steel

Due to the complex heterogeneous microstructure created by rapid heating and cooling during resistance spot welding process, it is challenging to accurately predict the local and global mechanical properties and failure behavior for resistance spot welded UHSS, such as hot-stamped Usibor® 1500. This chapter presents process, local microhardness and failure behavior prediction of 2T stack-up of Al-Si coated Usibor® 1500 by developing a quantitative understanding of weld microstructure and local constitutive behavior of HAZ sub-regions.

3.1 Approaches

3.1.1 Resistance spot welding experiment

The chemical composition of the Al-Si coated Usibor® 1500 sheet is shown in Table 3.1. For brevity, the registered trademark symbol is omitted hereafter. The sheet was 1.5 mm thick with an approximately 40-μm-thick Al-Si coating. There was no surface treatment of the samples prior to resistance spot welding. The as-received base metal (in press-hardened state) had a microstructure of lath martensite aligned within prior austenite grains, as shown in Figure 3.1. Some of the lathes seemed to have

contained fine carbides due to auto-tempering during press hardening. The Vickers hardness of the base metal was 493 ± 5 HV0.5.

Table 3.1 Chemical composition of Usibor 1500 (wt. %) [111]

C	**Mn**	**P**	**S**	**Si**	**Al**	**Nb**	**Ca**
0.21	1.22	0.013	0.001	0.265	0.056	<0.003	0.0024
Ni	**Cr**	**Mo**	**V**	**Ti**	**Cu**	**N**	**B**
0.01	0.19	<0.003	<0.003	0.033	0.01	0.0052	0.0031

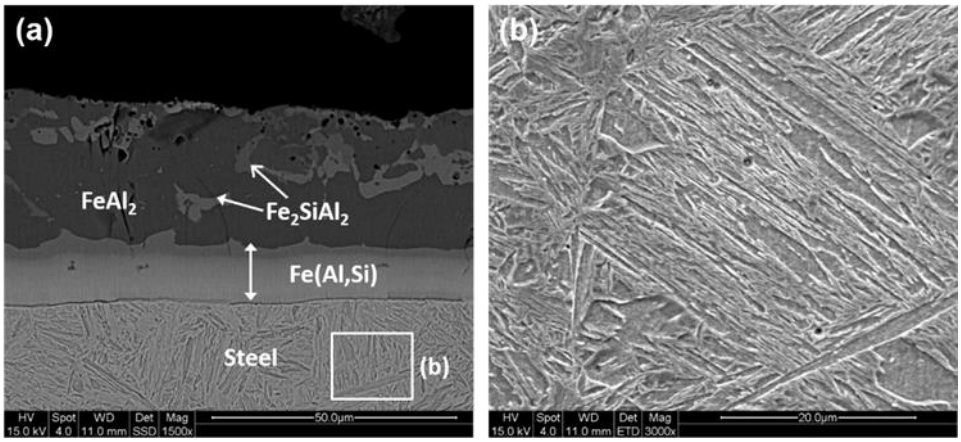

Figure 3.1 Base metal microstructure of hot-stamped Usibor 1500 in the press-hardened state.

Two sheets of Usibor 1500 steel (i.e., 2T stack-up) in a lap-joint configuration were welded using a single phase 60 Hz alternating current (AC) pedestal type resistance spot welder. The welding schedule was developed based on ISO standard 18278-2:2004 [112], and the welding parameters are listed in Table 3.2. After welding, a calliper was used to measure the smallest thickness of the joint, which was then used to calculate the indention. Next, the joint was carefully cross-sectioned along its centerline, ground from

240 to 800 grit sand paper, and then polished with 6, 3, and 1 μm diamond paste. After polishing, the specimens were etched with 2% Nital. A standard optical microscope was used to take images of the weld cross-section, which were used to measure the nugget size and electrode indentation in ImageJ, an open-source image analysis software developed by the National Institutes of Health (NIH).

Table 3.2 Parameters used for resistance spot welding of 1.5-mm-thick Usibor steel sheets. During RSW, a current waveform consisted of 3 impulses of 11 cycles of current-on followed by 2 cycles of current-off. 1 cycle = 1/60 of a second.

Root-mean square current (kA)	**Welding time (cycles)**	**Electrode force (kN)**	**Electrode diameter(mm)**	**Sheet thickness(mm)**
6.7	(11 + 2) × 3	4.413	6	1.5

3.1.2 Softening kinetics for the SCHAZ

Both Xia et al. [113] and Biro et al. [114][115] showed that softening in martensitic and high-strength DP steel spot welds was predominantly controlled by tempering of martensite in the SCHAZ, a region heated to peak temperature below A_{C1}. The intercritical heat affected zone (ICHAZ), a region adjacent to the SCHAZ that is heated to a peak temperature between A_{C1} and A_{C3}, also softens due to formation of fresh ferrite. The width of the ICHAZ is much narrower than that of the SCHAZ (e.g., ~0.1 mm for the former and ~1.7 mm for the latter). For simplicity, the softening kinetics of ICHAZ is not directly modelled but it is assumed to increase linearly from A_{C1} to A_{C3} isotherms in the present study.

For tempering of martensite, Biro et al. [114][115] showed that the kinetics under isothermal conditions was well described by the JMAK equation. In particular, the extent of softening due to tempering, ϕ, can be defined using a normalized hardness:

$$\phi = \frac{H_{BM} - H}{H_{BM} - H_{\infty}} \qquad \text{Equation 3.1}$$

where H_{BM} is the base metal hardness, and H is the hardness of tempered material. H_{∞} is the minimum hardness after complete tempering (i.e., ferrite + cementite mixture). The isothermal tempering kinetics described by the JMAK equation is given as [116,117]:

$$\phi = 1 - \exp(-(kt)^n) \qquad \text{Equation 3.2}$$

$$k = k_0 \exp\left(-\frac{Q}{RT}\right) \qquad \text{Equation 3.3}$$

where n is the JMAK exponent, t is the tempering time (s), T is the tempering temperature (K), k_0 is the pre-exponent constant (s^{-1}), Q is the activation energy (J/mol), and R is the universal gas constant (8.314 J/mol-K).

During RSW, tempering of martensite occurs under non-isothermal conditions consisting of rapid heating and cooling. To account for the non-isothermal tempering, Equation 3.2 and Equation 3.3 are modified based on the additive rule into [116,117]:

$$\phi(t) = 1 - \exp\left[-\sum_{i=1}^{m}\left(k_0 \exp\left(-\frac{Q}{RT_i}\right)(\Delta t)\right)^n\right] \qquad \text{Equation 3.4}$$

where $\phi(t)$ is the extent of tempering after time $t = m\,\Delta t$, Δt is the time step size, and T_i

is the temperature at the i-th time step.

As a first approximation, the kinetics parameters (Q, k_0, and n) are assumed to be independent of temperature, indicating that the tempering kinetics are governed by the same mechanism over the temperature range of interest in RSW. This approximation allows for extraction of the kinetics parameters in the JMAK equation from a series of isothermal tempering tests, as discussed in the following.

A prerequisite of designing isothermal tempering tests is choosing the tempering temperatures. As discussed previously, the martensite tempering takes place in the SCHAZ, a region that is heated to a peak temperature lower than the A_{C1} temperature. In this study, the A_{C1} temperature (along with A_{C3}) was experimentally measured using dilatometry in a thermo-mechanical simulator Gleeble® 3800 in accordance with ASTM standard A 1033-10, which is listed in Table 3.3. The A_{C1} and A_{C3} temperatures for the Usibor 1500 steel were found to be 714 °C (987 K) and 823 °C (1096 K), respectively, for the rapid heating rate expected during RSW. The tests were repeated twice and an average value was determined.

After determining A_{C1}, the temper temperatures were chosen from 350 ^{o}C to 650 ^{o}C (623 K to 923 K). At each temperature, tempering time ranged from 0.2 s to 10 s. The range of isothermal tempering conditions used is summarized in Table 3.4. Flat steel coupons with the dimensions of 90 mm × 12 mm × 1.5 mm were used. During testing, a coupon was heated at an average rate of 792 ± 88 ^{o}C/s in the Gleeble, which was comparable to the heating rate in the SCHAZ predicted by numerical simulation (to be described in detail

later). The coupon was then cooled by water-quenching to achieve a cooling rate of 1509 ± 35 ^{o}C/s. This preserved the as-tempered microstructure by minimising auto-tempering during cooling. A representative thermal profile for the rapid isothermal tempering test in the Gleeble 3800 is shown in Figure 3.2.

Table 3.3 Phase transformation temperatures of Usibor 1500 measured by dilatometry in Gleeble. M_s and M_f are the martensite start and finish temperatures, respectively

A_{C3}	A_{C1}	M_s	M_f
823 ^{o}C	714 ^{o}C	407 ^{o}C	274 ^{o}C

It is noted that despite the relatively fast heating rate (about 800 °C/s), some amount of tempering can occur during heating, which could contribute to a considerable fraction of the overall tempering in those tests with short tempering times (e.g., 0.2 s). Due to the equipment limitations, a further increase of heating rate tended to result in overheating the steel coupon above the specified tempering temperature and was thus not used. Hence, for this study, the contribution to the overtempering during heating was ignored to allow for extraction of kinetic parameters. The validation of such approximation is discussed in Section 3.5.3 where the predicted and experimental SCHAZ hardness are compared.

The minimum hardness (H_∞) due to complete tempering of martensite was determined by heat treatment of base metal at 650 ^{o}C for 1 hour in a conventional

furnace. The sample was water quenched immediately upon removal from the furnace. Further increase in furnace heat treatment time did not reduce the hardness.

Table 3.4 Summary of testing conditions for isothermal tempering experiments

Temperature (ºC)	**Tempering time (s)**
350, 400, 500 and 650	0.2, 0.5, 1, 5, and 10
650	3600 (in furnace)

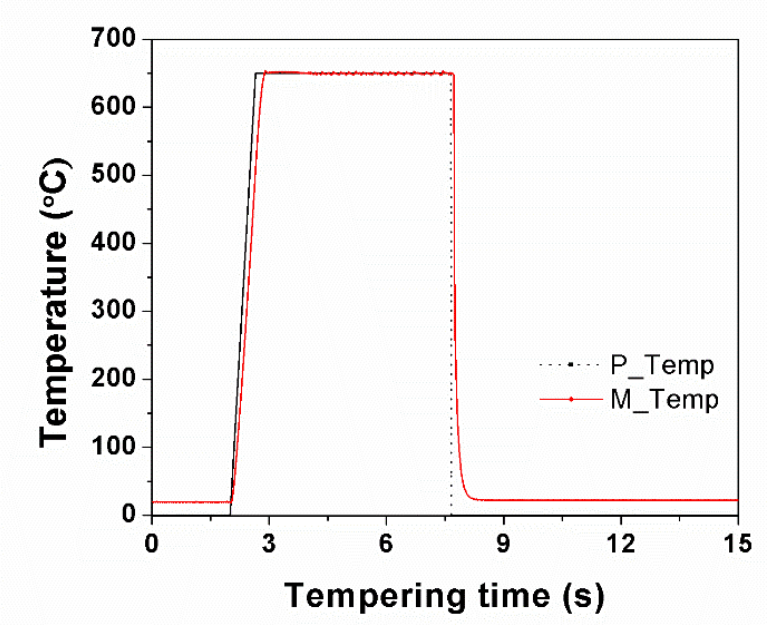

Figure 3.2 Typical thermal cycle used for isothermal tempering test in Gleeble 3800. For this case, the tempering condition was 650 ºC (923 K) for 5 s. P_Temp is the programmed temperature profile, while M_Temp is the actual temperature profile experienced by the steel coupon.

For each tempering condition, Vickers hardness was measured along the centreline of the tested coupon using a load of 500 g. An indent spacing of 500 µm was utilized to eliminate the effect of strain fields from previous indents on hardness measurement. Ten

hardness measurements were made for each tempering condition, and the average value of those ten points was then used to determine the JMAK kinetics parameters, as summarized below.

Applying the natural logarithm to both sides of Equation 3.2, a linearized JMAK equation in the form of y = a·x + b can be obtained:

$$\ln(-\ln(1-\phi)) = n\ln(t) + n\ln(k) \qquad \text{Equation 3.5}$$

In other words, a plot of $\ln(-\ln(1-\phi))$ versus $\ln(t)$ at a specific tempering temperature is expected to be a line with *n* and $n\ln(k)$ being the slope and y-intercept of the line, respectively. Next, applying the natural logarithm to both sides of Equation 3.3, the following equation can be obtained:

$$\ln(k) = -Q\frac{1}{R\,T} + ln(k_0) \qquad \text{Equation 3.6}$$

Similarly, a plot of ln(*k*) versus -1/(*R T)* can be generated from which the slope and y-intercept are used to determine *Q* and k_0, respectively.

It is noted that alloying of Al-Si coating with the steel during RSW is not considered in this study, despite the possibility of it affecting local softening behavior near the surface. This is because the deformation and failure behaviors of the spot weld are expected to be primarily influenced by the bulk softening of the SCHAZ.

3.1.3 RSW process modelling

In this study a 3D fully coupled electro-thermo-mechanical model has been

developed based on Abaqus, a commercially available finite element analysis software, to simulate RSW of Usibor 1500 steel sheets. It is noted that most RSW process models in the literature were based on 2D axisymmetric geometry. Although more computationally demanding, the 3D geometry accurately represents the rectangle-shaped coupons. Moreover, the 3D model can be easily extended to study asymmetries common in production welding, such as electrode misalignment and current shunting.

The FE model comprised a pair of electrodes and two steel sheets, using the same dimensions as the experimental ones. Taking advantage of symmetry, a quarter of the joint was considered and was meshed using a type of 3D solid elements with 8 nodes and trilinear displacement, electric potential, and temperature degrees of freedom (designed as Q3D8R in Abaqus). As shown in Figure 3.3, a fine mesh (element size between 0.1 and 0.2 mm) was placed at the regions of interest, i.e., weld nugget, HAZ sub-regions, and the portion of the electrode near the steel/electrode interface. A coarse mesh (element size between 0.8 mm and 4 mm) was placed elsewhere to reduce the total number of elements.

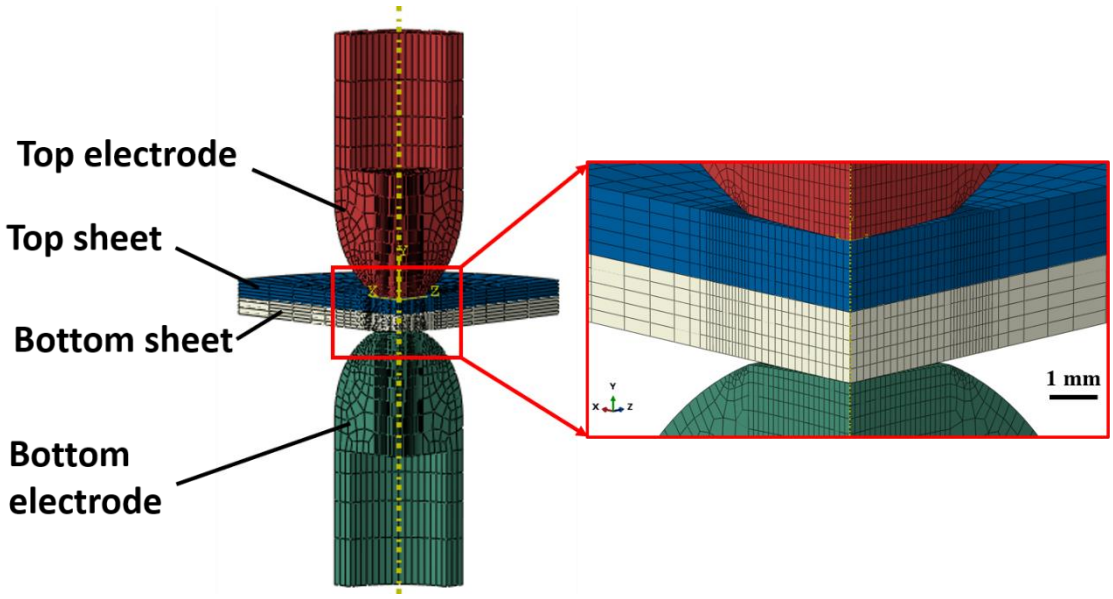

Figure 3.3 Geometry and mesh of the quarter process model for resistance spot welding of Usibor 1500 steel sheets.

3.1.3.1 ***Electro-thermo-mechanical analysis***

A detailed description of the equations solved for such coupled simulation is available in the literature [118]; hence, only salient features relevant to RSW are highlighted below. The electrical potential field as a function of time, $U = U(x, y, z, t)$, can be obtained by solving the following Laplace equation:

$$\frac{\partial^2 U}{\partial x^2} + \frac{\partial^2 U}{\partial y^2} + \frac{\partial^2 U}{\partial z^2} = 0 \qquad \text{Equation 3.7}$$

The current density distribution can be then calculated by:

$$j_x = -\mu \frac{\partial U}{\partial x} \qquad j_y = -\mu \frac{\partial U}{\partial y} \qquad j_z = -\mu \frac{\partial U}{\partial z} \qquad \text{Equation 3.8}$$

where j_x, j_y and j_z are the current density in the x, y, and z direction, respectively, and μ is the electrical conductivity. The heat generation rate per unit volume (q_j) due to bulk Joule heating is then given as:

$$q_j = \frac{1}{\mu}\left({j_x}^2 + {j_y}^2 + {j_z}^2\right) \qquad \text{Equation 3.9}$$

The temperature distribution $T = T(x, y, z, t)$ is obtained by solving the following thermal energy conservation equation:

$$\rho C_P \frac{\partial T}{\partial t} = \frac{\partial}{\partial x}\left(\lambda \frac{\partial T}{\partial x}\right) + \frac{\partial}{\partial y}\left(\lambda \frac{\partial T}{\partial y}\right) + \frac{\partial}{\partial z}\left(\lambda \frac{\partial T}{\partial z}\right) + q_j \qquad \text{Equation 3.10}$$

where ρ is the density, C_P is the specific heat, λ is the thermal conductivity, and q_j (W/mm^3) is the internal heat generation rate due to bulk Joule heating defined in Equation 3.9.

The mechanical simulation was based on the standard solution to the static force equilibrium equation considering elastic-plastic material constitutive behavior, as described elsewhere in the literature [118,119].

3.1.3.2 ***Contact resistance for Al-Si coated Usibor 1500***

Contact pairs were defined at both electrode/steel and steel/steel interfaces, where multiple surface interactions were included, as discussed in the following. The electric current (j_{int}), which flows through two points in contact at the interface, is described using the potential difference and the electrical contact resistance (r_g) as:

$$j_{int} = -\frac{1}{r_g}(U_A - U_B) \qquad \text{Equation 3.11}$$

where U_A and U_B are the electrical potential of two points in contact, one on each side of the interface. The formula of r_g as a function of local temperature and contact pressure, taken from that developed by Kaars et al. [69], is given as:

$$r_g(T,P) = r_0 \cdot \left(\frac{P - P_k}{P_0 - P_k}\right)^{\varepsilon_P} \cdot \left(\frac{T - T_{lim} + (T_0 - T)\cdot 2^{-\frac{1}{\varepsilon_T}}}{T_0 - T_{lim}}\right)^{\varepsilon_T} \qquad \text{Equation 3.12}$$

where r_0 is the base resistance value, P is the contact pressure, P_k is the corrective pressure, P_0 is the reference pressure, ε_P and ε_T are the pressure and temperature exponents, respectively, T is the local interface temperature, T_{lim} is so-called half-value temperature at which the magnitude of the base resistance r_0 is halved, and T_0 is the room temperature (293 K). For the RSW model (Figure 3.3), there were two contact pairs defined: one pair for the electrode/steel (E/S) interface, and the other pair for the steel/steel (S/S) interface. The values of contact resistance parameters for each pair are taken from Ref. [69], and they are listed in Table 3.5 for completeness. Figure 3.4 plots

the electrical contact resistance as a function of temperature and contact pressure calculated using Equation 3.12 for the two contact pairs. As shown in this figure, r_g dropped quickly from 12 to 1 mΩ·mm^2 as the temperature increased from room temperature to 400 °C (673 K) at a constant contact pressure of 80 MPa. The rate of drop in r_g (i.e., slope of the curve) levelled off as the temperature increased. A similar dependence was observed for r_g versus P at the room temperature; in other words, as P increased, the value of r_g decreased while the rate of drop was also reduced.

Table 3.5 Electric contact resistance parameters for E/S and S/S interfaces [69]

Parameter	**E/S Interface**	**S/S Interface**
r_0 (mΩ $\cdot mm^2$)	2.7823	17.851
P_0 (MPa)	20	20
P_k (MPa)	-5	-5
ε_P	$-\frac{1}{3}$	$-\frac{1}{3}$
ε_T	-1	-1
T_{lim} (K)	415	330

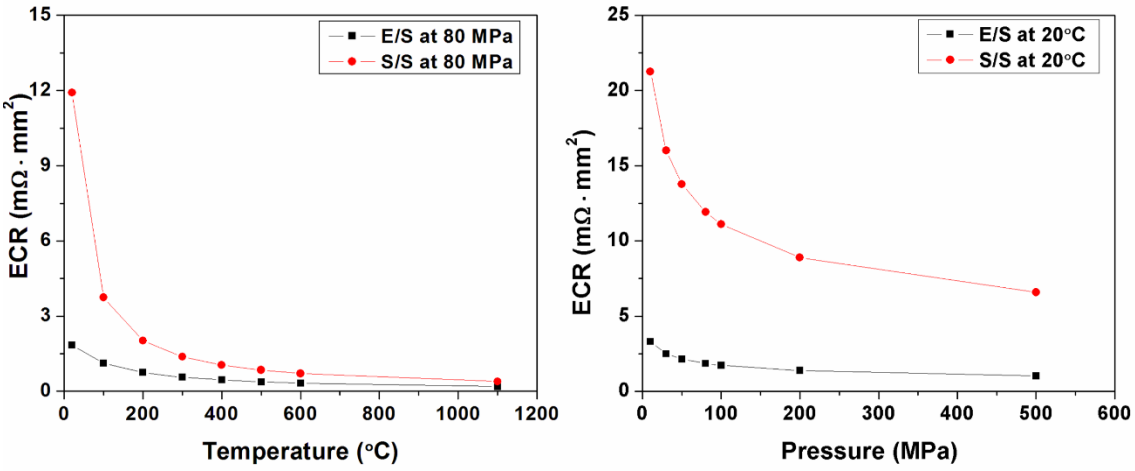

Figure 3.4 Representative curves of temperature- and pressure-dependent electrical contact resistance (ECR) at electrode/steel (E/S) and steel/steel (S/S) interfaces.

3.1.3.3 *Material properties and boundary conditions*

Temperature-dependent electrical conductivity, thermal conductivity, coefficient of thermal expansion, and specific heat of Usibor 1500 steel and the copper electrode are plotted in Figure 3.5. The specific heat of the copper electrode (Class 1 CuZr) is 376 J/(kg·K). The latent heat of fusion for Usibor 1500 is 220 kJ/kg. The temperature-dependent elastic modulus and yield strength of Usibor 1500 and the copper electrode are shown in Figure 3.6 [91][120]. Poisson's ratio of Usibor 1500 and copper electrode are 0.3 and 0.343, respectively. The flow stress data of Usibor 1500, taken from Ref. [120], was assumed to depend only on temperature, and the dependence of flow stress on microstructure formed during weld cooling was not considered for simplicity.

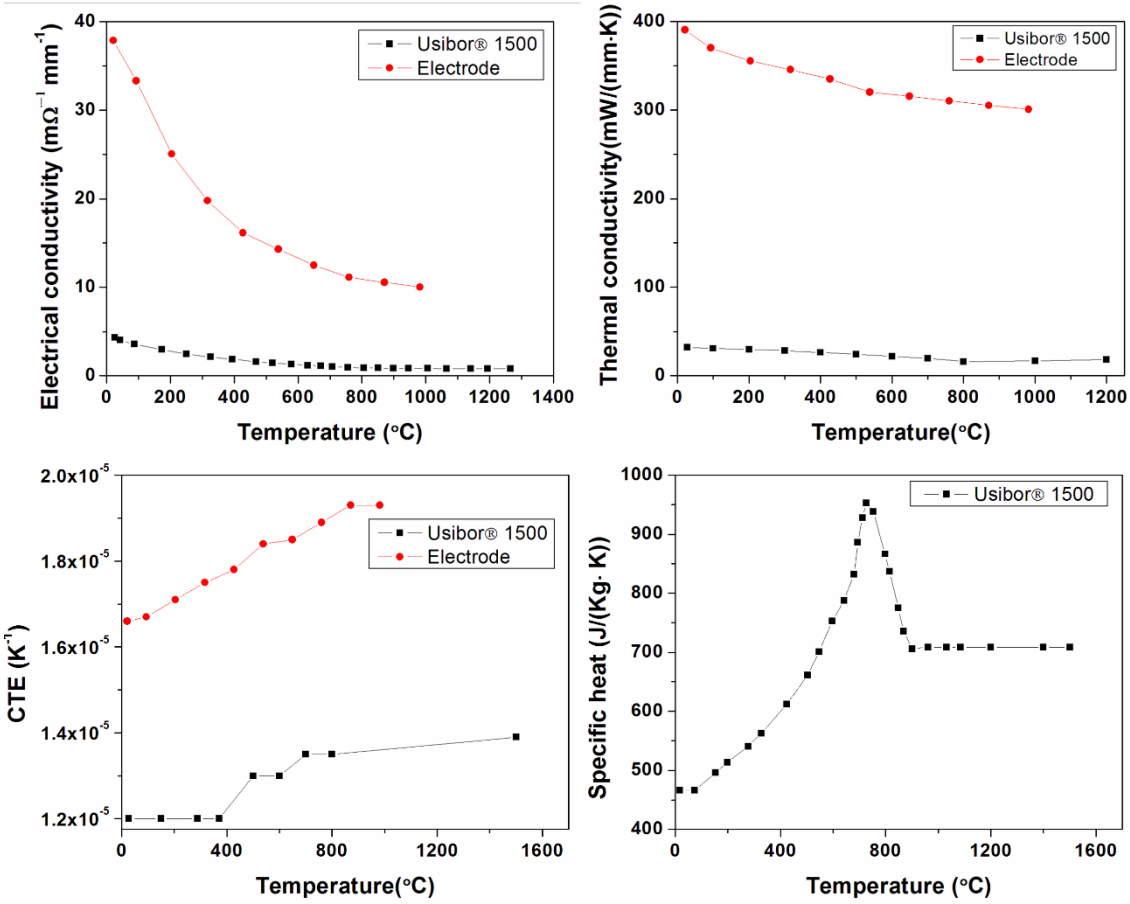

Figure 3.5 Temperature-dependent thermo-physical properties of Usibor 1500 steel and the copper electrode.

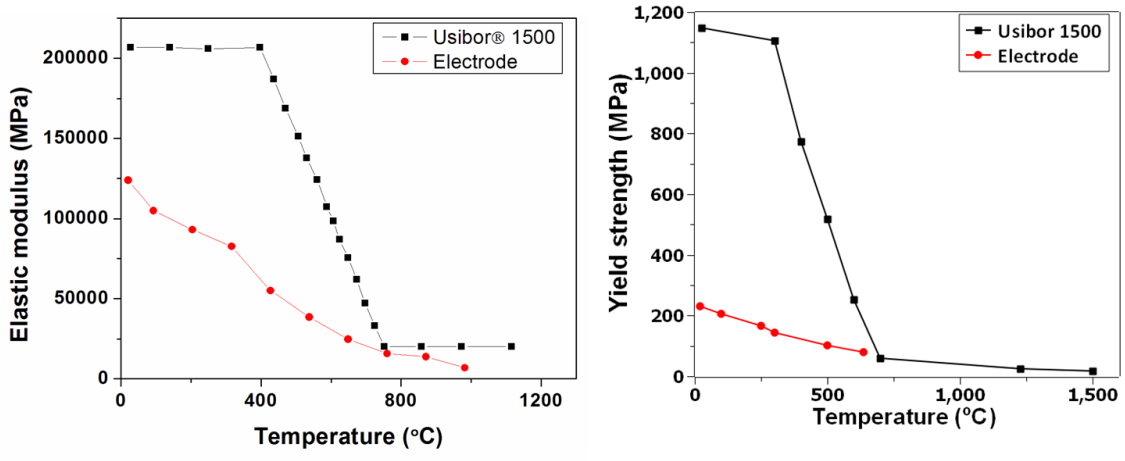

Figure 3.6 Temperature-dependent mechanical properties of Usibor 1500 steel and the copper electrode.

As noted earlier, a quarter of the joint was simulated, taking advantage of symmetry. The boundary and loading conditions applied in the quarter joint are schematically summarized in Figure 3.7. For mechanical analysis, the electrode force was applied through a pressure uniformly distributed on the annular end of the top electrode as shown in Figure 3.7(a). The bottom surface of the electrode was fixed in the vertical direction (U_Y=0). Symmetry was applied to the side surfaces, constraining the circumferential displacement to zero (U_X = 0 or U_Z = 0). For thermo-electrical analysis, a constant current was applied at the annular end of the top electrode while the electrical potential of the bottom surface of the lower electrode was set to 0 V. Convective heat loss was defined on the water-cooled inner surfaces with a film coefficient of 3800 W/m^2-K. For the exposed outer surfaces, a film coefficient of 19.4 W/m^2-K was used for heat loss to the ambient air, as shown in Figure 3.7(b). In the equations for convective heat loss marked in this figure, *T* is the surface temperature and 20 is the heat sink temperature set to the same value 20 ^{o}C (293 K) as the initial temperature of the joint.

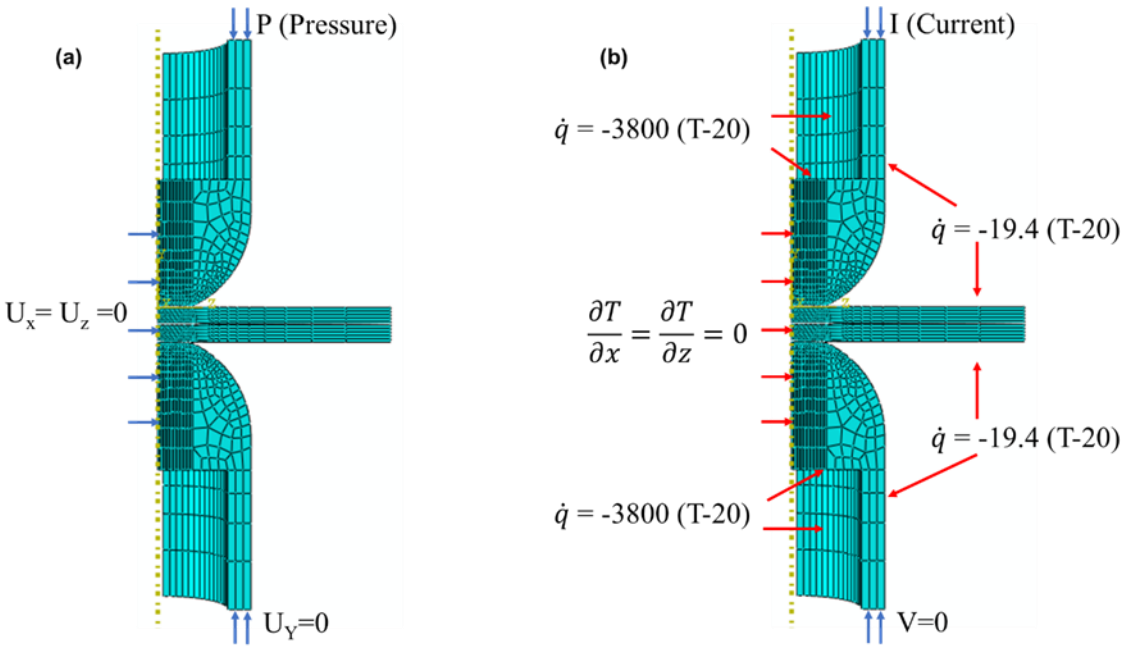

Figure 3.7 Schematic illustration of (a) mechanical boundary conditions, and (b) thermo-electrical boundary conditions applied in the process model.

It is possible to directly account for the AC profile used in RSW, although doing so would require very small time increments. For computational efficiency, the commonly used approach of inputting the Root-Mean Square (RMS) of the welding AC is used as [121]:

$$I_{rms} = \sqrt{\frac{1}{\pi}\int_0^{\pi} (I_m \sin(2\pi f t))^2 \, d(2\pi f t)} = \frac{I_m}{\sqrt{2}} \qquad \text{Equation 3.13}$$

where I_{rms} is the RMS (or equivalent) direct current (DC), I_m is the peak of the welding AC, f = 60 Hz, and t is the time. Simulation results by Li et al. showed that the temperature profiles were almost identical for AC and equivalent DC with the only difference of small temperature fluctuation in the case of AC current [121].

3.1.4 Stress-strain curve of local HAZ for post weld simulation

As reviewed in Chapter 2, CGHAZ and SCHAZ are two HAZ sub-regions that are prone to failure during mechanical testing of spot welds of UHSS. The stress-strain curves of these HAZ sub-regions are essential input for post-weld performance simulation to calculate the weld deformation and failure behaviors subjected to different mechanical loading conditions. This section describes two experimental approaches used to generate microstructure-specific stress-strain curves for CGHAZ and SCHAZ at room temperature.

3.1.4.1 *Physical simulation of CGHAZ and SCHAZ by Gleeble® 3800*

This approach creates tensile samples whose gauge section consisted of simulated HAZ microstructure using Gleeble® 3800. The sample was clamped between copper/stainless steel grips and heated up by resistance heating. A K-type thermocouple was percussion welded at the midsection of the sample to monitor the temperature profile and also used by a closed-loop thermal control system for accurate temperature control.

For SCHAZ simulation, copper grips were used to clamp the sample since copper has high thermal conductivity (385 W/m-K) and electrical conductivity (5.96×10^7 S/m). The use of the copper grips permitted a high heating rate applied to the sample, which was necessary to duplicate the heat rate in actual spot weld and to minimize tempering during heating and cooling. The sample was heated up to 700 ^{o}C with a high heating rate of 2000 ^{o}C/s, held for 0.5 seconds and then cooled by water quench with a cooling rate of more than 6000 ^{o}C/s.

For CGHAZ simulation, in order to create a large gauge region with uniform microstructure, half contact stainless steel grips were used to clamp samples. Due to the low thermal conductivity (12 – 45 W/m-K) and electrical conductivity (1.45×10^6 S/m) of stainless steel grips, a "slow" heating rate of 100 ^{o}C/s was used to heat the sample to a peak temperature of 1300 ^{o}C.

To measure the stress-strain curves, the Gleeble-simulated samples were tested by a MTS 810 tensile testing equipment with a displacement rate of 2.54 mm/min (i.e., quasi-static loading). The geometry of the dog-bone shaped sample for tensile testing is shown in Figure 3.8. Due to the small gauge length (10 mm), the local displacement and strain distribution was measured by Digital Image Correlation (DIC), an optical measurement technique. Black and white speckles were randomly created on the surface of tensile sample. A Nikon D7100 camera was used to take a video during loading. Images were extracted from the video and then analyzed by Ncorr and Post_Ncorr, open source 2D Digital Image Correlation Matlab software programs [122], for displacement and strain maps. A 2-mm-long virtual extensometer was applied across the strain localization and fracture region to extract the local displacement, which in turn, was used to calculate the engineering strain.

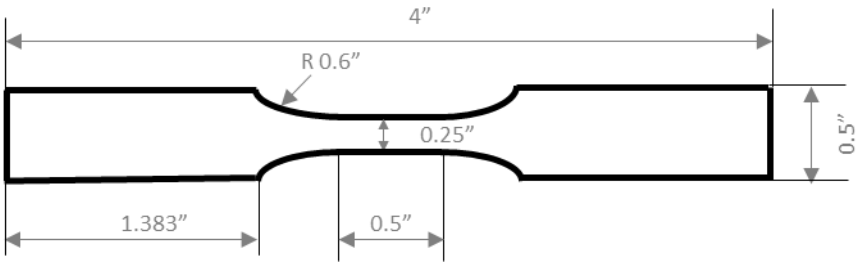

Figure 3.8 Tensile test sample geometry (dimension in inches)

3.1.4.2 ***Nanoindentation***

Nanoindentation measures the load-displacement response as a small indent is made onto the local HAZ region. The load-displacement data can be then used to extract stress-strain curve using existing models, thus potentially allowing a "direct" determination of microstructure-specific stress-strain data.

For nanoindentation sample preparation, the samples were vibratory polished using 0.05 μm colloidal silica for 1.5 hours after the standard sample grinding and polishing procedure described in Section 3.1.1. Then they were chemically etched in 2% Nital for 2 seconds. The topography of each sub-region, namely weld nugget, CGHAZ, intercritical heat affected zone (ICHAZ), and SCHAZ, were measured by optical profilometery (OP). The surface roughness parameter, Ra, of each sub-region was calculated based on the topographic profile, which is listed in Table 3.6. As shown in this table, the surface roughness was less than 82 μm for all the sub-regions, which is low enough to ensure the accuracy of nanoindentation measurement.

Table 3.6 Surface roughness of spot welded Usibor 1500 after vibratory polishing and etching in 2% Nital

Location	Nugget (1mm×1.3 mm)	HAZ (130 µm×95 µm)			HAZ (1mm×1.3 mm)
		CGHAZ (130 µm×95 µm)	ICHAZ (130 µm×95 µm)	SCHAZ (130 µm×95 µm)	
Ra (nm)	58.3	61.4	50.65	47.25	81.7

Nanoindentation was performed on a MTS Nano Indenter® XP system. The measurement was done in Continuous Stiffness Measurement (CSM) mode which allowed continuous measurement of the stiffness during loading, instead of just measuring the stiffness from unloading curve in a conventional measurement. The nanohardness was measured in the displacement control mode, with the maximum indentation depth of 1500 nm. This depth was chosen to prevent the indentation size effect (ISE), in which nanohardness increases with decreasing contact depth at small contact depths [123]. To prevent the effect of strain fields induced by prior indents, an indentation spacing of 100 µm (> 30 times of the penetration depth) was used. Before testing on actual welds, the Berkovich indenter was calibrated on fused silica with theoretical Young's modulus of 72 GPa and nanohardness on the order of 9 GPa [124].

From the measured load-displacement curve in nanoindentation, the mechanical properties of different HAZ sub-regions in Usibor® 1500 were predicted based on the reverse analysis approach proposed by Dao et al. [125]. In their approach, the elastoplastic behavior is assumed to follow the power law, where the true stress-strain is expressed as:

$$\sigma = \begin{cases} E\varepsilon, & \sigma \leq \sigma_y \\ K\varepsilon^n, & \sigma > \sigma_y \end{cases} \quad \text{Equation 3.14}$$

where E is Young's modulus, K is a material strength coefficient, n is strain hardening exponent, σ_y is yield strength, and ε is strain. From the reverse analysis, the yield strength σ_y , strain hardening exponent n, and Young's modulus E of different microstructure were extracted. To obtain the strength coefficient K, Equation 3.14 can be written for $\sigma = \sigma_y$:

$$\sigma_y = K\varepsilon_y^n \rightarrow K = \frac{\sigma_y}{\varepsilon_y^n} \quad \text{Equation 3.15}$$

where ε_y is the strain at yielding and is equal to $\varepsilon_y = \frac{\sigma_y}{E}$. A detailed description of the reverse analysis approach is available in Ref. [125] and thus not repeated here.

3.2 Model validation

Figure 3.9 (a) shows that both nugget geometry and electrode indentation profile calculated by the FE model were consistent with those measured experimentally for the welding current (equivalent DC) of 6.7 kA. The calculated temperature distribution showed a steep temperature gradient along the through-thickness direction. Particularly, over a short distance of 0.4 mm, the temperature dropped from the liquidus temperature of 1509 ^{o}C (1782 K) at the nugget boundary to around 1000 ^{o}C (1273 K) at the steel surface in contact with the water-cooled electrode. In addition, the predicted nugget diameter and nugget thickness as a function of welding current were found to correlate well with the

respective experimental data, as shown in Figure 3.9 (b) and (c).

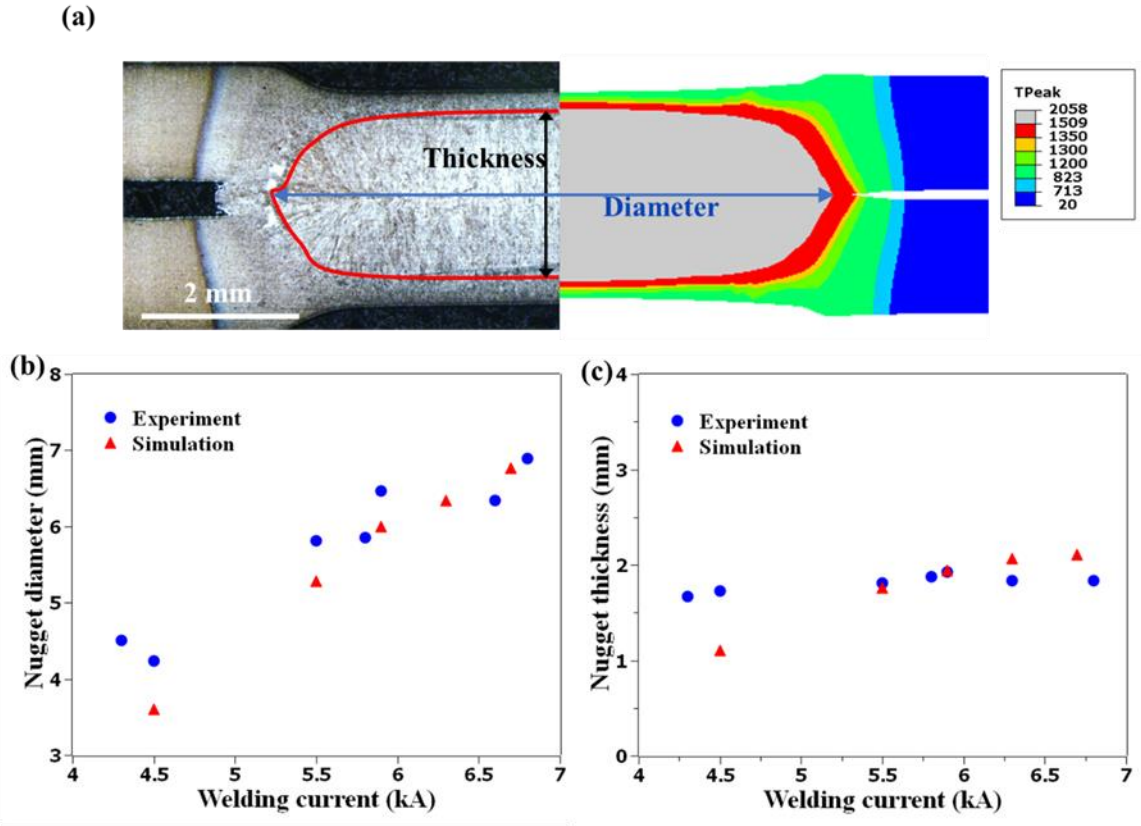

Figure 3.9 Comparison between the simulated nugget dimensions (i.e., nugget diameter and thickness) and experimental measurements. Calculated temperature is given in Celsius in (a). Welding current in (b) and (c) corresponds to the equivalent DC.

As discussed previously, the electrode indentation is a crucial parameter of weld quality that can affect the load-bearing capacity of a spot weld. Figure 3.10 shows that the predicted electrode indentation was consistent with the physical measurement over a wide range of welding currents. The electrode indentation increased with the welding current since a larger portion of the base metal was heated, softened, and then deformed under the applied electrode force. For the welding current range studied, the maximum

electrode indentation was about 0.15 mm. AWS D8.1M limits the maximum indentation to 30% of the sheet thickness [126]. For the 1.5-mm-thick Usibor 1500 sheet, the AWS limit is thus 0.45 mm. Hence, the maximum electrode indentation for spot welds made in this study is within the limit specified by AWS D8.1M.

The consistent results between the experiment and simulation over a wide range of welding currents shown in Figure 3.9 and Figure 3.10 supported the validity of the process model. In the next sections, the results calculated using the process model were used for further analysis of contact pressure, contact area, and nugget formation, and subsequently inputted into the JMAK equation to predict the HAZ softening.

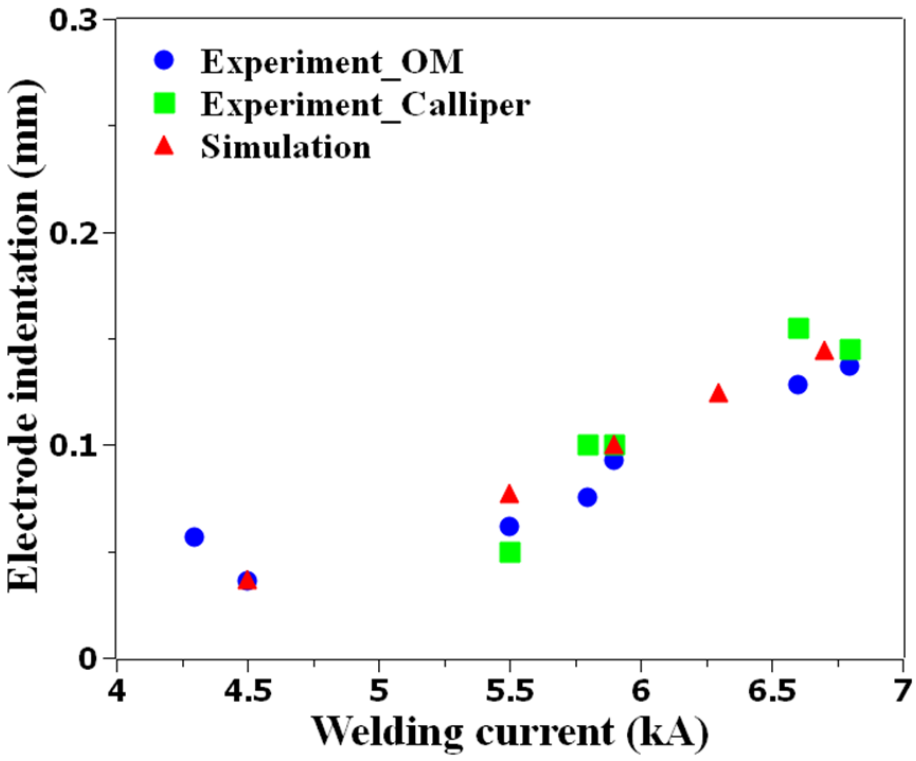

Figure 3.10 Comparison between the simulated and experimentally-measured surface electrode indentation as a function of welding current. OM is the indentation measured via optical microscope, and caliper is that measured using a caliper.

3.3 Temperature evolution and nugget formation

Figure 3.11 shows the calculated temperature distribution in the quarter joint at two different times during RSW. As the current flowed through the joint, both the bulk resistance of the steel sheets and the electrical gap resistance at the E/S and S/S interfaces contributed to rapid heating. The peak temperature occurred at the centre of the S/S interface due to the high current density locally, and the weld nugget initiated at approximately 6 cycles in the first impulse (t = 100 ms), as shown in Figure 3.11 (a). At the time of nugget initiation, the electrode indentation was fairly shallow. Subsequently,

as more heat was inputted to the joint by Joule heating, the weld nugget expanded in both the radial and through-thickness directions and reached its maximum size at the end of the third impulse, as shown in Figure 3.11 (b). At that time, a large region surrounding the weld nugget was also heated to elevated temperature (above A_{C3}), and that softened region resulted in the formation of a marked electrode indentation under the electrode force.

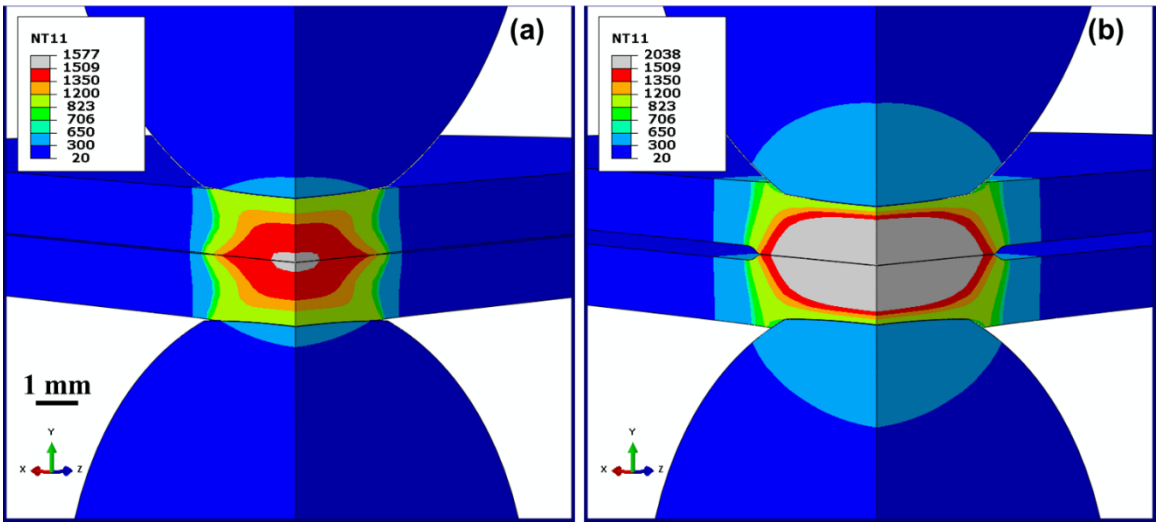

Figure 3.11 Calculated temperature field showing (a) initial nugget formation at the sixth cycle of the first impulse (t = 100 ms), and (b) fully-grown nugget at the end of the third impulse (t = 617 ms). The welding current was 6.7 kA.

Figure 3.12 plots the temperature profiles at five monitoring locations in the spot weld. These locations can be classified based on the local peak temperature. The weld nugget centre was heated above the liquidus temperature. Both the coarse-grained heat affected zone (CGHAZ) and fine-grained heat affected zone (FGHAZ) were heated above A_{C3} temperature, with the former well above and the latter close to A_{C3}. As described previously, the ICHAZ was heated in between A_{C3} and A_{C1}, while the SCHAZ was

heated below A_{C1}. Detailed description of the microstructure in those HAZ sub-regions is presented in the next section.

As shown in Table 3.2, the welding current profile was made of three impulses, with each impulse comprising 11 current-on cycles followed by 2 current-off cycles. The cool time between pulse is applied to increase the electrode life by cooling down the electrode/sheet interface and distThe temperature rose when the current was on and dropped when it was off, resulting in three spikes that were distinct in the temperature profiles of the weld nugget centre and CGHAZ (Figure 3.12). As the distance from the weld centre increased, the effect of pulsing on temperature fluctuation diminished, and the temperature spikes became unnoticeable in the SCHAZ. Figure 3.12 also shows that for locations closer to the weld centre, the peak temperature and heating and cooling rates were higher. Particularly, the weld centre temperature increased rapidly through the initial 6 cycles of the first impulse with an average heating rate of 15362 ^{o}C/s. The heating rate then tapered off for the remaining impulses. In addition, as the temperature passed through the solidus (1475 ^{o}C or 1748 K) to the liquidus temperature (1509 ^{o}C or 1782 K), the heating and cooling rates were temporarily reduced due to the effect of latent heat.

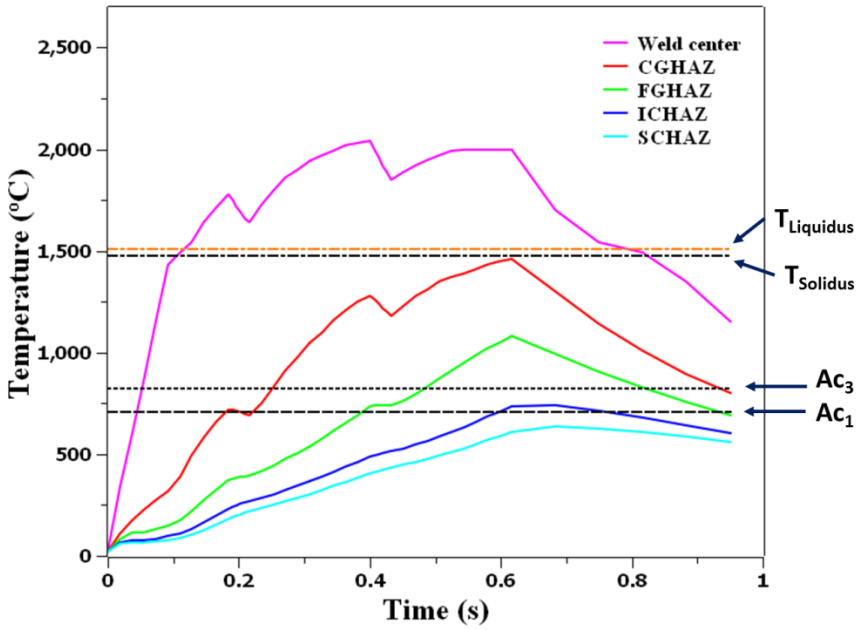

Figure 3.12 Temperature profiles at the centre of the weld nugget and four other locations in the HAZ (welding current = 6.7 kA).

3.4 Evolution of contact pressure during RSW

An understanding of contact conditions at the E/S and S/S interfaces is important when studying the electrode wear and liquid metal expulsion, respectively. As a first step, the contact pressure distribution calculated by the process model of RSW of Usibor 1500 steel was examined in the following.

A pair of dome-shaped electrodes were used in this RSW experiment. At the end of the squeeze cycle (prior to application of welding current), the contact at the E/S interface was limited to the tip of the dome, resulting in a peak contact pressure of 625 MPa at the electrode centre, as shown in Figure 3.13 (a). The contact pressure at the E/S interface quickly decreased along the radial direction. The initial contact radius at the E/S

interface was about 2.2 mm, which was smaller than the electrode diameter of 3 mm due to the limited deformation of Usibor 1500 at room temperature. The initial contact between the two flat steel sheets was more spread out, resulting in a contact pressure distribution similar to that of the E/S interface but with lower peak pressure (350 MPa), as shown in Figure 3.13(b). It is noted that the contact pressure distribution depends on the shape of the electrode. For instance, for flat truncated electrodes, the maximum contact pressure is found near the edge of the electrode at both the E/S and S/S interfaces [59]. Although such "pinching" force along the periphery of the contact area may help reduce liquid metal expulsion, it can also lead to undesirable electrode deterioration and mushrooming [60].

The initial contact pressure distribution was quickly altered once the welding current was applied. For example, at the end of the first impulse, the contact radius at the E/S interface was increased to 3 mm and that at the S/S interface to 3.5 mm. As the contact area expanded, the contact pressure at the centre of E/S and S/S interfaces was reduced to 140 and 151 MPa, respectively. Such expansion in contact area and the corresponding drop in the peak contact pressure was caused by heating, softening, and plastic deformation of the steel sheets. The expansion of contact area continued in the second and third impulses, although the rate of expansion was much reduced.

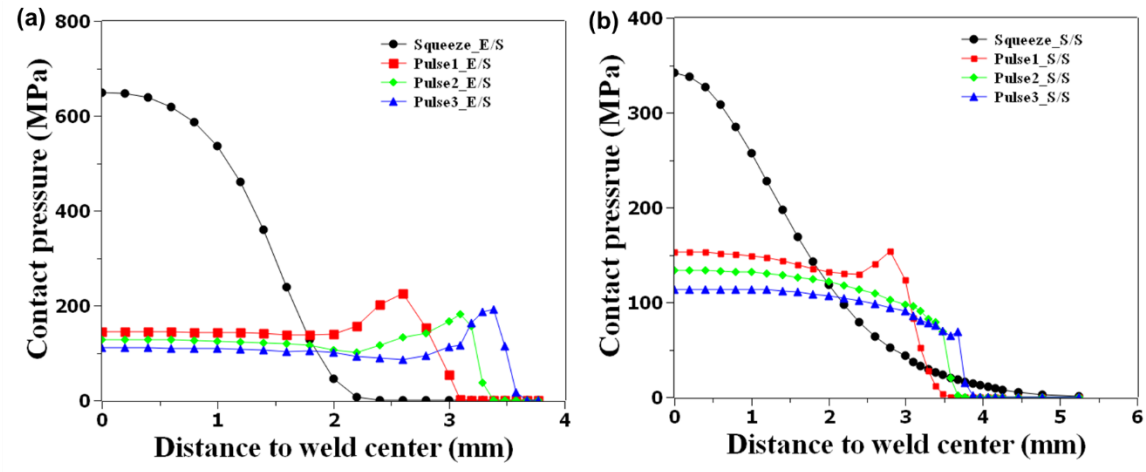

Figure 3.13 Evolution of contact pressure distribution at (a) electrode/steel and (b) steel/steel interfaces

As shown in Figure 3.13(a), once the welding current was applied, the contact pressure at the E/S interface was relatively uniform at the centre and reached its peak value at the periphery of the electrode. This was likely caused by local heating of the workpiece due to high current density and the resulting non-uniform temperature distribution. Specifically, the material near the centre of the joint was heated to a higher temperature and could consequently support lower stresses than the cooler material around the periphery of the joint. At the S/S interface (Figure 3.13(b)), the contact pressure distribution at the end of first impulse had a similar shape to that of the E/S interface, with peak pressure occurring along the periphery. However, as the contact area at the S/S interface continued expanding, the shape of the contact pressure distribution changed, and the pressure decreased gradually from the centre to the periphery along the radial direction. Such change indicated that the liquid metal was more likely to be expelled at the end of second and third impulses than the first impulse. It is noted that the

validity of the calculated contact pressure at the S/S requires further examination since the molten metal would fuse together, a phenomenon not considered in the mechanical simulation.

3.5 Weld microstructure and hardness

3.5.1 Experimental characterization of weld microstructure

This section discusses the weld microstructure characterized in optical and scanning electron microscopy (OM and SEM, respectively). Such information is essential to the prediction of location-specific mechanical properties (e.g., hardness) of the spot weld, to be presented in the next section.

Figure 3.14 (a) provides an overview of various regions observed on the cross section of the resistance spot welded Usibor 1500 steel. The weld nugget microstructure consisted of lath martensite, as shown in Figure 3.14 (b). Such fully martensitic microstructure was expected, as the calculated cooling rate in the nugget (about 1500 °C/s) was well above the critical cooling rate (30 ^{o}C/s) for martensite formation in Usibor 1500 [21]. It is interesting to note that in the literature, the weld nugget for fibre laser welded Al-Si coated boron steel was shown to contain α-ferrite and martensite along fusion boundary [127][128]. Such difference in weld nugget microstructure between RSW and fiber laser welding was caused by the Al-Si coating. Particularly, during RSW, the Al-Si coating was melted, squeezed out, and resolidified along the weld periphery on the surface, thus never mixing with the molten metal [55]. In the case of fiber laser

welding, the Al-Si coating mixed into the weld pool. Fusion boundary is enriched in Al due to inadequate mixing of Al-Si coating in the weld pool. Since Al is a ferrite stabilizer, ferrite forms in the fusion boundary, which make the weld to be susceptibility to premature failure along the fusion boundary. In another literature study, Sherepenko et al. [129] observed a 26-35% hardness drop at the fusion boundary in resistance spot welded Usibor 1500 steel. They hypothesized that the hardness drop was due to the formation of δ-ferrite and associated carbon depletion. It is noted that the fusion boundary microstructure of resistance spot welds produced in the present study was carefully examined and no softening was observed. Further study is needed to better understand the mechanism of RSW fusion boundary softening observed by Sherepenko et al. [129].

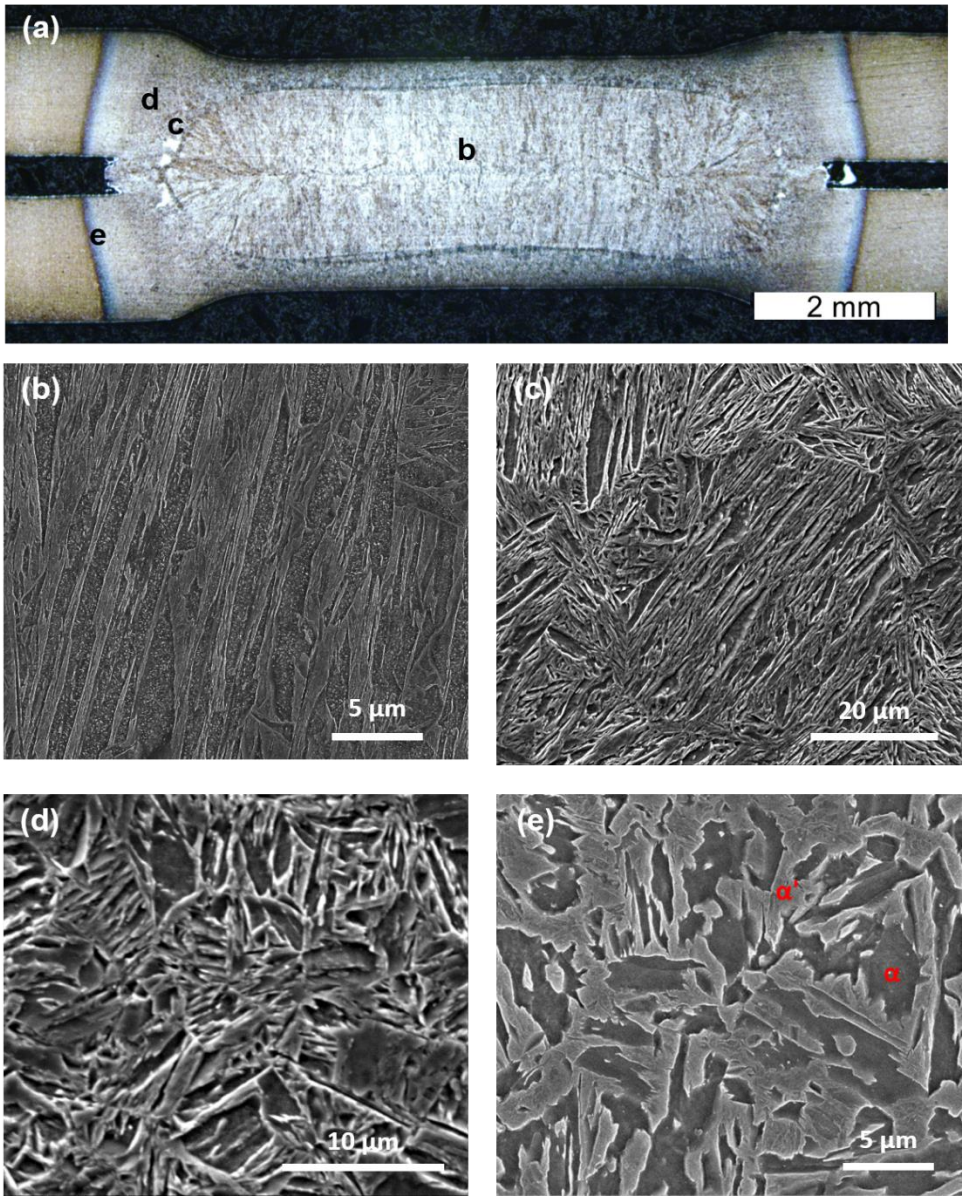

Figure 3.14 (a) macrograph of the spot weld cross section, and SEM images of (b) weld metal, (c) CGHAZ, (d) FGHAZ, and (e) ICHAZ. The locations of observation in (b) through (e) are marked in (a)

According to the temperature profile shown in, the CGHAZ was heated well above A_{C3}. As a result, significant grain growth took place at elevated temperatures, forming coarse prior austenite grains. The FGHAZ was heated above but close to A_{C3} and

consequently no significant grain growth occurred there. Regardless of grain size, both the CGHAZ and FGHAZ transformed completely into austenite upon heating, which was transformed back into martensite as the cooling rate in those two regions (about 1000 ^{o}C/s) also well exceeded the critical cooling rate. The typical CGHAZ and FGHAZ microstructures are shown in Figure 3.14 (c) and (d), respectively. The martensite lathes are shorter in the FGHAZ than the CGHAZ, possibly limited by the small prior austenite grain size in the former.

When the fully martensitic base metal was heated up to a temperature between A_{C1} (714 °C) and A_{C3} (823 °C), a mixture of fresh ferrite and austenite was formed. During subsequent rapid cooling, the austenite in the mixture transformed to martensite, resulting in the formation of a dual phase microstructure consisting of ferrite (α) and martensite (α'). This region is referred to as the ICHAZ, with a typical microstructure shown in Figure 3.14 (e). Within the ICHAZ, the volume fraction of martensite decreased as the location was further away from the weld centre. This is due to the lower peak temperature and consequent reduction in austenite formation during heating, which in turn reduced the amount of martensite formed during rapid cooling.

The last region of the HAZ, which is directly adjacent to the base metal, is the SCHAZ. Similar to the ICHAZ, there existed a gradient of microstructure within the SCHAZ, as shown in Figure 3.15 for locations at a distance of 10, 100, 300, 500, and 800 μm away from the boundary between the ICHAZ and SCHAZ (referred to as the A_{C1} boundary for brevity). The base metal martensite at a distance within 300 μm of the A_{C1}

boundary was completely decomposed, resulting in completely tempered martensite containing ferrite and fine, sub-micron cementite particles [115]. The latter precipitated along prior austenite grain boundaries and prior martensite lath boundaries as well as inside prior martensite laths, as shown in Figure 3.15 (a) to (c).

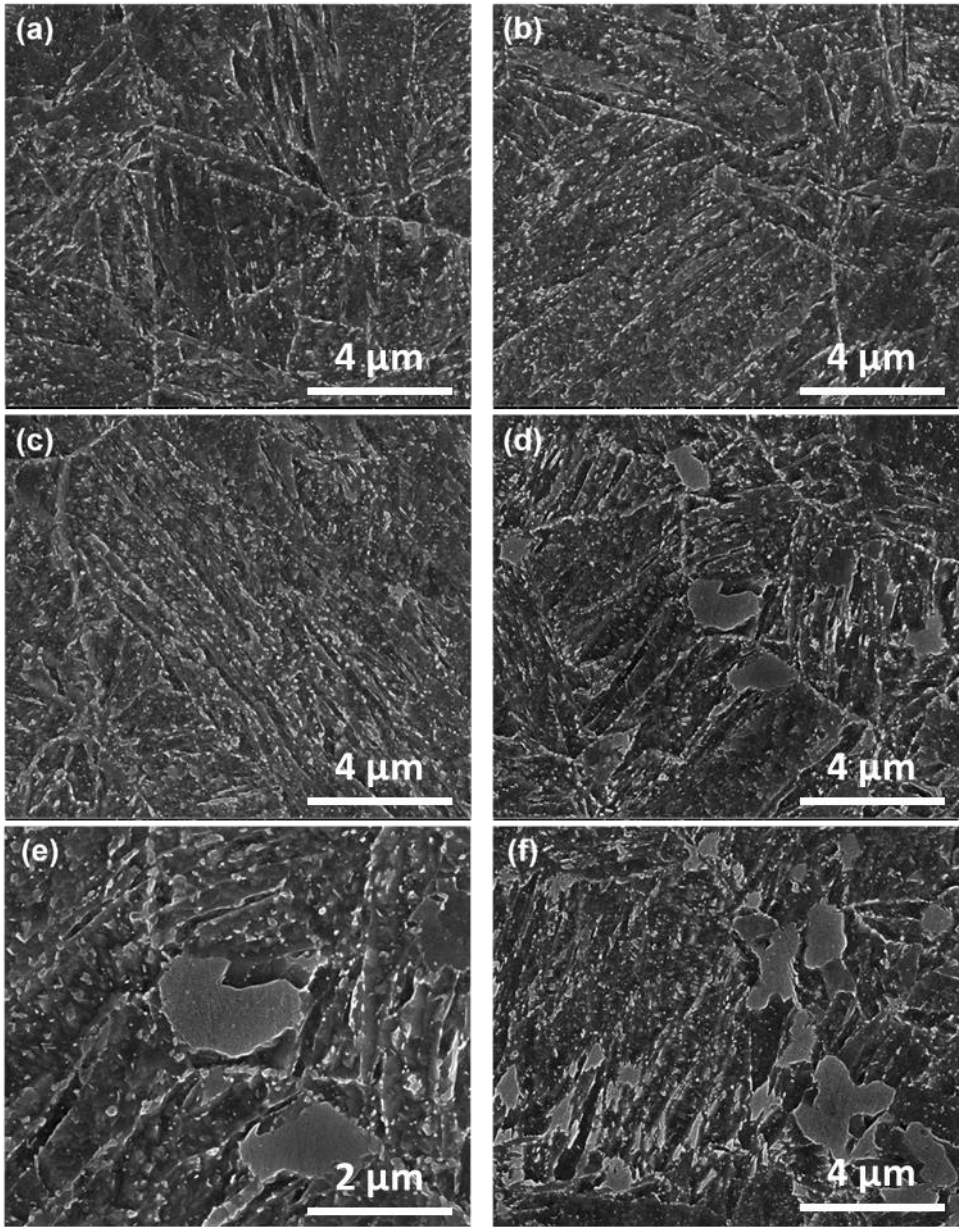

Figure 3.15 SEM images of tempered martensite in the SCHAZ at (a) 10 µm, (b) 100 µm, (c) 300 µm, (d) 500 µm, (e) zoomed-in view of (d), and (f) 800 µm away from A_{C1} boundary

At a location 500 µm away from A_{C1} boundary (see Figure 3.15 (d) and (e)), untempered martensite was observed, indicating that the local temperature and time were not high enough to allow complete martensite decomposition. In general, an increase in

distance from the A_{C1} boundary was associated with an increase in volume fraction of untempered martensite, with a corresponding decrease in cementite volume fraction and size. Similar changes in cementite's volume fraction and size in the SCHAZ were also observed in resistance spot welded DP steel [130].

3.5.2 Nanoindentation

The load-displacement curves for base metal and tempered martensite with the distance of 10 μm, 200 μm, 500 μm, 800 μm to A_{C1} line measured by nanoindentation were shown in Figure 3.16. With the same penetration depth of 1500 nm, base metal showed the highest indentation force of 0.27 N. On the other hand, the lowest indentation force of 0.20 N was at the location adjacent (10 μm) to A_{C1} line due to the high peak temperature experienced at this location. At 800 μm away from A_{C1} line, the indentation force was 0.25 N which was similar to that of the base metal. This correlated well with the microstructure at the 800 μm consisted of a larger amount of untempered martensite and a smaller amount of finer cementite as shown in Figure 3.15.

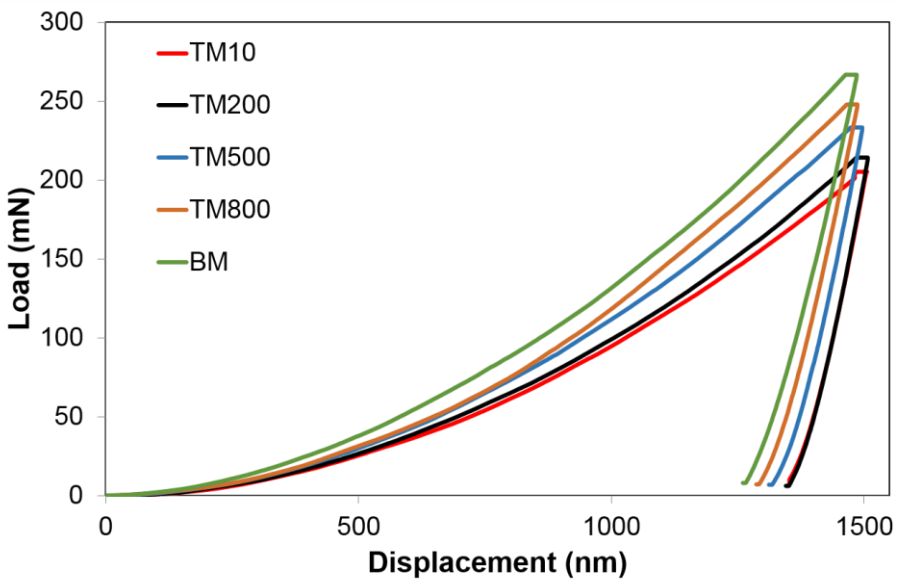

Figure 3.16 Load-displacement curves for base metal (BM) and tempered martensite with the distance of 10 μm (TM10), 200 μm (TM200), 500 μm (TM500), 800 μm (TM800) to A_{C1} line

Nanohardness with fine indent spacing of 100 μm was measured across the weld as shown in Figure 3.17. The nanohardness of the base metal was 5.6 ± 0.13 GPa. Due to the fully martensitic microstructure, the nanohardness of the weld nugget was about 5.76 ± 0.31 GPa, similar to that of the base metal. It is noted that the nanohardness of fully martensite microstructure in nugget and base metal corresponded well with that of martensite formed in water quenched steels with the carbon content of 0.2 - 0.25 wt. % (the same range of carbon content as that of Usibor® 1500) reported in the literature [131].

Nanohardness of the CGHAZ and FGHAZ was similar to that of the weld nugget, while the nanohardness of the ICHAZ decreased almost linearly as the location from the FGHAZ/ICHAZ boundary increased. This was due to a reduction of volume fraction of

martensite in the dual phase microstructure consisted of martensite and ferrite (see Figure 3.14).

Finally, the lowest hardness of 4 ± 0.07 GPa, which was about 66% of the weld nugget hardness, was observed in the location adjacent to A_{C1} line in the SCHAZ. The low hardness indicated a low strength of SCHAZ, making it prone to the premature failure during shear loading. As shown in Figure 3.17, the fine-spaced nanohardness measurement showed that the width of the SCHAZ was approximately 0.8 mm.

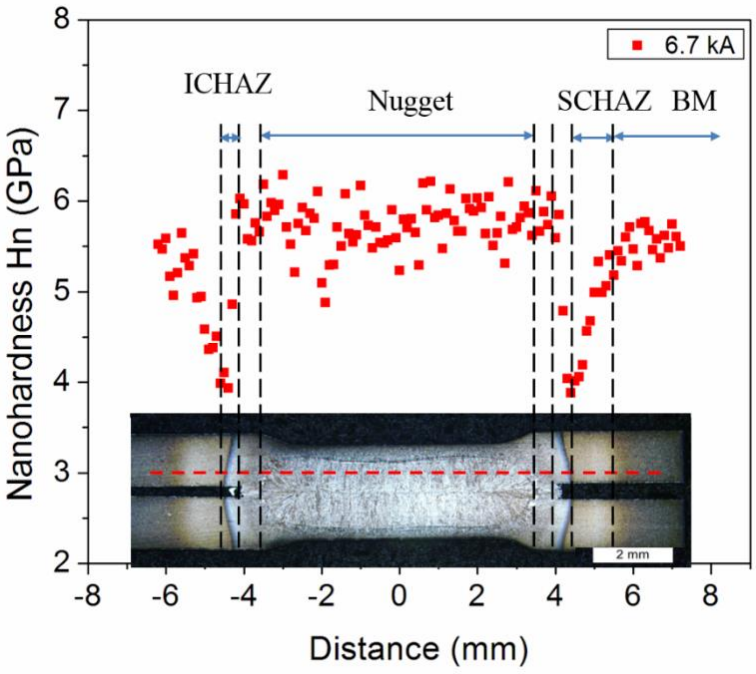

Figure 3.17 Transverse nanohardness profile of spot welded Usibor® 1500

3.5.3 Isothermal tempering tests for simulated SCHAZ

As discussed earlier, isothermal tests with various temperatures and times were performed in a Gleeble machine in order to establish the softening kinetics. The isothermal testing results are summarized in Figure 3.18(a). As shown in this figure, the extent of martensite tempering was found to be more sensitive to tempering temperature than time. For instance, the hardness dropped by 37.5% compared to base metal for martensite tempered at 650 ºC (923 K) for only 0.2 s. Upon further tempering to 10 and 3600 s, the hardness had an additional drop of only 5% and 13%, respectively. Compared to the high temperatures tested (500 °C/773 K and above), softening kinetics at low temperatures were much slower. For example, the hardness was reduced by approximately 8.7% for martensite tempered at 350 ºC (623 K) for 10 s.

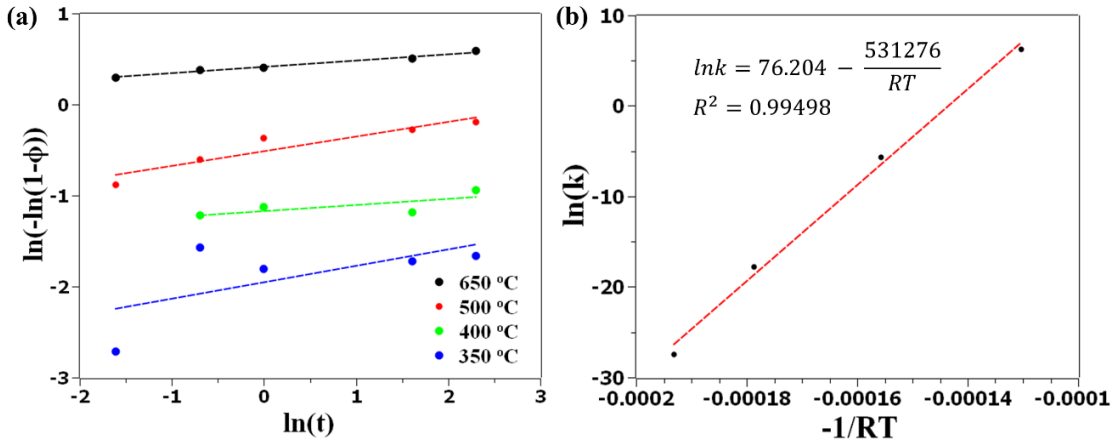

Figure 3.18 Linearized JMAK equation to extract tempering kinetics parameters.

By applying Equation 3.5 and Equation 3.6, the tempering kinetics parameters Q, k_0 and n were determined to be 531.276 kJ/mol, 1.24×10^{33} and 0.0658 respectively, as

shown in Figure 3.18 (b). It is noted that these values are not directly comparable to the literature values such as the activation energy for carbon diffusion in ferrite = 84 kJ/mol [132], the activation energy for diffusion of vacancies in ferrite = 210 – 315 kJ/mol [132], and the exponent = 0.67 for diffusion-controlled coarsening of cementite [133]. This is because the extent of softening ϕ used in this study is defined based on hardness, and the relationship of hardness with the volume fraction (or size) of cementite is likely non-linear.

The goodness of fit is illustrated in Figure 3.19, where the extent of tempering calculated using the JMAK equation is compared to the experimental value (used to extract the tempering parameters). Overall, the predicted value corresponded well with the experimental data, especially at high tempering temperatures (e.g., 650 ^{o}C/923 K) and longer times (e.g., 5 to 10 s). In the literature, Biro et al. [114] divided the softening process of martensitic steel M220 into two sub-steps: carbide nucleation and carbide coarsening. They found that the carbide nucleation step in M220 steel was very fast and could only be observed at low tempering temperature (T < 420 ^{o}C) for short tempering time (t < 1 s). Hence, the relatively poor goodness of fit for data points at low temperature and short time shown in Figure 3.19 could be due to the fact that a single set of activation energy and exponent was used in the fitting. Developing two sets of kinetics parameters (one for nucleation and the other for coarsening) is feasible, although it would require more data points to capture the nucleation step and add complexity when the equation is applied to non-isothermal condition. Given that tempering is most significant

at high temperature, the single set of kinetics parameters was deemed acceptable for predicting SCHAZ hardness in resistance spot welding.

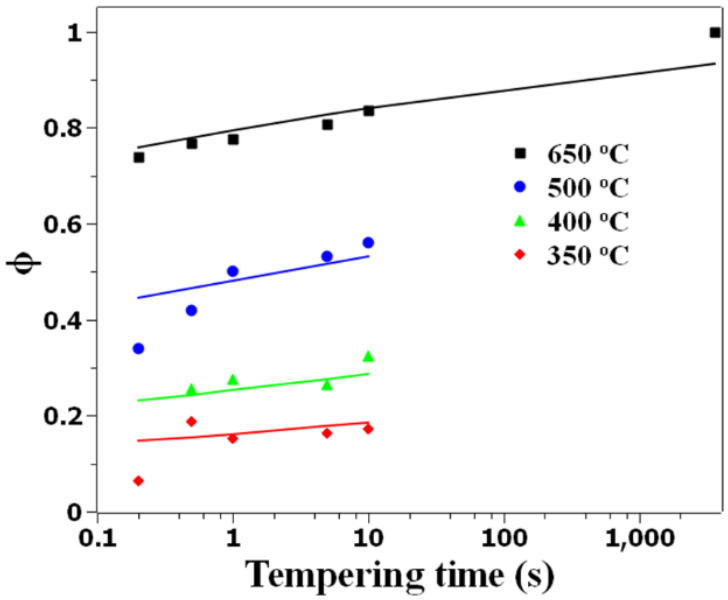

Figure 3.19 Comparison of measured softening (plotted as discrete points) to the calculated softening (plotted as curves) showing the goodness of fit for the extracted kinetics parameters.

3.5.4 Hardness map of resistance spot weld

As described previously in Sections 3.3, the temperature profiles in the spot weld were predicted by the RSW process model, and the softening kinetics parameters were extracted from the isothermal tempering tests, respectively. By inputting these two pieces of information into the non-isothermal JMAK equation (Equation 3.4), the hardness of the SCHAZ could be predicted. The following simplified treatments were used to obtain the hardness of other regions in the spot weld. Since the weld metal, CGHAZ, and FGHAZ consisted of fully martensitic microstructure, the base metal hardness of 493 HV

was assigned to those regions. As shown in Figure 3.14 (e), the ICHAZ consisted of a dual phase microstructure of martensite and ferrite, with the volume fraction of martensite decreasing as the local peak temperature dropped from A_{C3} to A_{C1}. Given this microstructure gradient within the ICHAZ, the hardness of ICHAZ was defined as a linear function of local peak temperature:

$$H_{IC} = f_M\, H_{FG} + (1 - f_M) H_{SC} \qquad \text{Equation 3.16(a)}$$

$$f_M = \frac{T_p - A_{C1}}{A_{C3} - A_{C1}} \qquad \text{Equation 3.17(b)}$$

where H_{IC} is the local hardness of the ICHAZ, H_{FG} and H_{SC} are the hardness of the FGHAZ and SCHAZ that is immediately adjacent to the ICHAZ, respectively, and T_p is the local peak temperature within the ICHAZ ($A_{C1} < T_p < A_{C3}$).

The predicted hardness and peak temperature distributions for the spot weld at welding current = 6.7 kA are shown side-by-side in Figure 3.20. The blue ring-shaped region is the location that experienced the most significant tempering effect, with a 30 – 40% hardness reduction compared to the base metal. For a more quantitative analysis, the predicted hardness was plotted along two monitoring paths: one parallel to the faying surface and the other on the cross section of a spot weld. As shown in Figure 3.21, the predicted hardness profile along both paths was consistent with that measured experimentally, especially in the softened region. As discussed previously, some degree of tempering likely occurred during heating to the testing temperature in the isothermal tempering experiment. Such tempering during heating, although undesirable, did not

seem to adversely affect the prediction of hardness, as indicated by the consistency between calculated and measured hardness profiles in Figure 3.21.

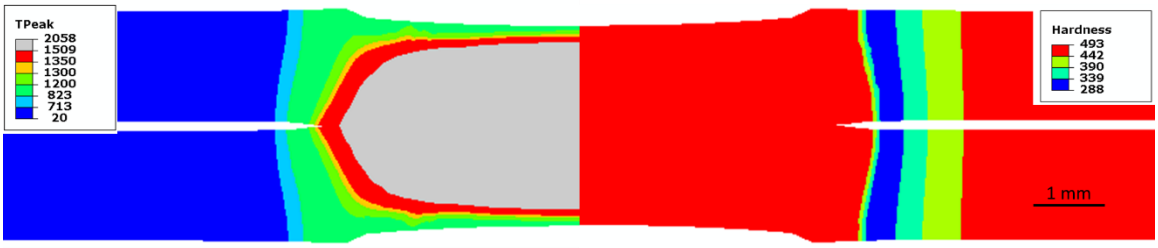

Figure 3.20 A composite picture of predicted temperature distribution (left) and hardness map (right) in resistance spot welded Usibor 1500 for welding current of 6.7 kA. Temperature is given in Celsius and hardness in Vickers.

Figure 3.21 shows some under-prediction of hardness for the CGHAZ and FGHAZ, and to a lesser extent the weld metal, due to the simplified treatment of assigning the base metal hardness to those regions. Although all are fully martensitic, the specific martensitic microstructure (e.g., lath size) is different for the CGHAZ, FGHAZ, and weld metal than that for the base metal (see Figure 3.1 and Figure 3.14). Future study is necessary to refine the hardness prediction, allowing it to account for the local martensitic microstructure in those regions as well as the microstructure-dependent mechanical properties. Nevertheless, the overall consistency between the calculated and measured hardness for RSW indicates that the non-isothermal JMAK equation, along with the kinetic parameters, can be used for studying SCHAZ softening of hot-stamped boron steel in other welding processes such as laser or arc welding.

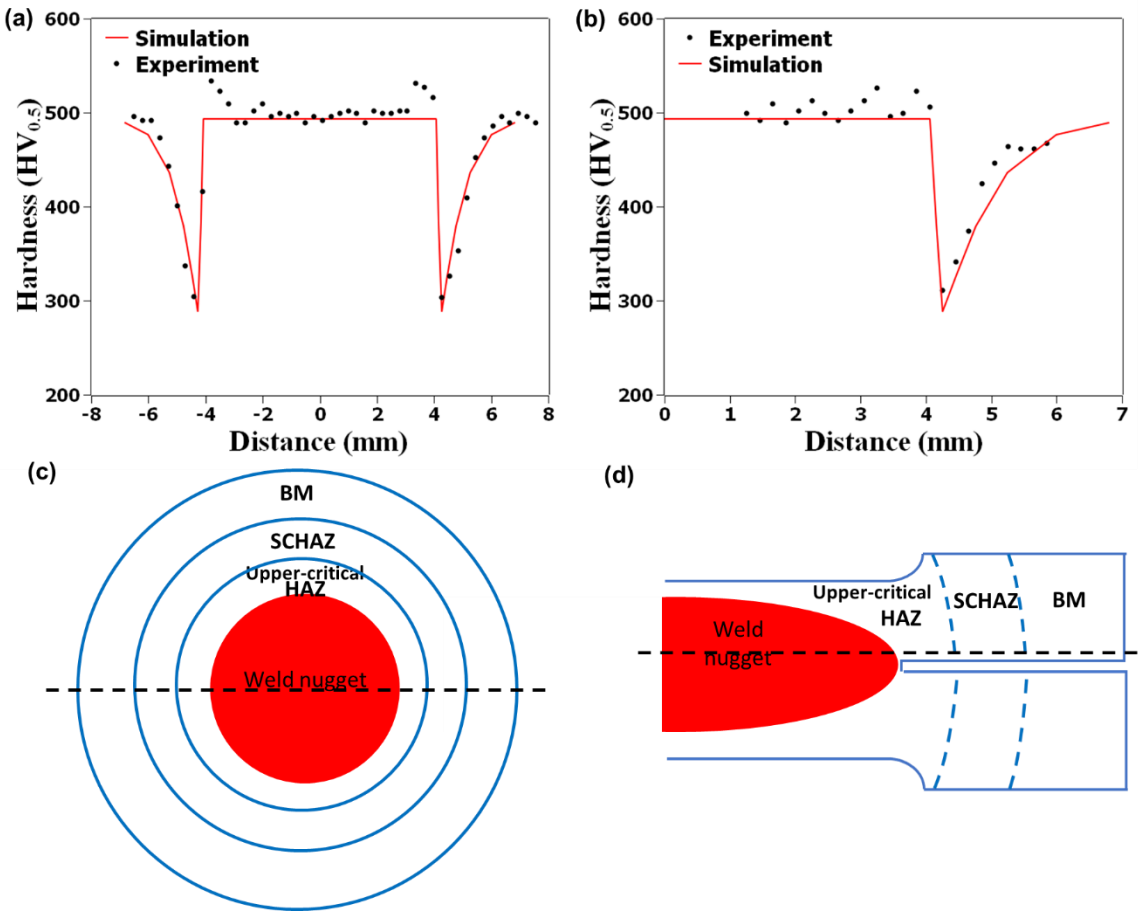

Figure 3.21 Predicted and measured hardness profiles along (a) one path parallel to faying surfaced, (b) another path on cross section of spot weld. The measurement locations in (a) and (b) are schematically shown in (c) and (d), respectively.

It is noted that to simplify the hardness prediction in SCHAZ, one may just consider the effect of peak temperature on softening since temperature has the most significant effect on hardness reduction. Figure 3.22 showed the tempering extent (volume fraction of tempered martensite) as a function of tempering temperature at the tempering time of 1 s. The volume fraction of tempered martensite was almost linearly increasing with tempering temperature. Figure 3.23 showed the comparison of the predicted hardness in SCHAZ based on two theories mentioned above, e.g. JMAK and peak temperature, with

the measured hardness profile. In general, the results predicted by solely considering about tempering temperature showed more softening compared to the one predicted based on tempering kinetics described by JMAK. The reason was that the non-isothermal temperature profiles in resistance spot welding consist of rapid heating and cooling, while the tempering time at the peak temperature was relatively short compared to the total welding time. However, if only peak temperature was considered in hardness prediction as shown in Figure 3.22 , it was assumed that martensite is isothermally tempered for 1 s at all temperatures, which may be quite off from the actual tempering condition experienced by the base metal. Therefore, to increase the accuracy of hardness prediction in the case that only peak temperature was considered, the equivalent tempering times at peak temperature need to be calculated. In summary, considering time-dependence can make the formula not only more accurate but also more useful for studying SCHAZ softening in other welding processes such as arc welding.

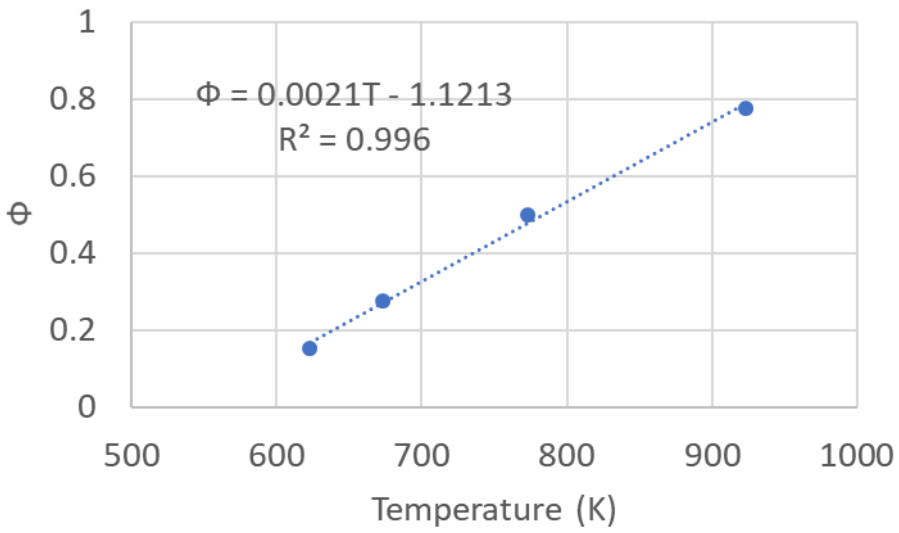

Figure 3.22 Tempering kinetics extracted by peak temperature with tempering time of 1 s

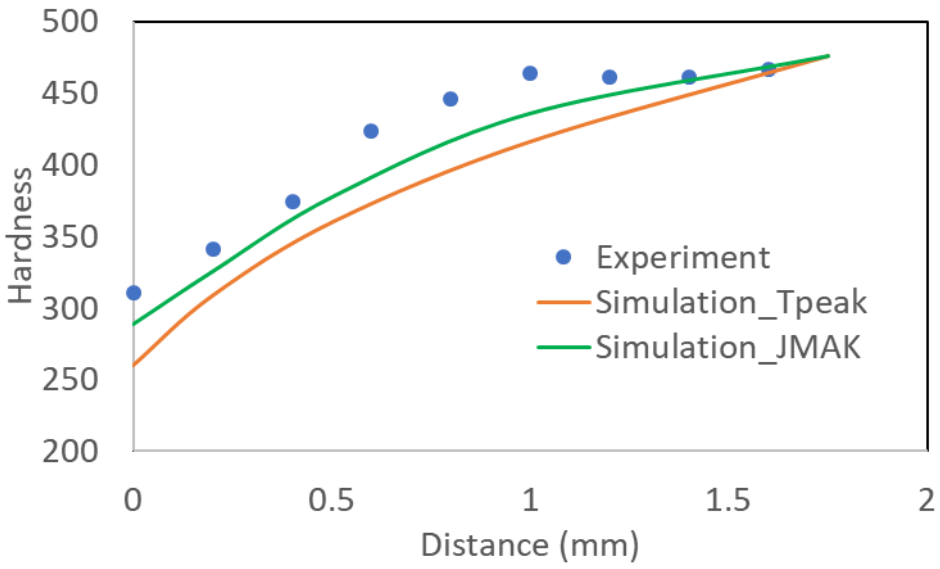

Figure 3.23 Comparison of predicted hardness using JMAK and peak temperature to the experimental results

In addition to the magnitude of hardness drop due to tempering, the width of the softened region is another important parameter to study the property gradient in the spot

weld. As shown in Figure 3.21 at a welding current of 6.7 kA, the overall width of the SCHAZ was about 1.7 mm. Within the SCHAZ, the region for which the hardness dropped below 60% of the base metal hardness was approximately 0.2 mm wide. Moreover, the width of HAZ sub-regions and the nugget diameter are plotted as a function of welding current in Figure 3.24. As their individual widths were difficult to measure experimentally, the CGHAZ, FGHAZ, and ICHAZ were grouped together into the "UpperCritical + ICHAZ." Both the experimental and calculated results showed a slight decrease in "UpperCritical + ICHAZ" width with an increase in welding current (or heat input). Such behaviour could be explained by the heat loss to the water-cooled electrodes. In particular, as the heat input was increased, the indentation and contact area with the electrode were also increased, leading to more heat loss to the electrode and more cooling in the region around the weld nugget, which in turn resulted in a smaller "UpperCritical + ICHAZ." Another interesting observation from Figure 3.24 is that the SCHAZ width did not vary markedly with welding current for the current range studied. This was due to the relatively low temperature necessary to cause tempering, which was less sensitive to the amount of heat conduction through the base metal.

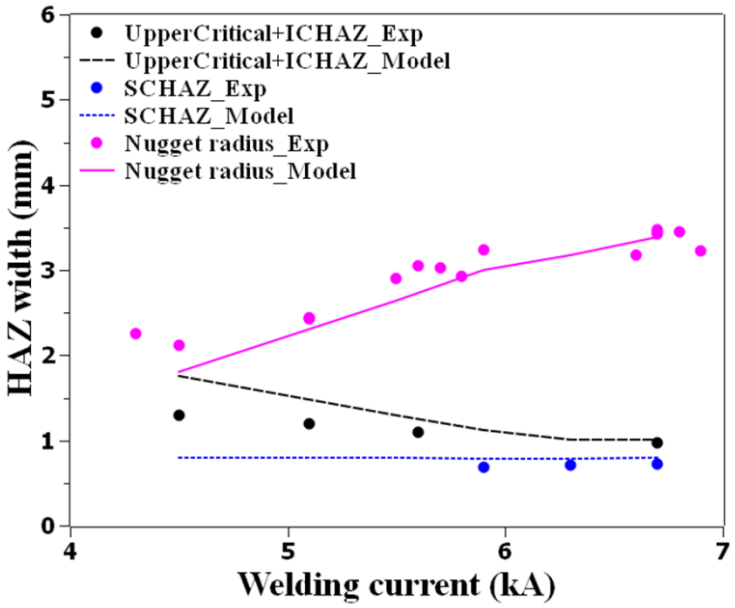

Figure 3.24 Effect of welding current on the width of HAZ sub-regions and weld nugget diameter

3.6 Local constitutive behavior for post weld simulation

3.6.1 Gleeble simulation of CGHAZ and SCHAZ

The peak temperatures of SCHAZ and CGHAZ simulation by Gleeble were set to be 700 ^{o}C (just below A_{c1}) and 1300 ^{o}C (significantly above A_{c3}), respectively. The Gleeble simulated thermal profiles of CGHAZ and SCHAZ are shown in Figure 3.25.

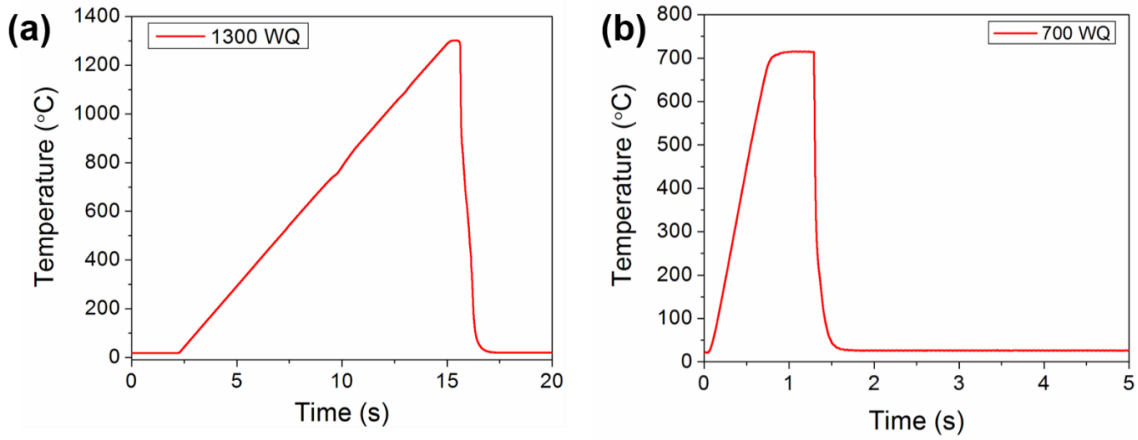

Figure 3.25 Temperature profiles of physically-simulated (a) CGHAZ and (b) SCHAZ by Gleeble® 3800

A comparison of CGHAZ and SCHAZ microstructure in actual weld and Gleeble simulated sample is shown in Figure 3.26. The microstructure of CGHAZ in actual weld and the Gleeble simulated sample were comparable; both comprised fully martensite. The nanohardness of the CGHAZ in actual welds was 5.75 ± 0.14 GPa. The nanohardness of Gleeble simulated sample cooled by water quench was about 6.39 ± 0.15 GPa, which was 10% higher than that of the actual CGHAZ (Figure 3.27). A possible reason could be that the auto-tempering of martensite occurred in actual weld toward the end of welding where the cooling rate was lowered after the removal of electrodes. For Gleeble simulated CGHAZ, the high cooling rate by water quench resulted in significant interstitial (carbon) solution strengthening effect.

It is noted that a large region (> 20 mm) with uniform martensitic microstructure was successfully generated in the tensile specimen for CGHAZ. The softened SCHAZ in the Gleeble simulated CGHAZ samples was in the clamped region of the tensile test sample.

This was essential to ensure that the tensile sample fractured within the gauge section for a complete measurement of the local stress-strain curve.

The microstructure of SCHAZ in actual welds and the Gleeble simulated sample was also comparable; both comprised tempered martensite. Cementite precipitated at the prior austenite grain boundaries, and interlath boundaries and intralath of martensite. Water quenched sample in Gleeble had a comparable hardness (3.55 ± 0.28 GPa) to the SCHAZ (3.91 ± 0.27 GPa) in actual spot weld. As discussed previously, to achieve high heating rate of 2000 ^{o}C/s, copper grips were used to clamp the sample. Microhardness examination showed that a 12 mm-long region with uniform tempered martensite microstructure was generated in water quenched tensile sample for SCHAZ.

In summary, coarse grain HAZ and subcritical HAZ microstructure was successfully recreated by Gleeble® 3800 thermo-mechanical simulator. These heat-treated samples were utilized for local mechanical properties (stress-strain curves) measurement in conventional quasi-static uniaxial tensile testing.

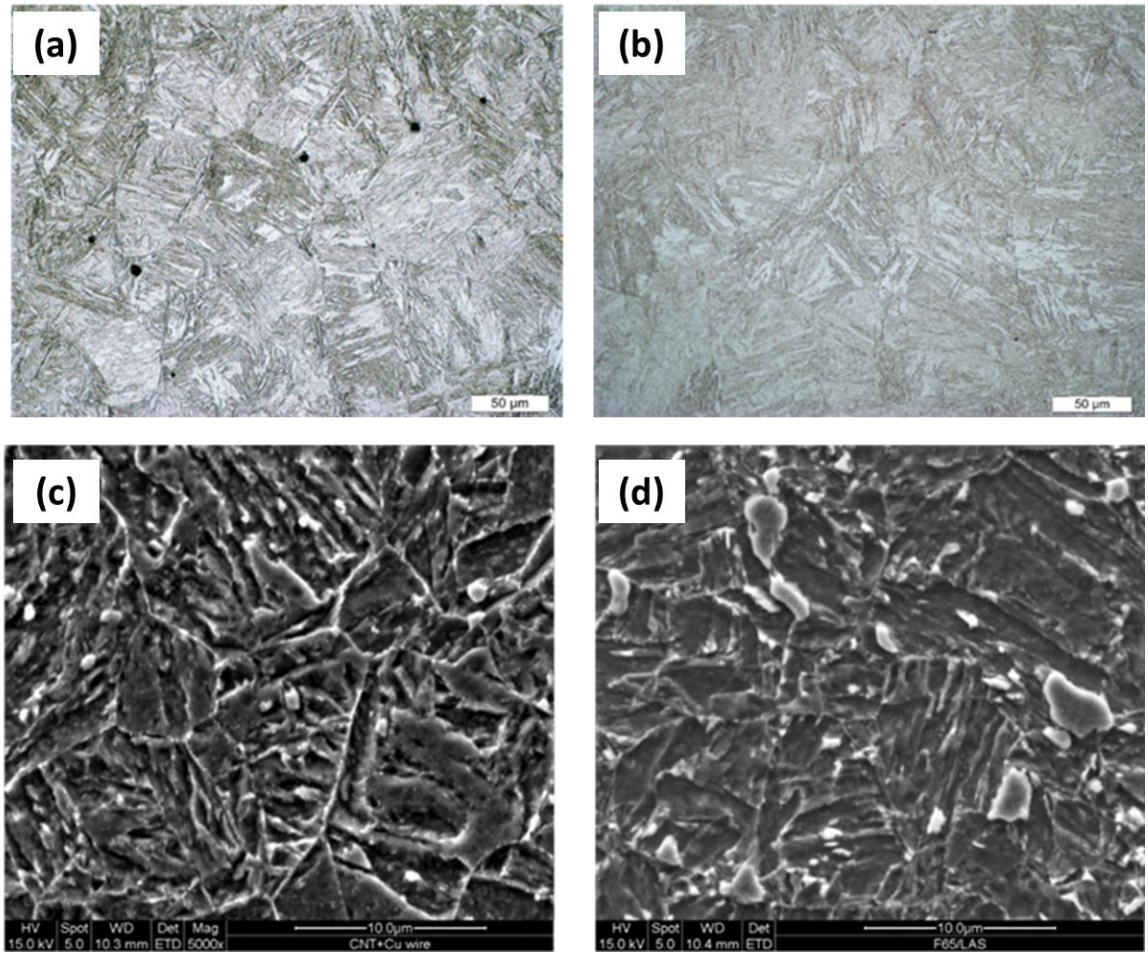

Figure 3.26 Comparison of microstructure of CGHAZ (a and b) and SCHAZ (c and d). (a) and (c) are for actual spot welds, and (b) and (d) are for Gleeble simulated samples

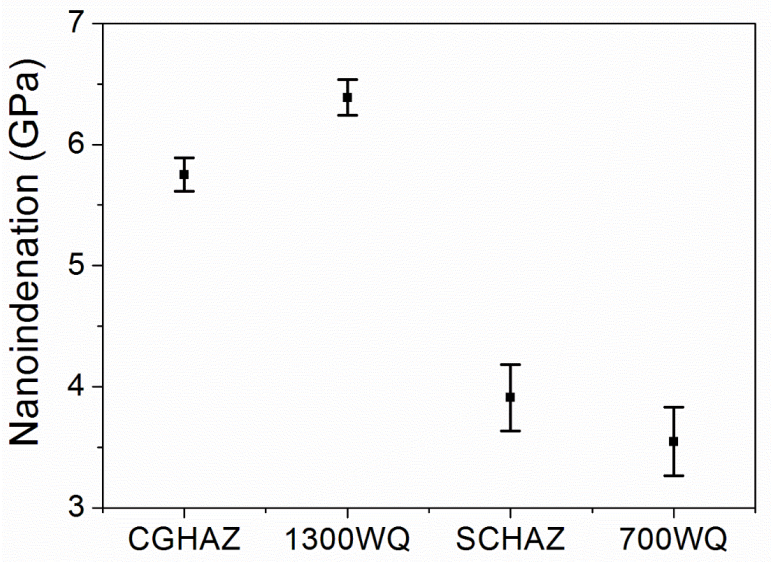

Figure 3.27 Nanohardness of CGHAZ and SCHAZ in spot welds and physically-simulated samples. 1300WQ and 700WQ are simulated CGHAZ and SCHAZ, respectively

3.6.2 Stress-strain curves of Gleeble simulated samples

The simulated CGHAZ and SCHAZ samples were quasi-static tensile tested with a displacement rate of 2.54 mm/min. The strain distribution on the surface of tensile sample just prior fracture was shown in Figure 3.28. Due to the low ductility of CGHAZ, necking was negligible, while strain localization and necking was clearly observed in Gleeble simulated SCHAZ.

From the DIC measured displacement map, a virtual extensometer was defined to measure the relative displacement between two points. The gauge length of the extensometer was an important parameter. Figure 3.29 showed the effect of the gauge length of virtual extensometer on the stress-strain curve extracted. The engineering stress-strain curves are consistent till the ultimate tensile strength, while discrepancy can be

observed after necking, with smaller strain extracted by larger gauge length of the virtual extensometer. The reason was that, prior to necking, the displacement field was uniform and thus the calculated strain was independent of the gauge length used. On the other hand, after necking, uniaxial loading transferred to biaxial loading with displacement localized at the necking region. Due to such non-uniform displacement field, the calculated strain became dependent on the gauge length used. Particularly, the larger gauge length of the virtual extensometer, the lower the calculated strain. Considering the typical mesh size used for spot weld failure simulation, a virtual extensometer with 2-mm-long gauge was used to extract the displacement, which was used subsequently to calculate the strain. The true stress-strain curves for CGHAZ and SCHAZ measured from the Gleeble-simulated samples are plotted in Figure 3.30. The true stress-strain curves of three samples were measured for base metal, CGHAZ and SCHAZ, a representative curve for base metal and each HAZ sub-region was shown due to the consistent testing results.

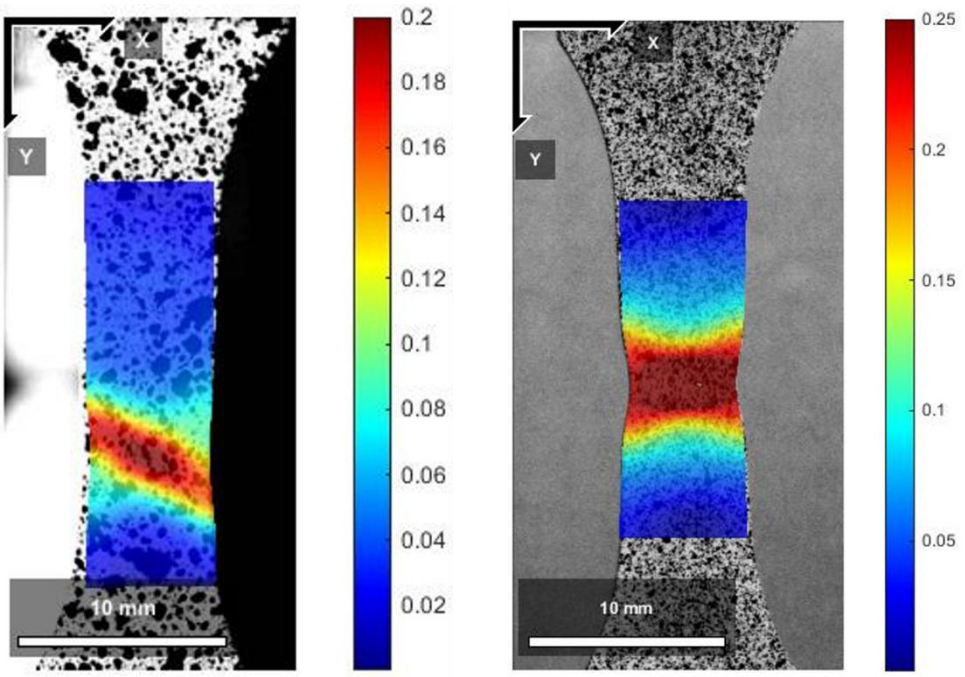

Figure 3.28 Distribution of normal strain in the vertical direction for (a) Gleeble simulated CGHAZ and (b) SCHAZ

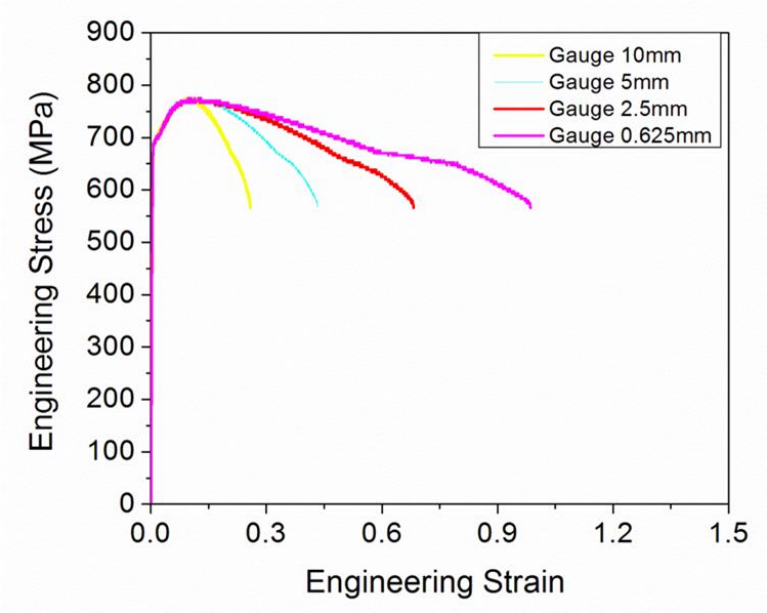

Figure 3.29 Comparison of engineering stress-strain curves extracted with varying length of the virtual extensometer

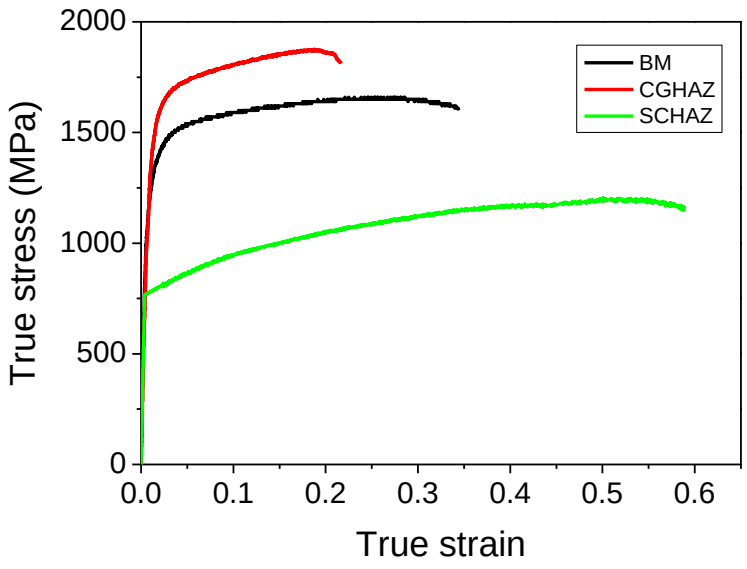

Figure 3.30 True Stress-strain curves for Usibor® 1500 base metal and Gleeble simulated CGHAZ and SCHAZ

3.6.3 Stress-strain curves extracted from nanoindentation

Yield strength and strain hardening exponent of BM and Gleeble simulated CGHAZ and SCHAZ was extracted based on load-displacement curve measured in nanoindentation. As shown in Table 3.7(a) and (b), the yield strength and coefficient K extracted from nanoindentation were comparable to those measured by tensile testing. However, the strain hardening exponent was overestimated by nanoindentation. In other words, the stress-strain estimated from the nanoindentation would indicate a significant hardening especially at high plastic strain. The reason for such overestimation requires a future study.

For a preliminary assessment of stress-strain curves generated based on nanoindentation, the strain hardening exponents obtained from the tensile testing data

were used to calculate the stress-strain curves using the power law (Equation 3.14). Values of two other parameters (K and σ_y) were those extracted from the nanoindentation testing data. The results were compared to the measured curves by tensile testing, as shown in Figure 3.31. The nanoindentation stress-strain curves agreed well with the experiment data for SCHAZ. However, for BM and CGHAZ, the nanoindentation curves only worked for small strains. Future work is needed to improve the strain hardening exponent extraction from nanoindentation.

Table 3.7 Strength coefficient (K, MPa) and strain hardening exponent (n) of BM, CGHAZ and SCHAZ

(a) Extracted by stress-strain curves in tensile testing

	BM	**CGHAZ (Gleeble simulated)**	**SCHAZ (Gleeble simulated)**
K	**2284**	**2639**	**1281**
n	**0.1261**	**0.1322**	**0.1237**
σ_y (MPa)	**1179**	**1342**	**618**
R^2	**0.96**	**0.94**	**0.99**

(b) Extracted from nanoindentation

	BM	**CGHAZ (actual weld)**	**CGHAZ (Gleeble sample)**	**SCHAZ (actual weld)**	**SCHAZ (Gleeble sample)**
σ_y (MPa)	**1147**	**1151**	**1279**	**611**	**622**
K (based on measured n)	**2229**	**2309**	**2530**	**1268**	**1292**
n	**0.258**	**0.26**	**0.267**	**0.29**	**0.27**

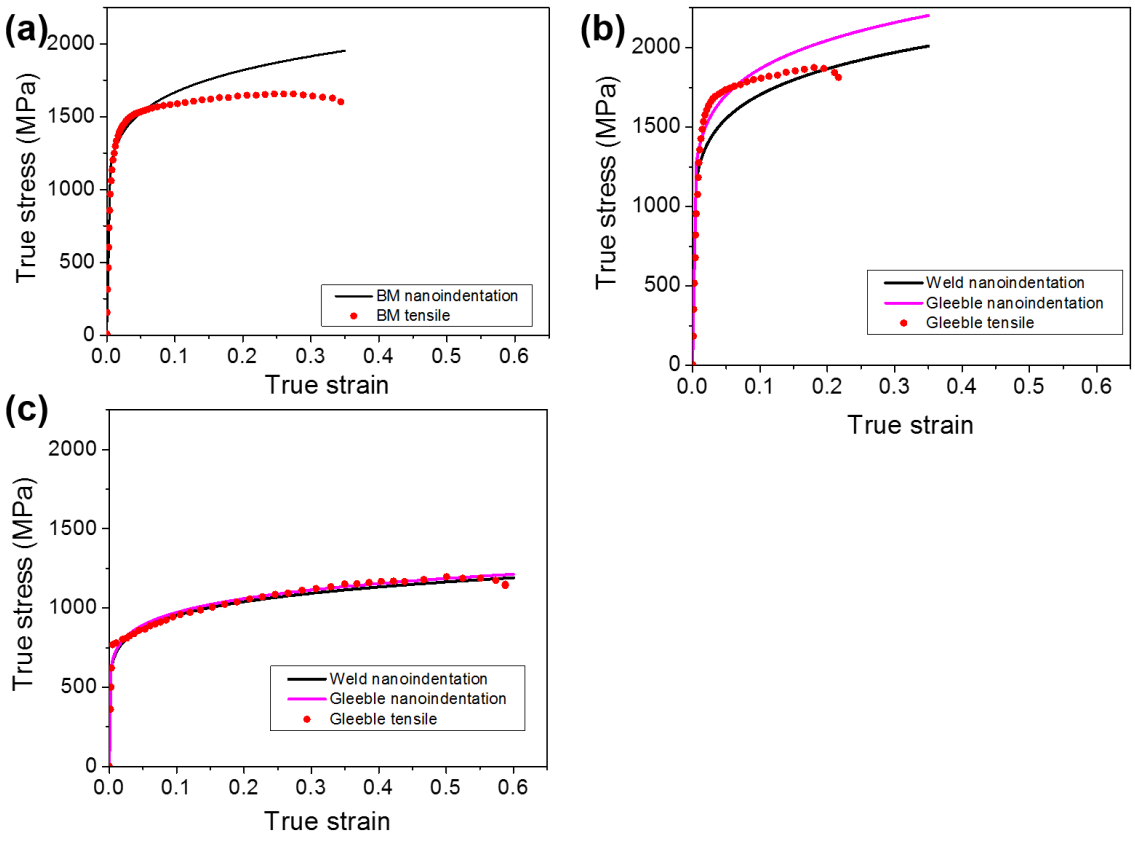

Figure 3.31 True stress-strain curves of (a) BM by tensile testing and nanoindentation extraction, (b) CGHAZ and (c) SCHAZ by tensile testing of Gleeble simulated sample and nanoindentation extraction on actual welds and Gleeble simulated sample

3.7 Summary and conclusions

In summary, a 3D fully coupled thermo-electro-mechanical model has been developed for resistance spot welding of hot-stamped boron steel, Usibor 1500. The model incorporates an existing electrical contact resistance formula for Al-Si coated boron steel taken from the literature. Tempering kinetics of martensite in the SCHAZ is described using a non-isothermal JMAK equation, where the kinetics parameters are generated from isothermal tempering tests. The microstructure of resistance spot welded

Usibor 1500, especially the CGHAZ and SCHAZ, is characterized using electron microscopy and nanoindentation. Two methods, i.e., Gleeble simulation and nanoindentation, are used to extract the local constitutive behaviors of CGHAZ and SCHAZ. The primary conclusions drawn from the experimental observation and modelling include:

(1) The weld nugget size and electrode indentation calculated are consistent with those measured experimentally over a wide range of welding currents, validating the process model incorporating the existing electrical contact resistance formula. For the dome-shaped electrodes used, the initial contact is limited to the centre at both electrode/steel and steel/steel interfaces. As a result, the current is constrained to flow through the centre, resulting in significant Joule heating and subsequent initiation of melting in the centre at t = 100 ms. As the steel sheet is heated further, the material is softened, leading to expanded contact area and more spread-out distribution of contact pressure. Nugget growth in width and thickness directions also occurs in this stage. The two current-off cycles at the end of each impulse lead to oscillation in thermal profiles for the region close to the centre (e.g., weld nugget and CGHAZ), while such effect on temperature profile is diminished for the SCHAZ, which is located furthest from the centre.

(2) A gradient of microstructure forms in the spot welded Usibor 1500. The weld nugget, CGHAZ, and FGHAZ all consist of fresh martensite formed upon rapid weld cooling. The ICHAZ consists of a duplex microstructure of ferrite and martensite, with volume fraction of the latter increasing towards the FGHAZ.

Finally, the SCHAZ consists of tempered martensite, with the extent of tempering decreasing towards the BM.

(3) Isothermal tempering tests for simulated SCHAZ show that the extent of martensite tempering depends more strongly upon temperature than time. From the isothermal tempering data, the activation energy Q and the exponent n are determined to be 531.3 kJ/mol and 0.0658, respectively. By inputting these kinetic parameters into the non-isothermal JMAK equation, the predicted local hardness of SCHAZ is found to be consistent with that measured experimentally.

(4) Both the nugget size and the electrode indentation increase as the welding current and thus heat input rises, which is an expected behaviour. On the other hand, the combined width of the CGHAZ, FGHAZ, and ICHAZ decreases slightly with the welding current, likely due to the increased heat loss to the water-cooled electrodes. The width of the SCHAZ does not vary markedly with the current. At a welding current of 6.7 kA, the total width of the SCHAZ is about 1.7 mm. The region within the SCHAZ for which the hardness has dropped below 60% of base metal is about 0.2 mm wide.

(5) Severe SCHAZ softening was observed with the reduced nanohardness of approximately 4 GPa in the resistance spot weld. The hardness and correspondingly the amount of untempered martensite was found to increase with an increasing distance toward the base metal from the ICHAZ/SCHAZ boundary. The degree of tempering measured by nanoindentation corresponded well with the microstructure characterized by SEM.

(6) CGHAZ and SCHAZ microstructure was successfully recreated by Gleeble® 3800 in bulk materials for measurement of local constitutive behavior by quasi-static tensile testing aided by DIC for strain mapping. CGHAZ with fully martensitic microstructure has a high UTS of 1800 MPa but a low fracture strain of 20%. On the other hand, SCHAZ with tempered martensite has a low UTS of 1100 MPa but a high fracture strain close to 60%.

(7) The local stress-strain curves were also extracted from the load-displacement curves of CGHAZ and SCHAZ measured by nanoindentation. The predicted yield strength and strength coefficient by nanoindentation were in good agreement with those measured by tensile testing of Gleeble simulated sample. However, the strain hardening exponent was overestimated.

The development of the integrated process-metallurgical model represents an essential step toward future study of microstructure gradient in complex stack-ups as well as deformation and failure behaviours of resistance spot welded hot-stamped boron steels by taking into account the local weld geometry and property. The local stress-strain curves of CGHAZ and SCHAZ will input into FEA software for fracture behaviour simulation of resistance spot welded hot stamped boron steel.

Chapter 4 Resistance spot welding of complex stack-ups

The previous chapter investigated the process-microstructure-property relation for RSW of 2T stack-up of Usibor 1500. Complex stack-ups, comprising more than two sheets with similar/dissimilar materials and equal/unequal sheet thickness, are increasingly utilized in smart structural design for further light-weighting, crash-resistance and cost-reduction. In this chapter, the experimental and modeling tools described in Chapter 3 are extended to study the resistance spot welding of complex stack-ups of 3T and 4T with different steels. This chapter starts with RSW of 3T stack-up of JAC 270, JSC 980, and JSC 590 steels. The second half of the chapter addresses RSW of 4T stack-up, which is the above 3T + Usibor 1500 studied in Chapter 3.

4.1 Resistance spot welding of 3T stack-up

4.1.1 Approach

A representative thin/thick/thick 3T stack, comprising 0.75 mm-thick galvannealed JAC 270/1.4 mm-thick JSC 980/1.4 mm-thick JSC 590 (Figure 4.1), is studied. The nominal compositions of the materials are shown in Table 4.1. The base metal microstructure of the three sheets are shown in Figure 4.2. Base metal of JAC 270 consisted of ferritic and pearlite with a hardness of 93 ± 2 $HV_{0.2}$. Both JSC 980 and JSC 590 base metal consisted of martensite and ferrite. The volume fraction of each phase was measured on SEM images

with the magnification of 5000X. Each phase was outlined based on its contrast and morphology and the volume fraction of the phase was measured by ImageJ. The volume fraction of martensite was approximately 40% and 19.4% for JSC 980 and JSC 590, respectively. Hardness of the dual phase steels is significantly affected by the volume fraction of martensite. With higher volume fraction of martensite, JSC980 possessed higher hardness of hardness of 316 ± 7 $HV_{0.2}$, while with lower volume fraction of martensite the hardness of JSC 590 base metal was about 210 ± 5 $HV_{0.2}$. The typical electrodes used in this study were CuZr dome-radius electrodes with a surface diameter of 6 mm.

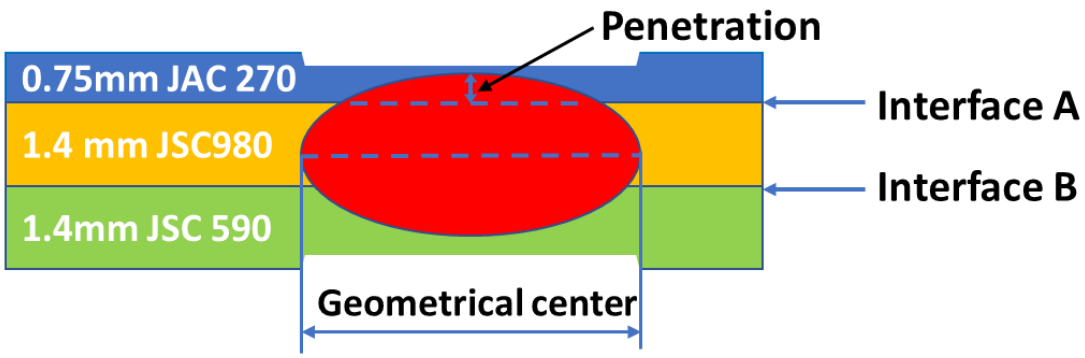

Figure 4.1 Schematics of the 3T stack of 0.75 mm JAC270/1.4 mm JSC980/1.4 mm JSC590 steels

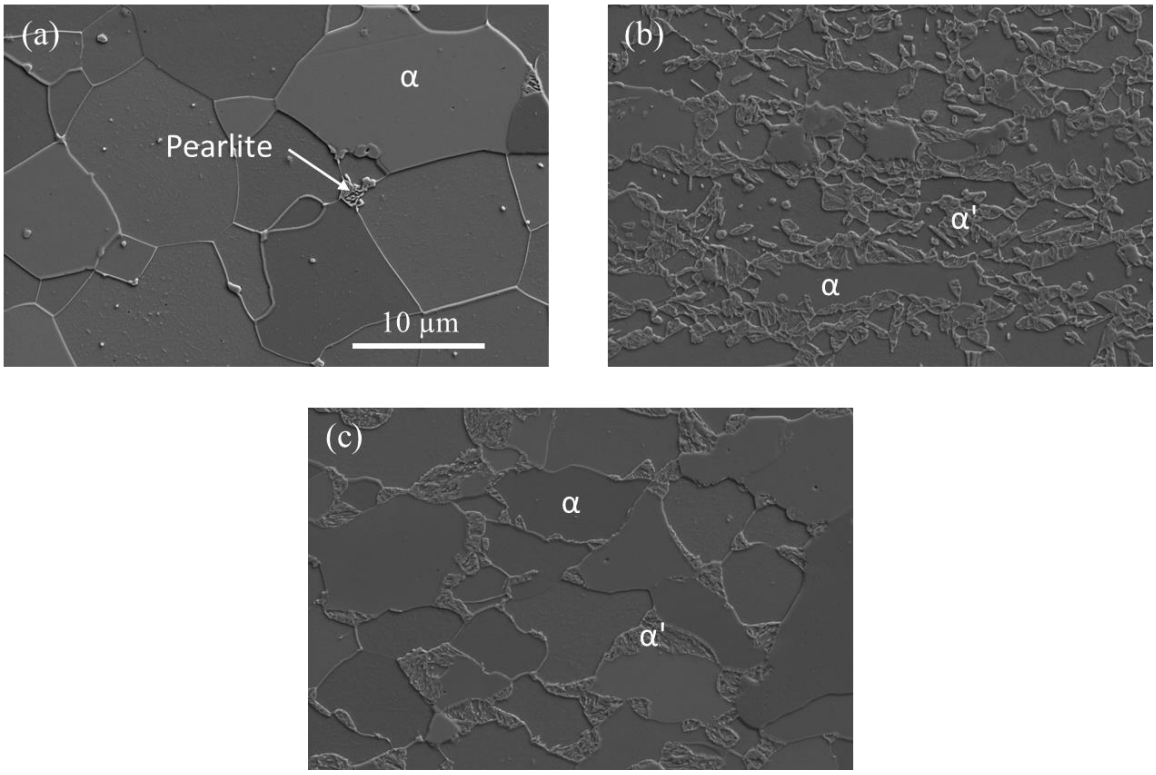

Figure 4.2 Base metal microstructure of (a) JAC 270, (b) JSC 980 and (c) JSC 590

Table 4.1 Nominal composition of materials

Steels	Thickness(mm)	Coating	C	Mn	Si	Cr	Ni	Mo
JAC270	0.75	GA	0.0015	0.107	0.068	0.009	0.01	0
JSC980	1.4	None	0.09	2.07	0.62	0.02	0.01	0.07
JSC590	1.4	None	0.123	1.09	0.297	0.03	0.02	0.006

Resistance spot welding of the 3T stack-up has been done on a medium-frequency direct current (MFDC) machine with electric servo welding gun. The welding parameters were given in Table 4.2. To study the effect of welding current on nugget growth, welding current was increased from 5 kA till expulsion (10 kA) while the electrode force and welding time were kept at 3.4 kN and 300 ms, respectively. Expulsion was identified by both visual observation and a sudden drop in dynamic resistance curve.

To study the effect of electrode force on nugget growth, the electrode force was increased to 4.4 kN while the other welding parameters were kept constant. Lastly, to investigate the effect of electrode electrical conductivity and electrode diameter on the nugget evolution, Class 3 electrode (52% IACs) with a surface diameter of 6 mm was used on the thin sheet side and CuZr electrode with a surface diameter of 8 mm was used on the thick sheet side.

Table 4.2 Welding parameters for resistance spot welding of 3T stack-up of steel sheets

Welding parameters (unit)	Value
Electrode force (kN)	3.4
Welding current (kA)	5 – 10 kA
Welding time (ms)	300
Pulsation	One impulse

After spot welding, the samples were cross-sectioned and prepared by following standard metallography procedures for macrostructure and microstructure characterization. After polishing, the specimens were etched in 2% Nital. Nugget diameters at interface A, B and the geometrical centre, nugget penetration into thin sheet, and electrode indentation into top and bottom sheets were measured by ImageJ (an open-source image analysis software developed by NIH) on the cross-sectional images. In this study, nugget penetration was calculated based on the equation as follows:

$$\%\, penetration = \frac{t_{max}}{t_s} \times 100\%$$

where t_s is the nominal sheet thickness measured before resistance spot welding (i.e., 0.75 mm), and t_{max} is the maximum penetration (in mill-meter) measured from the macrograph (see Figure 4.1).

4.1.2 RSW process simulation

To investigate the nugget evolution during RSW of the 3T thin/thick/thick stack-up, the 3D fully coupled thermo- electro-mechanical model [134], described in Chapter 3,

was extended to 3T. Some salient features of the extended model are highlighted in the following.

The model consisted of a pair of electrodes and three steel sheets with 0.75 mm-thick galvannealed (GA) JAC 270 as the top sheet, 1.4 mm-thick JSC 980 as the middle sheet and 1.4 mm-thick JSC 590 as the bottom sheet as shown in Figure 4.3. Taking advantage of symmetry, a quarter of the joint was considered and was meshed using the Q3D8R 8-node thermo- electro-mechanical solid elements. As shown in Figure 4.3, a fine mesh (element size between 0.1 and 0.2 mm) was used at regions of interest, i.e., weld nugget, HAZ sub-regions of the steel sheet, and the region of the electrodes near the steel/electrode interface. A coarse mesh (element size between 0.8 mm and 4 mm) was placed elsewhere to reduce the total number of elements.

The temperature-dependent electrical contact resistance (ECR) for GA coated steel was used for both the top electrode/ JAC270 interface and JAC270/JSC980 interface, while the uncoated ECR was used for both the bottom electrode/JSC590 and JSC980/JSC590 interface [92], as shown in Figure 4.4. It is noted that GA coating consisted of Fe-Zn intermetallics instead of pure Zn (as that in galvanized or GI). Due to limited data available, ECR of GA coating is assumed to be the same as that of GI coatings for simplicity. The temperature dependent thermo-physical and mechanical properties of the steels and copper electrode are shown in Figure 4.5 and Figure 4.6, respectively.

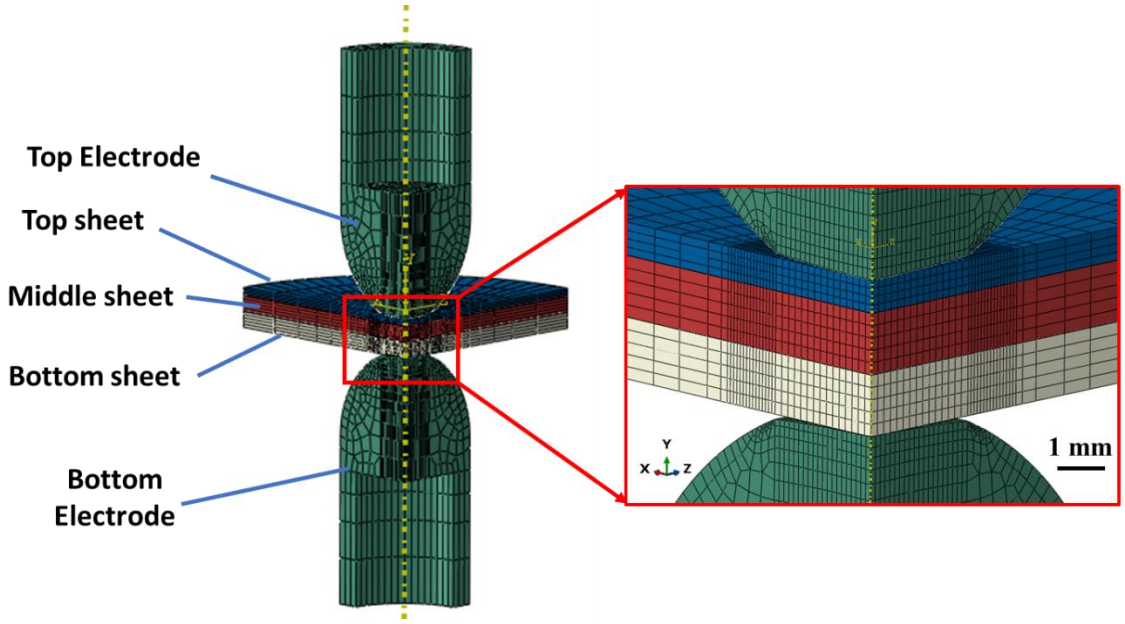

Figure 4.3 Geometry and mesh of the quarter process model for resistance spot welding of the 3T stack of 0.75 mm JAC270/1.4 mm JSC980/1.4 mm JSC590

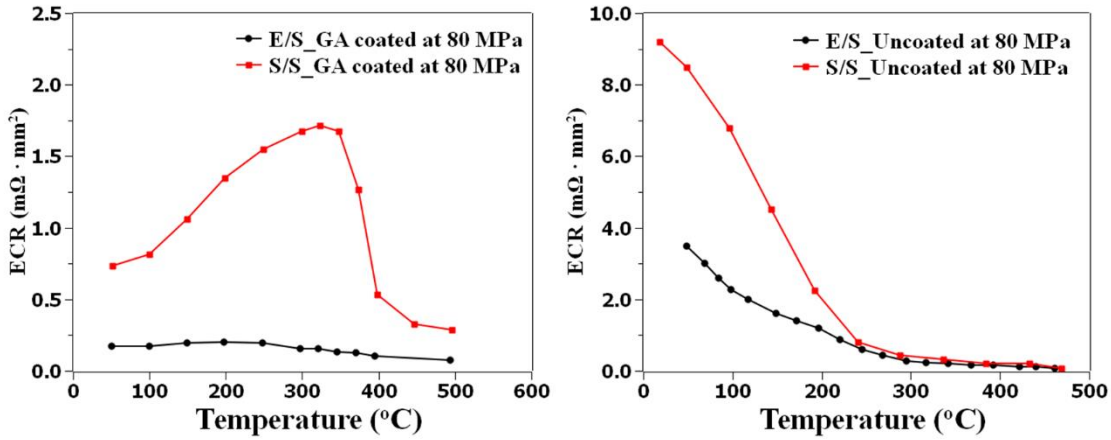

Figure 4.4 Temperature-dependent electrical contact resistance (ECR) at electrode/sheet (E/S) interface and sheet/sheet (S/S) interface for GA coated steel and uncoated steel [92]

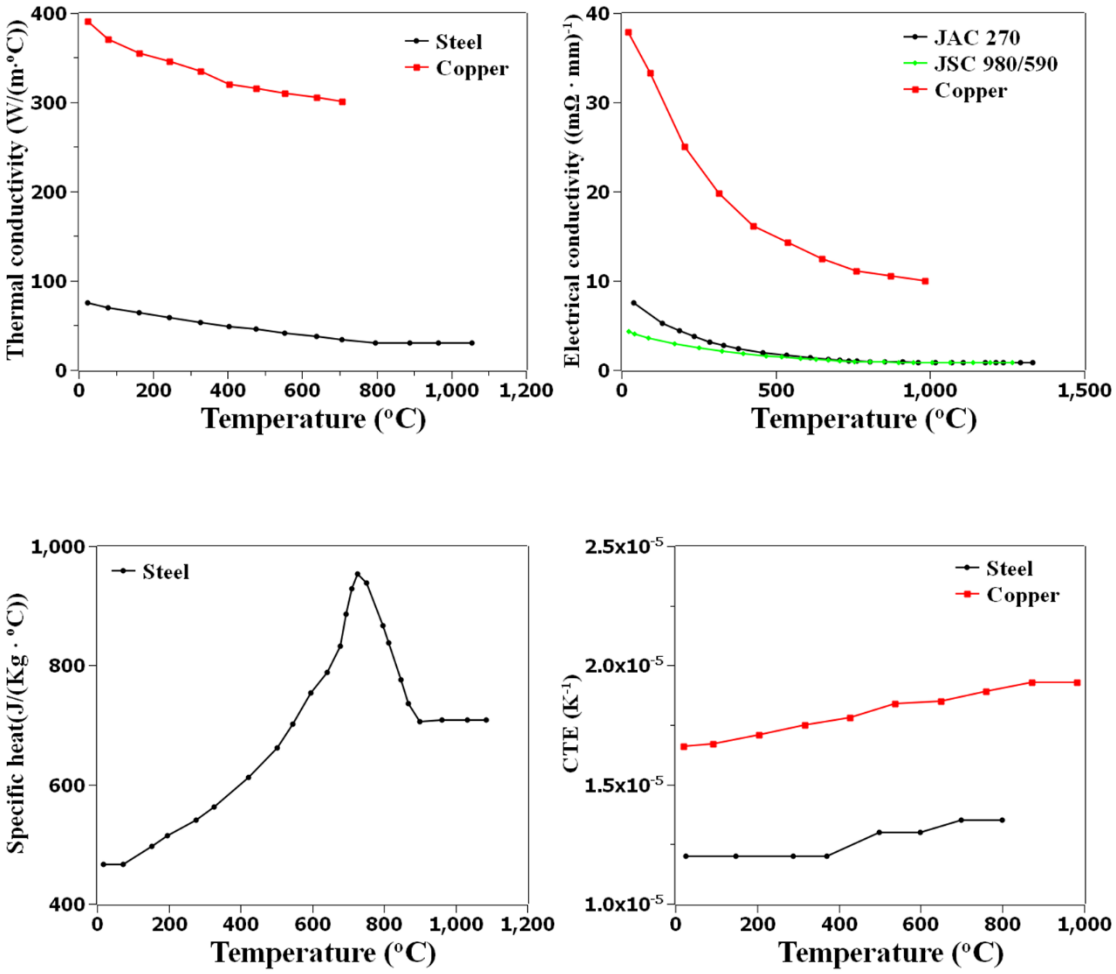

Figure 4.5 Temperature-dependent thermo-physical properties of steels and copper electrode[91]

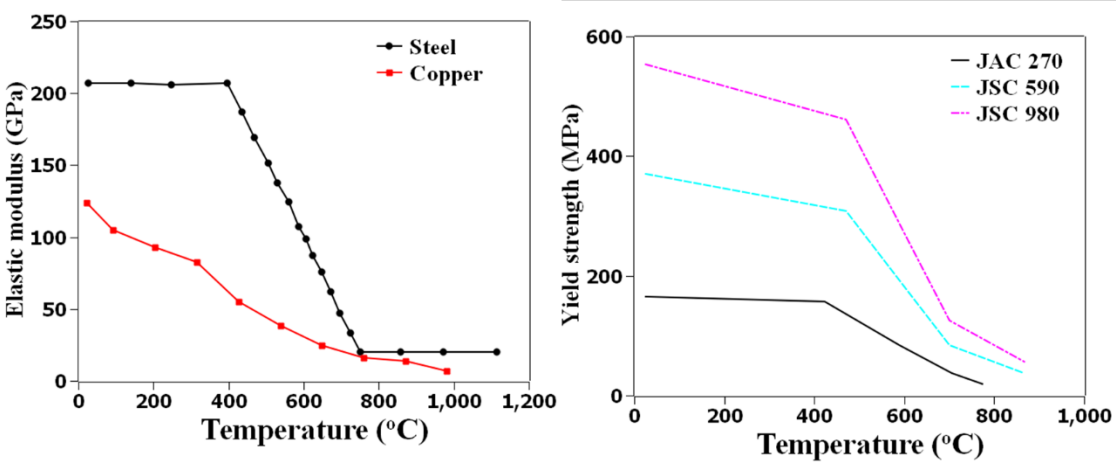

Figure 4.6 Temperature-dependent mechanical properties of steels and copper electrode[91]

4.1.3 Effect of welding current on nugget formation

Figure 4.7 shows the typical macrostructure of nugget formed in 3T stack-up at low welding currents of 5 and 6 kA and a high welding current of 9.5 kA. At low welding current of 5 kA, nugget forms at thick/thick sheet interface while there is no bonding at thin/thick sheet interface. For easier comparison and illustration, the thin sheet is still left in the cross-sectional macrograph. At welding current of 6 kA, the nugget still does not grow beyond the thin/thick sheet interface, although a solid-state bond forms at this interface. With welding current of 9.5 kA, a well-developed nugget with a reasonable penetration into thin sheet is obtained.

Figure 4.8 shows the effect of welding current on the nugget diameters at interfaces A/B and geometrical centre. The nugget diameter (ND) at interface B almost increases linearly with increasing welding current with the relation of $ND_B = 0.8518 \times I - 1.6619$ ($R^2 = 0.99$). Moreover, the nugget diameter at geometrical centre of the stack-up is

slightly larger than that at interface B when welding current is lower than 7 kA. On the other hand, the nugget diameter at interface B becomes slightly larger than that at geometrical centre of the stack-up as welding current is higher than 8 kA. Nugget diameter at interface A rapidly increases with welding current initially and tends to be saturated at 5 mm as welding current is between 9 kA to 10 kA. No further nugget growth at interface A when the welding current is higher than 9 kA indicates that heat balance is achieved, while more heat is accumulated at the thick sheet side. According to AWS standard, the minimum nugget sizes ($4\sqrt{t}$, where t is the thickness of the thinner sheet for dissimilar metal welding) at interface A and interface B are 3.46 mm and 4.73 mm respectively. The welding current range of the 3T stack-up JAC 270/JSC 980/JSC 590 is thus approximately 2 kA (8 kA – 10 kA) as shown in Figure 4.8.

Small penetration into thin sheet is a major concern in resistance spot welding of thin/thick/thick stack-ups. Figure 4.9(a) shows the effect of welding current on nugget penetration into thin sheet. There is no penetration into the thin sheet when the welding current is lower than 6 kA. Larger than 20% of penetration can be obtained as welding current is higher than 8 kA. In general, the penetration into thin sheet increases rapidly as welding current increases from 6 kA to 9 kA, then it tends to level off to be around 32%. Figure 4.9(b) shows the electrode indentation of top and bottom sheets changing with welding current. Larger indentation can be expected on thin sheet side due to low strength of JAC 270. The indentation increase rate is 4%/kA and 3.6%/kA on thin and thick sheet side respectively, as welding current increases from 5 kA to 8 kA. However, a rapid increase in indentation on thin sheet side occurs when welding current is higher

than 8 kA with the indentation increase rate of 9%/kA and quickly reaches 50% at the expulsion current of 10 kA. On the other hand, the indentation on thick sheet side is still less than 30% at the expulsion current.

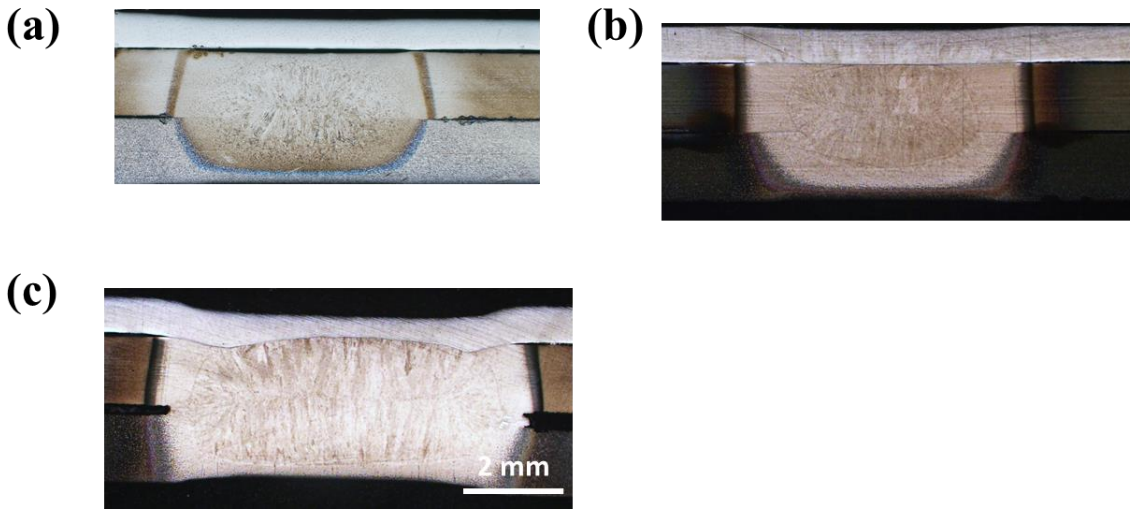

Figure 4.7 Optical micrograph of resistance spot welded 3T stack-up at welding current of (a) 5 kA, (b) 6 kA, and (c) 9.5 kA. Other welding parameters are electrode force: 3.4 kN, and welding time: 300 ms

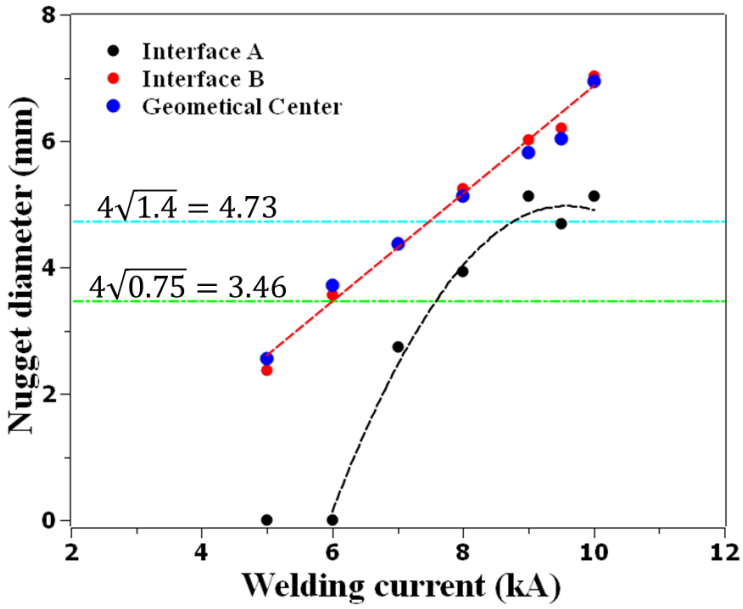

Figure 4.8 Effect of welding current on nugget size for 3T stack-up of 0.75 mm JAC270/1.4 mm JSC980/1.4 mm JSC590

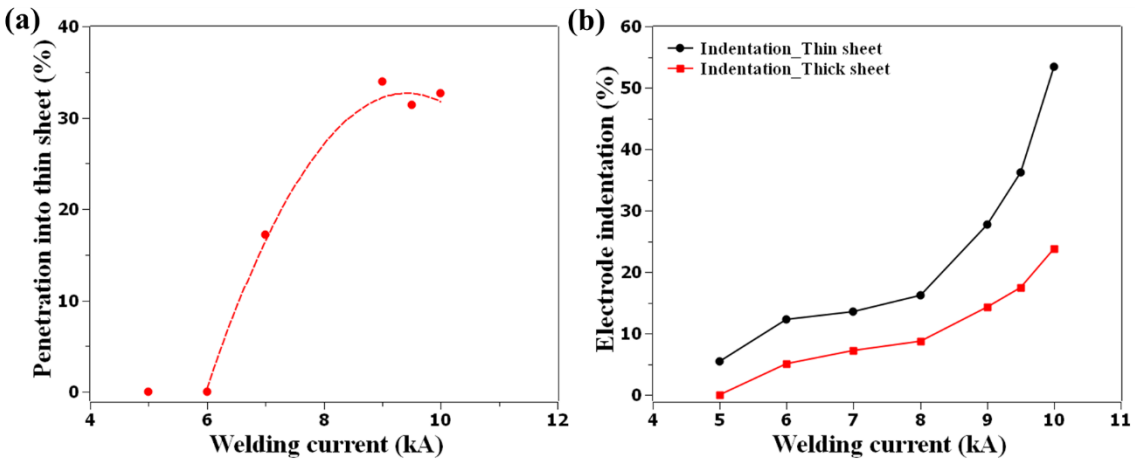

Figure 4.9 (a) Penetration into thin sheet, and (b) electrode indentation into top and bottom sheets for 3T stack-up

4.1.4 Effect of electrode force

Penetration into thin sheet can be affected by electrode force. Figure 4.10 shows the effect of electrode force on nugget diameter at interfaces A, B and geometrical centre and nugget penetration into the thin sheet. At high electrode force of 4.4 kN, nugget at interface A forms and penetrates into thin sheet when the welding current is higher than 8 kA. Thus, the lobe curve has a 2-kA shift to the higher current side which means a longer incubation time for nugget formation at thin/thick sheet interface compared to low electrode force of 3.4 kN. However, the nugget diameter at interface B is not significantly affected by electrode force. Once the nugget forms at interface A, the nugget diameter at this interface and penetration into the thin sheet are independent of electrode force as well. However, the electrode indentation into the thin sheet does increase with increasing electrode force. At welding current of 9.5 kA, the indentation on thin sheet side with higher electrode force (4.4 kN) is about 12.5% larger compared to that with lower electrode force of 3.4 kN. For the present stack-up considered, 3.4 kN is a reasonable electrode force for the 3T stack-up of steels to obtain sound nugget diameter while avoiding severe indentation.

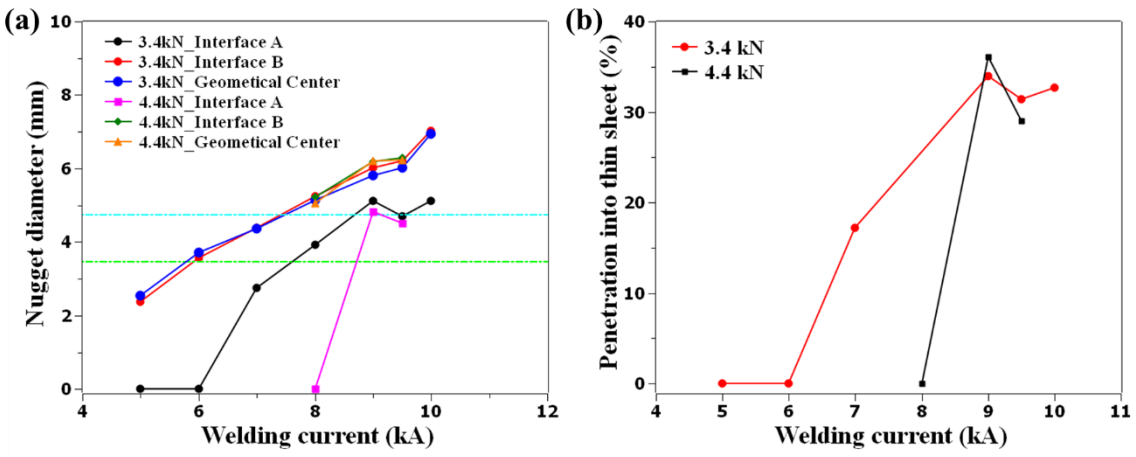

Figure 4.10 Effect of electrode force on (a) nugget diameter, and (b) penetration into thin sheet

4.1.5 Effect of electrode material

To shift the heat centre from the geometrical centre to the location near to interface A, Class 3 electrode with a surface diameter of 6 mm was used on thin-sheet side while Class 1 electrode with a surface diameter of 8 mm was used on thick-sheet side. Figure 4.11 shows the macrostructure of 3T stack-up resistance spot welded joints with different electrode geometry/materials. With Class 3 electrode on thin sheet side, the nugget penetration can be 53% which is approximately 20% higher than the one welded with traditional electrodes. The nugget diameter at interface A is about 4.9 mm which is comparable with that welded with Class 1 electrode. However, the nugget diameter at interface B is about 0.85 mm smaller which is due to smaller current density on thick sheet side with a larger surface diameter electrode. Thus, electrode materials and electrode geometry have predominant effect on nugget penetration and nugget size

compared to adjustment on welding schedules, consistent with the findings by Gould et al. [7]

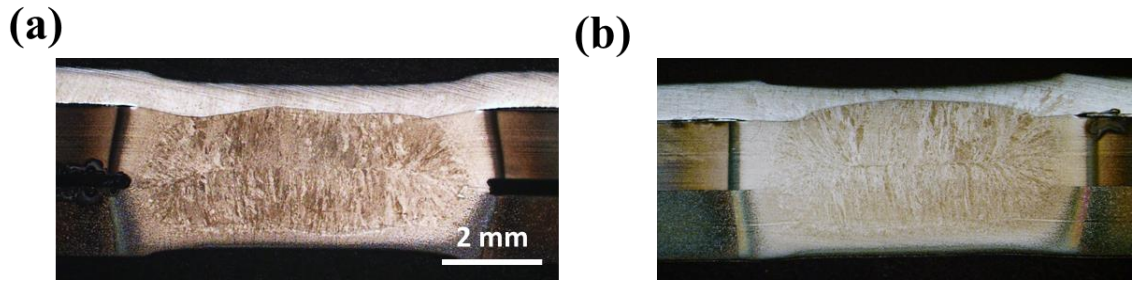

Figure 4.11 Macrostructure of resistance spot welding of 3T stack-up with (a) 6 mm Class 1 electrodes, and (b) 6 mm Class 3 electrode and 8 mm Class 1 electrode on thin and thick sheet side respectively. Other welding parameters are welding current = 9.5 kA, and electrode force = 4.4 kN

4.1.6 Microhardness distribution

Figure 4.12 shows the microhardness distribution on resistance spot welded 3T stack-up. The microhardness of the weld nugget is uniformly distributed with an average value of 395 $HV_{0.2}$ on the thick sheet side. The hardness of the weld nugget near to thin/thick sheet interface is 381 ± 4 $HV_{0.2}$ which is about 4% lower than that at thick/thick sheet side. Softening at sub-critical heat affected zone of JSC 980 is shown in Figure 4.12(b) with about 20% hardness reduction compared to that of the base metal. The hardness drop is caused by the formation of tempered martensite which is also observed in laser welded dual-phase steel and is comprehensively studied by Biro et al. [115,135].

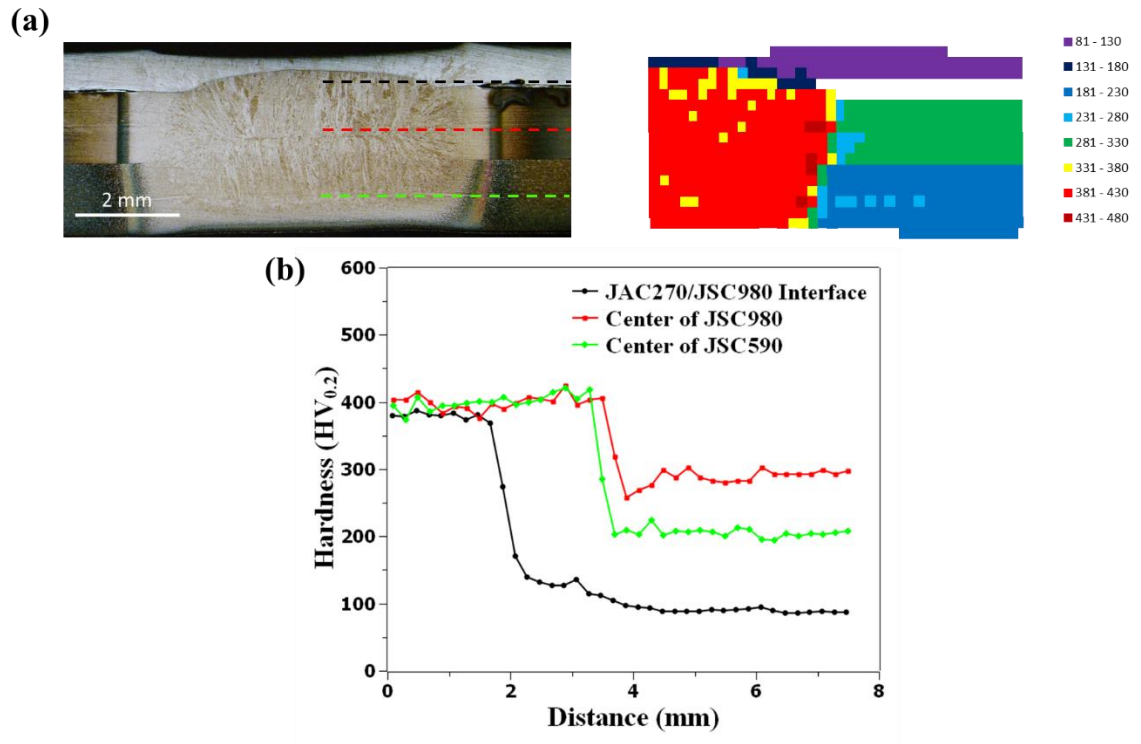

Figure 4.12 (a) Microhardness mapping of resistance spot welded 3T stack-up, and (b) microhardness profile across a half of the spot welds. Welding parameters are 6 mm-surface diameter Class 3 electrode on thin sheet side, and 8 mm-surface diameter Class 1 electrode on thick sheet side, welding current = 9.5 kA, and electrode force = 4.4 kN

4.1.7 Model validation

Figure 4.13 shows the comparison of predicted and experimentally measured total dynamic resistance between the bottom surface of the top electrode and the top surface of the bottom electrode at welding current of 8 kA. The good agreement between the predicted and the experimentally measured total resistance indicates that the model can accurately capture dynamic changing of contact condition, e.g. contact area, contact pressure, and thermo-physical and mechanical properties of the complex stack-up.

In the literature, Gedeon et al. [51] observed 6 stages for resistance curve of resistance spot welded GA steel, and Dickinson et al.[136] identified 5 stages for uncoated steels (including expulsion stage in both cases). In general, the dynamic resistance curve of the 3T complex stack-up is more comparable to the uncoated steels. For stage 1, the WTC software, used to record the dynamic resistance data in the present study, ignores the resistance data in the first 4 -5 ms which is the turn-on transient in many RSW machines [51]. Therefore, a portion of the initial sudden drop in resistance due to breakdown of oxide films is shown in Figure 4.13. The slight resistance increase due to bulk heating of the coating at electrode/sheet interface in Stage 2 is not observed in this study. The reason could be that the resistance reduces due to softening of the asperities at thick/thick sheet interface and bottom-sheet/bottom-electrode interface as heating progresses, which provides an opposite effect. The net effect from these two opposite mechanisms determines the shape of the resistance curve. Stage 6 and 7 reported by Gedeon [51] are observed for the resistance spot welded 3T complex stack-up . As welding time increases, bulk resistance plays a key role in heat generation instead of contact resistance. Resistance increases with increasing temperature in stage 3 due to an increasing electrical resistivity of the bulk steel. Although bulk resistivity increases with temperature as shown in Figure 4.13 for all three sheets, total resistance decreases in stage 4 due to larger contact area and thickness reduction of the stack-up caused by plastic deformation of steel sheets at elevated temperatures. The total resistance reduction (peak resistance - final resistance) is 45 μΩ from the peak resistance (~ 160 μΩ) to the end of welding with a welding current of 8 kA.

Figure 4.14 shows the comparison of the predicted nugget diameters changing with welding current at interfaces A, B and geometrical center. In general, the predicted nugget diameter is comparable with the experimental data. However, the nugget diameter can be overestimated when the welding current is higher than 9 kA when the experimental nugget diameter at interface A saturates to be approximately 5 mm between 9 – 10 kA.

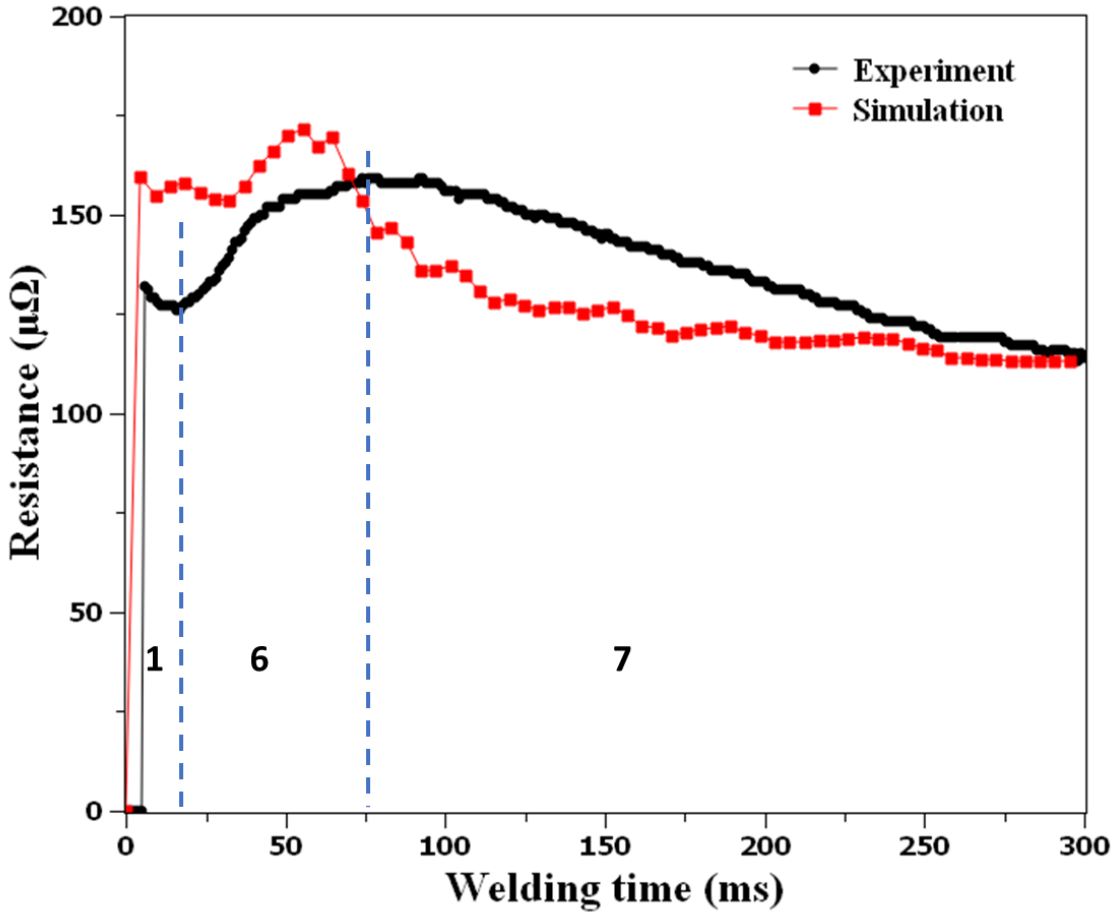

Figure 4.13 Predicted dynamic resistance curves versus experimentally measured dynamic resistance as a function of welding time for 8 kA

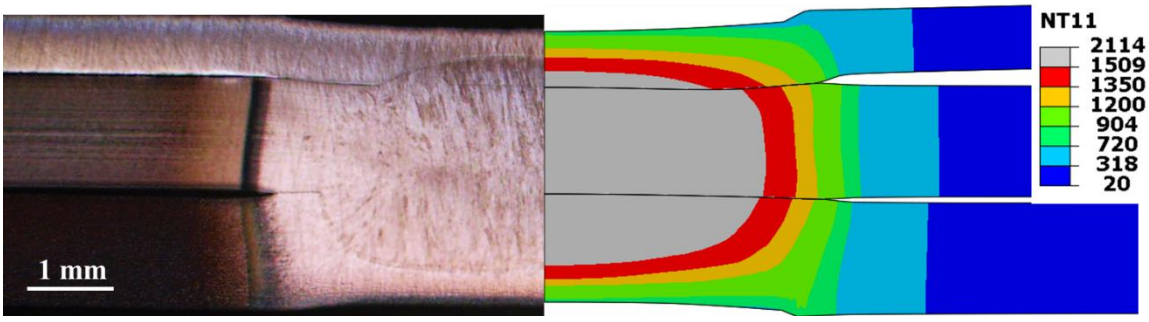

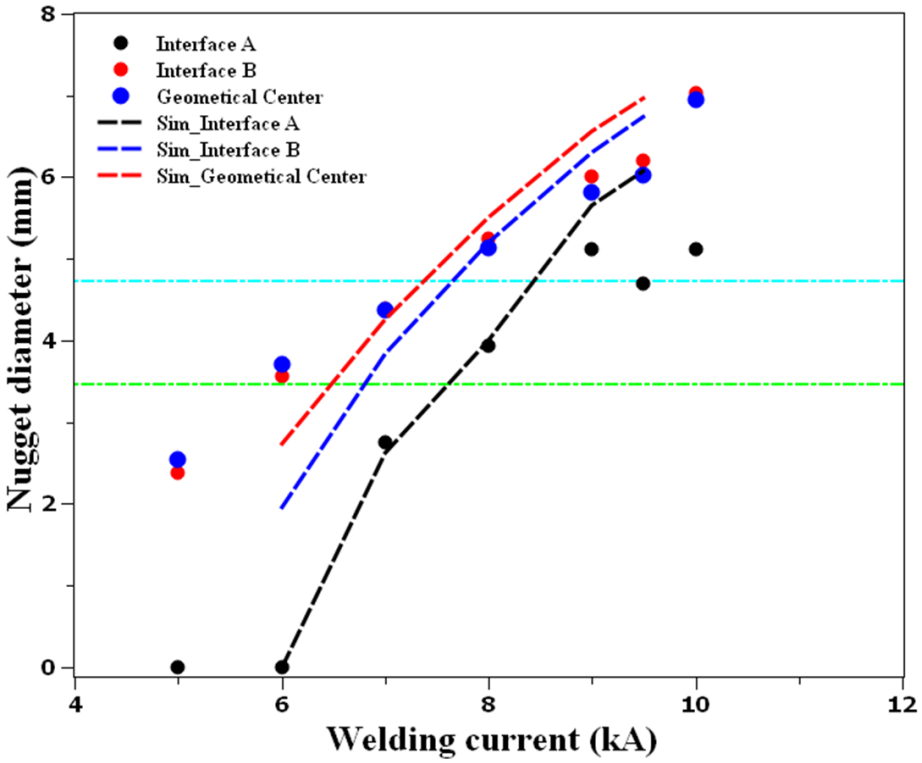

Figure 4.14 Comparison between simulated nugget sizes and experimental measurements for welding current of 8 kA

4.1.8 Nugget formation and Bonding mechanism

Heat generation by Joule heating, heat conduction from S/S interface (high electrical contact resistance region at the first few cycles in spot welding) to geometrical centre and

heat dissipation through water-cooled electrode and surrounding base metal all play a significant role in nugget formation. In resistance spot welding of two sheets with the same thickness and material, the S/S interface is the geometrical centre of the stack-up. Nugget initiates at the S/S interface due to high heat generation and low heat loss rate. However, the dissimilar welding of three steel sheets of thin/thick/thick stack-up shifts the geometrical centre to the thick sheet side. Pouranvari et al. [137] showed that the nugget formation can be affected by the thickness of sheet in equal-thickness 3T stack-up.

Using the process model, the transient temperature distribution and the nugget initiation are calculated. The results for welding current of 8 kA are shown in Figure 4.15 through Figure 4.17. At a short welding time of 5 ms, interface A has smaller contact area/larger contact pressure compared to interface B since thin sheet has low yield strength and tends to deform more easily compared to JSC 590 and JSC 980, as shown in Figure 4.15. Thus, high current density exists at interface A and localized heating can be observed in Figure 4.16. As welding time increases, current density decreases due to an enlarged contact area. Uniform distribution of current density is generated at the centre of the weld with localized high current density near to the notch, as shown in Figure 4.17. Current density at interface A is still slightly higher than that of the interface B at welding times of 200 ms and 300 ms. Therefore, heat generation is still substantial at interface A. However, bulk resistance dominates after the first few cycles of welding time. The bulk resistance of the thin sheet is smaller due to small thickness of the thin sheet while the heat loss of interface A through water-cooled electrode is faster. In contrast, the

geometrical centre of the stack-up has a high heat generation rate due to bulk resistance heating while it losses less heat compared to interfaces A and B. As a result, at the welding current of 8 kA, nugget initiates at the geometrical centre of the 3T stack-up at the welding time of 102 ms.

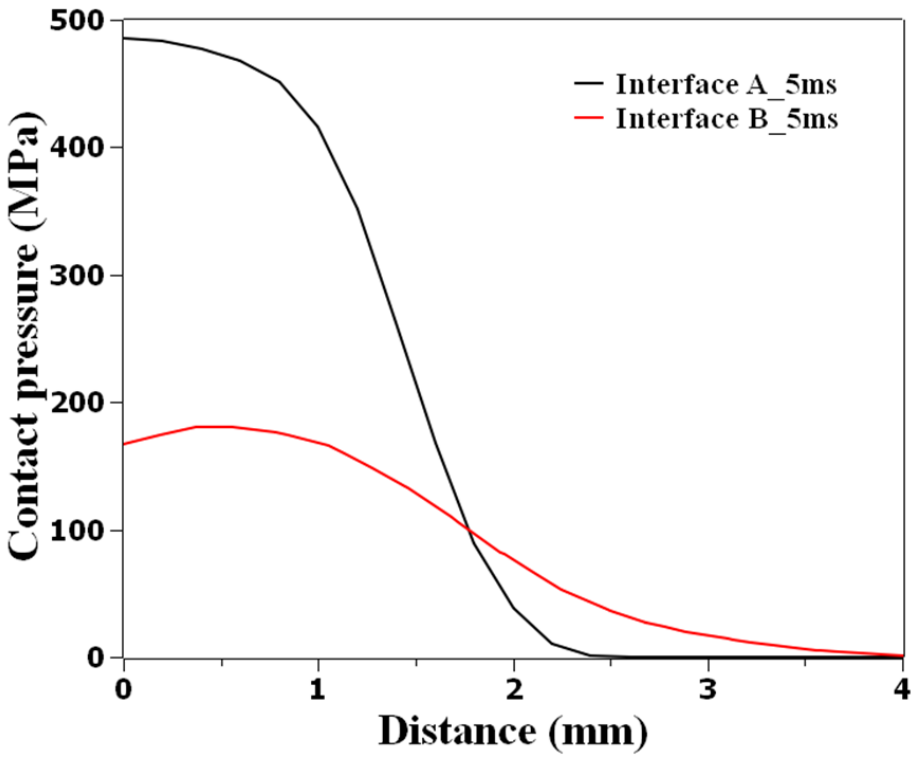

Figure 4.15 Contact pressure distribution at interface A and B with welding time of 5 ms, current of 8 kA and electrode force of 3.4 kN

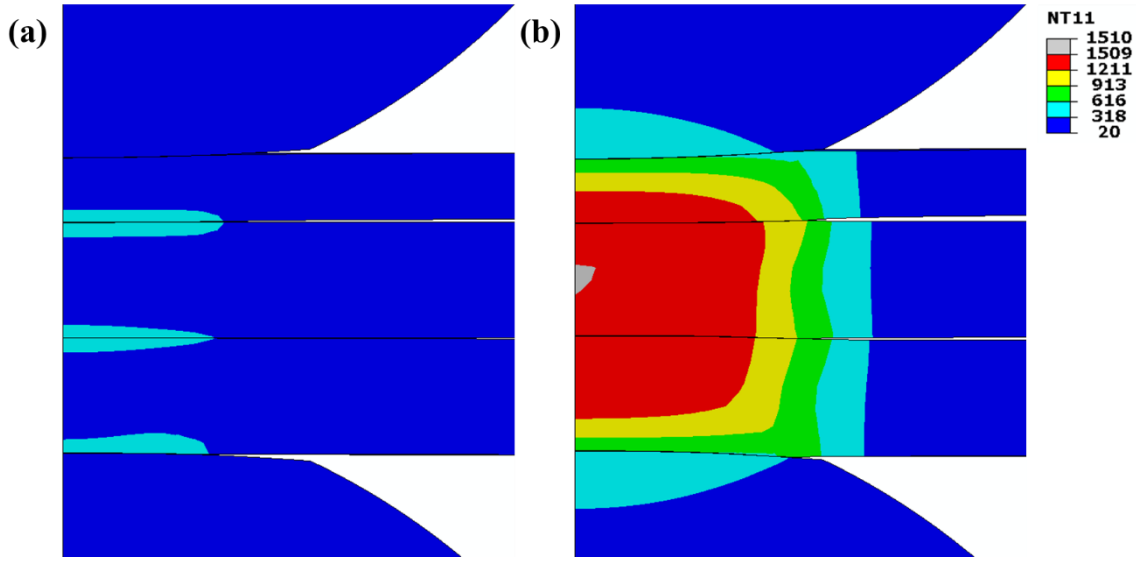

Figure 4.16 Nugget formation in resistance spot welding of 3T stack-up with welding current of 8 kA, electrode force of 3.4 kN and welding time of (a) 5 ms, and (b) 102 ms

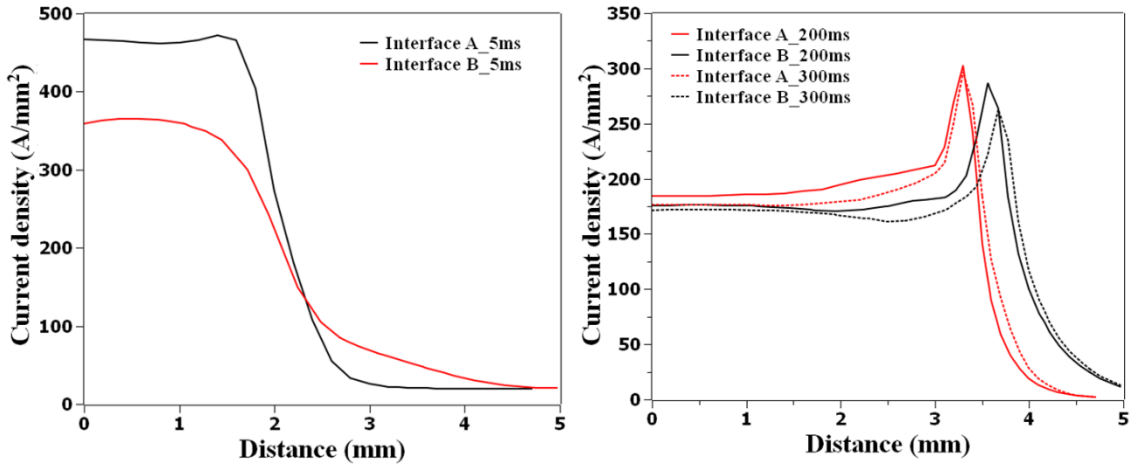

Figure 4.17 Current density distribution at interface A and B with welding time of 5 ms, 200 ms and 300 ms

Moreover, the nugget initiation location is affected by welding current. As welding current is lower than 8 kA, the nugget initiates at the geometrical centre. For the 3T stack-up with low/medium contact resistance, geometrical centre of the stack-up is the location

that has the smallest heat dissipation rate and more heat generation in bulk materials. However, at locations near to water-cooled electrode, such as interfaces A and B, the local heat build-up there is relatively small when low welding currents are used. Thus, nugget initiates at the geometrical centre instead of S/S interface. As welding current increases to 9 kA, the nugget initiates at locations near to S/S interface at the bottom sheet and the centre of the middle sheet. The reason could be that high current density at interface B results in high heat generation rate. Therefore, as welding current increases, the nugget initiation location shifts from geometrical centre to the interface B and 2nd sheet as more net heat (heat generation – heat loss) accumulated. Moreover, the incubation time for nugget formation decreases as welding current increases regardless of the nugget initiation location in the 3T stack-up, as shown in Figure 4.18.

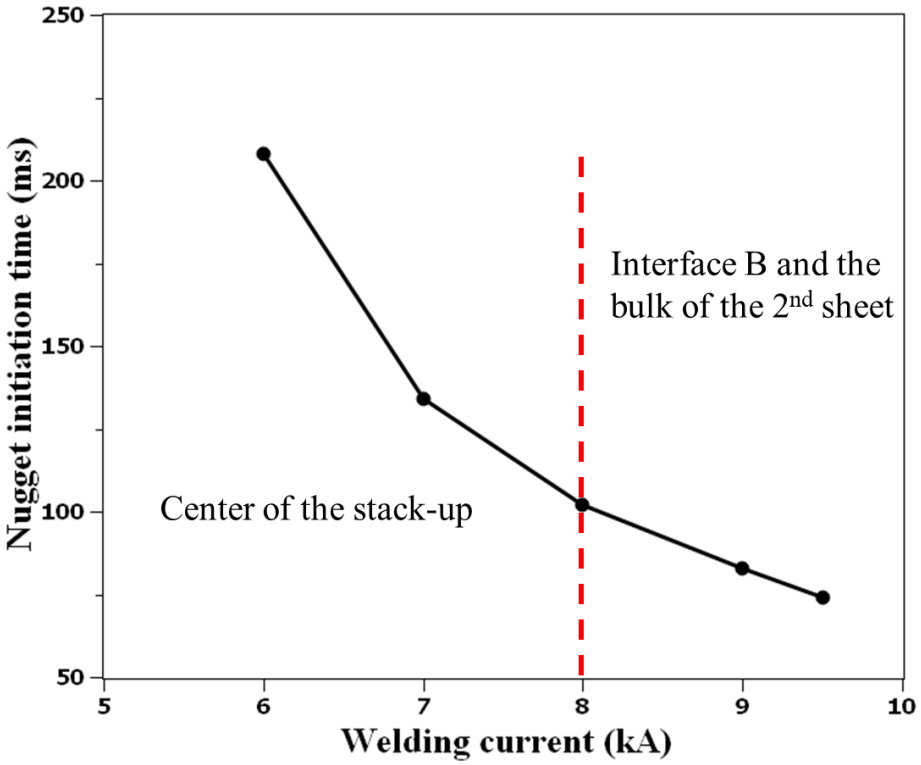

Figure 4.18 Effect of welding current on nugget initiation

Since rapid heat dissipation through water cooled electrode is the main issue that results in small nugget penetration, the methods that are able to reduce heat loss at interface A, i.e. high resistivity electrode on thin sheet side, and adding a cover sheet, can be effective for increasing nugget penetration into thin sheet.

4.1.9 Tempering kinetics of JSC980

The A_{C1} and A_{C3} temperature of JSC980 were determined to be 720 ^{o}C and 904 ^{o}C by using dilatometry in Gleeble. To predict local hardness in SCHAZ of resistance spot welded JSC980, isothermal tempering tests were performed, similar to those reported for Usibor 1500 in Chapter 3. The samples were tempered at 400 ^{o}C, 500 ^{o}C and 650 ^{o}C for

different tempering time from 0.2 seconds to 10 seconds. The minimum hardness was obtained by tempering the base metal at 650 ^{o}C for 1 hour. It is noted that the base metal of JSC980 is not normalized and quenched to be the fully martensitic microstructure.

The hardness is plotted as a function of H-J tempering parameter, as shown in Fig. 4.19. There is no obvious secondary hardening as fiber laser welded DP780 report in [138], which could be due to less amount of carbide forming elements in the JSC980 in this study. The tempering curve is almost linearly decreasing with the H-J tempering parameter as shown below:

Hardness = -0.0093 × H-J parameter + 393.03

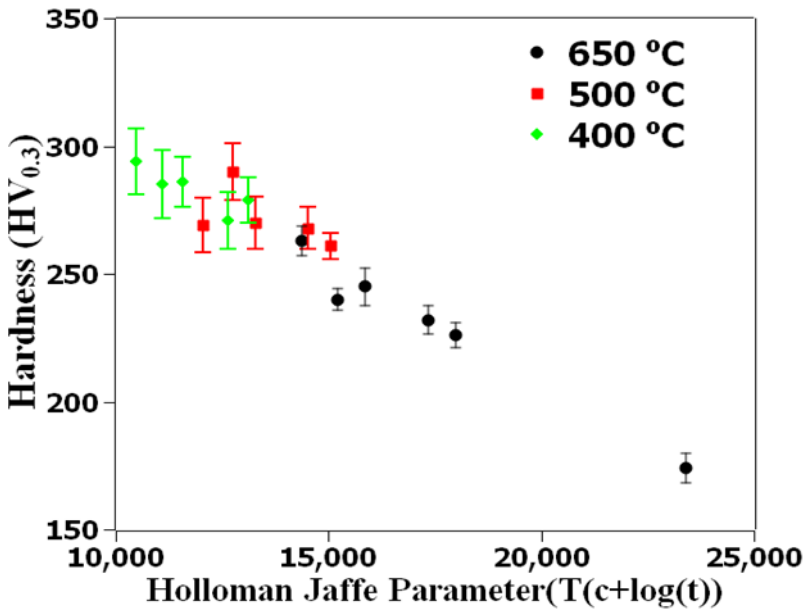

Figure 4.19 Hardness as a function of H-J parameter for JSC980

Hardness response to tempering was predicted with JMAK equation as illustrated in Chapter 3. The isothermal testing results were summarized in Figure 4.20. Compared to hot-stamped boron steel with fully martensitic microstructure, the hardness reduction for tempered dual phase steel JSC980 with approximately 40% of volume fraction of martensite in base metal is not significant. As shown in this figure, the hardness has dropped by 20% compared to base metal due to tempering at 650 ºC (923 K) for 1 s, which is comparable to the hardness drop in the actual SCHAZ of resistance spot welded JSC980. Upon further tempering to 10 and 3600 s, the hardness had an additional drop of only 7% and 24%, respectively. Compared to the high temperatures tested (500 °C/773 K and above), softening kinetics at low temperatures were much slower. For example, the

hardness was reduced by approximately 10% for tempering at 400 ^{o}C (623 K) for 10 s. Therefore, tempering tests at 350 ^{o}C was not conducted.

By applying JMAK equation, the tempering kinetics parameters Q, k_0 and n were determined to be 131.815 kJ/mol, 2.44×10^6 and 0.187 respectively, as shown in Figure 4.21. As mentioned previously, these values are not directly comparable to the literature values such as the activation energy for carbon diffusion in ferrite = 84 kJ/mol [132], the activation energy for diffusion of vacancies in ferrite = 210 – 315 kJ/mol [132], and the exponent = 0.67 for diffusion-controlled coarsening of cementite [133]. This is because the extent of softening ϕ used in this study is defined based on hardness, and the relationship of hardness with the volume fraction (or size) of cementite is likely non-linear.

The goodness of fit is illustrated in Figure 4.22 and Figure 4.23, where the extent of tempering and hardness calculated using the JMAK equation is compared to the experimental value (used to extract the tempering parameters). Overall, the predicted value corresponded well with the experimental data, especially at high tempering temperatures (e.g., 650 ^{o}C/923 K) and longer times (e.g., 5 to 10 s). The hardness in SCHAZ can be predicted by combining the thermal profiles predicted by process model with tempering kinetics described by JMAK equation.

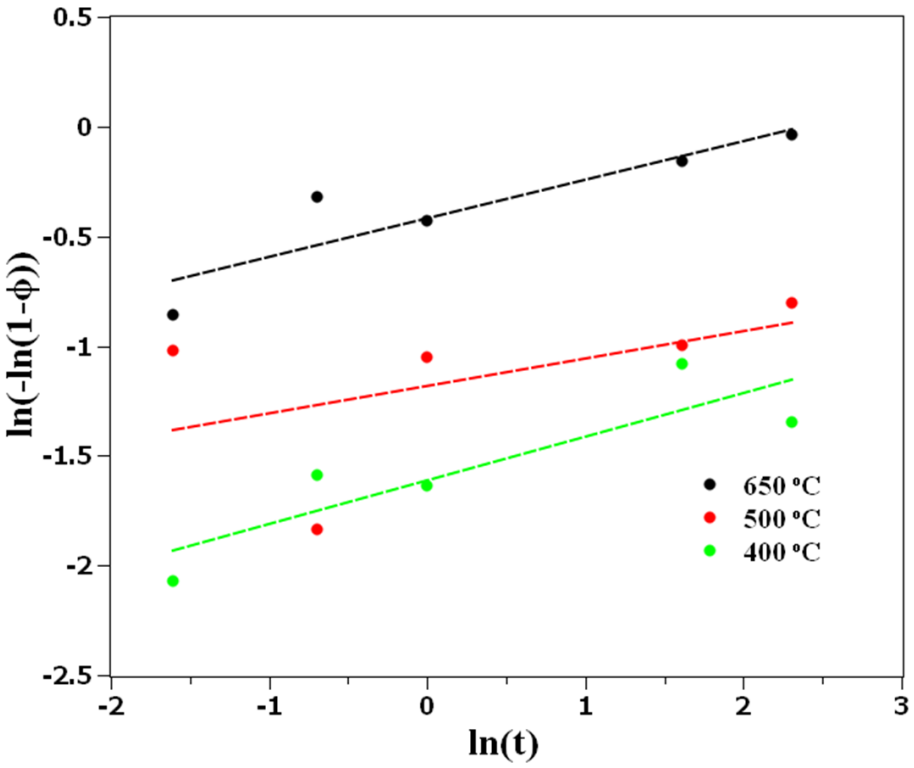

Figure 4.20 Linearization of JSC980 softening data obtained from isothermal tempering tests

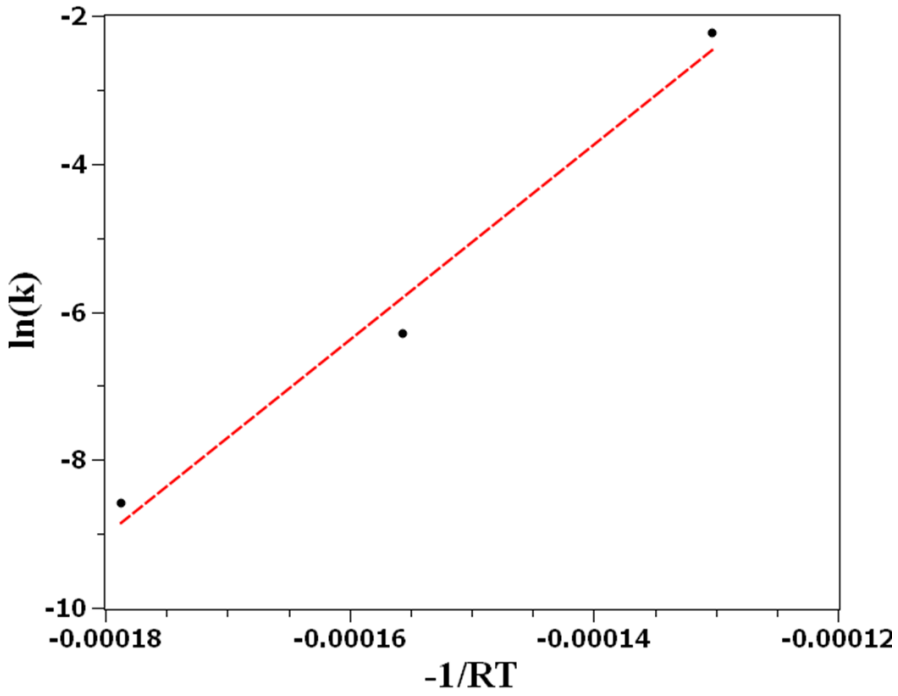

Figure 4.21 Linearized JMAK equation to extract tempering kinetics parameters for JSC980

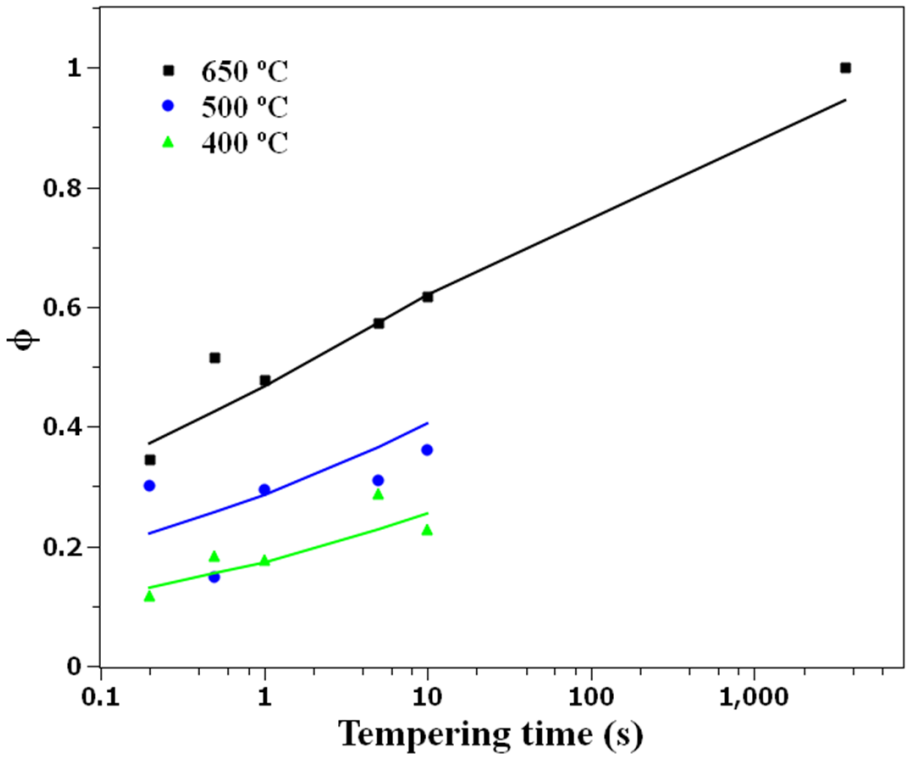

Figure 4.22 Comparison of the measured softening extent with the JMAK calculation using extracted kinetic parameters for JSC980

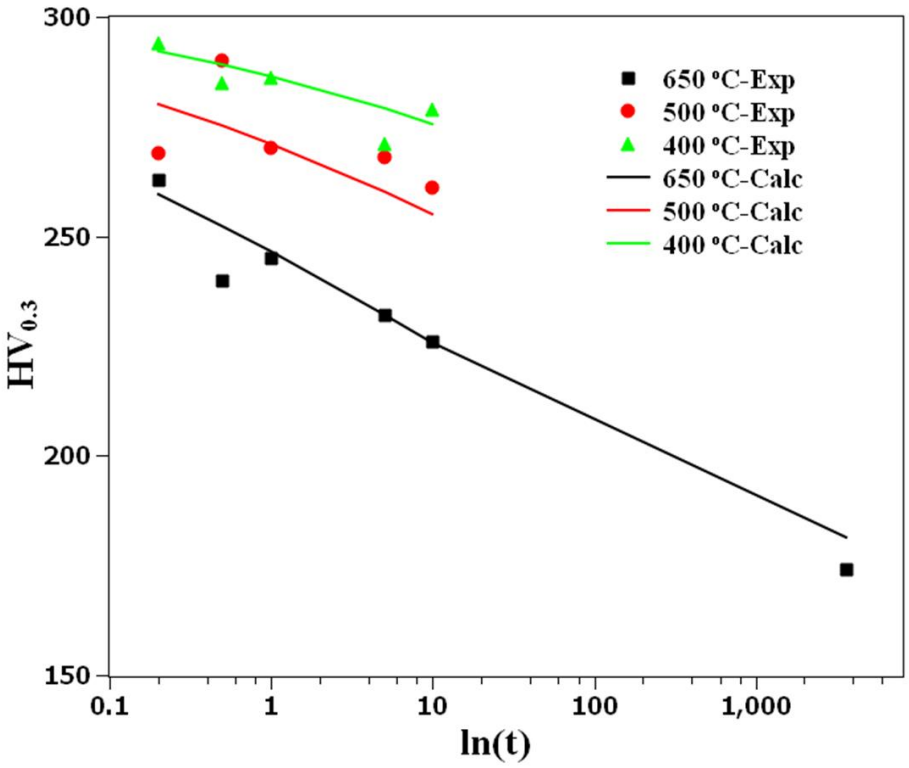

Figure 4.23 Comparison of measured hardness with JMAK calculation using extracted kinetic parameters for JSC980

4.1.10 Local stress-strain curve of JSC980 for post-weld simulation

For accurate prediction of post-weld deformation and failure behavior, the local constitutive behavior of the nugget and each heat affected zone sub-regions, especially that of the potential failure locations, needs to be developed. Similar to the methods described in Chapter 3, the microstructure of CGHAZ and SCHAZ of JSC980 were recreated in gauge section of flat tensile bars using Gleeble 3800. Quasi-static tensile testing was conducted with displacement rate of 2.54 mm/min and the strain was measured by DIC with a 2-mm virtual extensometer at the strain localized region for

engineering strain extraction. True strain can be simply calculated based on measured engineering strain. The detailed procedure was described in Section 3.1.4.1. The local stress-strain curves of BM and Gleeble simulated CGHAZ and SCHAZ of JSC980 are shown in Figure 4.24.

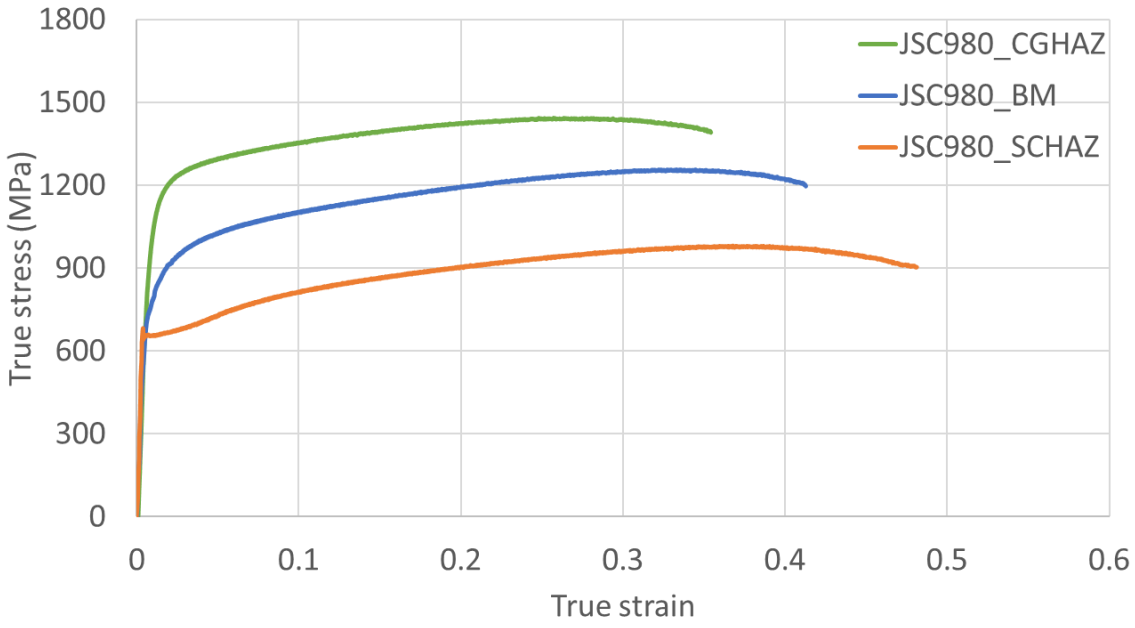

Figure 4.24 Local stress-strain curves of BM and Gleeble simulated CGHAZ and SCHAZ for JSC980

4.2 Resistance spot welding of 4T stack-up

4.2.1 Experiment

A representative thin/thick/thick/thick 4T stack–up, comprising 0.75 mm-thick galvannealed JAC 270/1.4 mm-thick DP 980/1.4 mm-thick DP 590/1.5 mm-thick Usibor 1500, was studied. In other words, this 4T stack-up is the addition of Usibor 1500 to the 3-

T stack-up described in Chapter 4.1. The chemical compositions of four sheets is listed in Table 4.3.

Table 4.3 Chemical compositions of steels (wt%) used in 4T RSW

Steels	C	Mn	Si	Cr	Ni	Mo	CE_N
JAC270	0.0015	0.107	0.068	0.009	0.01	0	0.013
DP980	0.09	2.07	0.62	0.02	0.01	0.07	0.331
DP590	0.123	1.09	0.297	0.03	0.02	0.006	0.28
Usibor®1500	0.21	1.22	0.265	0.19	0.01	<0.003	0.476

The microstructures of the four base metals, shown previously in Chapter 3 and Chapter 4.1, are shown together in Figure 4.25 for completeness. Base metal of JAC 270 consisted of ferritic and pearlite with a hardness of 93 ± 2 $HV_{0.2}$. JSC 980 and JSC 590 base metal consisted of martensite and ferrite with a hardness of 316 ± 7 $HV_{0.2}$ and 210 ± 5 $HV_{0.2}$ respectively. Usibor 1500 exhibited martensitic microstructure with a hardness value of 466 ± 7 $HV_{0.2}$.

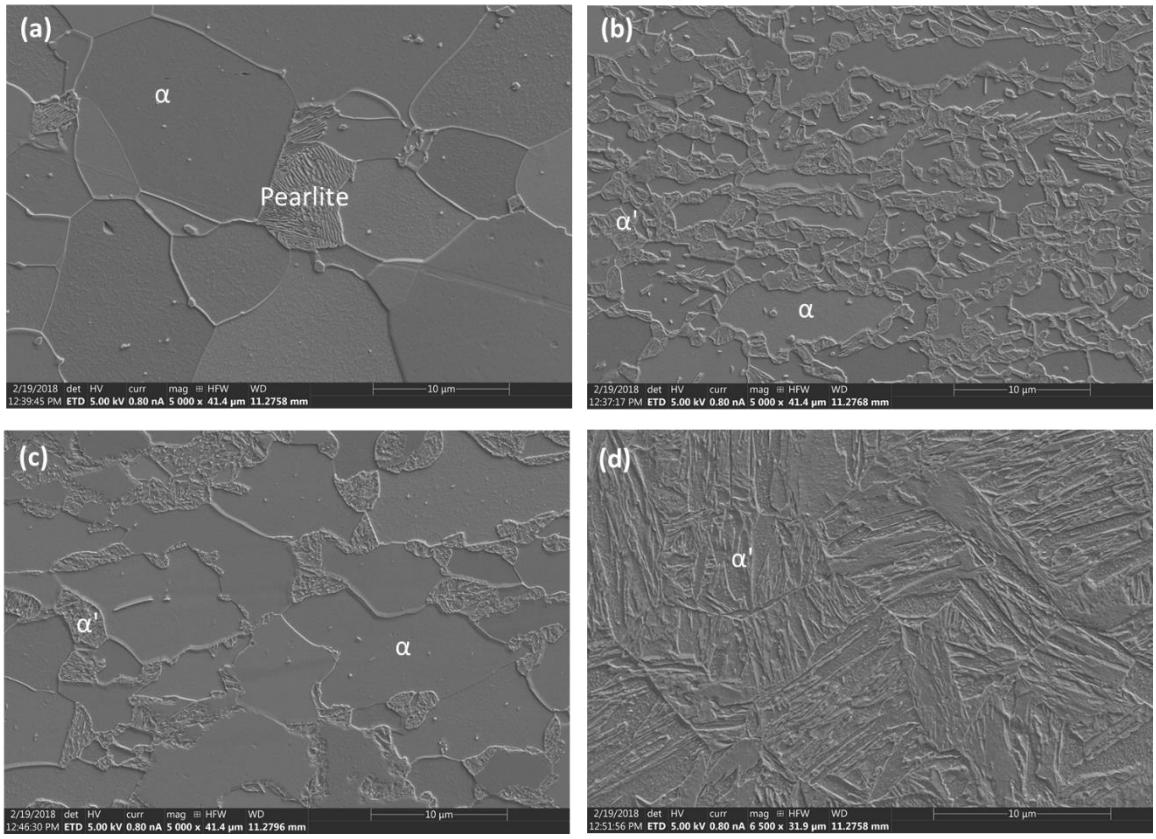

Figure 4.25 Base metal microstructure of (a) JSC 270, (b) JSC980, (c) JSC590, (d) Usibor1500

Resistance spot welding of the 4T stack-up was conducted on the same MFDC machine with electric servo welding gun as 3T RSW. Based on the concept that high current/short time can concentrate heat at sheet/sheet interface due to high contact resistance between sheet for the first few cycles and low current/long welding time was beneficial for better controlled nugget formation by taking advantage of bulk resistance, a tentative welding schedule was shown in Figure 4.26. During all experiments, the electrode force was kept at 3.432 kN. 3 impulses were used with 33 ms of welding time for the 1st impulse, 367 ms of welding time for the 2nd impulse, and 50 ms of welding time for 3rd impulse. There was also 33 ms of the cool time in-between two adjacent

impulses. The squeeze time and hold time were 500 ms and 250 ms respectively. In order to increase heat generation and reduce heat dissipation, the electrode on the thin sheet side was a Class 1 electrode that had Class 3 material as a surface insert. The Class 3 material was Alloy 18000, a low-cost Beryllium free copper nickel alloy with the electrical conductivity of 52% International Annealed Copper Standard (IACS). The geometry of the electrode is identical to Class 1 electrode, dome-radius shaped with a surface diameter of 6 mm. To prevent early expulsion between sheets or severe surface expulsion, Class 1 dome-radius electrode with a surface diameter of 8 mm was used on thick sheet side.

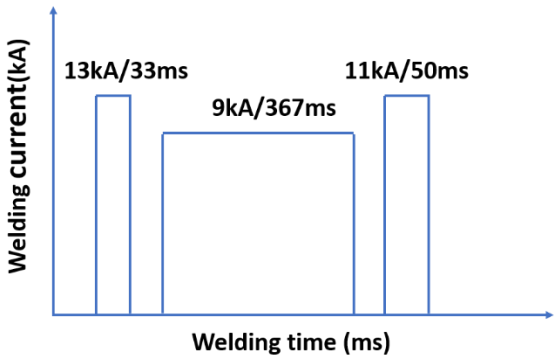

Figure 4.26 Schematics of welding schedule of resistance spot welding of 4T stack-up comprising 0.75 mm thick JAC270 / 1.4 mmt thick DP980 / 1.4 mm thick DP590 / 1.5 mm thick Usibor® 1500

Samples for microstructure characterization were prepared based on standard metallography procedure. Optical microscopy was used to observe macrostructure. The penetration of the weld nugget into the thin sheet has been measured based on Honda Standard. The penetrations at a quarter, a half and three quarters of the weld nugget at

JAC 270/JSC 980 interface have been measured. Microstructure of the samples was characterized by scanning electron microscopy (SEM). Microhardness mapping was performed on a half of the cross-section of the sample, using 200 g load with an indent spacing of 200 µm.

As shown in Figure 4.27, peel test was conducted at thin/thick sheet interface, and the button size was measured on the fracture sample by a caliper. In addition, lap shear tensile testing with displacement rate of 1 mm/min was conducted at the JSC590/Usibor 1500 interface.

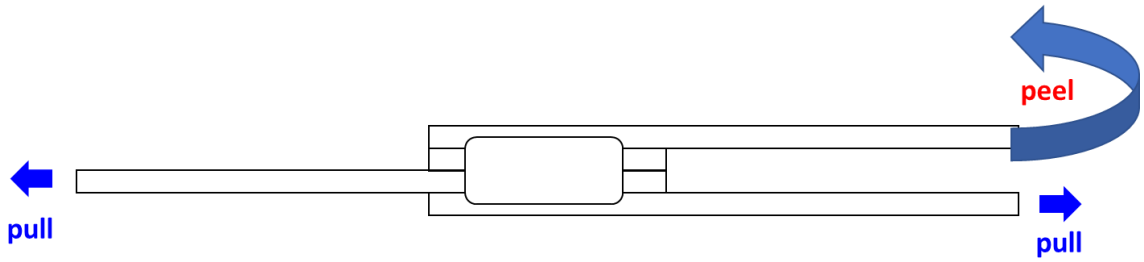

Figure 4.27 Schematics of mechanical testing for resistance spot welded 4T stack-ups

4.2.2 Effect of pulsation on nugget formation

Similar to RSW of 3T stack-up, the main problem for resistance spot welding of 4T stack-up is no/limited penetration into the thin sheet. Figure 4.28 (a) shows such a case with limited penetration into the thin sheet when a low current (10 kA) and long welding time (50 ms) were used for the 1st impulse. It is noted that the failure mode at 1st/2nd sheet interface can exhibit a small button pull-out on the thin sheet even with limited penetration, which is most likely due to solid-state bonding. However, a metallurgical

bond is required at $1^{st}/2^{nd}$ sheet interface with a reasonable penetration (above 20% based on AWS D8.1M) to ensure consistency in the mechanical strength and failure modes.

After optimizing the impulse parameters, a substantial penetration into the thin sheet can be obtained as described in the following. Some typical macrostructures of the resistance spot welded 4T stack-ups with more than 30% of penetration into thin sheet are shown in Figure 4.28(b)-(d). The general shape of the weld nugget is that the largest nugget diameter is created at the $3^{rd}/4^{th}$ sheet interface, with decreasing nugget diameter at the $2^{nd}/3^{rd}$ sheet interface and the smallest at the $1^{st}/2^{nd}$ sheet interface. A square-shaped notch/bi-notch is commonly observed at the $3^{rd}/4^{th}$ sheet interface. For instance, a square notch exists on the left side of the nugget shown in Figure 4.28(b), and a bi-notch can be observed on both sides of the nugget in Figure 4.28(d). However, sharp notch is generated at the other interfaces. Voids can be observed at the geometry center of the stack-ups, which usually will not affect the mechanical properties of the welds as long as the area and length of each pore/void are below those minimum requirement of AWS D8.1M.

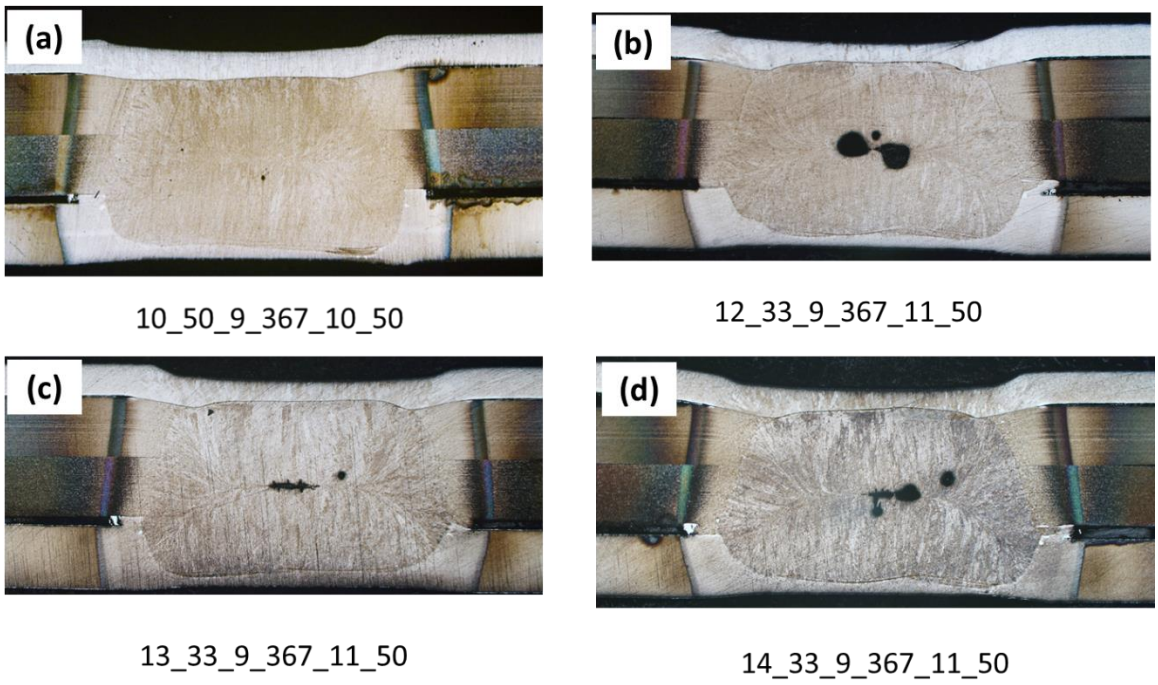

Figure 4.28 Macrostructure of the resistance spot welded JAC270/JSC980/JSC590/Usibor 1500 with different welding schedules (the format of the label is 1st impulse current_1st impulse time_2nd impulse current_2nd impulse time_3rd impulse current_3rd impulse time; cool time between the impulses = 33 ms).

4.2.2.1 ***Effect of 1st impulse current on nugget formation***

The effect of 1st impulse welding current on nugget diameter is shown in Figure 4.29. The nugget diameter at the 1st/2nd and 2nd/3rd sheet interfaces is approximately 5 mm and 6.2 mm respectively, when the welding current is higher than 11 kA, while the nugget diameter at the 3rd/4th sheet interface gradually increases form 6.5 mm to 7.1 mm as welding current increases from 10 to 14 kA. Expulsion occurs at the 3rd/4th sheet interface when the 1st impulse welding current is 15 kA, at which the largest nugget diameter shift to the 2nd/3rd sheet interface. The effect of welding current on the nugget penetration into the thin sheet is shown in Figure 4.30. With increasing 1st impulse welding current, the

penetration into thin sheet increases gradually with the largest penetration of between 55% to 65% at expulsion condition. Welds made with 1st impulse current ranging from 10 to 14 kA can meet the AWS standard required for nugget diameter and nugget penetration.

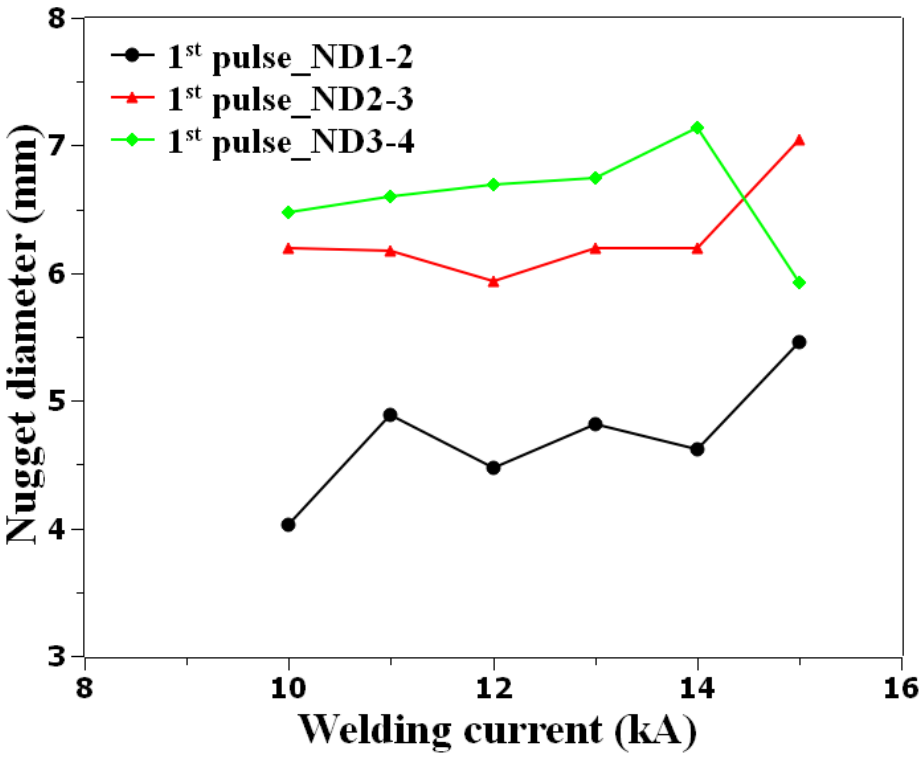

Figure 4.29 Effect of the welding current of the 1st impulse on nugget diameter

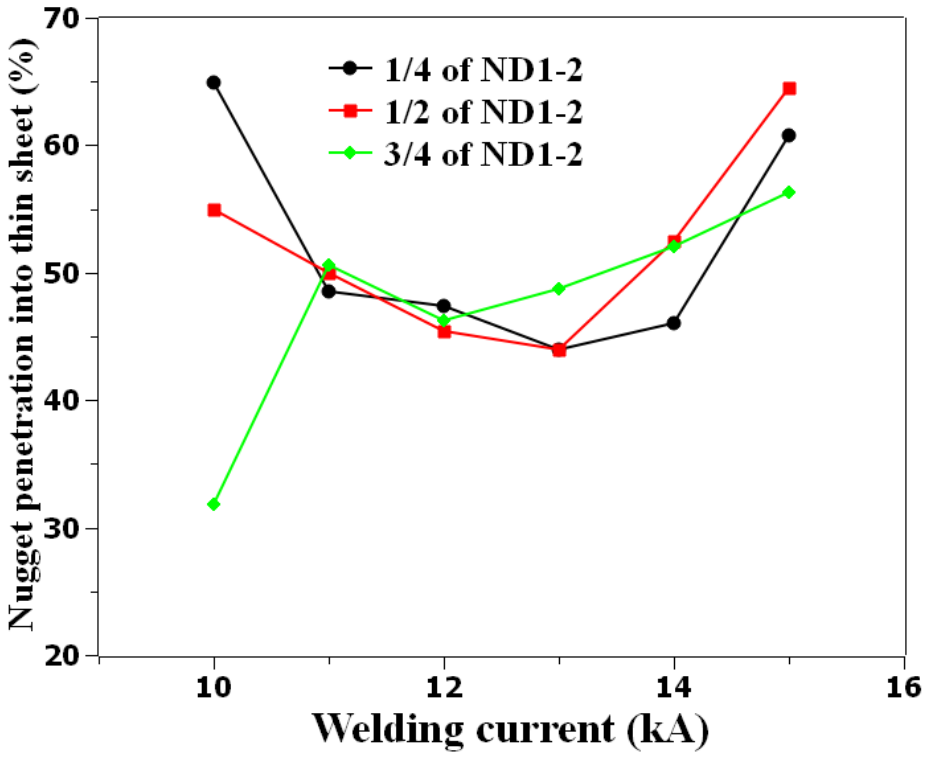

Figure 4.30 Effect of the welding current of the 1st impulse on nugget penetration into thin sheet

4.2.2.2 ***Effect of 2nd impulse current on nugget formation***

The effect of this main impulse on nugget diameter at each interface and nugget penetration into the thin sheet are shown in Figure 4.31 and Figure 4.32, respectively. In general, the optimum welding current for the main pulse is 9 kA. Expulsion takes place if the welding current is at or above 9.5 kA.

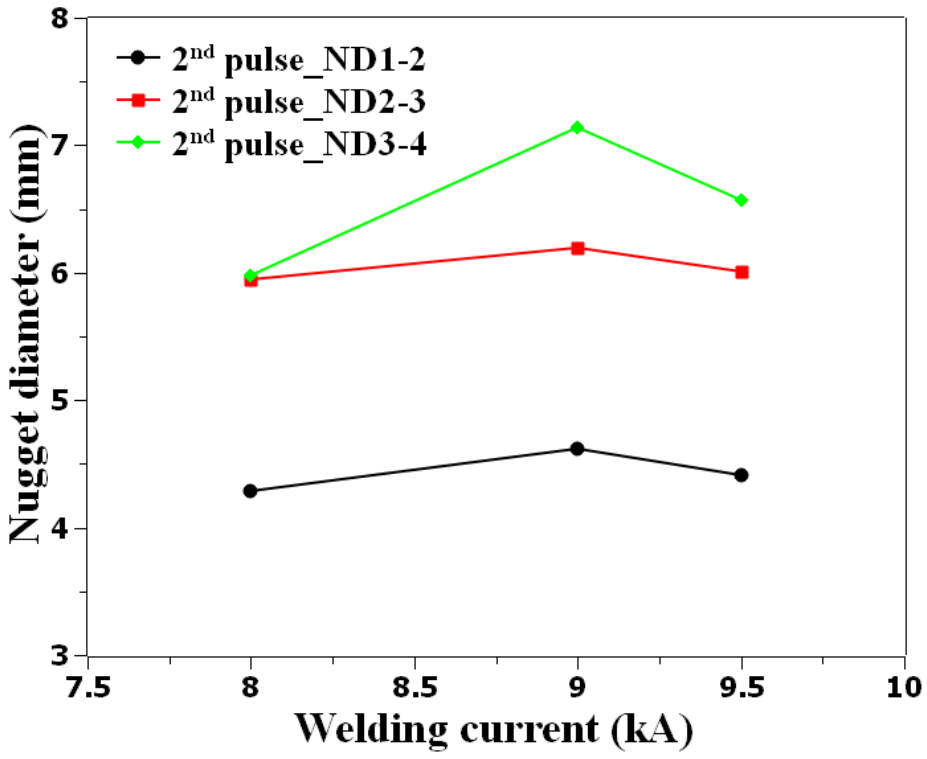

Figure 4.31 Effect of the welding current of the 2nd impulse on nugget diameter

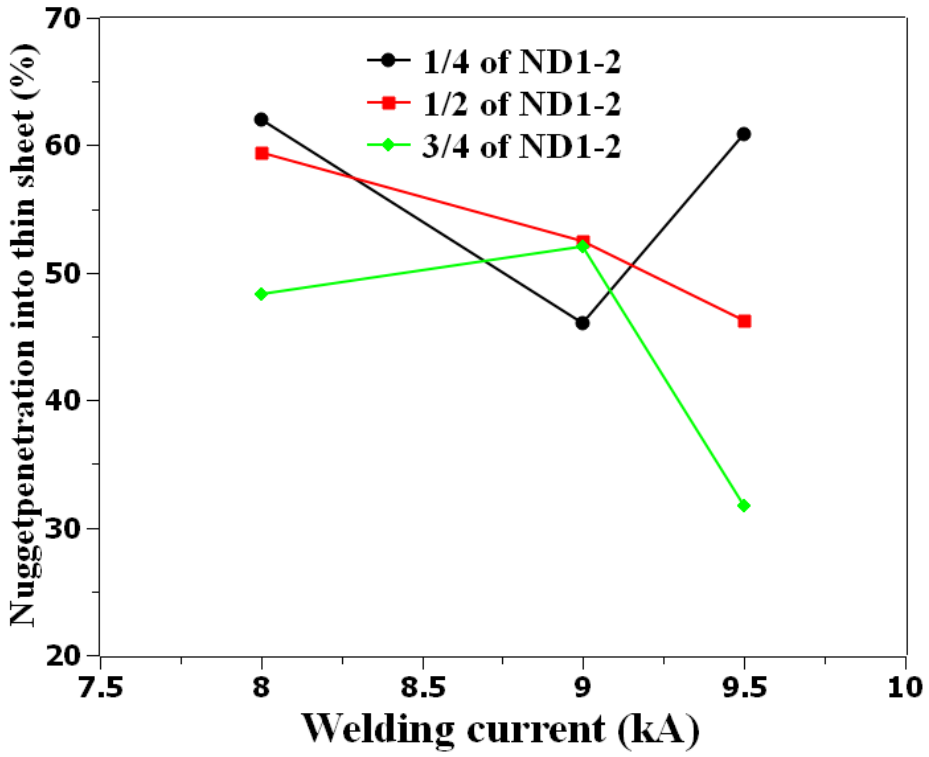

Figure 4.32 Effect of the welding current of the 2nd pulse on nugget penetration into thin sheet

4.2.2.3 *Effect of 3rd impulse current on nugget formation*

To investigate the effect of the 3rd impulse current on nugget formation in 4T stack-up, the welding current for this impulse is varied from 10 kA to 14 kA, and the nugget geometry is compared to the one welded without the 3rd impulse. It is noted that all the welding currents of the 3rd impulse tested in this study are higher than that of the main pulse. The effect of the 3rd impulse welding current on the nugget diameter and the nugget penetration into the thin sheet are shown in Figure 4.33 and Figure 4.34. The nugget diameter at each interface is higher than that without a 3rd pulse (represented by

data points at 0 kA). As welding current increases from 10 kA to 14 kA, the nugget diameter increases obviously at the 2nd/3rd and 3rd/4th sheet interfaces. The nugget evolution is necessary for a better understanding of the nugget formation process in each impulse, as discussed next.

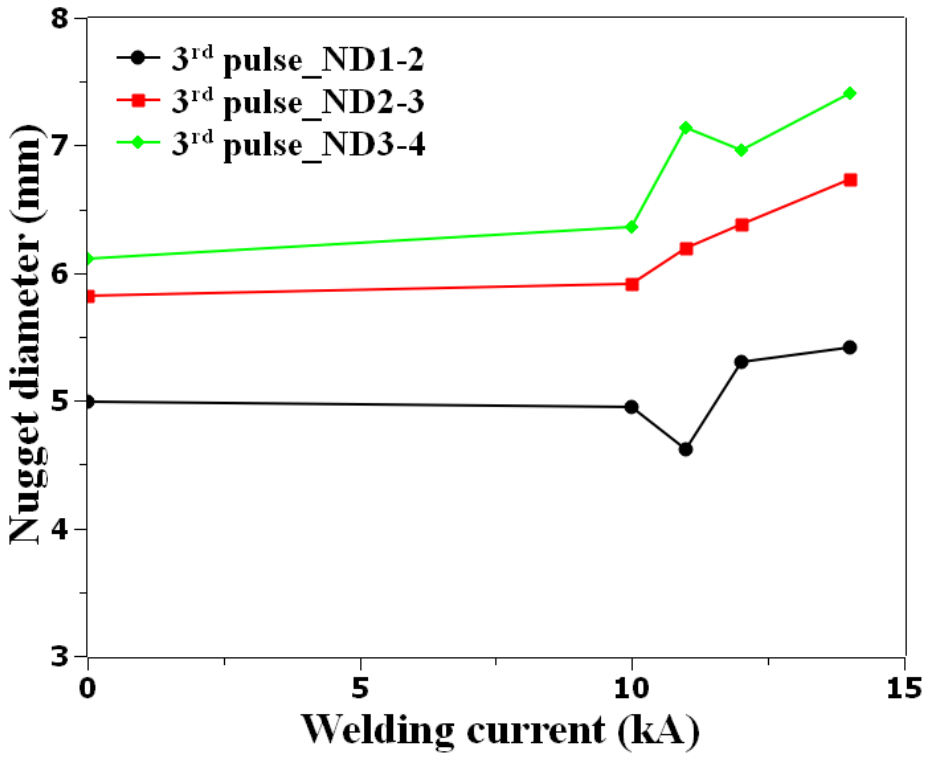

Figure 4.33 Effect of the welding current of the 3rd pulse on nugget diameter

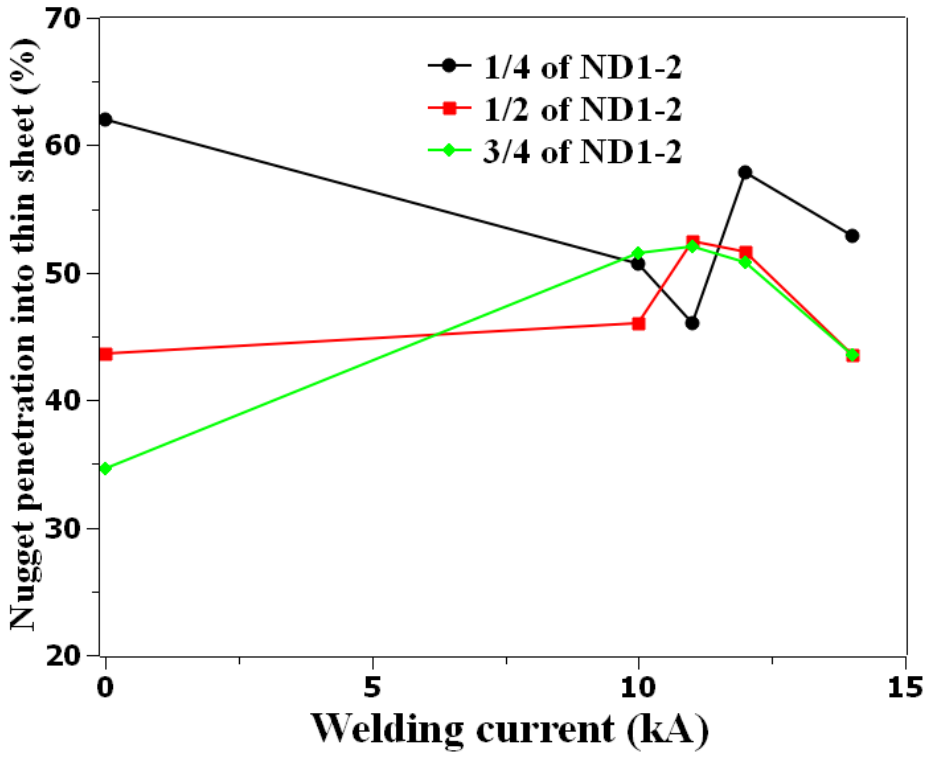

Figure 4.34 Effect of the welding current of the 3rd impulse on nugget penetration into thin sheet

4.2.3 Nugget formation kinetics

To understand the nugget formation kinetics, Sherepenko et al. [139] conducted stop-action (or interrupted) test during resistance spot welding of 22MnB5. Welding was interrupted at various times of the typical welding schedule, and the weld geometries/attributes were measured on the interrupted weld samples. In this study, the interrupted test approach is used in the resistance spot welding of 4T stack-ups to determine the nugget initiation location and nugget growth process. A typical welding schedule for the 4T stack-up is shown Figure 4.35. A welding current of 11 kA and

welding time of 50 ms is used in the 1st and the 3rd impulses, while a welding current of 9 kA and a welding time of 367 ms is used in the 2nd impulse.

First, the dynamic resistance curve for the entire welding schedule is obtained and is shown in Figure 4.35. It is noted that it typically takes 4 – 5 ms to achieve the set current (11kA/9kA) with the MFDC machine used in this work. In addition, there is no data recorded by the machine during cool time/hold time. Next, to investigate the nugget formation during the first two impulses, two different welding times (30 ms and 50 ms) are used for the 1st impulse, and three different welding times (20 ms, 50 ms and 150 ms) are used for the 2nd and main impulse. The corresponding locations are marked in the dynamic resistance curve in Figure 4.35. The weld is stopped as soon as the set welding time is reached for each impulse.

The optical micrographs of the faying interfaces at JAC270/JSC980 interface and JSC590/Usibor 1500 interface are shown in Figure 4.36. With a short welding time of 30 ms in the 1st impulse, the GA coating on JAC270 is removed and the radius of a discolored area is 2.1 mm, as indicated by the red circle in the macrograph. For the Al-Si coating on the surface of Usibor 1500, coating melts initially at several separate spots. With increasing welding time to 50 ms, the radius of coating removal area increases to 2.6 mm on the JAC270 sheet at JAC270/JSC980 interface. The coating removal spots on the surface of Usibor 1500 become connected and Al-Si coating is squeezed to the periphery of the interface. In summary, no bond formed at the end of the 1st impulse with the welding time up to 50 ms.

For the 2nd impulse, the welding current used is relatively low (9 kA). At a short welding time of 20 ms, the coating removal regions at JAC270 and Usibor 1500 do not appear to have obvious increase. With increasing welding time to 50 ms, the dynamic resistance increases (see Figure 4.35), possibly due to heat generation by bulk resistance of the steels. A solid-state bonding is created at JSC590/Usibor 1500 interface though melting of the IMCs as shown in Figure 4.37, since heat is generated due to high contact resistance of Al-Si coating. However, there is not yet a nugget formation at JSC590/Usibor1500 interface. As shown in Figure 4.38, with further increasing of welding time to 150 ms, nugget is formed through the four sheets, which corresponds to a dynamic resistance reduction of 15 μΩ from the peak resistance of the 2nd impulse. The dynamic resistance drops 5 μΩ during cool time between the 2nd impulse and the 3rd impulse, and there is a slight resistance increase of 2 μΩ during the 3rd impulse. Therefore, the main function of the 3rd impulse with high welding current and short welding time is to ensure the consistency of the weld quality.

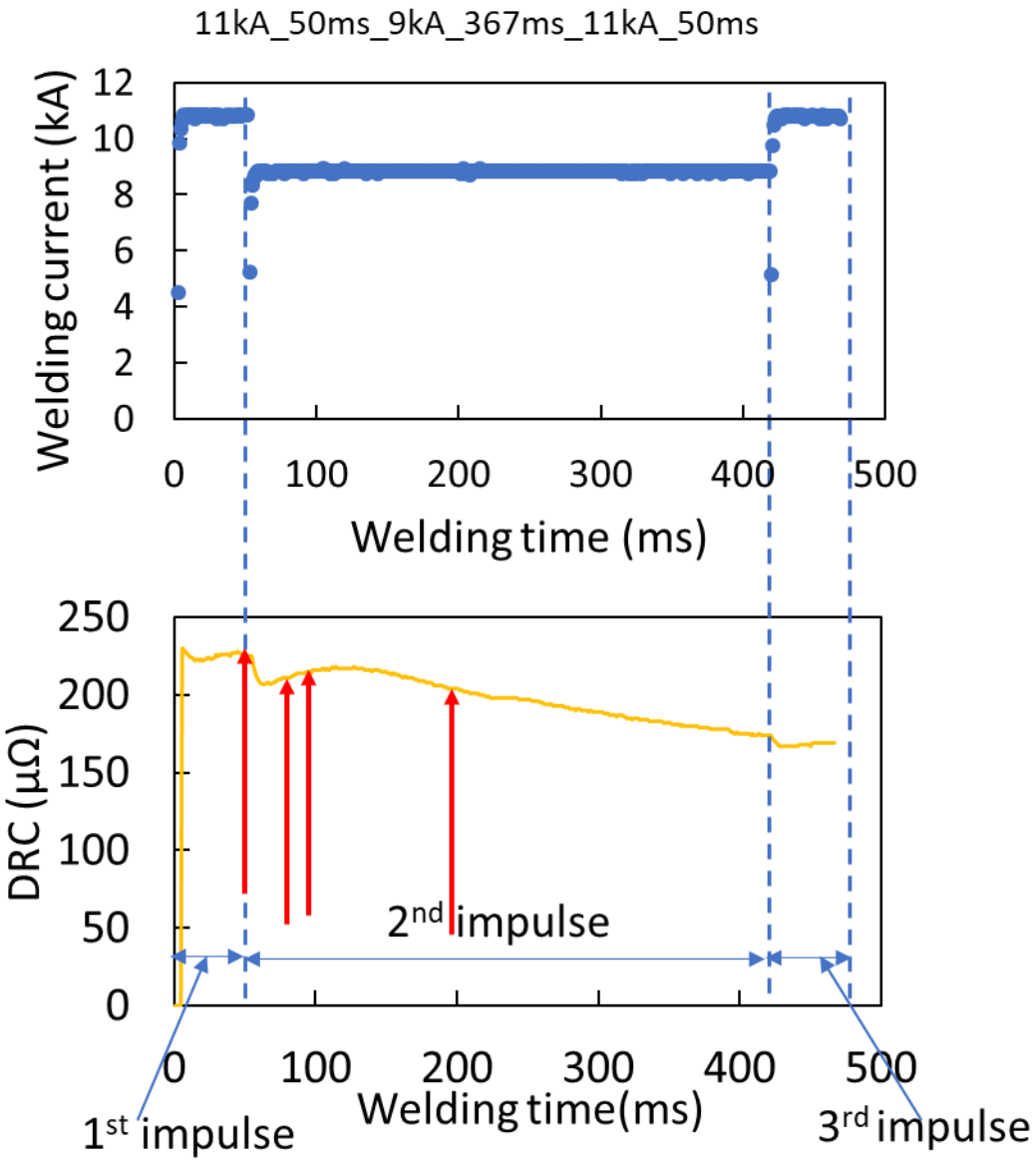

Figure 4.35 Welding current and corresponding resistance curves for the 4T stack-up welds with the welding schedule of 11kA and 50ms in the 1st impulse, 9kA and 367ms in the 2nd impulse, and 11kA and 50 ms in the 3rd impulse

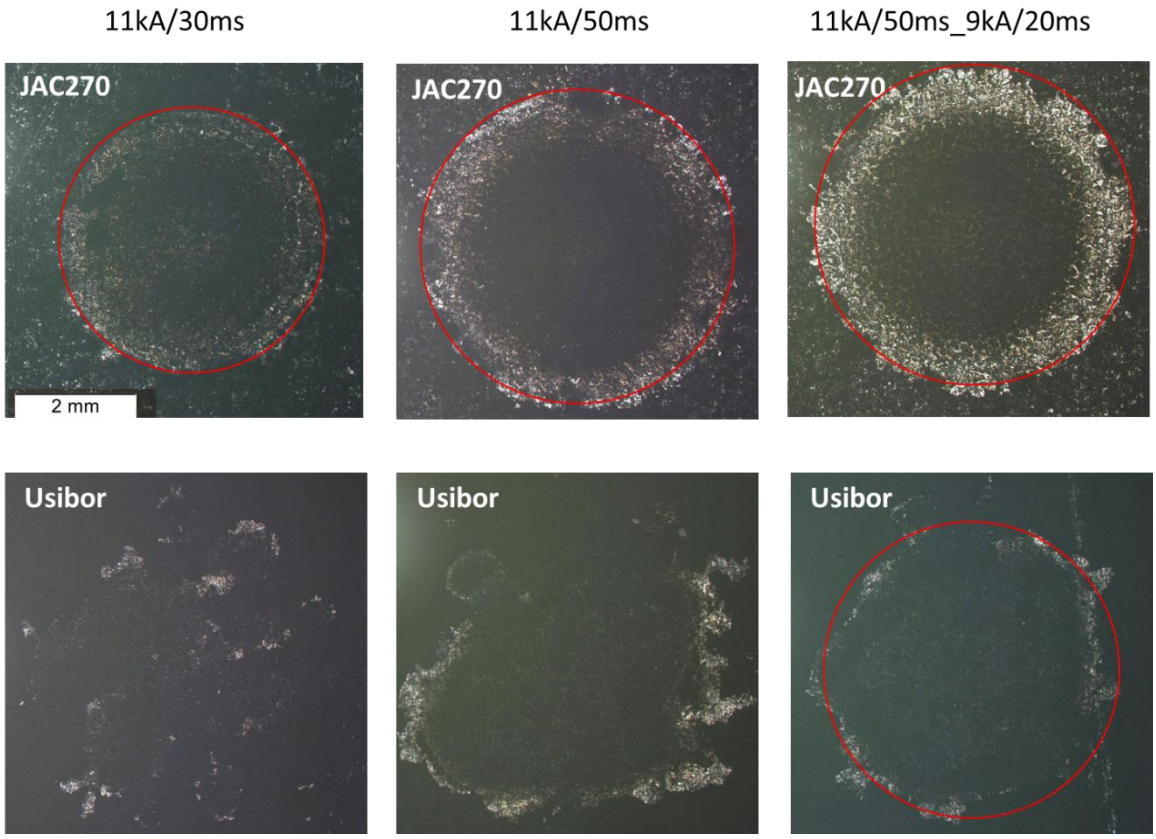

Figure 4.36 Optical macrographs showing the coating removal at JAC270 and Usibor 1500 during the initial stage of welding. The left and middle columns had only the 1st impulse, and the right column had the 1st and 2nd impulses.

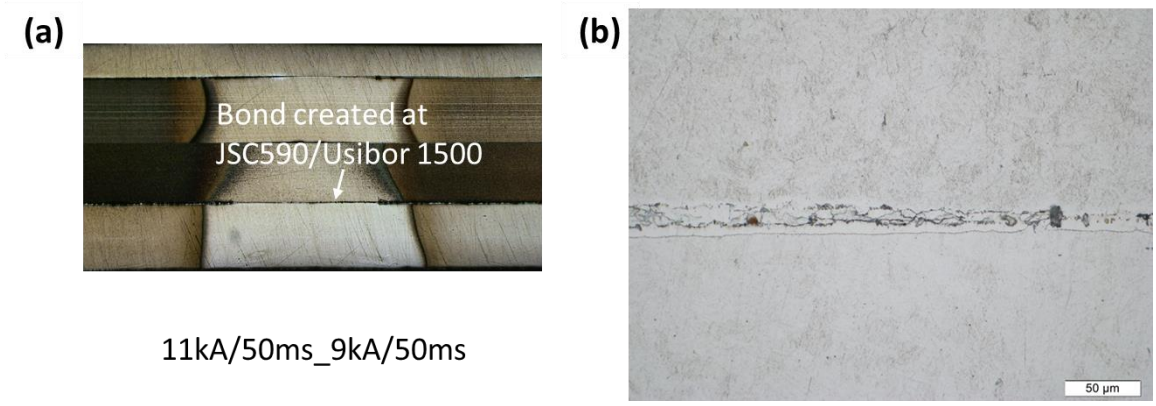

Figure 4.37 Optical images showing (a) bond creation at JSC590/Usibor 1500 interface, and (b) zoomed-in image of the IMCs formed at this interface after the welding time of 2nd impulse = 50 ms

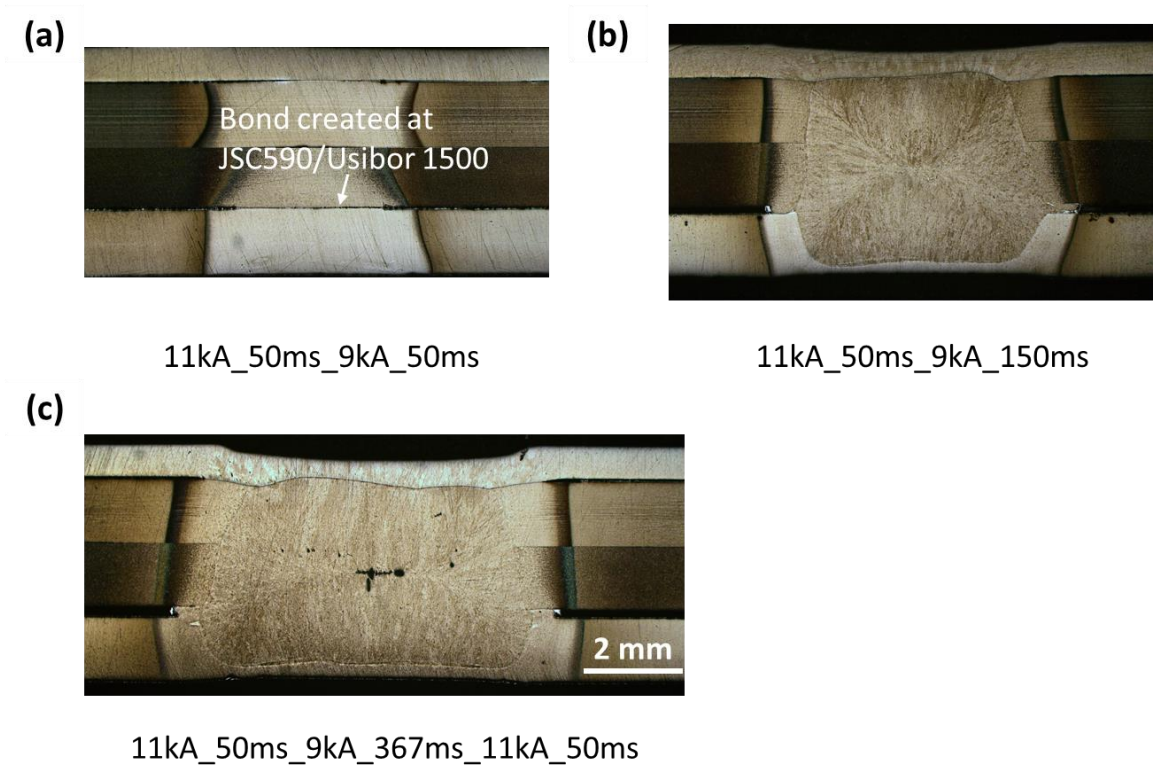

Figure 4.38 Nugget formation kinetics for the 4T stack-up welds observed by interrupted tests: (a) and (b) had only two impulses, and (c) included all three impulses

4.2.4 Microstructure and microhardness

Microhardness map of a half spot weld, made with the welding current of 13 kA and the welding time of 33 ms for the 1st impulse, 9 kA/367 ms for the 2nd impulse, and 11 kA/50 ms for the 3rd impulse, and the electrode force of 3.434 kN, is shown in Figure 4.39. On the thick sheet side (JSC980/JSC590/Usibor 1500), the hardness within the weld nugget is uniform, which is approximately 418 $HV_{0.2}$. Local softening can be observed at the SCHAZ of JSC980 and Usibor 1500. The hardness distribution along the centre of each sheet is plotted in Figure 4.40. The hardness of the upper-critical HAZ (CGHAZ+FGHAZ) in Usibor 1500 is 476 ± 6 $HV_{0.2}$, which is comparable to the hardness of the base metal but is

58 $HV_{0.2}$ higher than the weld nugget. In resistance spot welding of 2T Usibor 1500, the microhardness of weld nugget, upper-critical HAZ and the base metal are comparable. The lower weld nugget hardness of weld nugget compared to upper-critical HAZ in Usibor 1500 in the 4T stack-ups is caused by the dilution of the other steels with low concentration of carbon content. There is a 40% of hardness reduction in SCHAZ compared to the base metal of Usibor 1500, with the lowest hardness of 285 $HV_{0.2}$. The hardness reduction in SCHAZ of JSC980 is approximately 13% with the lowest hardness of 276 $HV_{0.2}$. Therefore, despite the higher ultimate tensile strength of Usibor 1500 compared to JSC980, the microhardness/strength is similar in the SCHAZ of the two sheets. There is approximately 7% of hardness reduction in the SCHAZ of JSC 590 compared to base metal, which is negligible. Since 3 impulses are utilized in resistance spot welding of 4T stack-ups, remelting can take place and more than one fusion boundaries can be observed in JAC 270 and Usibor 1500, which might have effect on the microstructure near to the fusion boundaries. However, only one fusion boundary was observed in in the horizontal direction, which indicates continuous increase in nugget diameter in lateral direction.

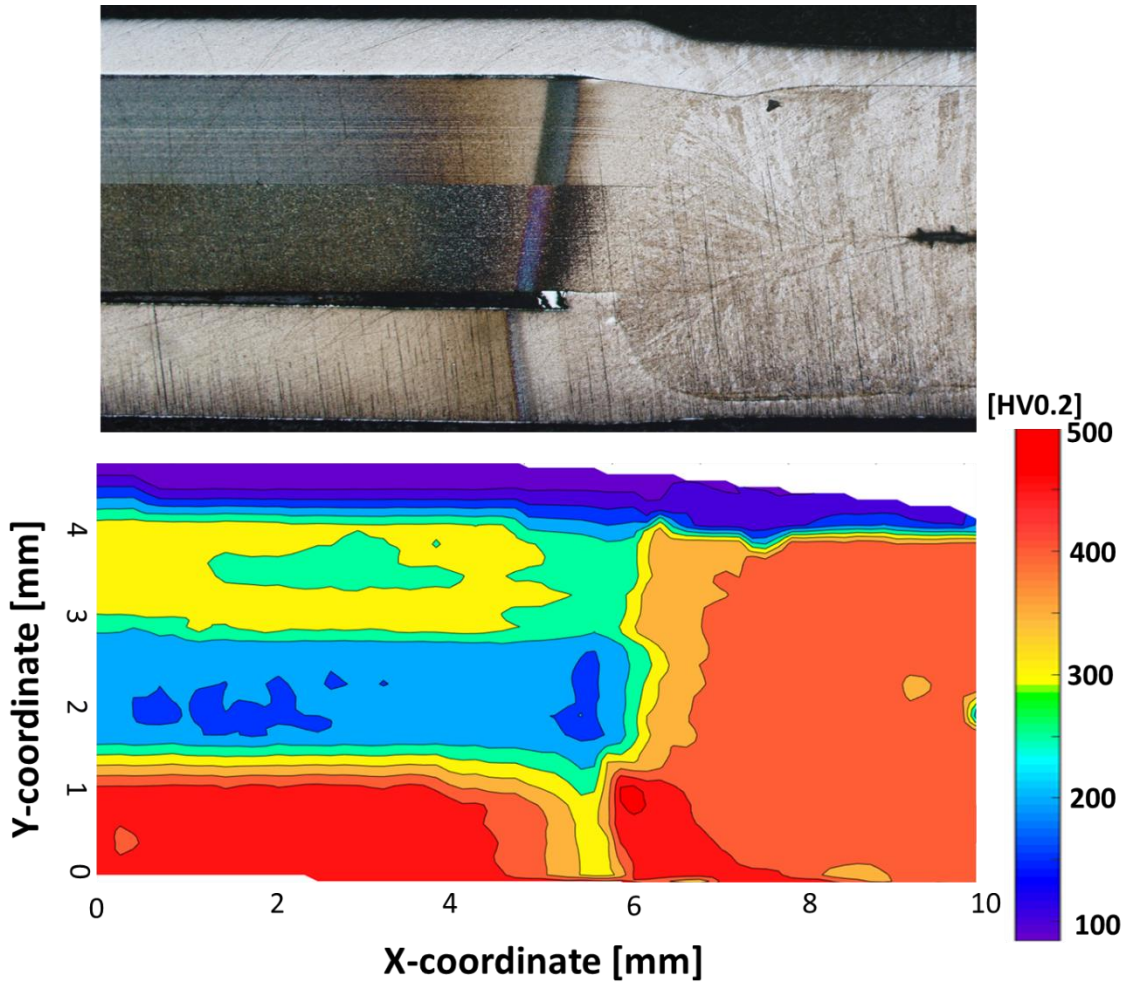

Figure 4.39 Microhardness map on the cross-section of the 4T stack-up (the welding currents for the 1st, 2nd and 3rd impulses are 13kA, 9kA and 11kA respectively)

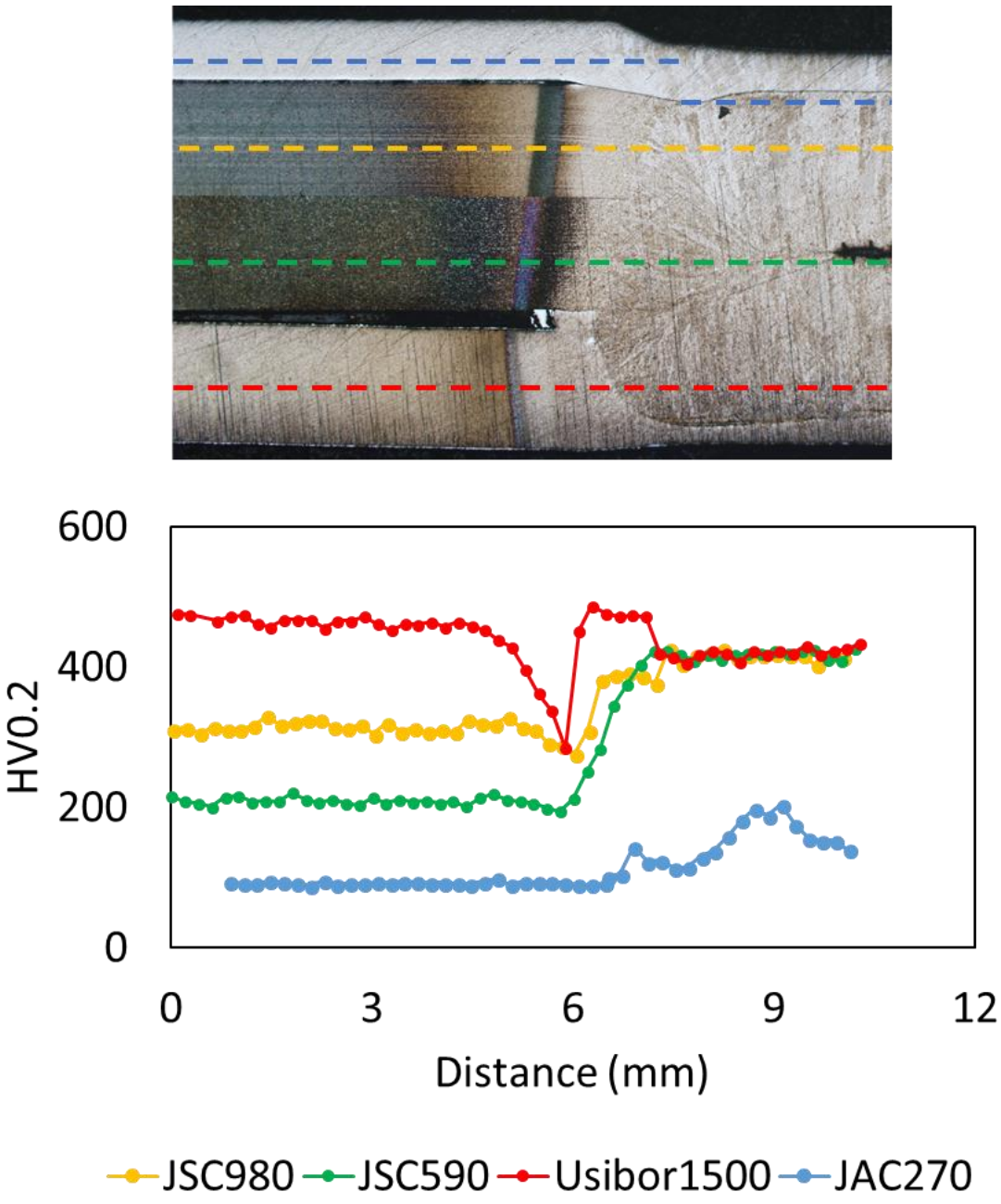

Figure 4.40 Hardness profile along the center of each steel sheet

4.2.5 Failure behavior

Since the JAC270 is not designed as a primary load carrying member, the actual load bearing capacity is less critical for the JAC270/JSC980 interface. In addition to the aforementioned the nugget penetration and metallurgical bonding, a simple peel test was conducted at that interface. A button with the diameter of 6.715 mm can be pulled out from the JAC270 base metal. However, based on the measurement of the nugget size at the cross-section of the 4T stack-up, the maximum nugget diameter at thin/thick sheet interface is approximately 5 mm, which is much lower than the button size. Thus, brazing by zinc at the periphery of the nugget is likely causing the larger button size in the peel test. Twist test will be utilized in the future work to reduce the effect of zinc brazing on the button size.

To test the load bearing and energy absorption capacity of the 4T stack-up, lap shear tensile testing was conducted at JSC590/Usibor 1500 interface. The final failure takes place at the base metal of JSC590 with a peak strength of 29.975 kN.

Figure 4.41 Button pull-out on JAC270 during peel test and button pull-out from JSC 590 during lap-shear tensile testing

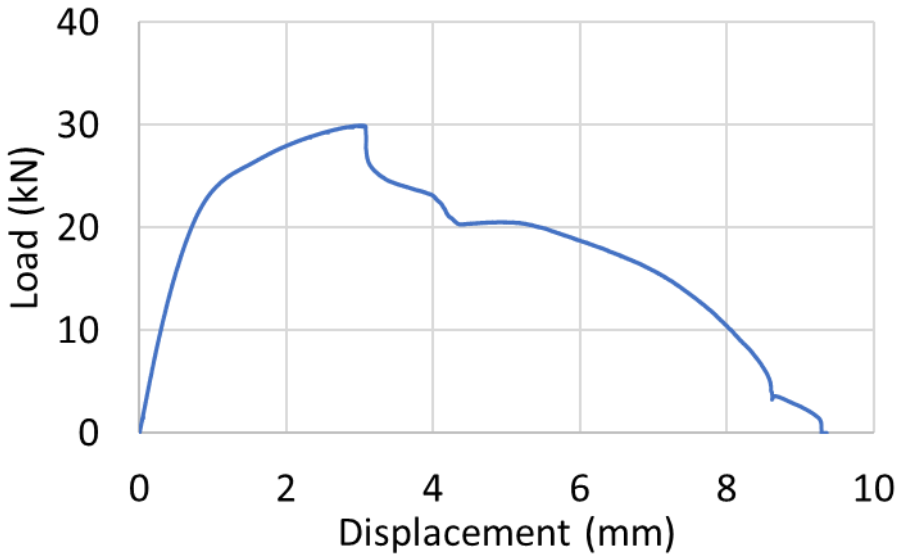

Figure 4.42 Load-displacement curve of resistance spot welded 4T stack-up at the JSC590/Usibor 1500 interface

4.2.6 RSW process simulation of 4T stack-ups

The 3D fully coupled thermo-electro-mechanical model, described in the first part of the chapter, is further extended for the 4T stack-ups with GA and Al-Si coatings at the top and bottom sheets respectively. The temperature distribution at the end of the 1st impulse is shown in Figure 4.43. High heat is generated at both JAC 270 and Usibor 1500 interfaces. Moreover, high temperature can also be observed at electrode/sheet interfaces, especially at Usibor 1500/bottom electrode interface. The high heat generation at the two interfaces is important to remove the coatings on JAC270 and Usibor 1500 (see Figure 4.36 for experimental observation). Nugget initiates first in the 2nd impulse at JSC590/Usibor 1500 interface due to high heat generated by the high contact resistance of Al-Si coating (Figure 4.44). Nugget penetrates into the thin sheet with longer welding

time in the 2nd impulse and slight nugget increases can be observed at the end of the 3rd impulse (Figure 4.45).

The predicted dynamic resistance curve is compared to the measured value as shown in Figure 4.46. The basic trend and the value of the predicted resistance is comparable to the experimental results, with initial reduction of resistance due to reduction of contact resistance, further increase in resistance due to bulk resistivity increasing with temperature followed by resistance reduction due to increasing contact area and reduction in sheet thickness. However, the resistance reduction between 1st and 2nd impulses is not accurately predicted. Therefore, further validation and improvement of the process model for the 4T stack-up is still necessary for a better description of contact condition and a better understanding of bonding mechanism.

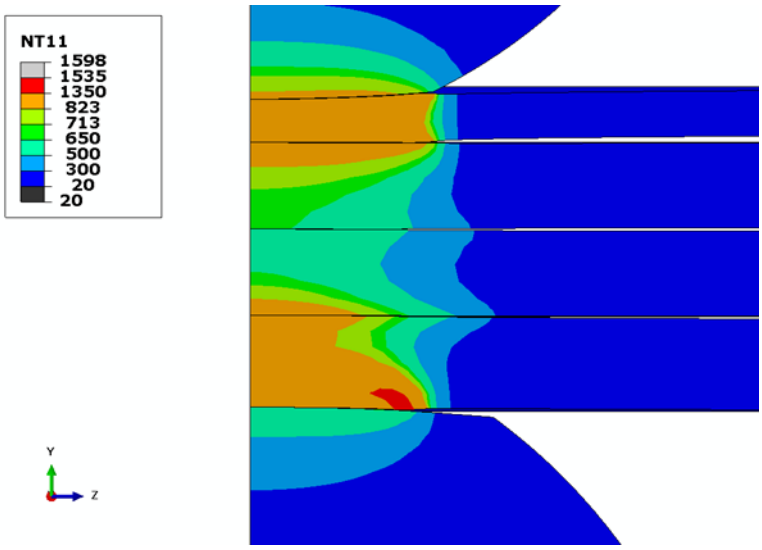

Figure 4.43 Calculated temperature distribution at the end of the 1st impulse (welding schedule: 14kA/33 ms in the 1st impulse, 9kA/367ms in the 2nd impulse, and 11kA/50ms in the 3rd impulse)

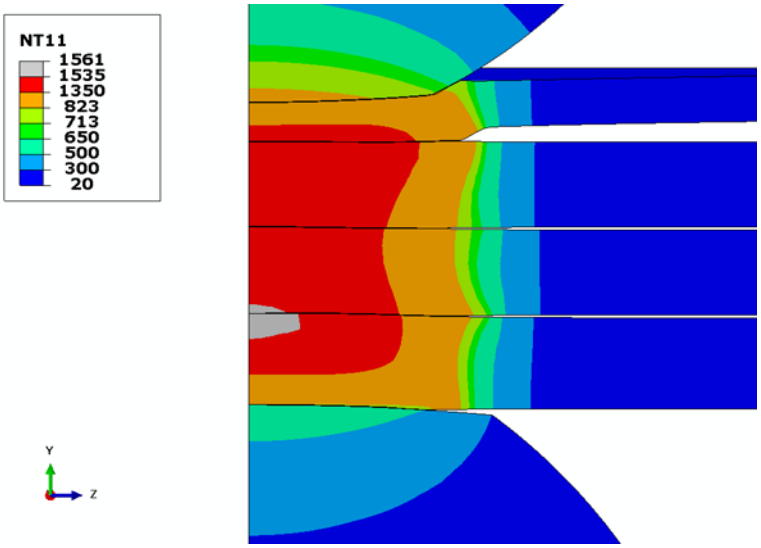

Figure 4.44 Nugget initiation in the 4T stack-ups during the 2nd impulse

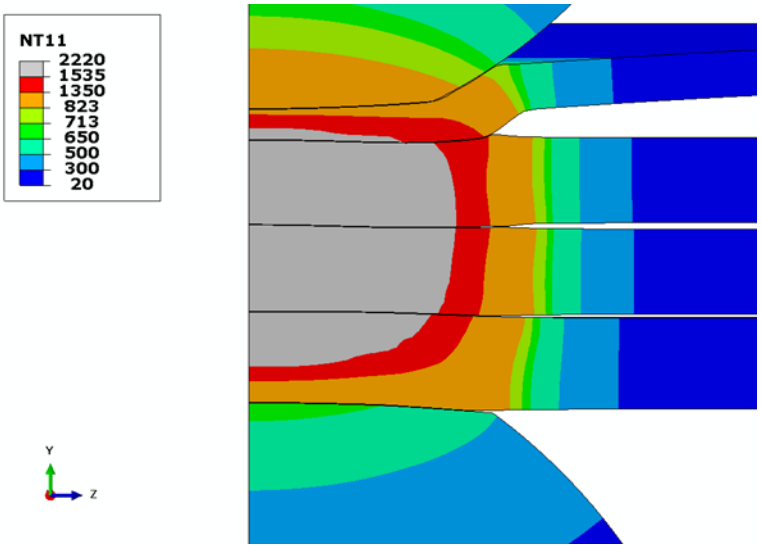

Figure 4.45 Nugget formed in the 4T stack-ups at the end of the 3rd impulse

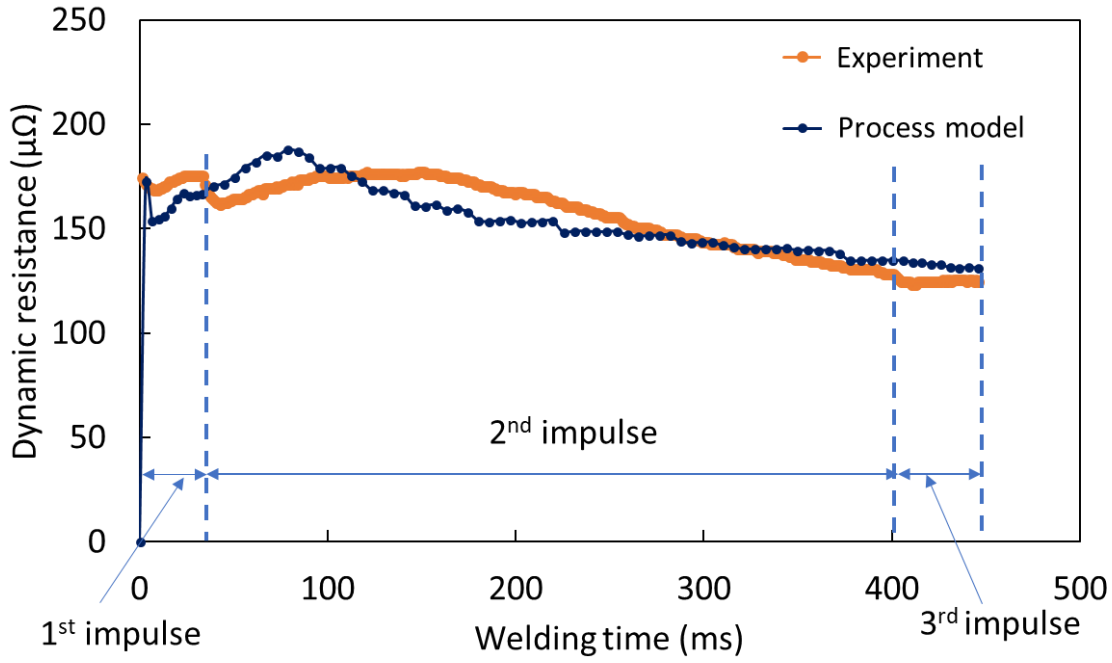

Figure 4.46 Comparison of predicted and measured dynamic resistance curves (welding schedule: 14kA/33 ms in the 1st pulse, 9kA/367ms in the 2nd pulse, and 11kA/50ms in the 3rd pulse)

4.3 Conclusions

In summary, 3T stack-up comprising 0.75 mm-thick galvannealed JAC 270/1.4 mm-thick JSC 980/1.4 mm-thick JSC 590 and 4T stack-up comprising 0.75 mm-thick galvannealed JAC 270/1.4 mm-thick JSC 980/1.4 mm-thick JSC 590 were resistance spot welded. The effect of various welding parameters, such as welding current, electrode force, electrode materials/geometry, on nugget size and penetration into the thin sheet was investigated. The 3D fully coupled thermo-electro-mechanical model, described in the previous chapter, was extended for investigation of temperature distribution and nugget formation in these complex stack-ups. The main conclusions are as follows.

For 3T stack-ups:

- Nugget size at the interface B and geometrical centre increase almost linearly with welding current. On the other hand, the nugget size at interface A increases rapidly initially and then saturates to 5 mm as welding current is higher than 9 kA. The effect of welding current on nugget penetration into the thin sheet is similar to that on the nugget size. It increases rapidly at low welding current and saturates to 32% when the welding current is higher than 9 kA.

- With increasing electrode force from 3.4 kN to 4.4 kN, the current for nugget formation at interface A is 2 kA higher while the nugget formation at interface B is not significantly affected. Once the nugget penetrates into the thin sheet, the effect of electrode force on nugget size and penetration at both interfaces is negligible. However, the electrode indentation on thin sheet side with a higher electrode force (4.4 kN) is about 12.5% larger compared to that with a lower electrode force of 3.4 kN at welding current of 9.5 kA.

- With Class 3 electrode on the thin sheet side, nugget penetration can be 53% which is approximately 20% higher than the one welded with traditional electrodes. Therefore, electrode materials/geometry have the most significant effect on nugget formation and penetration into the thin sheet.

- The calculated results of the process model show that heat generation at interface A is high at the initial stage of the welding process. Nugget initiation location can be current dependent. Nugget initiation at the geometrical centre

of the stack-up when the welding current is lower than 8 kA. As welding current increases, the nugget initiation location shifts from geometrical centre to interface B and the middle sheet.

For 4T stack-ups:

- 4T stack-ups of AHSS can be resistance spot welded with high welding current/short welding time for the 1st and 3rd impulses and low welding current/long welding time for the 2nd impulse. The main function of the 1st impulse is coating removal on the top and bottom sheets, the 2nd impulse is for nugget initiation and growth, and the 3rd impulse is for ensuring consistency of the nugget diameter.

- Nugget diameter and penetration into the thin sheet increases with the welding current of the 1st impulse and the 2nd impulse. The nugget diameter increases with the welding current of the 3rd impulse while the nugget penetration is not obviously increasing with the 3rd impulse.

- Process simulation of RSW of 4T stack-up was conducted to obtain the temperature evolution in the joint. The calculated results show that high heat is generated at both the top and the bottom sheets during the 1st impulse. Nugget initiates at the JSC590/Usibor 1500 interface and grows in both through-thickness and lateral direction during the 2nd impulse. Slight increase in nugget diameter can be observed in the 3rd and final impulse. Further validation and improvement of the process model (e.g., better ECR formula) is necessary for

a better understanding of nugget formation and the key factors controlling nugget initiation and growth.

Chapter 5 Ultrasonic + resistance spot welding of Al to steel

5.1 Introduction

In the previous two chapters, it is studied the welded structures made of AHSS including 2T stack-up of ultrahigh strength steel and complex stack-ups of different grades of AHSS. To achieve further weight reduction, multi-materials design of vehicle structure is increasingly utilized. A representative multi-materials design is one that makes use of AHSS in critical locations for crash performance and aluminum alloys elsewhere in the structure for adequate strength and corrosion resistance [94]. As discussed in the literature review in Chapter 2, fusion welding of Al to steel is susceptible to solidification cracking and severe formation of brittle intermetallic compounds (IMCs). Moreover, there exist various solid-state mechanical and joining processes for connecting Al to steel, although each has its own shortcomings (e.g., high equipment and consumable cost, long cycle time, and poor fatigue life of the joint).

In this chapter, a new joining process, i.e. ultrasonic plus resistance spot welding (abbreviated as U + RSW), was developed for cost-effectively joining of dissimilar sheet metals. Particularly, the process-microstructure-mechanical property relation for U+RSW of aluminum to low carbon steel was investigated to demonstrate the feasibility and potential of this new process for dissimilar metal joining in multi-materials structure.

5.2 Feasibility study

5.2.1 Experiment

5.2.1.1 *Materials*

The base materials in this study were 1 mm-thick aluminum alloy AA6061-T6 and 0.9 mm-thick cold rolled, uncoated AISI 1008 steel. Flat coupons of 100 mm in length and 38 mm in width were cut from the Al and steel sheets with the length direction aligned with the rolling direction. A 0.4 mm-thick aluminum alloy AA6061-T6 was used as the interlayer (or insert).

5.2.1.2 *Ultrasonic + resistance spot welding*

Figure 5.1 was a schematic diagram showing the U+RSW process. In the 1st step, the insert, 0.4 mm-thick aluminum alloy 6061-T6, was ultrasonic spot welded with 1008 steel to create an intermediate joint. Imprint was created on aluminum alloy interlayer. Then primary joint was created by resistance spot welding of 1 mm-thick aluminum alloy 6061 onto the interlayer side of the steel. Detailed procedure is provided as follows.

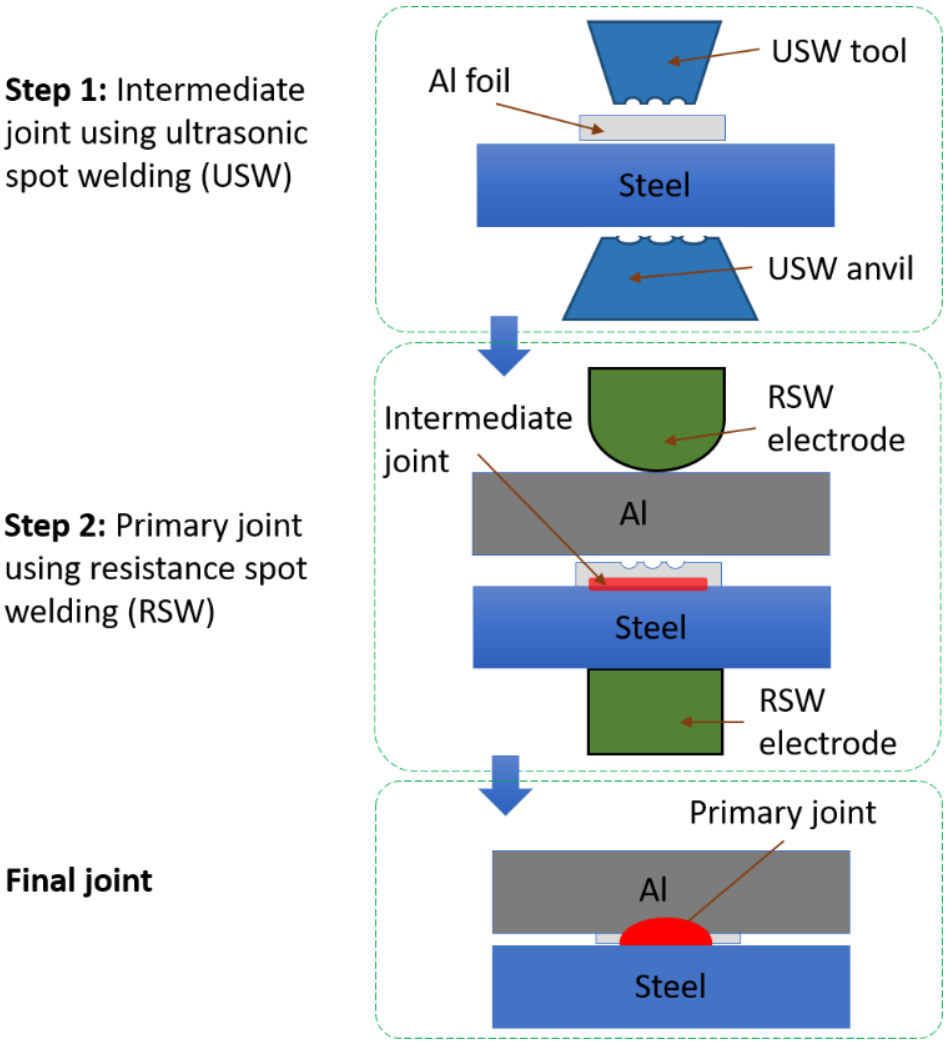

Figure 5.1 Schematic diagram of U+RSW welding procedure

5.2.1.3 ***Ultrasonic spot welding for intermediate joint***

A 0.4 mm-thick AA6061-T6 and a 0.9 mm-thick cold rolled 1008 steel were ultrasonic spot welded to create an intermediate joint. An Amtech Ultraweld® 20 2.4-kW lateral driven ultrasonic spot welder, designed to operate at 20 kHz with a maximum peak-to-peak amplitude of 80 µm, was used for welding. The dimensions of sonotrode tip were 8 mm × 6 mm and the anvil tip 12 mm × 12 mm. Both sonotrode and anvil surfaces had

pyramid knurl patterns to facilitate firm gripping of the samples. The vibration direction (VD) of the sonotrode was parallel to the short dimension of the samples (thus perpendicular to the rolling direction). The samples were grinded with 240 grade sand paper and cleaned by ethanol before welding. The USW parameters for the intermediate joint, developed based on those used a previous study [140], were welding energy = 255 J – 275 J, vibration amplitude = 50 μm peak-to-peak, and normal force = 1.75 kN. Extensive optimization of USW and the effect of interlayer material on subsequent RSW were not attempted in the present study.

To understand how much the microstructure and mechanical properties of the primary joint was affected by the weld quality of the intermediate joint, the intermediate joints were produced with varying welding energy, i.e. 50 J, 150 J and 255J – 275J.

5.2.1.4 ***Resistance spot welding of Al to the intermediate joint***

The 1-mm-thick Al sheet was resistance spot welded onto the Al insert side of the steel in a single phase 60 Hz alternate current (AC) resistance spot welder. The welding parameters were listed as follows: electrode force of 3.56 kN, and welding time of 5 cycles. A short welding time was used to reduce IMCs thickness and electrode wear due to alloying between aluminum alloy and copper electrode. The electrode on Al side was dome-shaped FB25Z13 with 6 mm face diameter. Z-Trode (CuZr electrode) made by Luvata possesses a high electrical conductivity of at least 85% IACS (the International Annealed Copper Standard) and a minimum hardness of 65 HRB at ambient temperature. The electrode on steel side was flat electrode with a surface diameter of 15.875 mm. 4

samples were welded at each condition, of which three welds were used for lap-shear tensile testing and one for microstructure characterization. For comparison, conventional resistance spot welding of aluminum alloy to steel without interlayer was done and the mechanical behavior of the samples were compared with that welded by U+RSW.

5.2.1.5 ***Bond quality characterization***

The welded samples for interfacial microstructure characterization were cross-sectioned through the weld center perpendicular to the weld surface. The cross sections of the spot welds were cold mounted with epoxy to prevent aging of aluminum alloys during hot mounting. Then the samples were ground till 1200 grade sand paper, polished with 3 μm and 1 μm diamond paste, and finished with a final vibratory polish using 0.05 μm colloidal silica for 1 hour. The IMCs at Al/steel interface and fracture surface were analyzed by Scanning Electron Microscope (SEM) with Energy Dispersion Spectroscopy (EDS). Then, the cross-sections of the dissimilar welds were chemically etched with Keller's reagent (2ml HF (48%) + 3ml HCl + 5ml HNO_3 + 190ml H_2O) for Al alloy and 2% Nital for 1008 steel. The nugget sizes were observed by Optical Microscope (OM). The mechanical properties of the spot welds were tested by lap shear tensile testing and the geometry of the test specimens was shown in Figure 5.2. Quasi-static lap-shear tensile testing was performed using an MTS 810 tensile testing machine with a displacement rate of 1 mm/min. The peak load was determined by the average of three samples per welding condition. The fracture energy of the spot-welded joints was calculated based on the load-displacement curve (area under the load-displacement curve till peak strength).

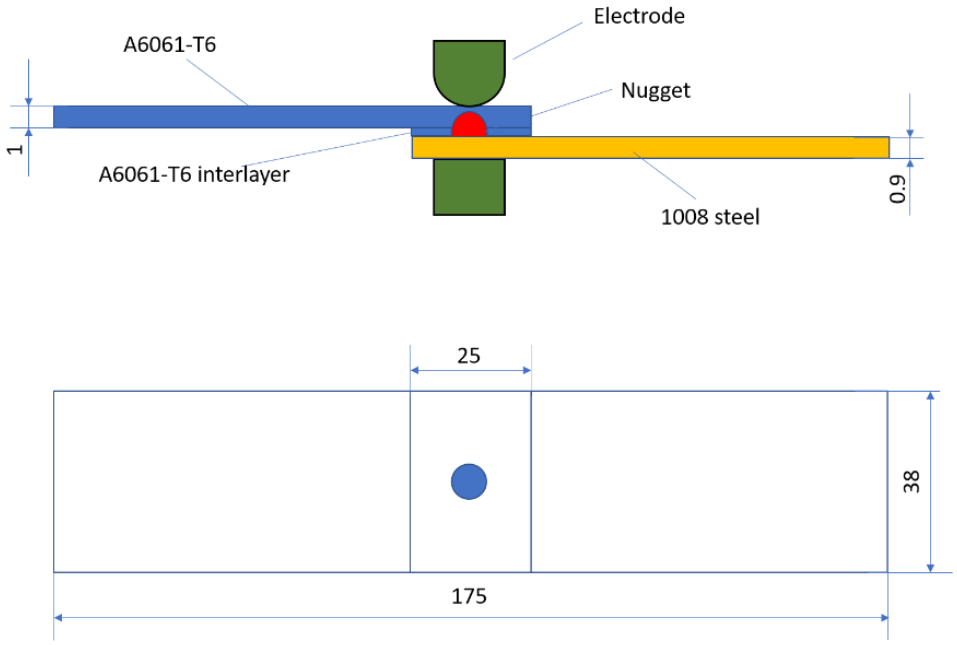

Figure 5.2 Sample geometry for lap-shear tensile testing (mm)

5.2.2 Microstructure and mechanical properties of the intermediate joint

Figure 5.3 shows the cross-sectional microstructure of the intermediate joint created by ultrasonic spot welding of aluminum alloy 6061 insert to cold rolled 1008 steel. Due to the low welding energy/short welding time in USW, the IMCs formed at Al/steel interface was too thin to be observed using SEM. In the literature, Xu et al. measured the IMC layer using transmission electron microscope (TEM) for ultrasonic spot welded 1-mm-thick AA6111 to DC04 steel at welding time of 0.3s. It was found only less than 200 nm-thick IMCs in the form of discontinuous islands at Al/steel interface; the IMCs were further identified as Fe_2Al_5 [141].

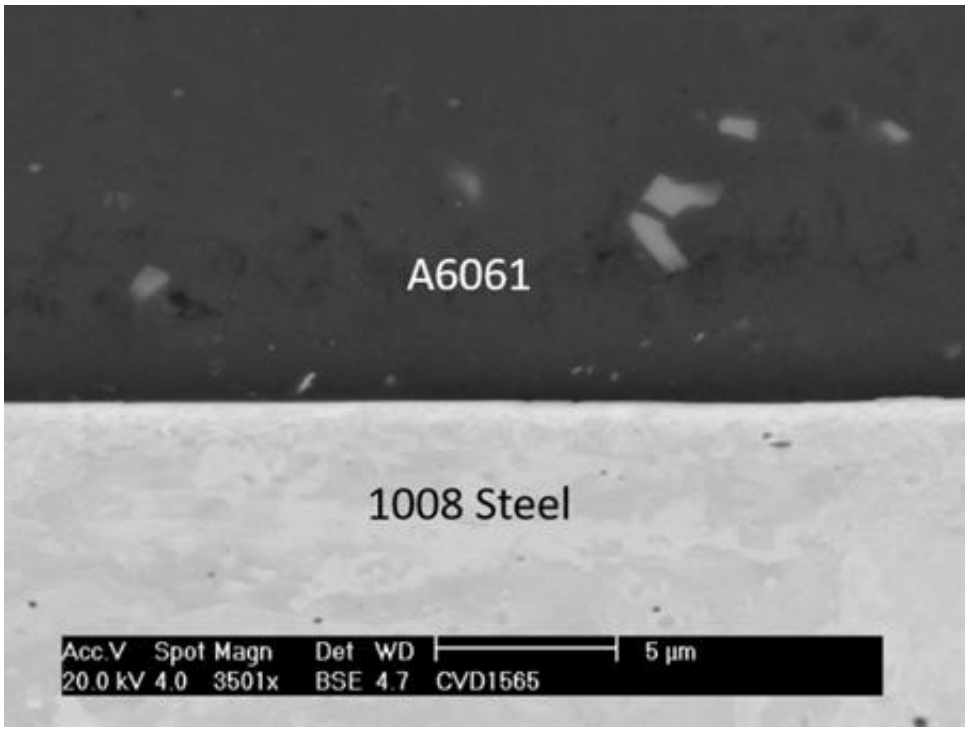

Figure 5.3 Cross-sectional microstructure of the intermediate joint by ultrasonic spot welding of 6061 aluminum alloy with 1008 steel (welding parameters: vibration amplitude = 50 µm, normal force = 1.75 kN, and welding energy of 255 J)

The load-displacement curves for ultrasonic spot welds are plotted in Figure 5.4. At ultrasonic energy of 50 J, there was no metallurgical bond formed at insert/steel interface, which showed a higher threshold energy for bond initiation compared to 0.4 mm thick Al/Al ultrasonic spot welds [140]. The reason could be that a thicker bottom sheet of cold-rolled 1008 steel was a better heat sink. Thus, higher ultrasonic energy was required for asperity softening and local weld formation. When the energy increased to 150 J, an interfacial fracture occurred for the intermediate joint.

A nugget pull-out failure mode was obtained with ultrasonic energy around 255J – 275J, during which a high peak load of 1.4 kN to 1.6 kN can be obtained. The peak load

of the intermediate joint was approximately 1.6 kN, comparable to that of ultrasonic spot welded 0.4-mm-thick Al/Al joint [140]. It was deemed that the intermediate joint welded with this energy of 255-275J had a metallurgical bond between Al interlayer and steel that was sufficiently strong for subsequent RSW.

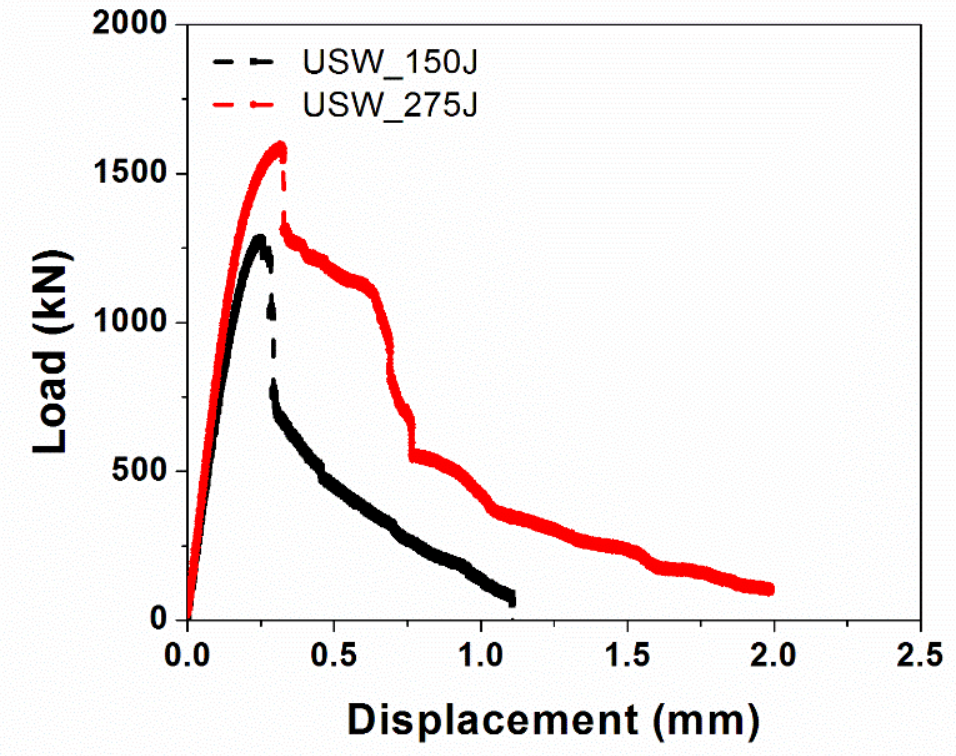

Figure 5.4 Load-displacement curves for intermediate joint welded by ultrasonic spot welding of 0.4 mm-thick AA6061 with 0.9 mm-thick uncoated low carbon steel AISI 1008

5.2.3 Microstructure of U+RSW welds

The cross-sectional macrostructure of direct RSW joined versus U+RSW joined AA6061 to 1008 steel were shown in Figure 5.5. As observed in Figure 5.5 (a), in direct resistance spot welding of Al to steel, the weld is essentially formed via a welding-

brazing process as illustrated in [14] . The interface temperature at the center of the Al/steel interface can be approximately 1000 ^{o}C which is higher than the melting temperature of aluminum alloy but lower than that of steel [65]. Liquid aluminum wets and spreads on the solid steel surface, creating a special brazed joint.

In U+RSW welds, similar macrostructure can be observed. A nugget formed on aluminum alloy side, joining the 0.4 mm-thick aluminum alloy insert with 1 mm-thick aluminum sheet. Moreover, a fusion zone/heat affected zone forms on steel side. These features were commonly observed in Al/steel resistance spot welding with an insert [14][16]. No apparent interface can be observed between aluminum sheet and the insert in fusion zone which indicated complete melting of the insert and the aluminum sheet on top of the intermediate joint. The nugget formation on aluminum alloy side was thought to be caused by Joule heating generated on steel side which in turn was conducted into the Al side. The indentation for direct resistance spot welds was 0.231 mm, which was about 0.1 mm larger than the one with U+RSW at the welding current of about 13 kA. The reason is that expulsion already took place at Al/steel interface in direct resistance spot welding at this welding current.

At welding current of 13.3 kA, the penetration of nugget into 1 mm-thick aluminum alloy was just 3% but it increased to 86% with increasing current to 16.1 kA. The nugget diameter at both Al/insert and insert/steel interface increased with increasing welding current, as shown in Figure 5.6. The minimum nugget size in AWS standard is $4\sqrt{t}$, which should be 4 mm at Al/insert. However, nugget pull-out failure mode occurred

when the nugget size was above 5 mm at Al/insert interface and 6 mm at insert/steel interface, which was about $5\sqrt{t}$. No welding defects was observed within the aluminum weld nugget or at insert/steel interface at low welding current. However, at high welding current of 16.1 kA, shrinkage voids with irregular shape formed at insert/steel interface. It was noted that such voids were commonly observed on Al/Al and steel/steel resistance spot welds. This could be caused by high current density generated with a small electrode diameter at high welding current on aluminum alloy side.

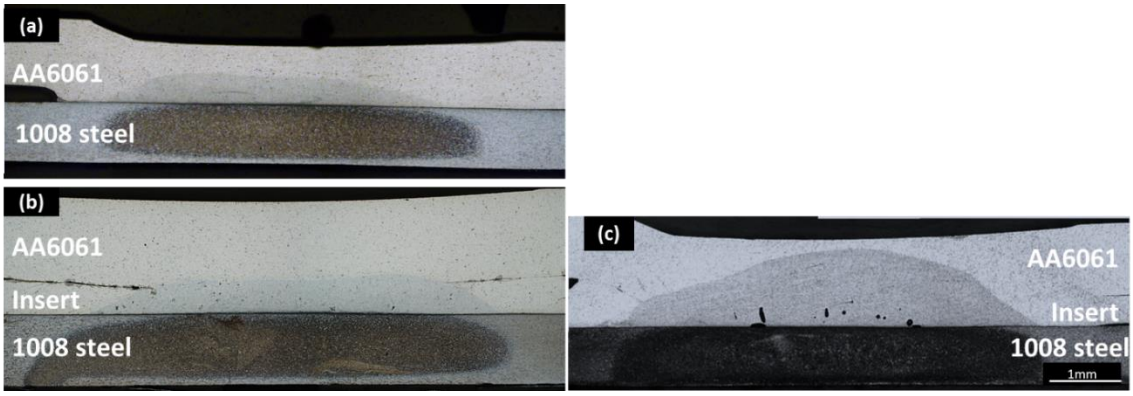

Figure 5.5 Cross-sectional macrostructure of dissimilar metal joints of aluminum alloy 6061 to 1008 steel by (a) direct RSW (13 kA – 5 cycles – 3.56 kN), and (b) U+RSW low current (13.3 kA – 5 cycles – 3.56 kN electrode force), and (c) U+RSW high current (16.1 kA - 5 cycles – 3.56 kN electrode force)

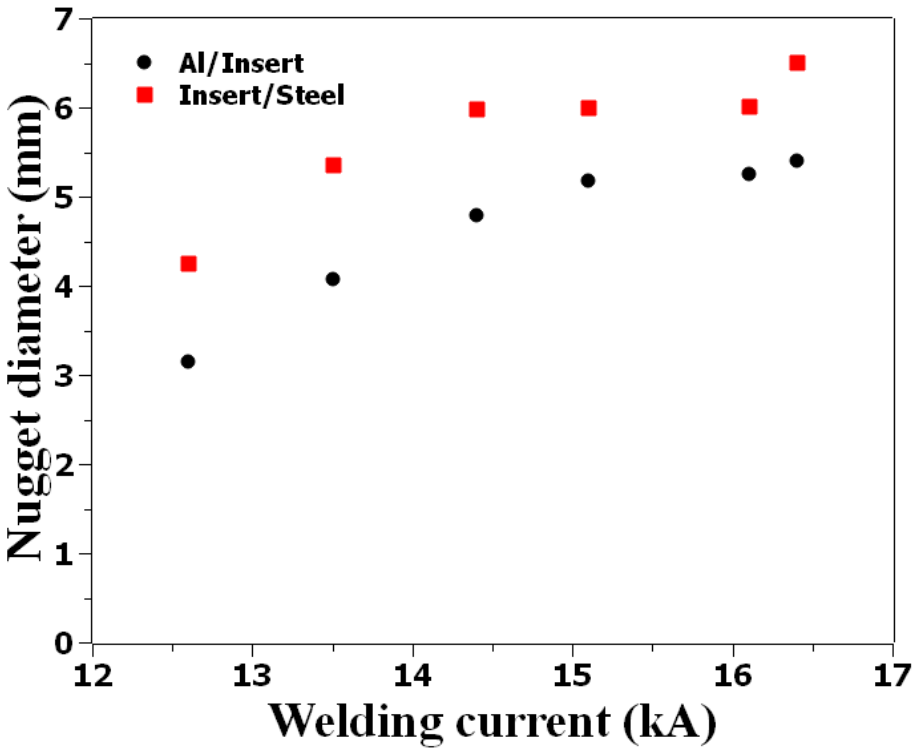

Figure 5.6 Effect of welding current on nugget diameter with welding time of 5 cycles and electrode force of 3.56 kN

Fe-Al intermetallics formed at insert/steel interface was due to the limited solubility of iron in aluminum. Figure 5.7 shows the morphology of IMCs across the insert/steel interface and element distribution across the interface at the center of the welded joints with the optimum welding condition (16.5 kA-5cycles-3.56 kN electrode force). A 1.25 µm-thick IMCs formed at the weld center with a flat interface between IMCs and steel side, while some needled-like shaped IMCs grew into Al sheet. This morphology was similar to what has been observed in direct resistance spot welding of Al to steel. However, the thickness of IMCs welded at 16.5 kA is still 1.75 µm thinner than that formed in the direct resistance spot welded Al/steel with welding current of 9 kA and

relatively short welding time of 100 ms [102]. Actually, the thickness of IMCs created at the insert/steel interface by U+RSW method was similar to that created by ultrasonic spot welded AA 6111/uncoated low carbon steel DC04 with welding time of 1.5 s [141].

The Fe and Al distribution across insert/steel interface is shown in Figure 5.7. It indicated that the formation of the IMCs was mainly controlled by inter-diffusion of Fe and Al across the interface of liquid aluminum alloy and solid steel [102]. Based on EDS analysis, the IMCs formed at insert/steel interface are Fe_2Al_5 and $FeAl_3$. Figure 5.8 shows the thickness distribution of IMCs across the insert/steel interface. The maximum thickness of IMCs was found at the center of the weld due to the highest interfacial temperature and longer interaction time at elevated temperature. As the location was approaching the periphery of the weld, the thickness of IMCs reduced gradually.

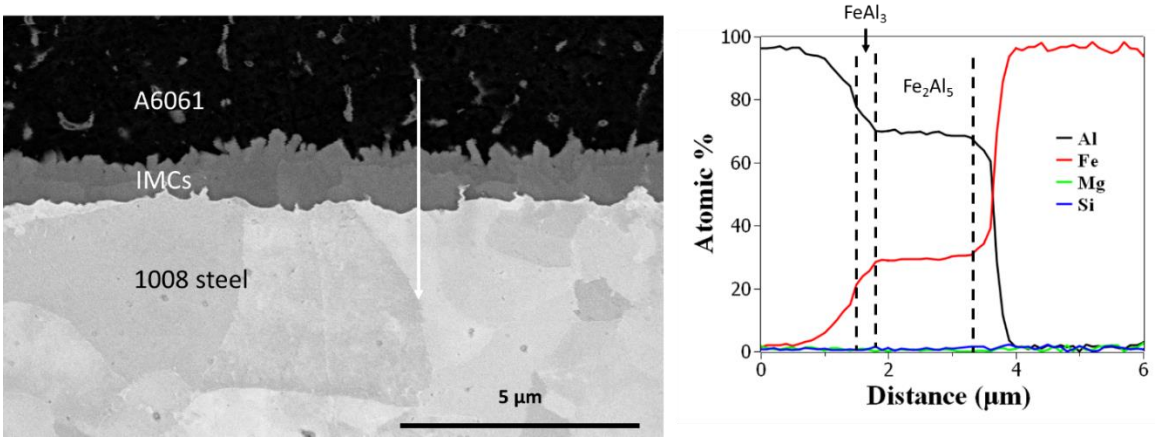

Figure 5.7 IMC morphology at the center of the weld and EDX line scan data at insert/steel interface (16.5 kA-5 cycles - 3.56 kN)

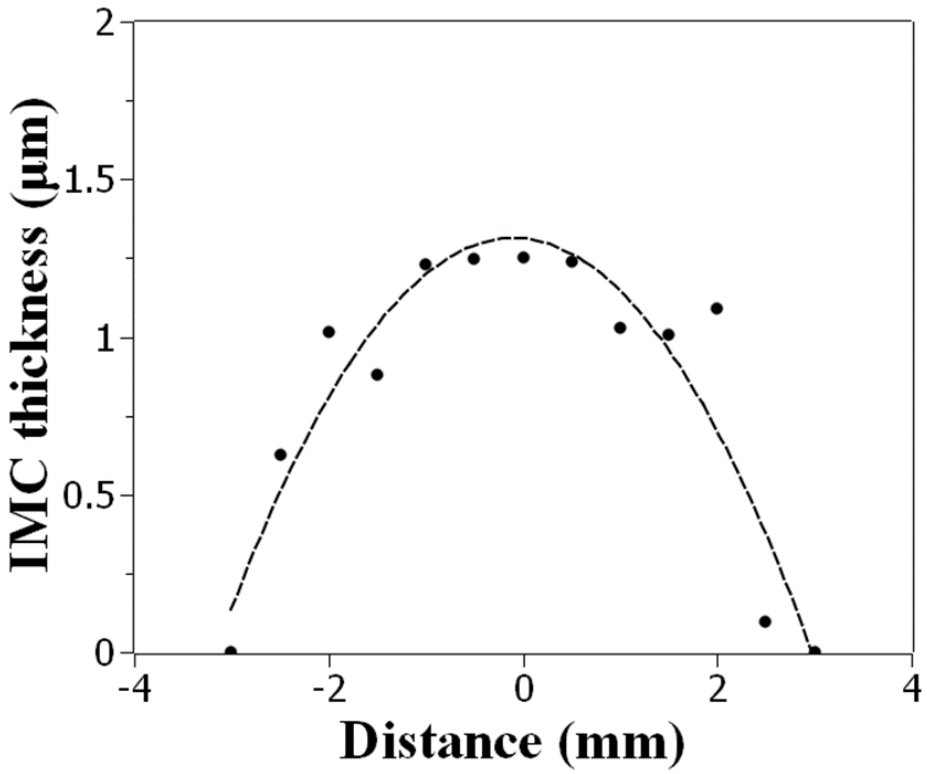

Figure 5.8 IMCs thickness across the insert/steel interface as a function of distance to the weld center (16.5 kA-5 cycles - 3.56 kN)

5.2.4 Bond formation in U+RSW

As discussed previously, RSW was used to create the primary joint in U+RSW. To better understand the bond formation for the primary joint, a 3D, fully coupled thermo-electro-mechanical model was created based on commercially available FEA software Abaqus. A detailed description of the RSW process model is provided in Chapters 3 and 4 as well as in the literature [134]. Some salient features are summarized in the following.

RSW of two dissimilar metal joints was modeled: one for direct RSW of Al to steel without any insert, and the other for RSW of Al/steel with 0.4 mm thick AA6061 as an

insert. For both models, the electrical contact resistance (ECR) at Al/steel interface was treated as the ECR of electrode/steel interface [68] by multiplying a correction factor to take into account of the effect of aluminum oxide layer. The detailed methodology was described by Wan et al. in their numerical simulation of resistance spot welding of Al to steel [66]. In U+RSW, due to the metallurgical bonding at insert/steel interface, the electrical contact resistance (ECR) at insert/steel interface was set to be a half of the ECR reported in [68]. It is noted that the intermediate joint created by USW (e.g., surface indents on the Al insert) was not considered for simplicity.

Figure 5.9 shows the comparison of nugget sizes predicted by numerical simulation and measured experimentally for direct resistance spot welding of aluminum alloy to steel. The good consistence of predicted nugget size with experimental results showed that the model can accurately capture the interaction between electrode/sheet and sheet/sheet interface. Figure 5.10 (a) shows the temperature profiles at the center of aluminum/steel interface of the welded joints during direct resistance spot welding versus U+RSW welding. The interfacial temperature at Al/steel interface increased rapidly in the initial 20 ms and the heating rate reduced when the temperature was above the solidus temperature of aluminum alloy 6061 (582 ^{o}C) due to the latent heat of fusion. The temperature dropped rapidly when the current was turned off due to high thermal conductivity of aluminum alloy. The peak temperature at Al/steel interface of the weld by direct resistance spot welding was about 844 ^{o}C, which was approximately 100 ^{o}C higher than that at insert/steel interface joining by U+RSW. Such lower temperature at Al/steel

interface and less amount of time at elevated temperature is expected to be a key factor for forming the thinner IMCs during U+RSW.

To further illustrate the importance of metallurgical bond between insert and steel, a third model with 0.4-mm-thick Al inert was also created. Unlike the halved ECR in U+RSW, the ECR for the insert/steel interface had the full value as that in direct RSW. As shown in Figure 5.10 (a), the temperature profile at insert/steel interface was similar to that at Al/steel interface during direct resistance spot welding. Therefore, early expulsion was still likely to take place at insert/steel interface when Al/steel was resistance spot welded with an insert of Al6061.

Figure 5.10 (b) showed the temperature profiles at different locations along insert/steel interface for U+RSW weld. The temperature profiles at weld center and 1 mm away from the weld center were similar due to rapid heat dissipation of aluminum alloy. At location of 2.4 mm away from the weld center, the peak temperature was less than the melting temperature of aluminum which was expected to lead to the formation of thinner/discontinuous IMCs. Therefore, the morphology and thickness distribution of IMCs shown in Figure 5.7 and Figure 5.8 were significantly affected by the thermal profiles along Al/steel interface.

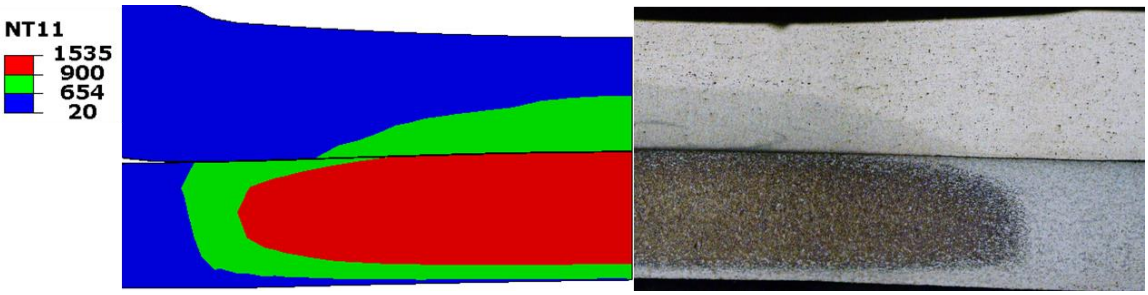

Figure 5.9 Nugget of Al-Steel RSW joint at welding current of 13 kA: simulation (left) versus experiment (right). Temperatures are in °C. 654 is the liquidus temperature of Al, and 1535 is that of the steel

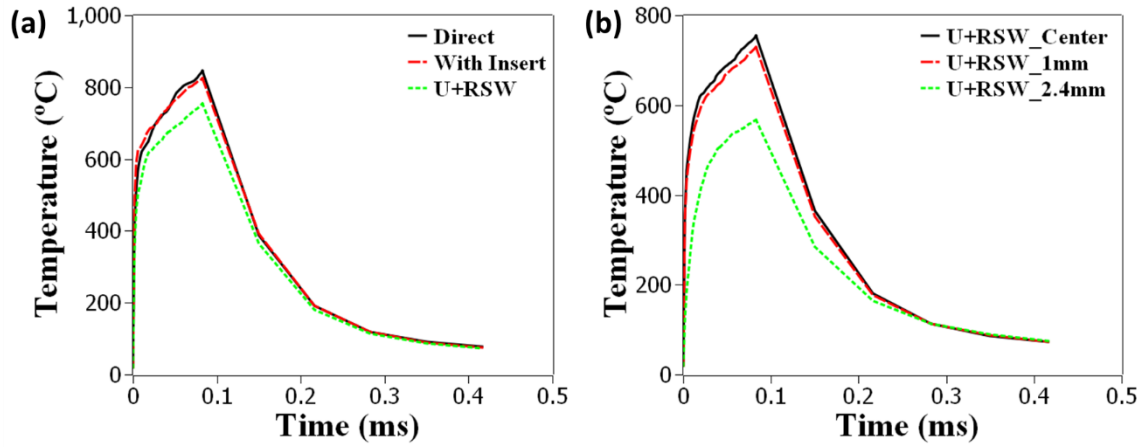

Figure 5.10 Temperature profile (a) at Al/steel interface during direct RSW and U+RSW (welding current: 13 kA, and welding time: 5 cycles), and (b) at center of the weld, 1 mm and 2.5 mm away from the weld center for U+RSW weld

5.2.5 Mechanical properties of U+RSW joints

Figure 5.11 shows the tensile shear strength of Al/steel joints welded by U+RSW method, where the data for direct resistance spot welding without interlayer was superimposed for comparison. It was noted that direct resistance spot welding of aluminum alloy to steel was only conducted at low welding currents since severe

expulsion occurred at welding current above 13.6 kA with the electrode geometry utilized in the feasibility study. Moreover, mild expulsion at Al/steel interface was observed at low welding current of 12.3 kA in direct resistance spot welding, which was not observed until 16.5 kA in U+RSW. Thus, a larger weldable current range and better weldability can be expected for Al/steel welding using U+RSW method.

As shown in Figure 5.11, the tensile shear strength and fracture energy were significantly improved for U+RSW welded AA6061 to 1008 steel compared to direct resistance spot welding without an insert. The peak load of U+RSW joints was 0.76 kN higher than resistance spot weld joints at the welding current of 13.6 kA. At high welding current of 16.5 kN, a peak load of 3.2 kN with button pull-out was obtained for the U+RSW joint, which was comparable to that of resistance spot welded 1 mm-thick 6XXX series aluminum alloy 6082-T6 [142]. For button pull-out fracture mode, the strength and joint efficiency of the spot welds can be calculated as follows:

$$\text{strength} = \frac{3200}{2\pi \times 2.7 \times 1} = 188.6\ Mpa$$

$$\text{joint efficiency} = \frac{188.6}{340} = 55\%$$

which is similar to the joint efficiency in [110].

For direct resistance spot welding of aluminum alloy to steel, interfacial fracture was observed with low fracture energy of less than 0.2 J. In Al/steel joints by U+RSW method, fracture energy increased with welding current with a peak value of

approximately 1 J at welding current of 16.5 kA. The high peak load and fracture energy for Al/steel joints using U+RSW method was due to a combination of factors including (1) large nugget size, (2) thin IMCs (< 2 μm) formed using U+RSW method, and (3) no expulsion taking place at Al/steel interface.

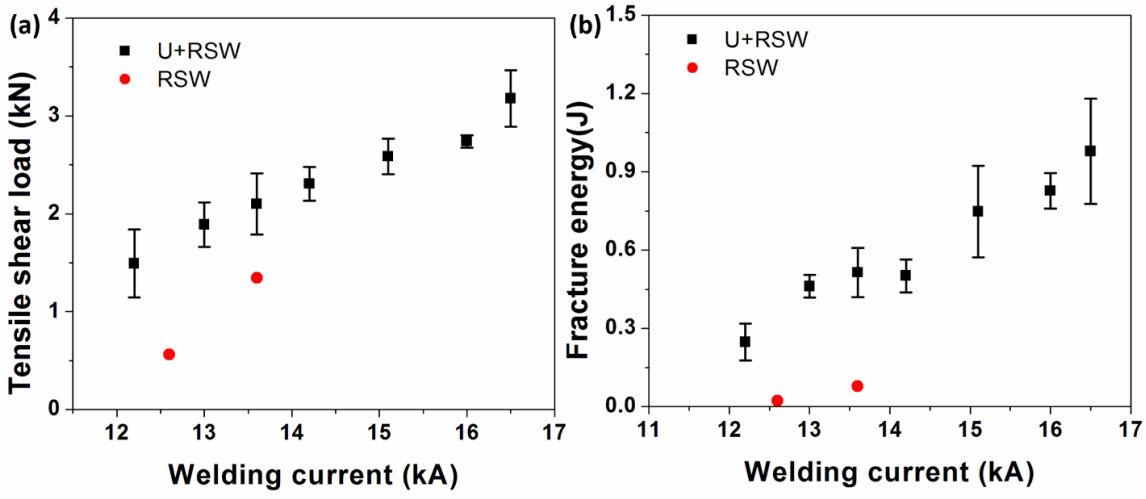

Figure 5.11 Effect of welding current on tensile shear strength and fracture energy of welded joints of aluminum alloy 6061 and AISI 1008 steel

5.2.6 Fracture mechanism in U+RSW

Interfacial fracture and button pull-out failure mode are two common fracture modes observed in resistance spot welding of aluminum alloy to steel without insert [11]. However, more complicated fracture modes were observed in U+RSW Al/steel joints with an intermediate joint created by ultrasonic spot welding of thin AA6061 to 1008 steel. Based on the fracture modes reported in resistance spot welded aluminum to steel with aluminum cladded steel as an insert [14], the fracture modes in U+RSW welded Al/steel can be divided into four categories, which are schematically shown in Figure

5.12. These four types of fracture modes are shear fracture at Al/insert interface (Type 1), partial/full nugget pull-out from insert (Type 2), button pull-out from Al sheet (Type 3), and interfacial fracture through insert/steel interface (Type 4). The optical micrographs of representative fracture surface of four types of failure modes are shown in Figure 5.13. Type 1 and 3 failure modes were similar to interfacial and button pull-out failure modes in resistance spot welding of aluminum alloys, respectively. Type 2 and 4 failure modes were unique to Al/steel welded joints with crack propagation through IMC layer.

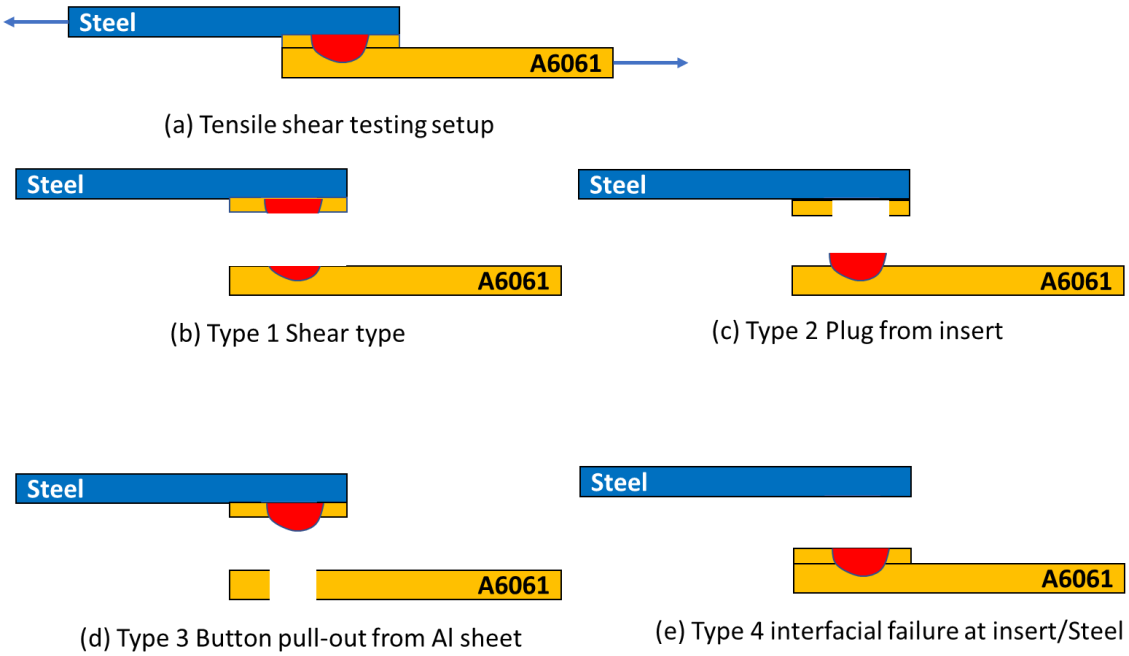

Figure 5.12 Fracture modes in lap shear tensile testing of U+RSW welded Al/steel joints

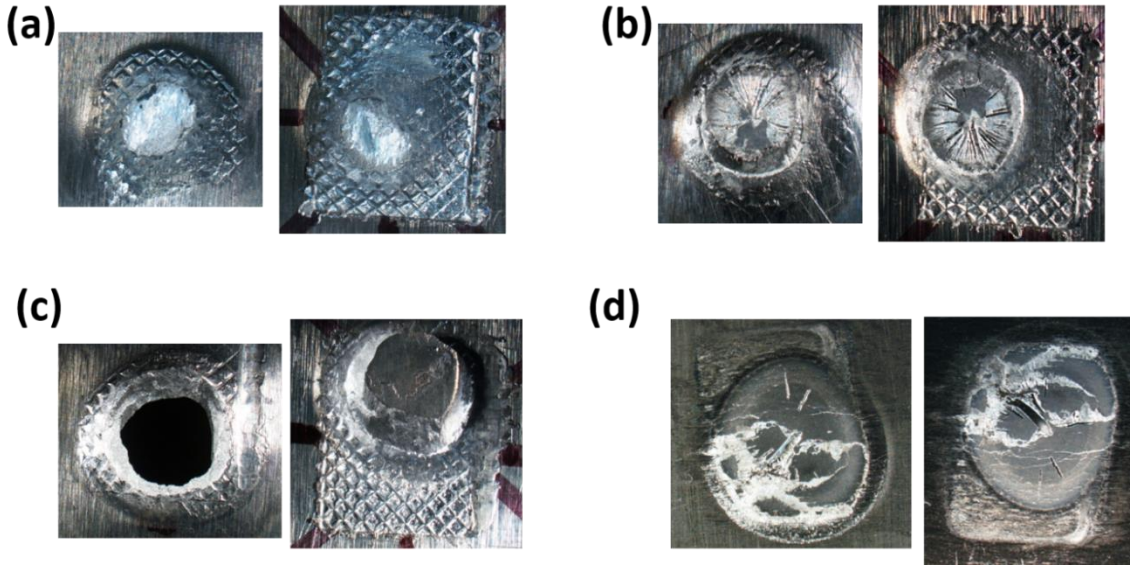

Figure 5.13 Representative fracture surface for four types of fracture modes at aluminum side (left) and steel side (right): (a) Type 1 (shear fracture at Al/insert interface; (b) Type 2 (partial/full nugget pull-out from insert); (c) Type 3 (button pull-out from Al sheet); and (d) Type 4 (interfacial fracture through insert/steel interface)

Among the four types of failure modes in U+RSW welded samples during lap shear tensile testing, Type I failure mode was similar to the interfacial failure mode that has been commonly observed in resistance spot welding of aluminum alloy 6061 [143], in which crack initiated and propagated through Al/Al interface. Thus, this failure mode was not characterized further.

Figure 5.14 shows the SEM images of the fracture surface for Type 2 failure mode. Mixed features can be observed with dimples at region 1 and brittle fracture at region 2. EDX results showed that region 1 was aluminum and region 2 was Fe_2Al_5. Zhang et al. [102] explained that mixed fracture feature could be caused by aluminum nugget bulging into steel side, which relieved stresses. However, there was no obvious nugget bulging

observed at Al/steel interface in this study. The possible reason for mixed failure mode was that the IMCs at the periphery of the nugget was thin and discontinuous, which reduced its detrimental effect on mechanical properties. The crack initiated at Al/insert interface may deviate in through-thickness direction of the insert at the early stage of fracture. Therefore, ductile features can be observed with aluminum dimples left on the fracture surface at steel side. However, the crack may propagate through IMCs at regions near to the weld center due to thicker IMCs formed.

Figure 5.15 shows the fracture surface of Type 3 button pull-out failure mode. Deep dimples can be observed at region 1, indicating ductile failure. Figure 5.16 shows the fracture surface of Type 4 failure mode, which is commonly observed in resistance spot welding of Al to steel [12]. Crack initiated and propagated through Al insert/steel interface. Similar to Type 2 failure mode, mixed features can be observed with dimples from aluminum insert strongly bonded to steel at region 1 and brittle fracture at region 2.

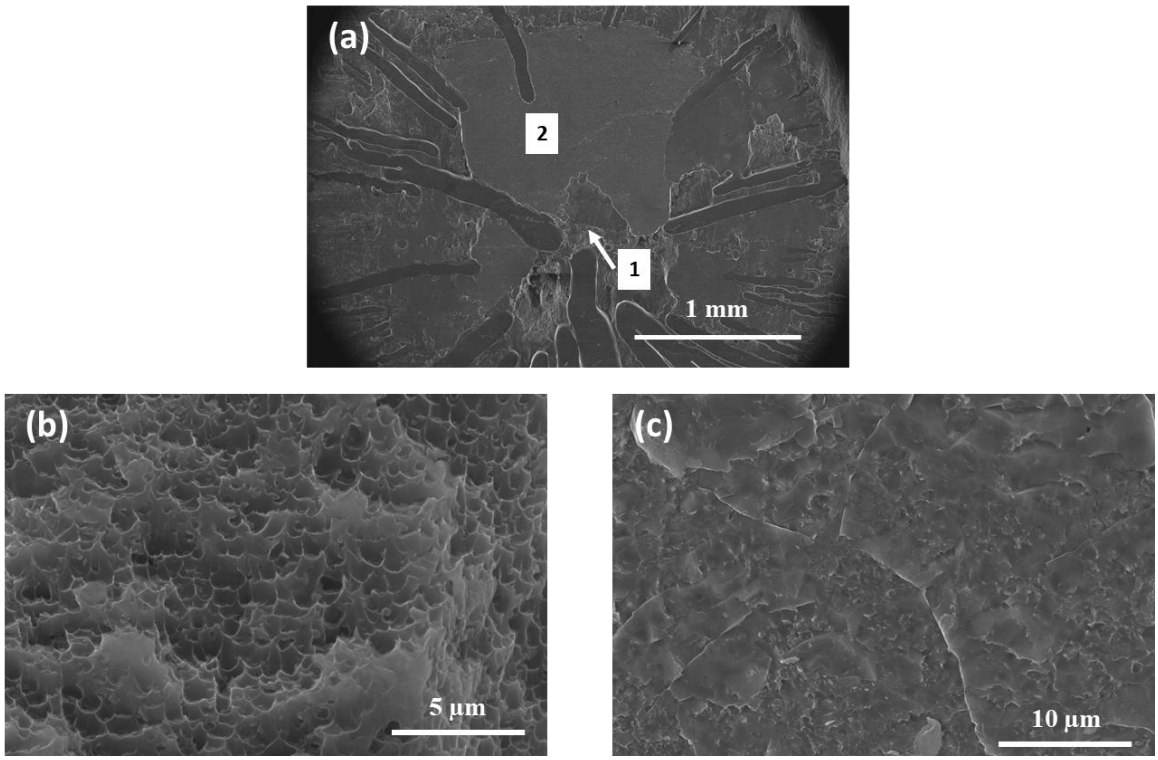

Figure 5.14 SEM images of fracture surface on steel side for Type 2 (partial/full nugget pull-out from insert): (a) Overall view, (b) Zoomed in morphology of Region 1, and (c) Zoomed in morphology of Region 2

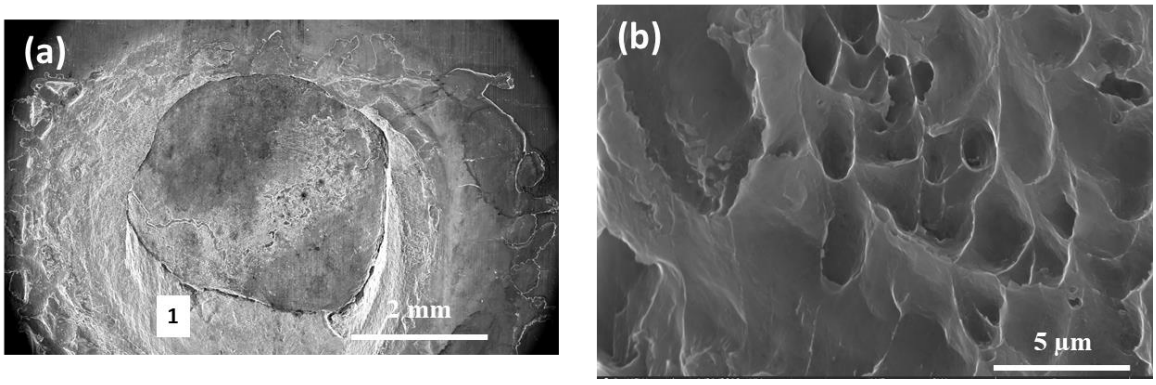

Figure 5.15 SEM images of fracture surface on steel side for Type 3 (nugget pull-out from Al sheet): (a) Overall view, and (b) Zoomed in morphology of Region 1

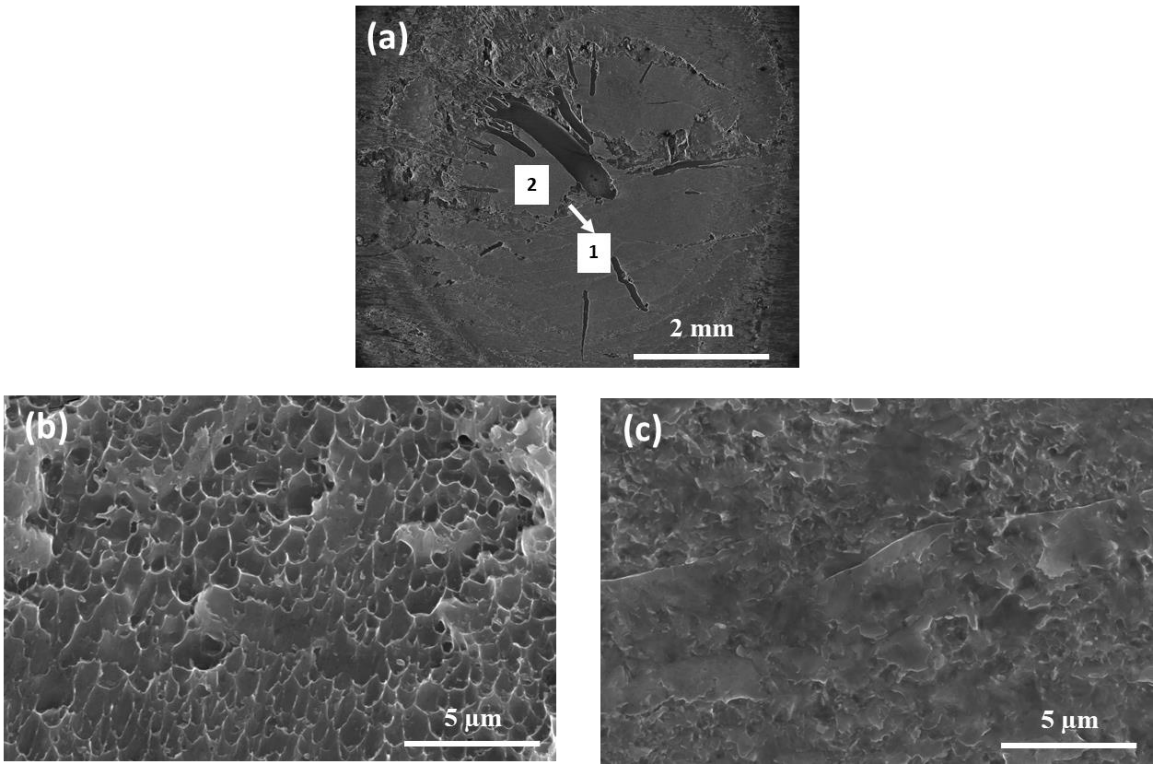

Figure 5.16 SEM images of fracture surface on steel side for Type 4 (interfacial fracture): (a) Overall view, (b) Zoomed in morphology of Region 1, and (c) Zoomed in morphology of Region 2

Fracture modes were significantly affected by welding current as shown in Figure 5.17. As welding current was less than 13.6 kA, due to the small nugget size at Al/insert interface and limited penetration into Al sheet, shear fracture took place at Al/insert interfaces with low tensile shear strength and fracture energy. Nugget diameter at Al/insert and insert/steel interfaces increased with increasing welding current. As the nugget size at Al/insert interface was larger than the critical value of 4 mm, through-thickness crack formed in the insert and propagated through insert/steel interface. Thus, fracture mode transferred to partial/full nugget pull-out from insert as welding current was between 13.6 kA and 15.2 kA. As welding current was higher than 15.2 kA,

partial/full nugget pull-out from insert (Type 2), nugget pull-out from Al sheet (Type 3) and interfacial fracture across Al/steel interface (Type 4) were observed, although Type 4 fracture seldom happened in the weld joint by U+RSW method. Thus, nugget size at Al/insert and insert/steel interface and the IMCs thickness were the two key factors that determined the failure modes in U+RSW spot welds. Increasing nugget diameter at two interfaces while keeping the maximum IMCs thickness at the weld center to be less than 2 μm may increase the peak load of the spot welds with the failure mode of button pull-out from thick Al sheet. Besides these two factors, Zhang et al. [102] and Chen et al. [12] observed steel bulging into aluminum nugget in direct resistance spot welding of aluminum alloy to steel and emphasized the effect of steel bugling height on the lap shear strength and failure mode. However, there was limited steel bulging into aluminum observed in this study. It was possibly that the flat electrode with large surface diameter used on steel side resulted in less heat generation on steel side with rapid heat dissipation through the water-cooled electrode. As another evidence, there was negligible indentation on the bottom surface of 1008 steel even at high welding current of 16.5 kA. This could be one of the possible reasons for mixed failure modes (Type 2, Type 3 and Type 4) observed at high welding current instead of consistent nugget pull-out.

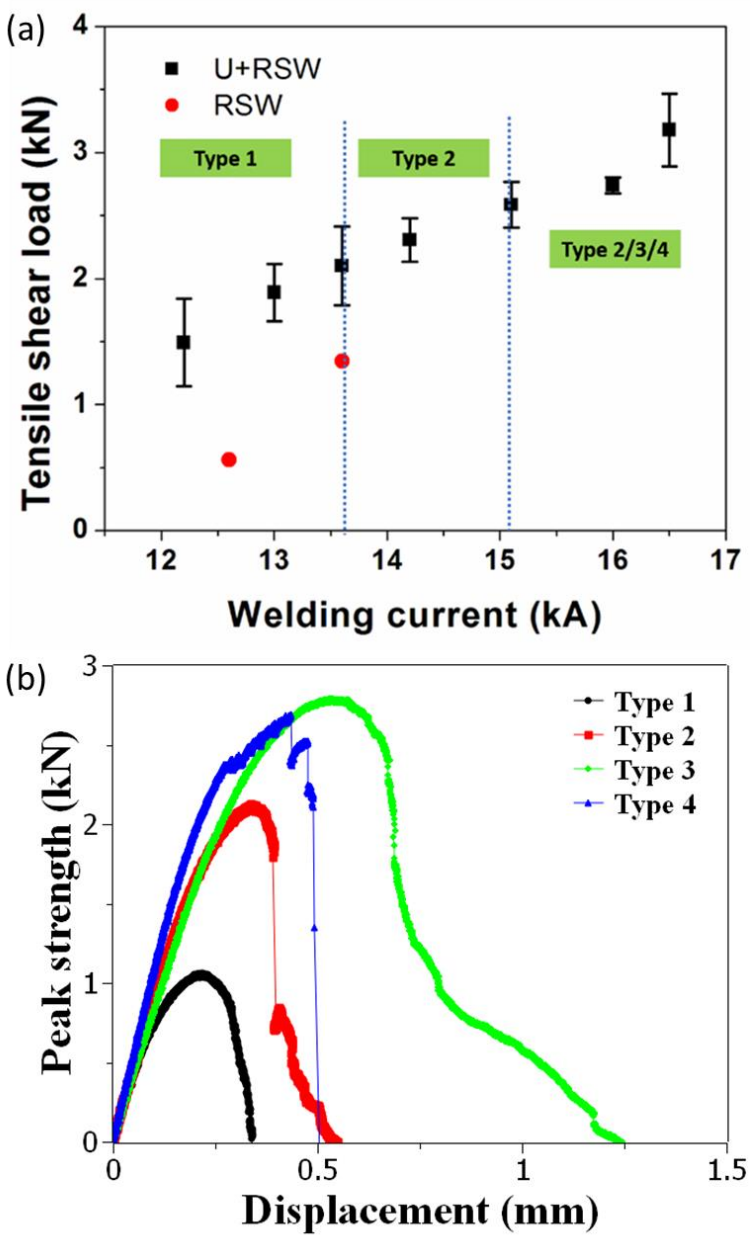

Figure 5.17 (a) Effect of welding current on fracture mode, and (b) typical load-displacement curves for the four types of failure modes in lap shear tensile testing of direct RSW and U+RSW welded AA6061/1008 steel

5.2.7 Effect of intermediate joint on mechanical properties of primary joints

Figure 5.18 shows the effect of the intermediate joint quality on mechanical properties of the primary joint. With low ultrasonic energy of 50 J, the tensile shear strength of the primary joint was approximately 2.5 kN, which is 1 kN lower than the bond strength obtained with ultrasonic energy of 150 J. Moreover, expulsion was observed at insert/steel interface with substantial amount of porosity. On the other hand, when the ultrasonic energy was above 150 J, the effect of ultrasonic energy on primary joint was limited. A nugget pull-out failure mode was observed with a peak load of 3.5 kN. Thus, the formation of metallurgical bond resulted in reduction in contact resistance at insert/steel interface and prevention of early expulsion due to high current density at local regions. The high tolerance of primary joint to the weld quality of the intermediate joint can increase the weldability and consistency of the joints.

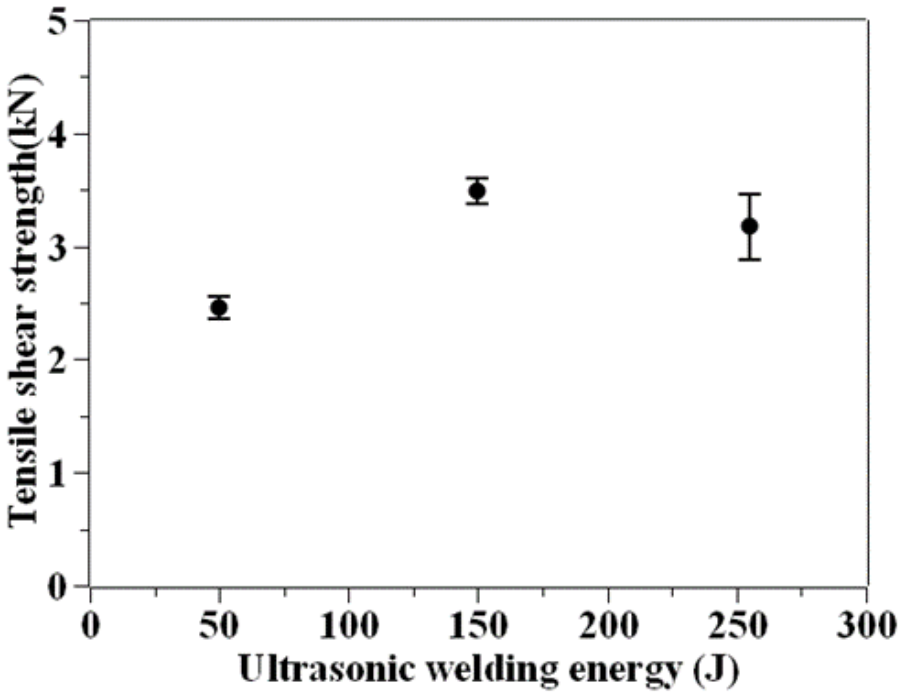

Figure 5.18 Effect of the bond quality of the intermediate joint on tensile shear strength of primary joints in U+RSW spot welded AA6061/1008 steel joints

5.3 Insert material

In the previous section, the feasibility of U+RSW of AA6061 to AISI 1008 steel using 0.4-mm-thick AA6061 insert was successfully demonstrated. Next, the effect of various welding parameters (such as insert material, AC versus DC spot welder, and electrode geometry) were studied.

5.3.1 Experiment

A 0.3-mm-thick AA3003-H14 was used as the insert, which was welded to the 0.9 mm-thick cold rolled 1008 steel by USW to create an intermediate joint. The samples

were grinded with 240 grade sand paper and cleaned by ethanol before welding. For the AA3003 insert, the intermediate joint with the sound weld quality can be obtained with welding energy of 170 J, peak-to-peak vibration amplitude of 40 μm, and normal force of 1.02 kN.

Al to the intermediate joint was then resistance spot welded using both AC and MFDC resistance spot welders. The welding parameters were listed as follows: electrode force of 3.56 kN, and welding time of 83 ms or 200 ms. The electrode on Al side was a F-type electrode. The electrode on steel side was a dome-shaped electrode with surface diameter of 8 mm. 4 samples were welded at each condition, of which three welds were used for lap-shear tensile testing, and one for microstructure characterization.

5.3.2 Effect of AC and DC machine on mechanical properties

Since both AC and MFDC resistance spot welding machines are commonly used in automotive industries, the nugget size and mechanical properties of the U+RSW Al/steel spot welds welded by the two types of machines were compared. Figure 5.19 and Figure 5.20 show the nugget size and peak strength as a function of welding current for AC and MFDC. Nugget size and peak strength increased with increasing welding current for both cases. The nugget size and peak strength were independent of the power source and expulsion occurred only at high welding current of 20 kA-21kA with welding time of 200 ms. To get consistent button pull-out with welding time of 200 ms, the nugget diameter at Al/insert and insert/steel interface should be larger than 6 mm and 7.3 mm respectively.

At the high welding current of 19 kA, the peak strength of the U+RSW welds can be 3.7-4 kN with a consistent button pull-out failure mode.

For button pull-out fracture mode, the strength and joint efficiency of the spot welds produced in AC versus MFDC machines, calculated in the following, were comparable, indicating an insignificant effect of the type of machine used.

For MFDC machine, Al/steel welded with welding current of 19 kA

$$\text{strength} = \frac{3712}{2\pi \times 3.28 \times 1} = 180.1\ Mpa$$

$$\text{joint efficiency} = \frac{180.1}{340} = 53\%$$

For AC machine, Al/steel welded with welding current of 19 kA

$$\text{strength} = \frac{3963}{2\pi \times 3.62 \times 1} = 174.2\ Mpa$$

$$\text{joint efficiency} = \frac{174.2}{340} = 51\%$$

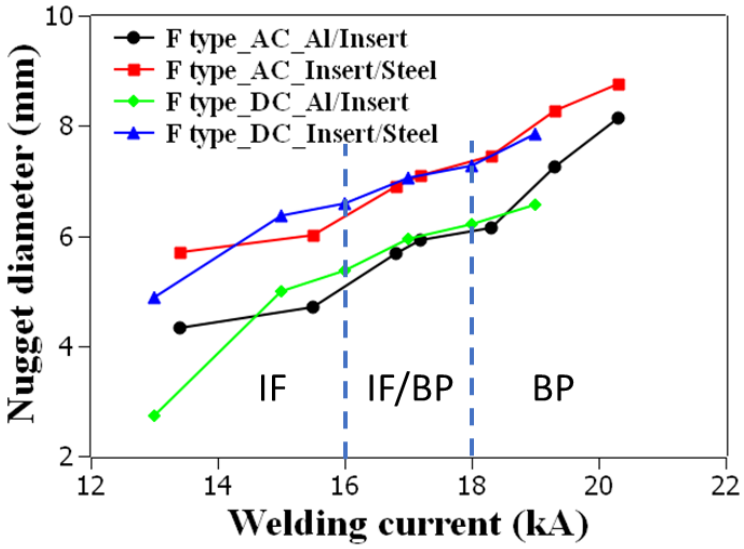

Figure 5.19 Effect of power source (AC/MFDC) on nugget diameter (electrode force: 3.56 kN, and welding time: 200 ms)

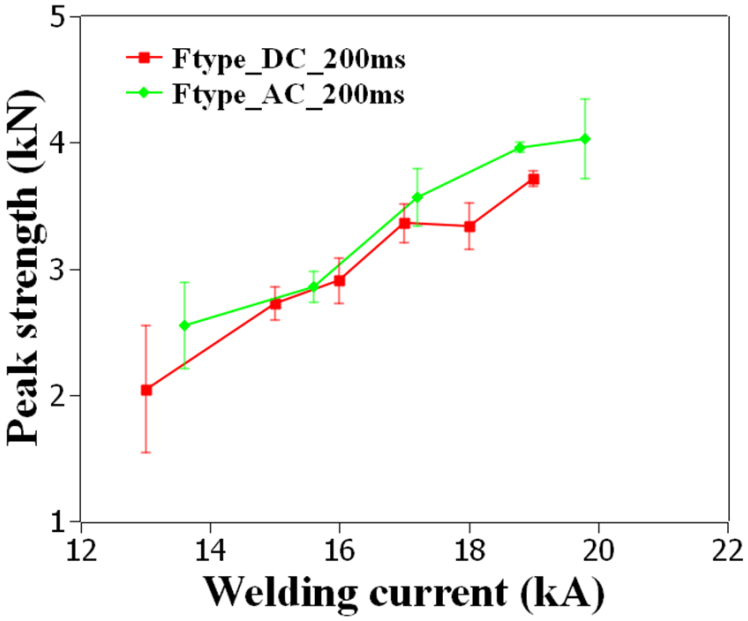

Figure 5.20 Effect of power source (AC/MFDC) on lap-shear strength of U+RSW welds

5.3.3 Effect of the insert on mechanical properties

To study the effect of the insert on the mechanical properties of the final joint, the 0.3 mm-thick AA3003 and 0.4 mm-thick AA6061 were ultrasonic spot welded with the optimum welding parameters which resulted in the highest strength for the intermediate joint. The maximum strength for ultrasonic spot welded AA3003 and AA6061 were approximately 0.561 kN and 1.5 kN respectively. The intermediate joint was resistance spot welded to Al sheet with the electrode force of 3.56 kN, and welding time of 83 ms using MFDC machine. Figure 5.21 shows the peak strength changing with welding current for two different insert materials. It can be seen that the peak strength of the final joints with AA6061 and AA3003 as an insert was comparable. Consistent button pull-out can be obtained with welding current of 19 kA. As welding current increased to 20 kA, expulsion took place at the insert/steel interface when using AA6061 as an insert, and likely resulted in a mixed failure of button pull-out and interfacial fracture. Since there is no obvious advantage in joint strength by using AA6061, and AA3003 had a lower cost over AA6061, the 0.3-mm-thick AA3003 was selected as an insert in the following studies.

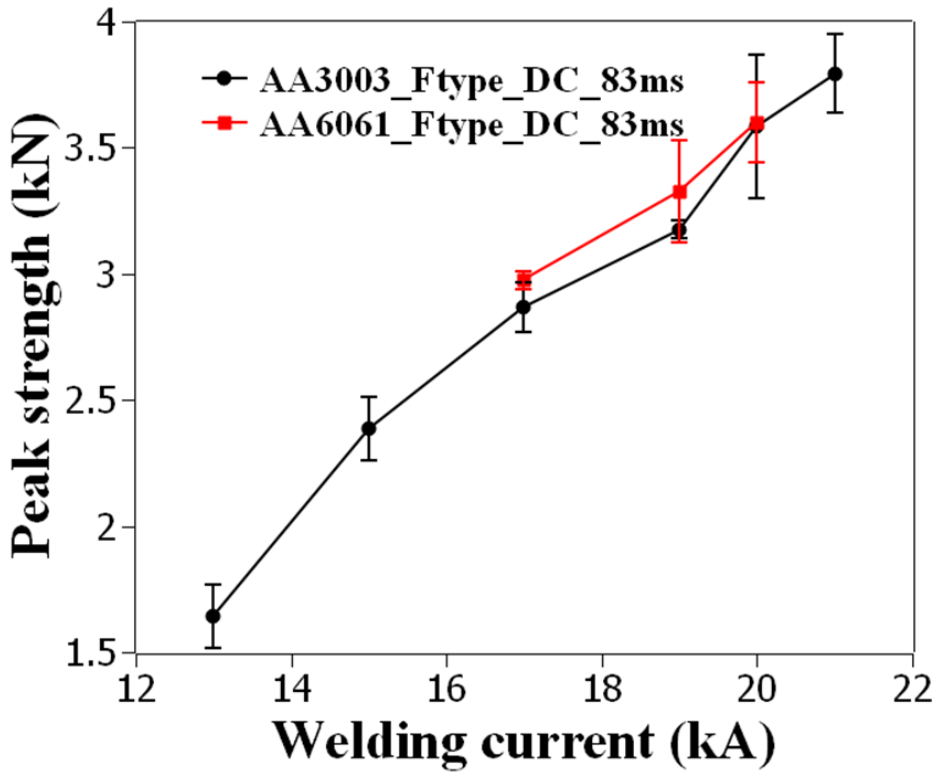

Figure 5.21 Effect of welding insert on the peak strength

5.3.4 Effect of electrode geometry on mechanical properties

Figure 5.22 shows the typical macrostructure of Al/steel weld made by U+RSW using MFDC machine with a dome-shaped electrode on the steel side. In this case, steel bulged into aluminum, and the bulge height increased with increasing welding current, which was expected to increase the strength of the welds by mechanical locking in lap-shear tensile testing according to a literature study [12].

Figure 5.22 Macrostructure of Al/steel welds using U+RSW with a dome-shaped electrode on the steel side (welding current of 19 kA, welding time of 67 ms, and MFDC machine)

Figure 5.23Figure 5.23 shows the effect of welding current on nugget diameter for U+RSW welds joined with the dome-shaped electrodes and AA3003 as an insert in MFDC machine. Nugget diameters at Al/insert and insert/steel interface increased gradually with increasing welding current with both the dome-shaped and F-type electrodes. The dome-shaped electrode tended to result in expulsion when the current was above 17 kA. On the other hand, it is clear that the F-type electrode resulted in higher joint strength. Hence, the F-type electrode is considered to an improved geometry than the dome-shape electrode.

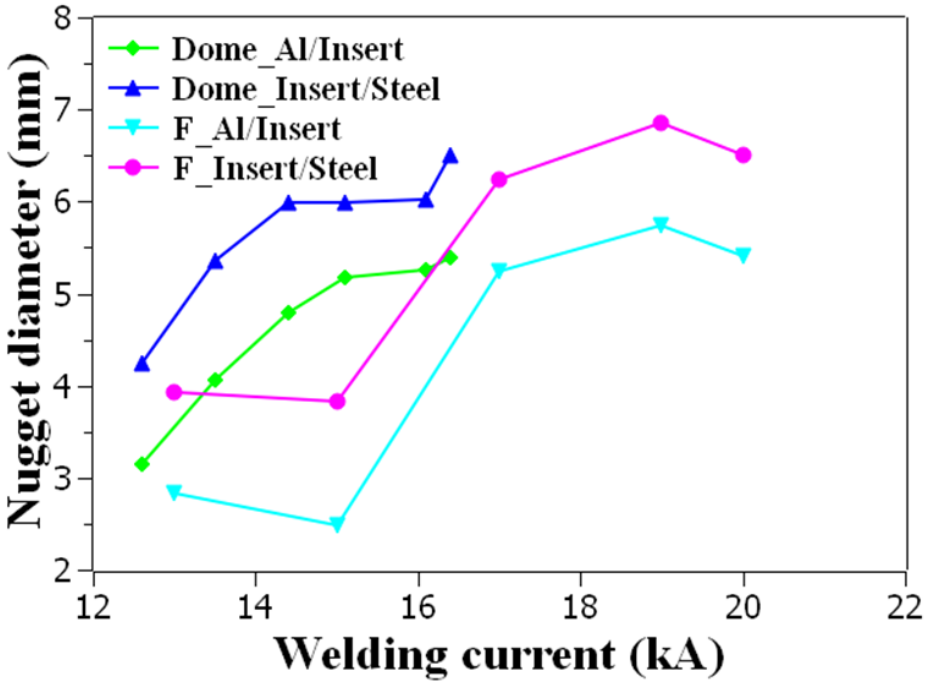

Figure 5.23 Effect of welding current on nugget diameter for the dome-shaped versus flat electrodes

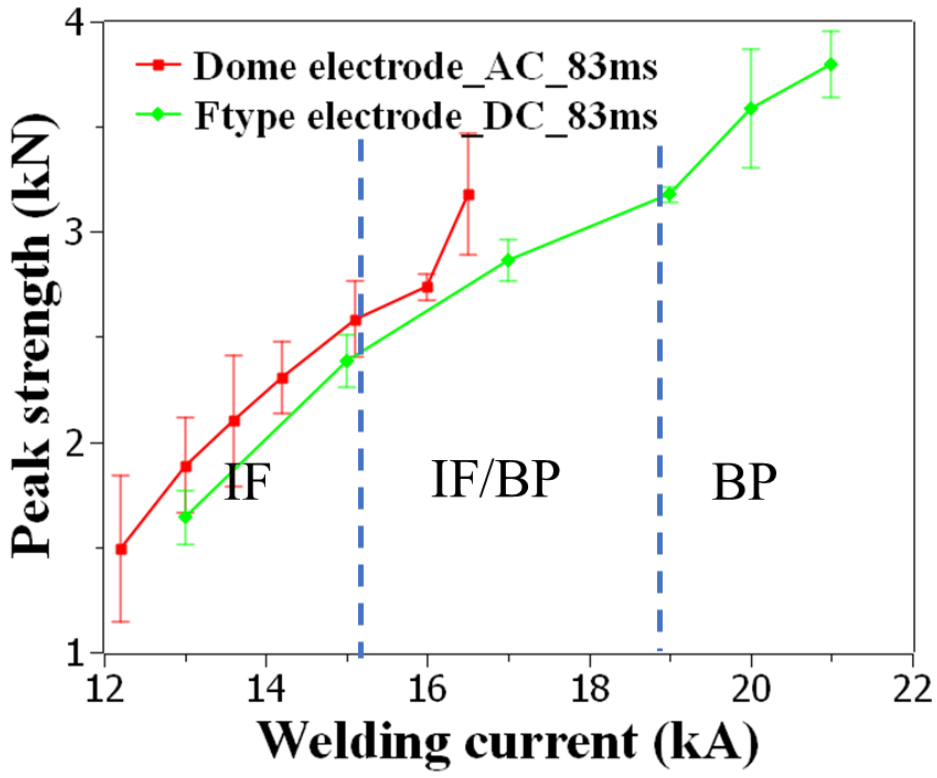

Figure 5.24 Effect of welding current on peak strength and failure modes for dome-shaped versus F-type electrodes

5.3.5 Effect of welding time on mechanical properties

Relatively long welding time, i.e. 200 ms – 800 ms was used by Chen et al.[12] for resistance spot welding of Al to steel. To investigate the effect of welding time on nugget size and mechanical properties of spot welded joints by U + RSW method, the results were compared between the short welding time of 83 ms and relatively long welding time of 200 ms. The nugget diameters at both Al/insert and insert/steel interfaces increased with increasing welding time, as expected. At welding current of 19 kA, the nugget diameters at Al/insert and insert/steel interfaces were 6.56 mm and 7.845 mm,

respectively, with welding time of 200 ms. These diameters were about 21.5 % and 8.7 % larger than those welded with welding time of 83 ms. Corresponding to a larger nugget diameter, the peak strength of the spot welds was higher with welding time of 200 ms than that with welding time of 83 ms. At welding time of 19 kA, the peak strength of the spot welds with welding time of 200 ms was 3.71 ± 0.06 kN, which was 0.54 kN higher than that with welding time of 83 ms. Moreover, the peak strength with welding time of 200 ms and welding current of 19 kA was comparable to that with a shorter welding time of 83 ms but a higher welding current of 21 kA. However, severe melting of the top surface of aluminum alloy can occur with the long welding time of 200 ms, which may result in rapid electrode degradation due to alloying of aluminum with copper electrode. A typical over-melted aluminum surface is shown in Figure 5.25. Based on EDS analysis, Al_2Cu formed due to alloying of copper with aluminum sheet.

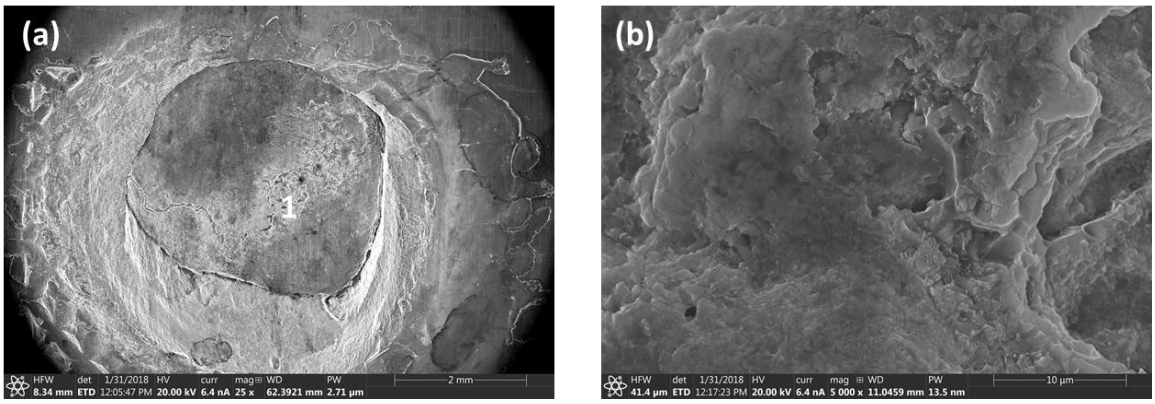

Figure 5.25 (a) macrostructure, and (b) zoomed-in image of the IMCs formed on the top surface of aluminum sheet due to over-melting when long welding time of 200 ms was used

Consistent nugget pull-out can be observed at/above the welding current of 18 kA for welding time of 200 ms, while consistent nugget pull-out occurred at/above the welding current of 19 kA with welding time of 83 ms. Thus, relatively short welding time, i.e. 83 ms (5 cycles), resulted in better weld quality according to the optimization criteria, i.e. high peak load, longer electrode life, and less porosity.

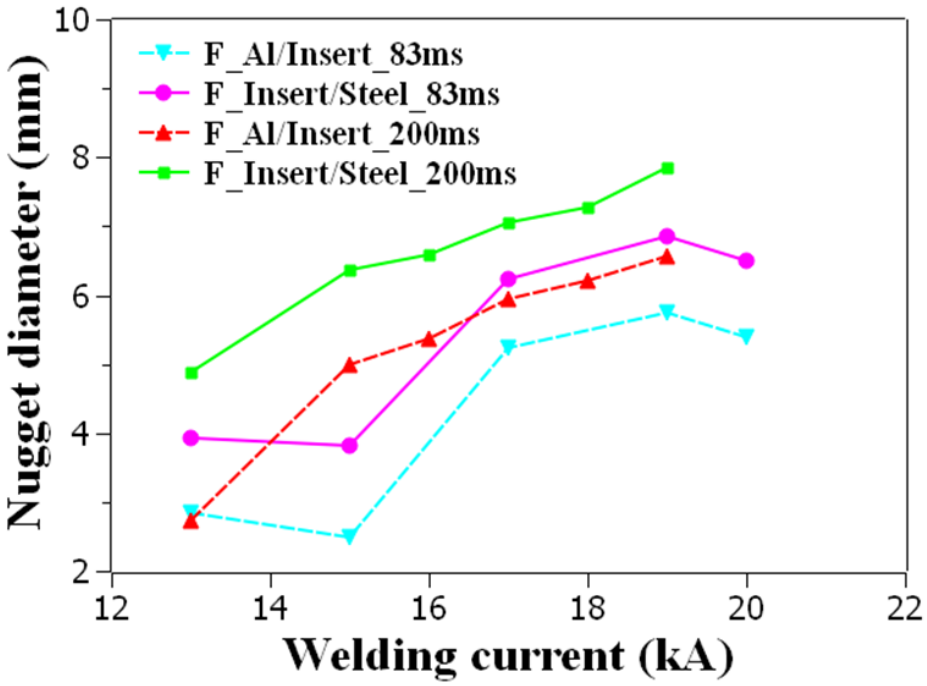

Figure 5.26 Effect of welding time on nugget diameter with 0.3 mm-thick AA3003 as an insert using the MFDC welder

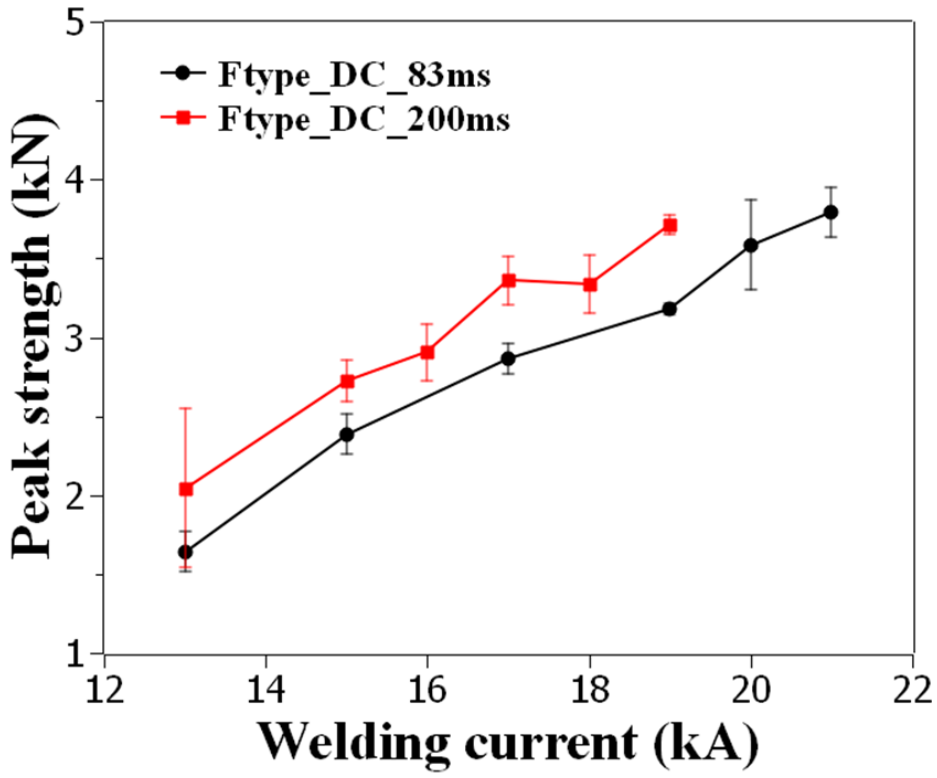

Figure 5.27 Effect of welding time on peak strength with 0.3 mm-thick AA3003 as an insert using the MFDC welder

5.3.6 Effect of the intermediate joint on strength of the final joint

Figure 5.28 shows the effect of the intermediate joint quality on mechanical properties of the primary joint with the dome-shape electrode and using AA3003 as an insert. The overall trend is similar to that reported previously in Figure 5.18 (i.e., AA60601 as an insert and flat electrode). With low ultrasonic energy of 100 J, the tensile shear strength of the primary joint was approximately 3.1 kN. However, a large variation of peak strength of the primary joints indicated the inconsistency of the weld quality with low intermediate joint strength. Moreover, expulsion was observed at insert/steel interface.

When the ultrasonic energy was above 125 J, the effect of ultrasonic energy on primary joint was significantly reduced. A consistent nugget pull-out failure mode was observed with a peak load of 3.5 kN. Thus, the formation of metallurgical bond resulted in reduction in contact resistance at insert/steel interface and the prevention of early expulsion due to high current density at local regions. The high tolerance of primary joint to the weld quality of the intermediate joint can increase the weldability and consistency of the joints.

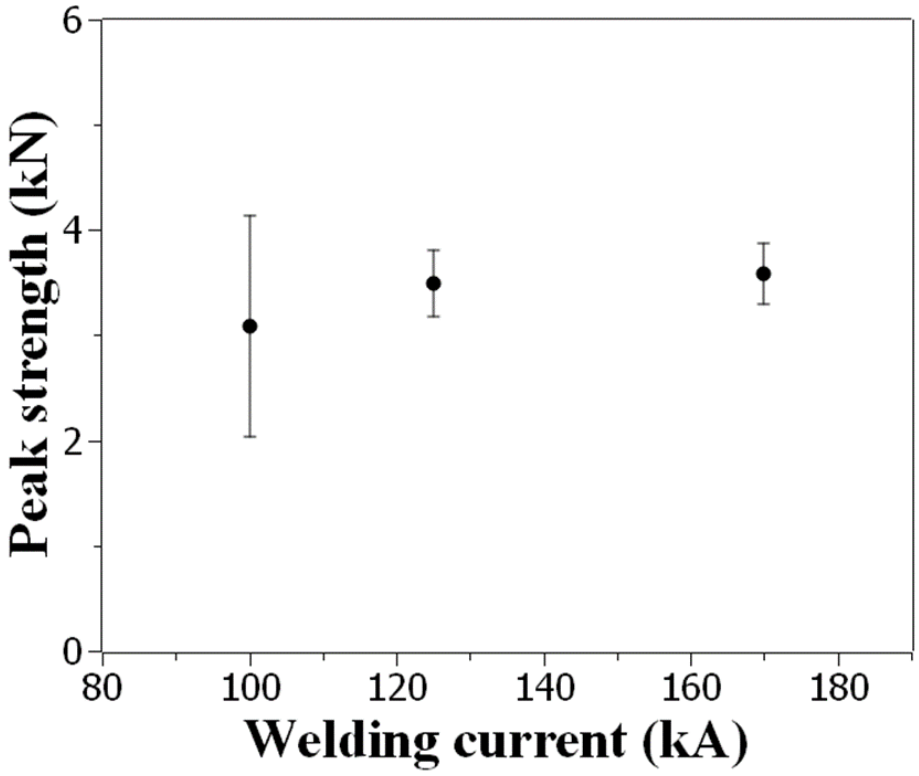

Figure 5.28 Effect of intermediate joint quality on peak strength of the U+RSW welds for AA3003 as an insert with dome-shaped electrodes

5.4 Wedge testing of U+RSW welds

5.4.1 Experiment

To in-situ observe the strain localization, crack initiation and propagation, a single-sided wedge test [80], was used for testing Al/steel joints welded by U+RSW. The dimensions of the wedge and the sample are shown in Figure 5.29. The detailed procedure of single-sided wedge testing with DIC for resistance spot welded equal-thickness Usibor 1500 is available in [80]. Therefore, only the unique features of the testing set-up for unequal-thickness Al/steel U+RSW joints are presented in the following. To keep consistency with the lap-shear tensile testing set-up of Al/steel U+RSW joints, one side of the sample was clamped by the fixture, while the wedge was inserted at the aluminum/insert interface on the other side and pushing inward with the displacement rate of 2.5 mm/min. Special fixture was used to reduce the misalignment of the wedge and the sample [144]. To investigate the effect of welding current on Mode I failure behavior, low welding current of 17 kA and high welding current of 19 kA and 20 kA were used. It is noted that in lap-shear tensile testing, welds with 17 kA failed with Type 2 failure mode, while welds with 19 kA and 20 kA failed with button pull-out from aluminum sheet.

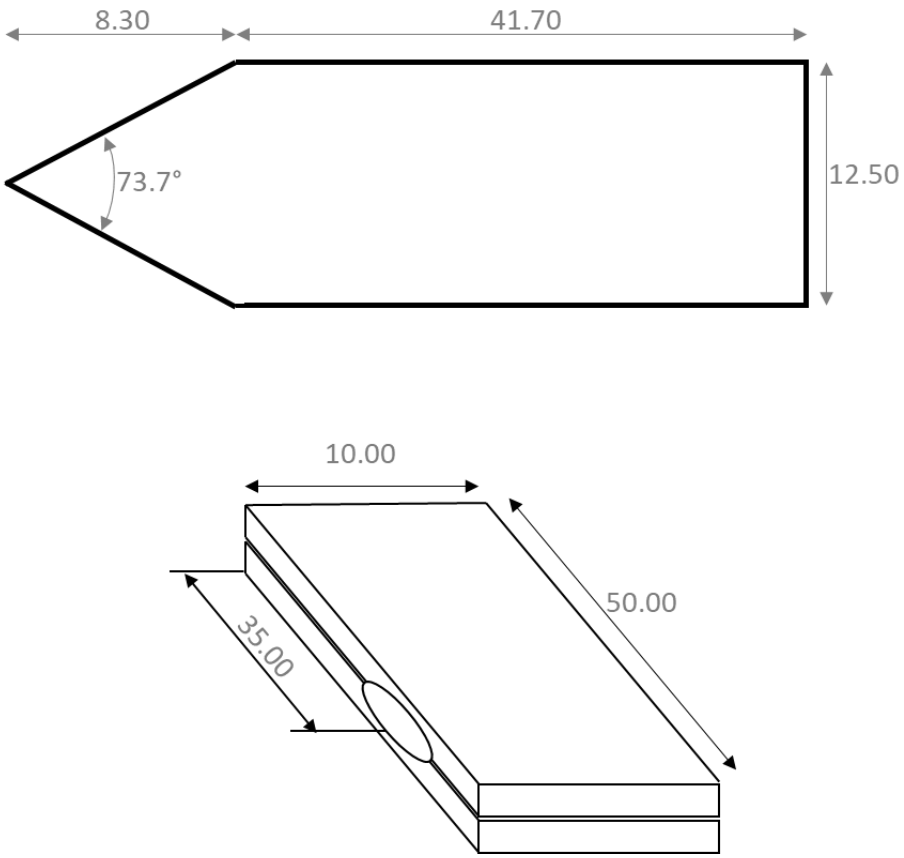

Figure 5.29 Dimensions of the wedge and sample in single-sided wedge test

5.4.2 Effect of welding current on half weld

The load-displacement curves of the welds with different welding currents are shown in Figure 5.30. Two stages can be observed in the load-displacement curve for Al/steel U+RSW welds. In Stage I, force gradually increased from 0 to 0.123 ± 0.013 kN within the initial 1 -1.5 mm insertion, and then the insertion force was kept at 0.123 kN until around 10 mm, at which the tip of the wedge has been fully inserted at insert/Al interface. In Stage II, the force rapidly increased from 0.123 kN to peak strength and crack initiated and propagated. For welding current of 17 kA with the nugget sizes of 5.2 mm at

Al/insert interface and 6.2 mm at insert/steel interface, both Type 2 and Type 3 failure modes may occur. With increasing welding current above 19 kA, the failure modes were consistent button pull-out.

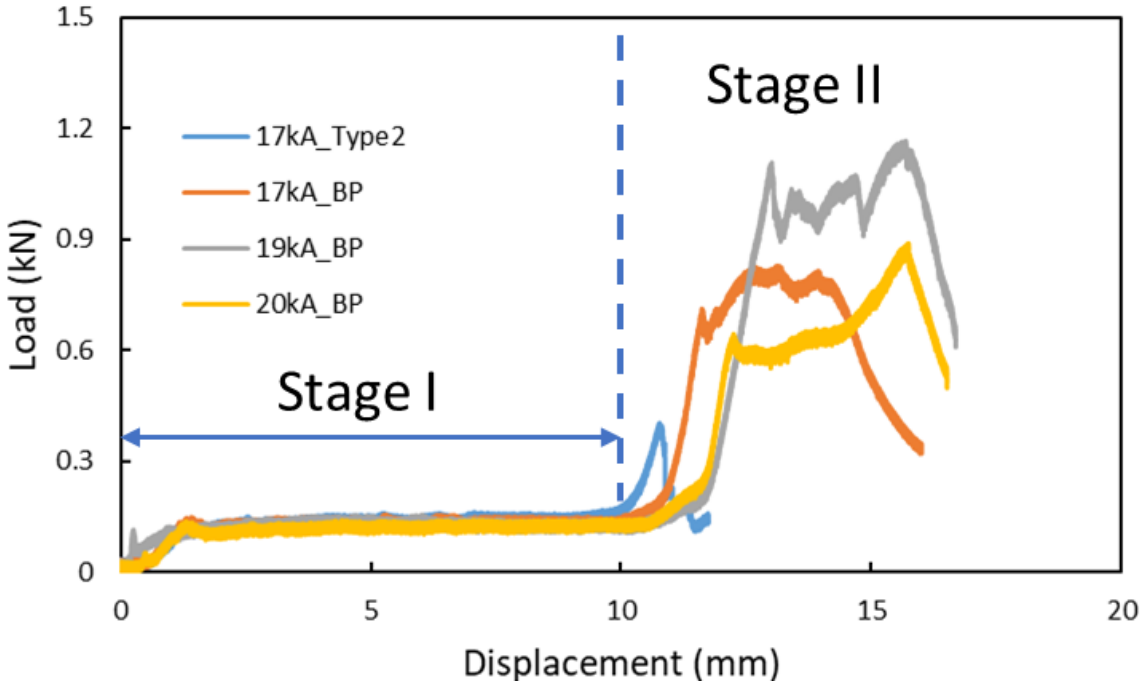

Figure 5.30 Load displacement curves of different failure modes occurring at different welding currents. Tested by single-sided wedge test

The load-displacement curve and the corresponding strain distribution at different stages can be seen in Figure 5.31. At Stage I, the wedge was inserted into Al/insert interface with small strain localization at the indentation of the Al sheet. However, there was no obvious strain localization observed at both Al/insert and insert/steel notches. At the peak load, strain localization can be clearly observed at the Al sheet (left leg), at which the wedge was in contact with the Al sheet and crack initiated at the Al sheet. However, as crack propagated in the Al sheet, strain localized at insert/steel interface

with the maximum value of 0.16. And the final failure took place at insert/steel interface with button pull-out from the insert. Therefore, there are two competing cracking mechanisms at welding current of 17 kA: one is strain accumulation and necking at Al sheet; the other is stress concentration at insert/steel notch for large nugget size or stress concentration at Al/insert interface for small nugget size. The final failure depended on the lowest force required of the two competing mechanisms. As the nugget sizes at Al/insert and insert/steel interface increased at welding current of 19 and 20 kA, the only failure mode observed was button-pullout with strain localization at the base metal near to fusion boundary in Al sheet as shown in Figure 5.32 and Figure 5.33.

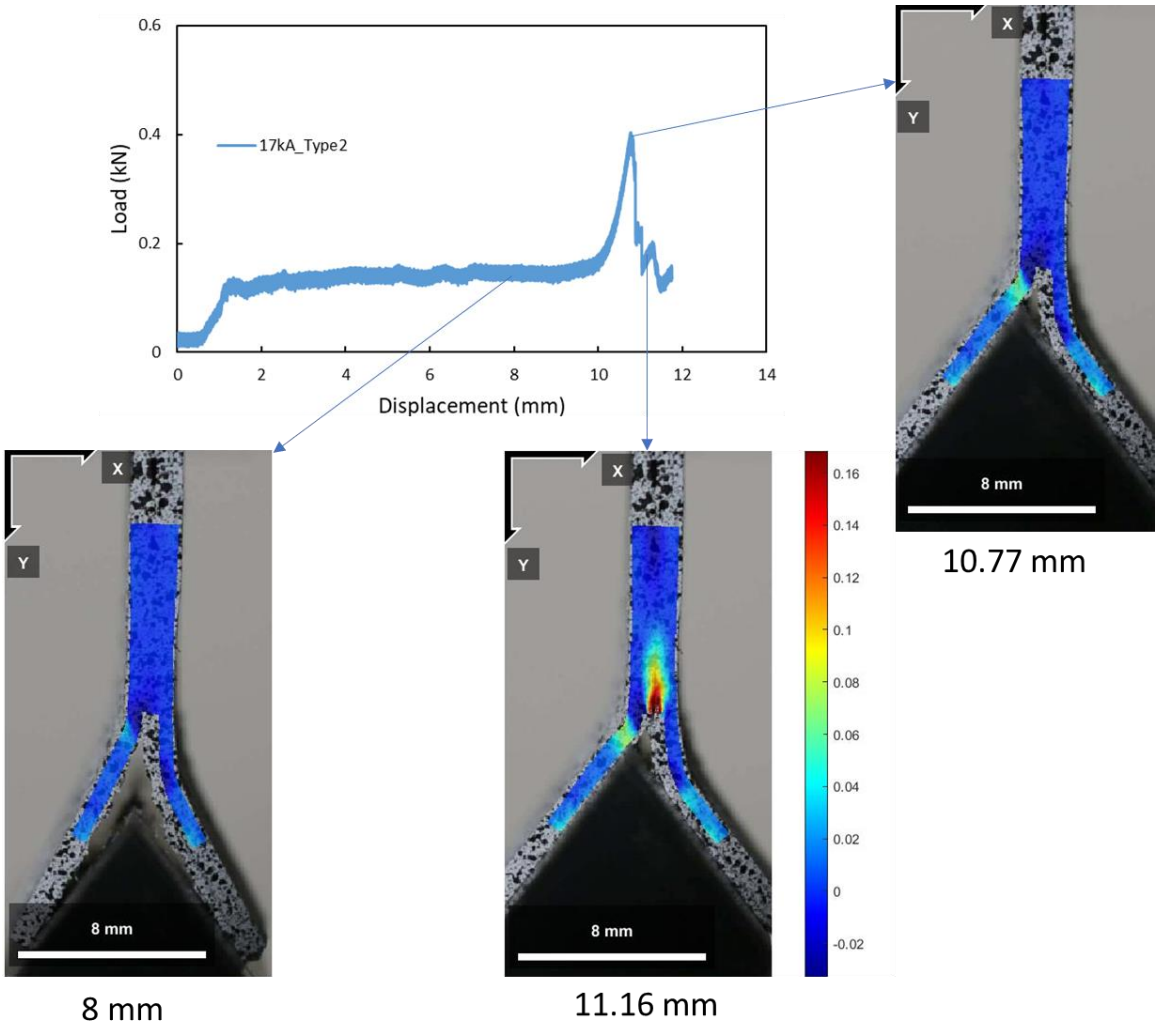

Figure 5.31 Strain (ε_{xx}) distribution for Type 2 failure. The left leg is the Al sheet, and the right leg is the insert and steel

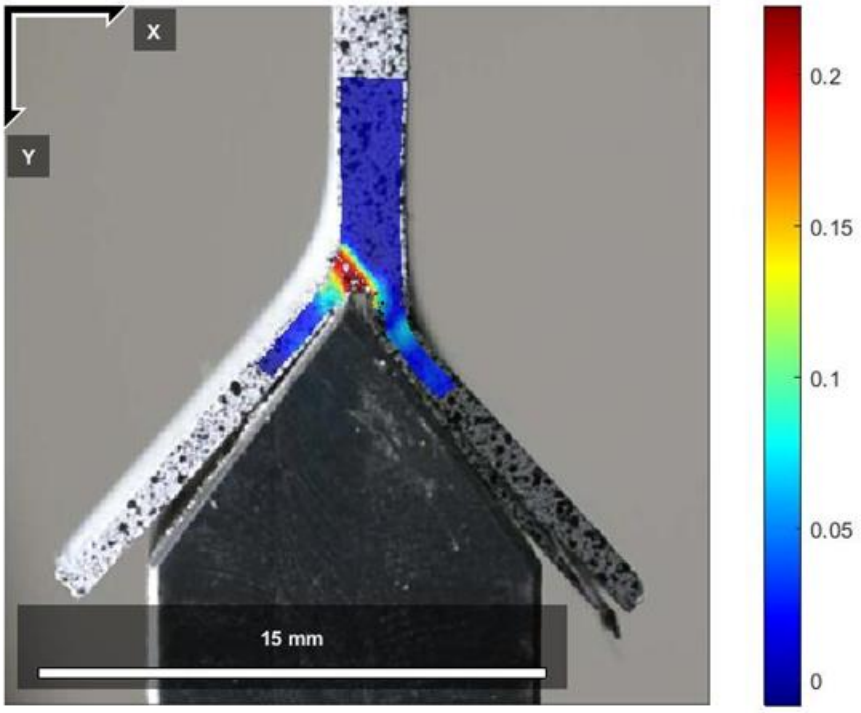

Figure 5.32 Strain distribution for button pull-out failure mode (Type 3) with welding current of 19 kA

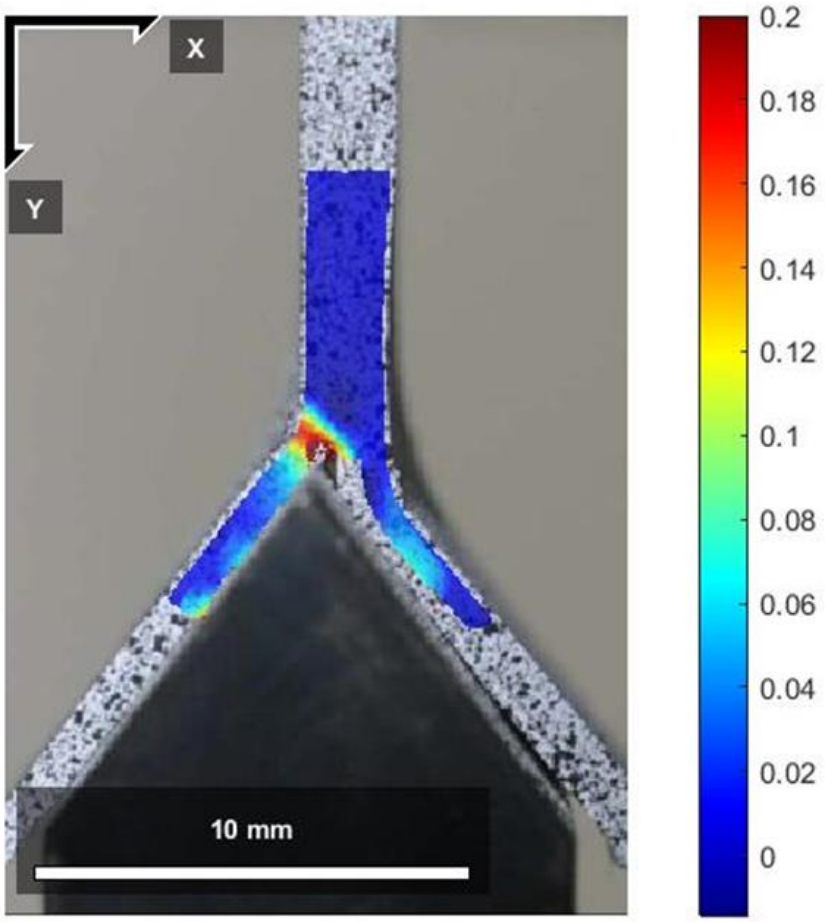

Figure 5.33 Strain distribution for button pull-out failure mode (Type 3) with welding current of 20 kA

5.4.3 Comparison of full weld with half weld

The half weld cross-sectioned through the weld center was for in-situ observation of the deformation and crack path. However, it was essential to investigate the relation of the load-bearing capacity and failure modes of the half weld versus the full weld. Moreover, wedge test, as a new testing method for spot welds, was initially designed to

represent cross-tension test. Therefore, the peak load and failure mode of wedge test in this study and the two traditional mechanical testing methods for spot welds, i.e. cross-tension and coach-peel test results in the literature for Al/steel spot welds are compared in this section.

Figure 5.34 showed the typical load-displacement curves for full weld and half weld welded at welding current of 19 kA. The load-displacement curves of both welds consisted of two stages, i.e. initial leg opening stage with relatively low insertion force and the following severe deformation/cracking stages with rapid increase in insertion force. At Stage I, the insertion force of the full weld was approximately 0.256 kN, which was about twice of that of the half weld (0.123 kN). However, the rule cannot be applied to the peak load of the full weld versus half weld. The comparison of peak loads for full weld and half weld at different welding currents is shown in Figure 5.35. For full weld, a consistent full/partial button pull-out can be obtained with the welding current of 19 kA. The failure modes changed to Type 2 at a relatively lower welding current of 17 kA or a higher welding current of 20 kA. Larger variation on peak load can be observed at the welding current of 20 kA since necking may occur at the Al sheet, however, the large stress concentration at insert/steel interface at the final stage resulted in the final failure with insert detached from steel sheet. The average ratio of the peak load for full weld and half weld was approximately 1.73, instead of 2, which can be caused by the different restrain and the residual stress of the full weld versus half weld. A further study, such as one using finite element method to simulate the stress distribution of the full weld and

half weld, will be needed to develop a better understanding of the deformation and failure behaviors of full weld versus half weld.

Chen et al. [145] measured the peak load of direct resistance spot welded 1.2 mm thick AA 6022-T4 Al alloy and 2 mm thick GI low carbon steel in cross-tension and coach-peel tests. The fracture modes changed from interfacial fracture, partial thickness fracture to partial button pull-out, as welding current increased with welding time kept at 200 ms. The maximum peak load was approximately 1.5 kN with partial button pull-out failure mode in cross-tension test. The peak load and failure mode of the cross-tension test by Chen et al were comparable to the results shown in this study. However, full button pull-out can be observed at welding current of 19 kA in this study and the ratio of full button pull-out with partial button pull-out was 1.73:1.

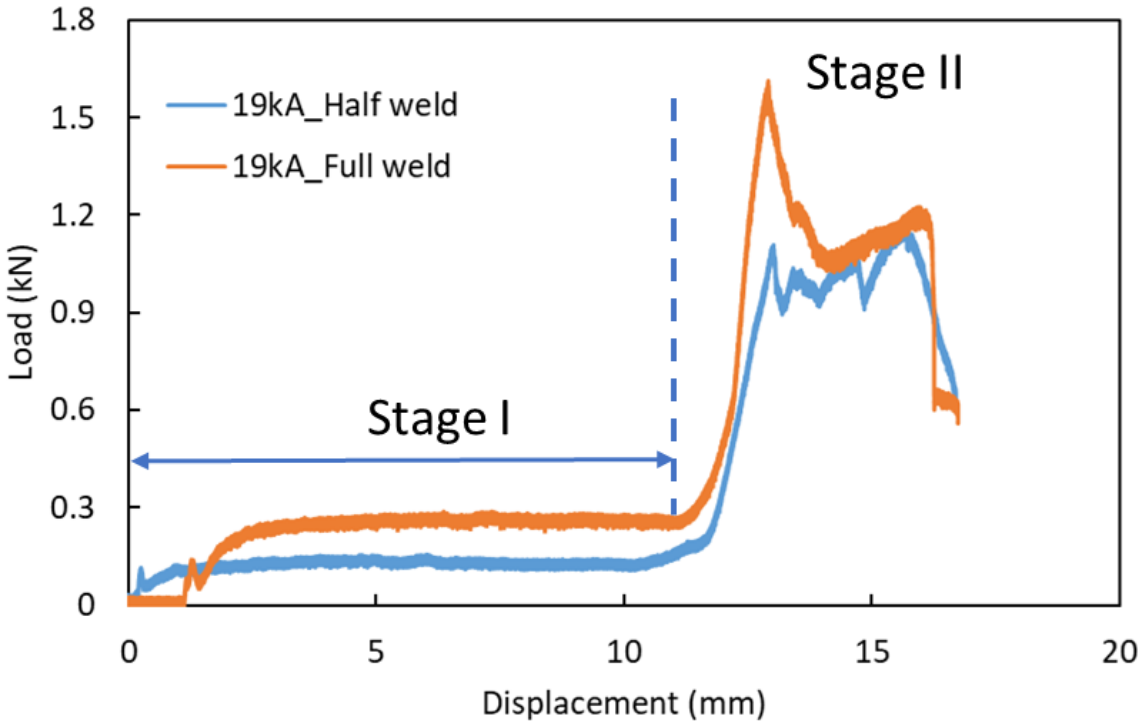

Figure 5.34 Load displacement curves of full weld and half weld (welding current: 19 kA) for single-sided wedge testing

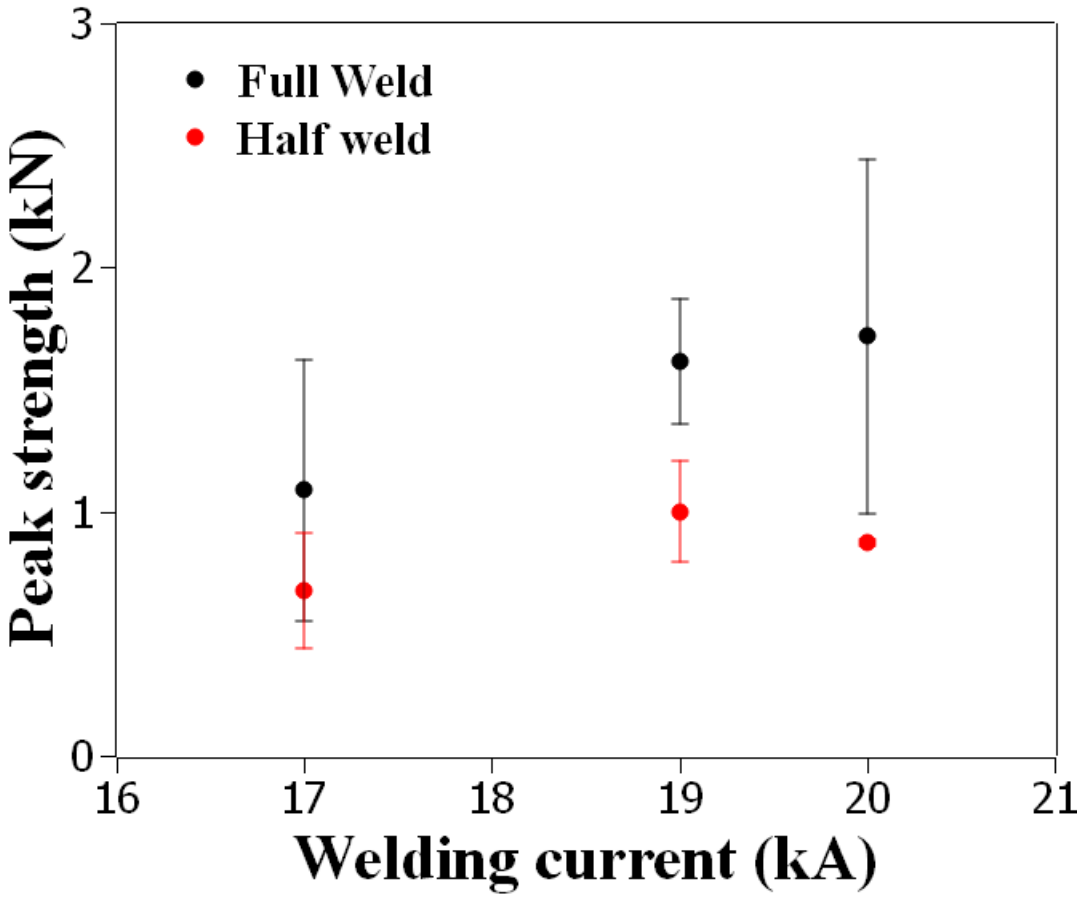

Figure 5.35 Comparison of peak strength of full weld versus half weld tested by single-sided wedge testing

5.5 Conclusions

In summary, a novel process, U+RSW, was developed for dissimilar metal joining of aluminum alloy AA6061-T6 to cold-rolled 1008 steel. The effect of welding parameters and the intermediate joint quality on microstructure, mechanical properties and failure mode of the primary joint were investigated. The main conclusions are as follows:

Feasibility study (AC spot welder, AA6061 as an insert, and welding time of 5 cycles (83 ms))

- Al/steel joints created by U+RSW show a brazing feature with liquid aluminum wetting and spreading on solid steel surface. There is no expulsion observed at insert/steel interface up to a high welding current of 16.5 kA. The nugget diameters at both Al/insert and insert/steel interfaces are crucial parameters for tensile shear strength and failure behavior. The minimum nugget size for button pull-out failure mode is about $5\sqrt{t}$, with the nugget diameter of 5 mm at Al/insert interface and 6 mm at insert/steel interface. Less than 2 μm-thick IMCs are observed at weld center which do not deteriorate the bond strength of the joints welded by U+RSW method.
- Tensile shear strength of the U+RSW joint is about 0.76 kN higher than that welded by direct resistance spot welding without an insert at welding current of 13.6 kA. Tensile shear strength and fracture energy increase with increasing welding current for U+RSW. At the maximum welding current of 16.5 kA, a peak load of 3.2 kN can be obtained which is comparable to resistance spot welding of 1 mm-thick A6068 aluminum alloy.
- Four different types of failure modes can be observed, and they are significantly affected by welding current. As the welding current is less than 13.6 kA, a shear fracture can occur at Al/insert interface (Type 1 failure mode). With welding current between 13.6 kA and 15.2 kA, crack initiates at Al/insert interface, deviates into the insert and propagates through insert/steel interface (Type 2 failure mode). As the welding current is higher than 15.2 kA, Type 3 (nugget pull-out from aluminum sheet), Type 2 and Type 4 (interfacial fracture) failure modes at insert/steel interface can be observed.

- The quality of the intermediate joint affects the strength of the primary weld. Particularly, at a low ultrasonic spot welding energy of 50 J, a strong metallurgical bonding was not formed at insert/steel interface. Consequently, the tensile shear strength of primary joint is low. The tensile shear strength increases with the ultrasonic welding energy and does not depend the ultrasonic welding energy used as long as it is higher than 150 J.

Effect of other welding parameters:

- With 0.3 mm-thick 3003 as an insert, F-type electrode on Al side and dome-shaped electrode on steel side, a consistent nugget pull-out failure mode can be observed as welding current is at/above 19 kA and the welding time of 83 ms in lap-shear tensile testing. The nugget size and peak load for the spot-welded joints with AC versus MFDC machines are comparable, which indicates that the results are not sensitive to the power supply. Similar to AA 6061 insert, the tensile shear strength is not adversely affected by the intermediate joint quality as the ultrasonic welding energy is higher than the threshold energy, i.e. 125 J, when AA3003 is used as an insert. 83 ms is found to be the optimum welding time in this study since although there is a 0.5 kN increase in peak joint strength with welding time of 200 ms, severe electrode wear can be observed at the electrode on Al side, especially at high welding current.

Single-sided wedge testing:

a. Wedge test is successfully applied in Al/steel U+RSW welds for in-situ observation of deformation and failure. At welding current of 17 kA, two

competing mechanisms exist with the final failure at insert/steel interface. At high welding current of 19 kA, necking occurs at Al sheet with the final failure mode of button pull-out. The load displacement curve can be divided into two stages for Al/steel U+RSW welds, with relatively low opening force of 0.123 kN at Stage I and rapid increasing of opening force at Stage II.

b. The failure modes of full weld at welding current of 17 kA and 19 kA are comparable to that of the half weld. However, inconsistency of failure modes of full weld and half weld can be observed at welding current of 20 kA, which could be due to occasionally-occurred expulsion at high welding current of 20 kA. The insertion force at Stage I of the full weld is about twice that of the half weld. However, the ratio of the peak insertion force of the full weld to the half weld at Stage II is about 1.73. The maximum peak joint strength of the full weld is approximately 1.6 kN, which is comparable to the maximum peak strength in cross-tension test of AA6022/low carbon steel reported in literature.

Chapter 6 In-situ relative motion measurement during ultrasonic spot Introduction

6.1 Introduction

As discussed in the previous chapter, Ultrasonic Spot Welding (USW), a solid-state welding process, is used to produce the intermediate joint in the U+RSW process. An improved understanding of bonding mechanism especially in terms of process-microstructure-property relation is essential to achieve a sound dissimilar metal joint of Al to steel. USW is a highly dynamic process involving complex mechanical, thermal and metallurgical interactions among sonotrode, workpieces, and anvil. As a first step toward developing such an improved understanding of bonding mechanism, USW of aluminum sheets is studied using a novel measurement technique in this chapter.

Spot welding of aluminum alloys (AAs) is widely used in a variety of industry applications such as automotive lightweight frames [146], electrical wire harnesses, and battery packs [147]. Among different processes for spot welding, Resistance Spot Welding (RSW) consumes approximately 50 to 100 kJ per weld [148] due to the high electrical conductivity of AAs. Friction Stir Spot Welding (FSSW), a solid-state welding process, consumes a much lower amount of energy (3 to 6 kJ per weld) for joining AAs [149].USW has an even lower energy consumption (less than 1.5 kJ per weld) and short

welding time (less than 0.5 sec) [150]. Furthermore, the peak temperature experienced by metals in USW is typically about 573 K (300 ^{o}C), approximately 50% of the melting temperature of AAs [151] [152]. Such short times at low temperatures not only mitigate common problems encountered in fusion welding of AAs such as gas porosity and solidification cracking, but also minimize the size and extent of Heat Affected Zone (HAZ) formation that can have a detrimental effect on base metal properties [148].

Although there is extensive research on the general mechanism of bonding in USW, a fundamental understanding of bond formation, which is essential for weld optimization, is still evolving. Moreover, USW is a highly dynamic process, making direct observation of bond formation difficult. As a result, a large body of research studying the bonding mechanism has relied on post-weld microstructure characterization coupled with various mechanical testing techniques such as lap-shear tensile testing [153], push-pin testing [154], and peel testing [155]. By characterizing the weld grain structure using electron backscatter diffraction (EBSD), Mariani and Ghassemieh [156] attributed dynamic recrystallization (DRX) at the weld zone, which reduced the grain size, to the main bonding mechanism. Dehoff and Babu et al. [157] observed that the recrystallized zone at the bonding interface in ultrasonic additive manufacturing (UAM) of AA3003-O had a thickness of approximately 15 μm and was comprised of fine grains. It was confirmed that the bonding mechanism was plastic deformation of the faying surfaces followed by DRX and grain boundary migration across the nascent surface. Gunduz et al. [158] emphasized the significant effect of atom diffusion on bonding by suggesting that

enhanced diffusion was driven by a significant local vacancy concentration increase at 513 K resulting from high strain rate (~ 10^3 s^{-1}) plastic deformation.

An obvious limitation with post-weld characterization is that it does not provide direct information about bond formation during welding. To improve the understanding of bond initiation and development during USW, the process has been monitored real-time using various experimental techniques. de Vries [159] investigated sonotrode vibration dynamics with a laser vibrometer. As the measurement was limited to a single spot, the relative motion between different parts (sonotrode, coupons, and anvil) was not studied. In addition to the vibrometer, a force sensor was assembled at the anvil and used to measure the interfacial force during USW. The measured shear force was then correlated to weld quality. Li et al. [160] used thin-film microsensors for heat flux measurement at the faying surfaces. It was shown that the welding process consisted of a friction heating dominated stage, deformation heating dominated stage, and diffusion bonding stage. A high-speed camera technique was used by both Sasaki et al. [161] and Lee et al. [162] to image the vibration dynamics during USW; Digital Image Correlation (DIC) was then used to process the images and map the velocities. Both studies showed the importance of relative motion in understanding the bond formation mechanism. It is noted that the high speed imaging used in previous research had a spatial resolution limited to about 2 μm of vibration amplitude. Moreover, the measurement time was limited to 600 ms due to focal limitations of the high speed camera.

Laser Doppler Vibrometers (LDVs), such as the one used by Balle and Wagner [163], measure the Doppler frequency shift of a wave to determine the velocity of a moving object. Compared to a high speed camera, LDVs can readily achieve higher displacement resolutions and longer measuring times. Although earlier LDVs were limited to velocity measurement of a single spot at a time, modern LDVs can measure multiple spots. For instance, Photonic Doppler Velocimetry (PDV) allows velocity measurement of multiple objects simultaneously by using several synchronized measurement channels. PDV was used for velocity measurement in electromagnetic pulse welding [164] and laser impact welding [165] in which the samples moved with velocities exceeding 50 m/s. More recently, it was used by Foster and Taber [166] for velocity measurement in UAM, where a thin foil was bonded to a thick substrate by a rolling sonotrode horn (similar to linear ultrasonic welding). Vibration kinetics were measured for the sonotrode, foil, and substrate to study the relative motion between the three different parts [167]. Finally, Heinz et al. [168] applied laser scanning vibrometry where the laser beam(s) scanned a grid and measured the velocity at each grid point, which was then used to construct a 3-D velocity map. The scanning vibrometry was used to characterize the vibration kinetics and high-cycle fatigue behavior of Ti-6Al-4V. Currently, the application of PDV to study the relative motion between different parts during USW of AAs is limited.

In the present research, a PDV system was used for in-situ measurement of vibration kinetics at multiple locations simultaneously over the entire duration of USW of AA 6061-T6 sheets. The measured velocity profiles were used to study the relative motion between the sonotrode tip, aluminum sheets, and anvil. The vibration kinetics were

correlated to the lap-shear tensile strength and weld microstructure to understand bond formation during welding.

6.2 Experiment

6.2.1 Ultrasonic spot welding

The dimensions of samples used for welding were 25 mm × 100 mm. The samples were cut from 400 μm thick AA 6061-T6 sheets such that the short dimension was perpendicular to the rolling direction (RD) of the sheets. An Amtech Ultraweld® 20 2.4-kW lateral driven spot welder, designed to operate at 20 kHz with a maximum peak-to-peak amplitude of 80 μm, was used for welding. The dimensions of sonotrode tip were 8 mm × 6 mm and the anvil tip 12 mm × 12 mm. Both sonotrode and anvil surfaces had machined pyramid knurl patterns of grooves and lands to facilitate firm gripping of the samples. The spacing between lands was about 0.63 mm. The depth of the groove was 0.16 and 0.08 mm for the anvil and sonotrode knurl patterns, respectively. Images of the anvil knurl pattern are provided later in the discussion section. The vibration direction (VD) of the sonotrode was parallel to the short dimension of the samples (thus perpendicular to the RD), as shown in Figure 6.1. The through-thickness direction is marked as the normal direction (ND). The samples were welded without any prior surface treatment or cleaning.

USW systems typically operate in either a time- or energy-controlled mode. As a highly dynamic process, USW can be sensitive to variations in the normal clamping force

and surface conditions such as oxide layers and contaminants. Particularly, the amount of vibration energy utilized for welding at a given time can vary from weld to weld even when all welding parameters are held constant, thus energy-control is often used to reduce the inconsistency in weld quality. In the present study, the welding energy was varied from 10 to 300 J to systematically investigate bond evolution while keeping a 50 μm peak-to-peak vibration amplitude. A normal force was applied by a pneumatic cylinder filled with compressed air. An air pressure of 50 psi was used, corresponding to a normal force of 1754 N. The values of vibration amplitude and normal force were selected based on preliminary experimental tests as likely to produce sufficiently strong bonds. Particularly, a sufficiently strong bond corresponded to a nugget pull-out fracture mode in the lap-shear test. Moreover, the joint strength exceeded the minimal value specified for RSW, the *de facto* standard spot welding process. Such minimal average strength for RSW of 0.4-mm-thick AA6061 was 625 N in accordance to AWS D17.2M:2013 - Specification for Resistance Welding for Aerospace Applications. Finally, the maximum energy was kept to 300 J since over-welding and severe sonotrode sticking occurred when the welding energy was higher than 300 J. The welding time to reach the set energy was determined by the spot welding machine.

6.2.2 Velocity measurement using PDV

The PDV system used for in-situ velocity measurements is described in detail by Johnson et al [164]; the salient features are summarized as follows: the system used a 1550 nm wavelength erbium fiber laser. A LeCroy WaveSurfer 104MXs digitizer with

three channels was utilized to synchronously record beat signals of three individual laser points at a sampling rate of 20 MHz (1000 times faster than the vibration frequency). The locations of the three laser points are illustrated in Figure 6.2. Two of the three spots were focused on the edges of the top and bottom foils where a fine spot size of 90 μm was used to help maintain the laser focus on the foil edges during the entire duration of welding. The third spot was focused on a location on the sonotrode close to the sonotrode tip/top foil interface. For a few selected parameter sets, experiments were repeated with the third spot focused on the anvil tip to measure the anvil vibration velocity. It is noted that a fourth channel can be added to the digitizer for simultaneous measurement at four spatial points; however, such equipment was not available at the time of this study. The raw data recorded in the digitizer was processed using an existing data analysis procedure in Matlab® to obtain the velocity profiles as a function of time [169].

6.2.3 Bond quality characterization

Lap-shear tensile testing was performed with a MTS 831.10 Elasto-meter with a displacement rate of 1 mm/min. The welded samples for interfacial microstructure characterization were cross-sectioned parallel to the ultrasonic vibration direction. The cross section was ground with 800 SiC paper, polished with 6 μm and 1 μm diamond paste, and finished with a final vibratory polish using 0.05 μm colloidal silica for 2 hours. Scanning electron microcopy (SEM) was performed on a Quanta 200 SEM. EBSD was performed with a FEI/Philips XL-30 ESEM with an accelerating voltage of 15 kV, working distance of 22 mm, and step size of 0.15 μm. Finally, an optical profilometer

(OP) was used to measure the topographical profiles of indentation on the foils, particularly the penetration depth of the anvil tip into the bottom foil.

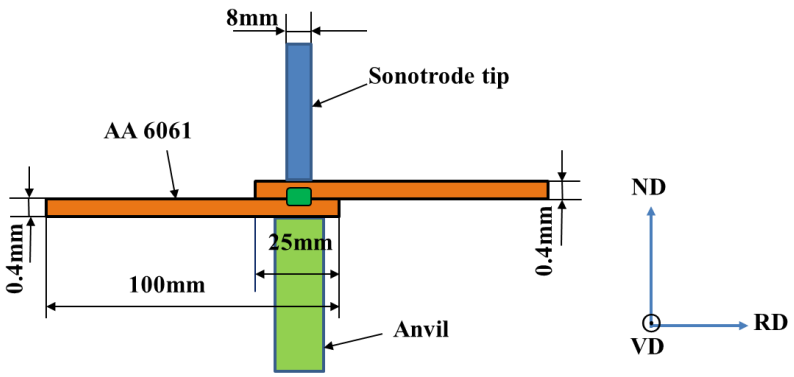

Figure 6.1 Schematics of ultrasonic spot welding setup

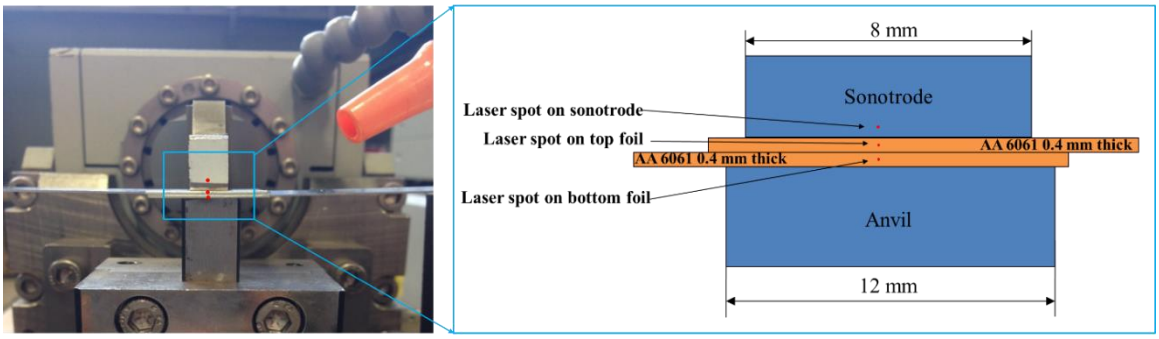

Figure 6.2 In-situ PDV velocity measurement setup with a zoomed-in view showing the focus of laser spots (0.09 mm in diameter) on sonotrode tip, top and bottom foils

6.3 Results

6.3.1 Motion of sonotrode tip and specimens

The velocity profile of the sonotrode tip and specimens for the entire welding time consists of several thousands of cycles, each cycle with tens of data points as shown in Figure 6.3. To facilitate analysis of such a large volume of data, the average of the

maximum velocity for every four contiguous cycles is extracted [170]. An example of such averaging is shown for the four cycles inside the dashed box in Figure 6.3. This average of the maximum velocity for every four cycles, abbreviated simply as the maximum velocity profile, is plotted as a function of time in Figure 6.4. It is noted that the phase angle data of vibration can also be extracted from the velocity profile; however, this data is noisy, possibly due to plastic deformation during welding. Moreover, the overall trend in phase angle difference between locations is found to be similar to that of the maximum velocity difference, thus only the maximum velocity profile is used to analyze the bond evolution during USW.

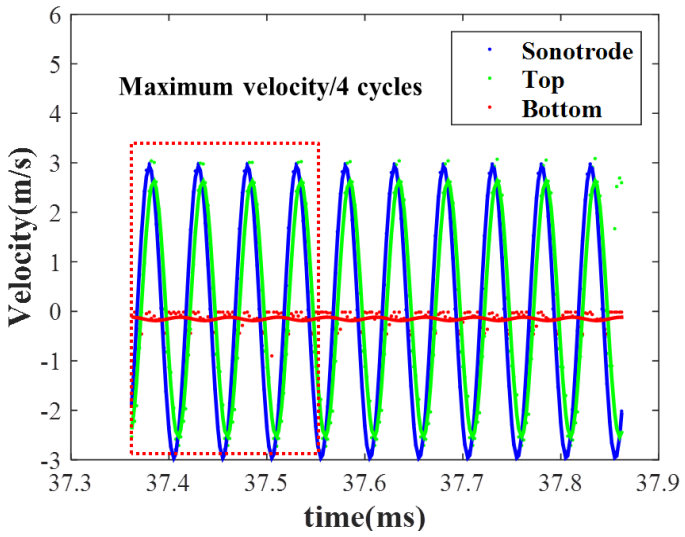

Figure 6.3 Example showing the average of the maximum velocity obtained for four contiguous cycles of velocity profiles. The welding parameters: vibration frequency = 20 kHz, peak-to-peak vibration amplitude = 50 µm, and normal force = 1754 N

Figure 6.4 shows the maximum velocity profiles of the sonotrode tip and two foils for welding energies ranging from 10 to 300 J while all other welding parameters were held constant. When the welding energy is fairly low, e.g., 10 J, the entire welding cycle lasts

only 45 ms as shown in Figure 6.4(a). During this short amount of time, the velocity of the top foil increases rapidly to reach a sonotrode velocity of 3 m/s, while the bottom foil remains almost stationary. For a welding energy of 20 J, the sonotrode vibration continues for another 15 ms, and the top foil velocity decreases while the bottom foil velocity increases as shown in Figure 6.4(b). Such trend continues until a welding time of 100 ms is reached, at which the two foils are coupled and vibrate at a similar velocity of about 2 m/s (lower than the sonotrode velocity of ~ 4 m/s) as shown in Figure 6.4(c).

At welding times exceeding 100 ms, the velocity of the two coupled foils increases gradually until they move at the same velocity as the sonotrode tip (~ 4 m/s) as shown in Figure 6.4(d). Finally, as the welding energy is further increased to 300 J (welding time > 240 ms), a rapid decrease of the maximum velocities of bottom and top foils is observed as shown in Figure 6.4(e).

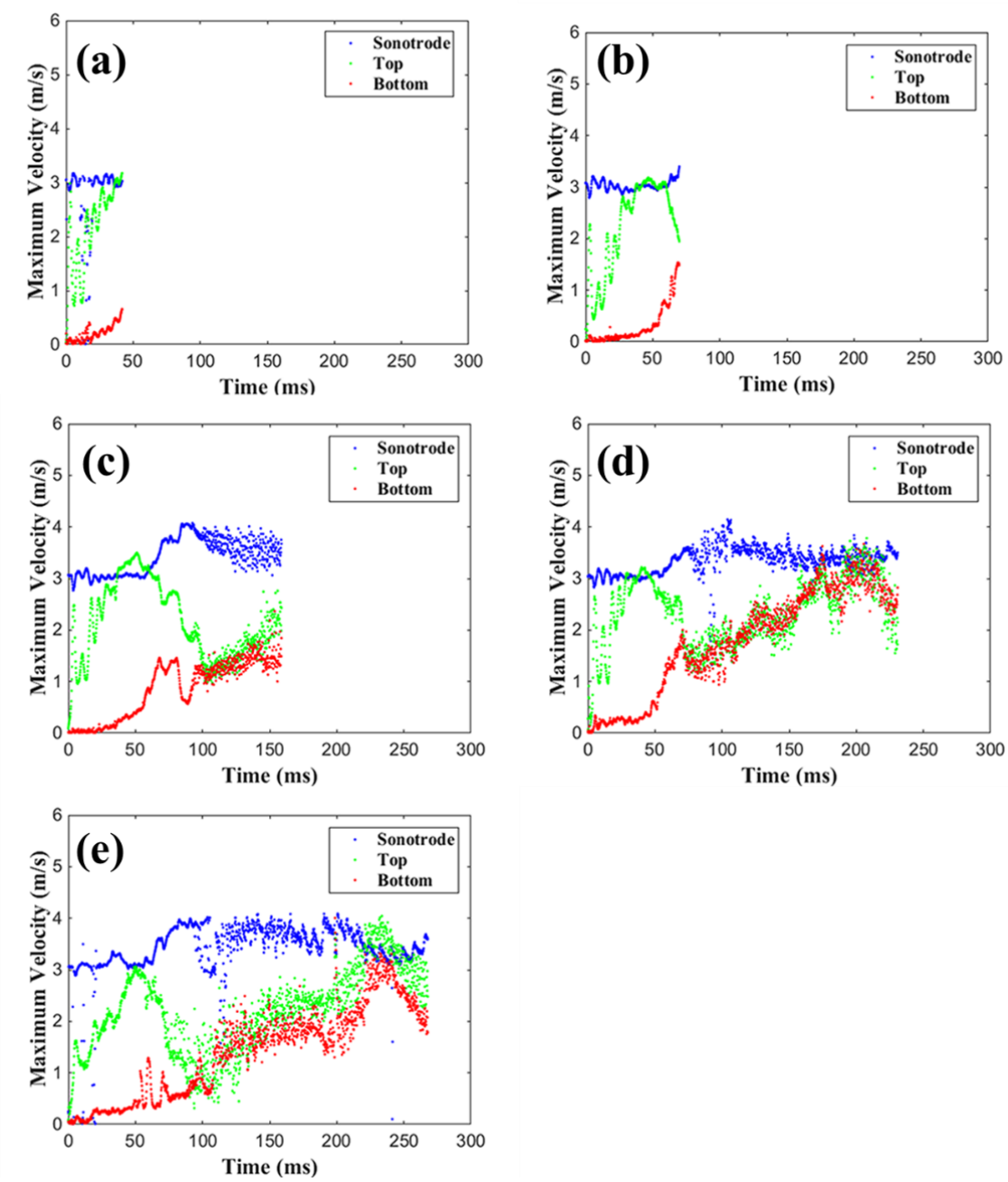

Figure 6.4 Maximum velocity profiles of the sonotrode, top foil, and bottom foil for welding energies of (a) 10 J, (b) 20 J, (c) 100 J, (d) 250 J, and (e) 300 J. Measurement was done on five different samples

It is noted that although the overall trends are consistent in the velocity profiles shown in Figure 6.4, there is some scatter in the exact values (e.g., maximum velocity values of top and bottom foils which are vibrating together). The reason for such scatter is likely due to the difficulty in maintaining consistent focus of laser spots on the thin foil edges and the effect of severe plastic deformation. The theoretical maximum velocity of the sonotrode is 3.14 m/s at the set vibration amplitude of 50 μm, which is supposedly held constant during welding. The measured maximum velocity of the sonotrode is relatively steady at 3 m/s at the beginning of the weld; however, it increases and then fluctuates as the welding time exceeds 60 ms. Such fluctuation of the sonotrode vibration velocity is likely due to the over- or under-adjustment applied by the spot welder as it tries to maintain the set vibration amplitude under the constantly changing contact conditions and vibration dynamics among different parts. Despite the scatter, the maximum velocity profiles are nonetheless useful to study the relative motion between different parts and to understand bond formation as discussed later.

6.3.2 Lap shear strength and fracture mode

The load-displacement curves for spot welds made at different energies are plotted in Figure 6.5 where the inset images show the fracture surfaces. When the energy is lower than 20 J, there is essentially no bond and the foils can be easily torn apart by hands; these samples are not tested in the tensile machine. Interfacial failure is observed when the welding energy is less than or equal to 150 J. The fracture surface shows a transition from a few scratch marks at 10 J to extended partial bonded areas at 100 J. A button pull-

out failure mode is observed when the welding energy is equal or higher than 250 J. The average ratio of the nugget area measured on the pulled-out button to the sonotrode tip area is 60% and 73% for welding energies of 250 J and 275 J, respectively, indicating an expanded bonded region with the increased welding energy.

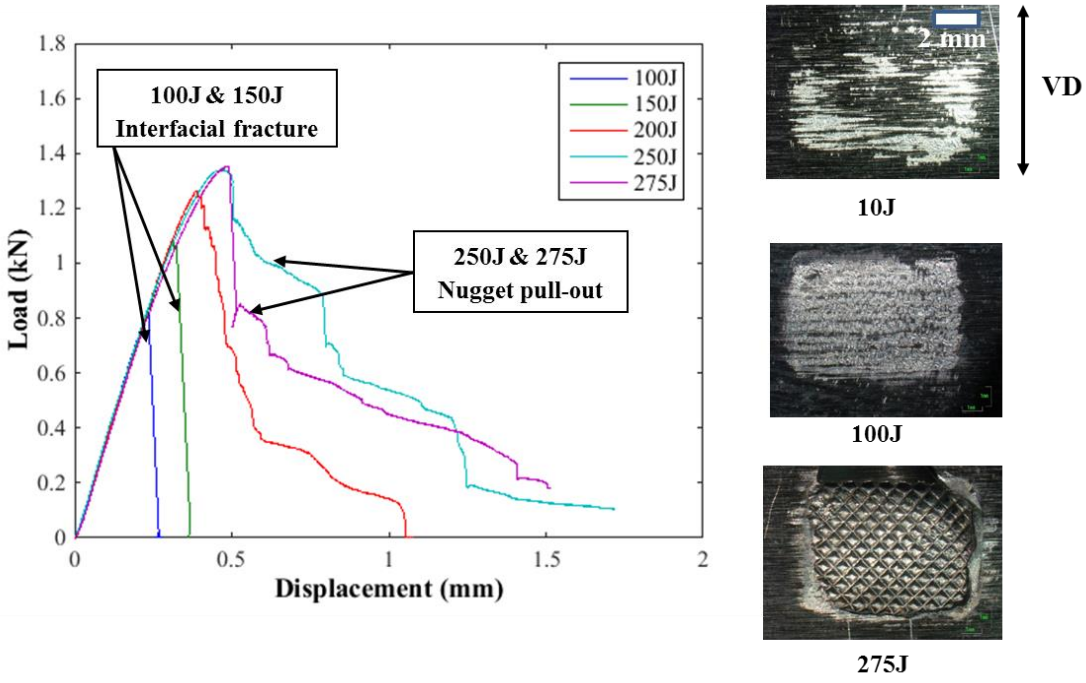

Figure 6.5 Load-displacement curves for "interfacial failure" mode and "nugget pull-out" mode

The lap-shear strength marked by the peak load in the load-displacement curve is plotted as a function of welding energy in Figure 6.6(a). The weld strength increases with welding energy until it peaks at a welding energy between 250 J and 275 J. Tip sticking (over-welding) happens when the welding energy is 300 J or higher. The tensile strength tested for over-welded samples is likely lower than the absolute joint strength of the specimen since extra force had to be used to tear the stuck specimen off the sonotrode tip

which might have damaged the bond; however, it is included in the figure to show the overall trend of change in weld strength with welding energy. Another indicator of bond quality, the fracture energy, was calculated by integrating the area below the load-displacement curve and is plotted in Figure 6.6(b). The fracture energy increases slowly when the welding energy is less than 100 J. A rapid increase of fracture energy with welding energy occurs between 100 J and 250 J, corresponding to the transition from "interfacial failure" to "nugget pull-out" as shown by the inset images in Figure 6.5. The fracture energy tends to level out between 250 J and 275 J.

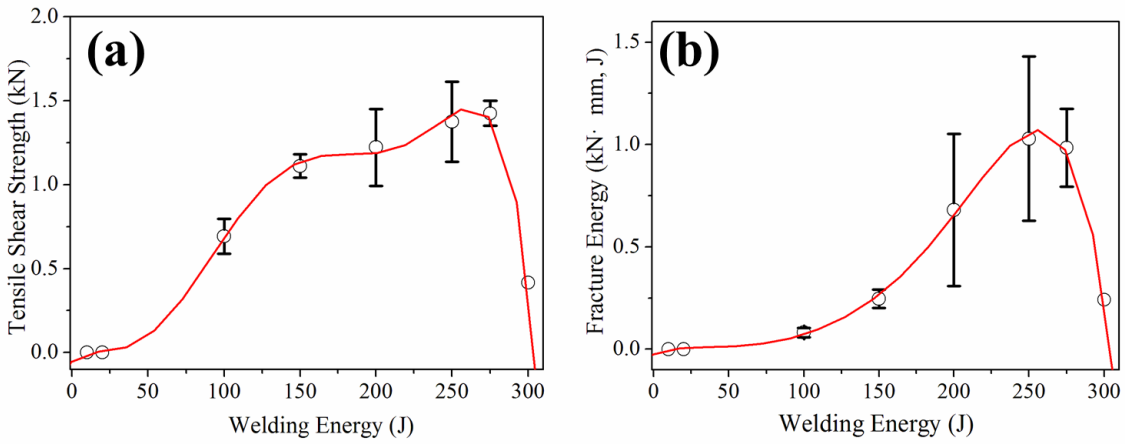

Figure 6.6 Effect of welding energy on (a) the average tensile shear strength, and (b) fracture energy

6.3.3 Weld interface microstructure

The cross-sectional microstructure of AA 6061 welded with an energy of 100 J is shown in Figure 6.7(a). The original large grains from the base metal (approximately 10-20 μm in size) are transformed into fine recrystallized grains at the local bonded region

with no obvious weld line present. Large grains still exist at either side of the interface between unbonded foils as shown in Figure 6.7(b). At this welding energy, there is a fairly low fraction of bonded (recrystallized) regions observed in the cross section, which corresponds to a low joint strength (0.7 kN) and interfacial failure mode. As the weld energy is increased to 275 J, a much higher density of recrystallized regions is observed at the weld interface. A typical grain structure near the weld interface, characterized by EBSD with 0.15 μm spacing, is shown in Figure 6.8(a). The bond zone extends 5 - 10 μm into the top and bottom foils with fine recrystallized grains varying in size from 0.5 - 6.7 μm as shown by the higher magnification image in Figure 6.8(b). 65% of the grains at the weld interface in Figure 6.8(a) have high misorientation angle (15^o - 60^o), indicating that DRX took place during welding [171]. Away from the weld line, large grains with the size about 18 μm from the base metal are present. A partially bonded region is shown in Fig. 8(c) comprised of a recrystallized region marked by the top dashed box and the unbonded region by the bottom box. Only coarse grains retained from the base metal are observed in the unbonded region, thus the EBSD results suggest that significant plastic deformation occurs near the weld interface, which has been commonly observed by other researchers. It is noted that the an extensive plastic deformation could occur across the bulk of the materials in ultrahigh power ultrasonic spot welding [150].

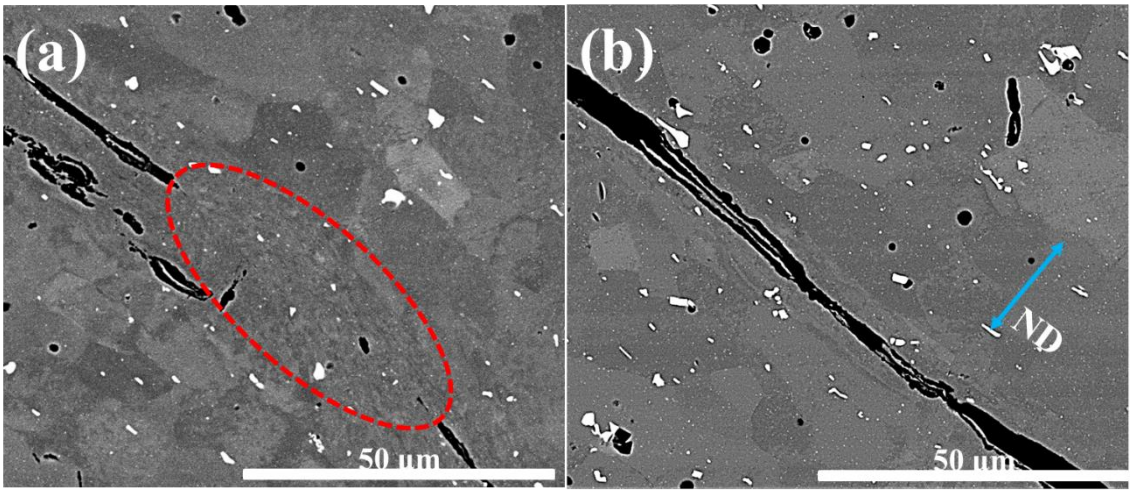

Figure 6.7 SEM images of an AA 6061 sample welded with an energy of 100 J, showing (a) partially bonded region near the weld line marked in the dashed oval, and (b) unbonded region

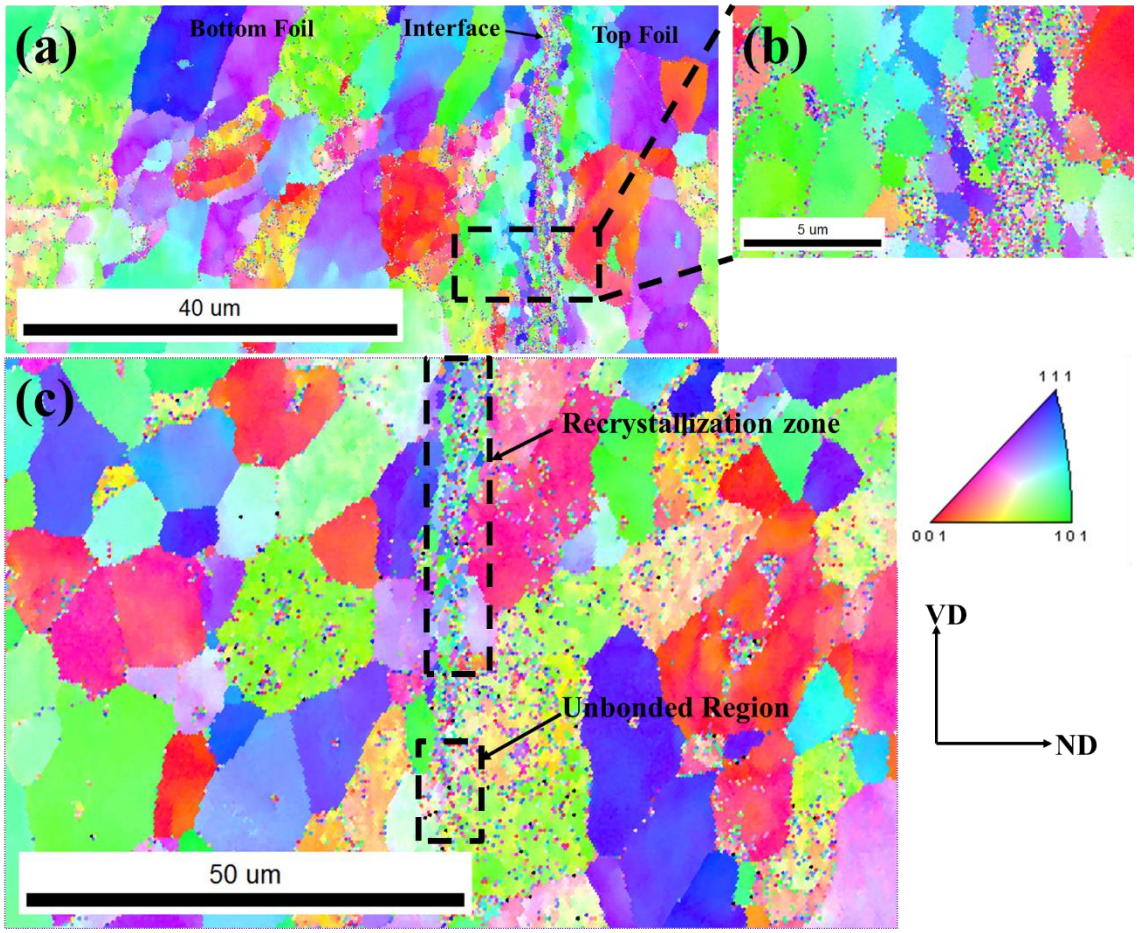

Figure 6.8 EBSD inverse pole plot of an AA 6061 sample welded with an energy of 275 J, showing (a) bonded region near the weld line, (b) higher magnification view of fine grains marked in the dashed box in (a), and (c) partially bonded region at a different location from (a)

6.4 Discussion

6.4.1 Bond evolution

To understand bond evolution, the maximum velocity profiles for the sonotrode tip, top foil, bottom foil, and anvil for a welding energy of 300 J are plotted together in Figure 6.9(a). The profiles for the first three locations are the same as those in Figure

6.4(e). As discussed earlier, the PDV system used had three channels for simultaneous measurement; the velocity of the anvil was measured separately in a repeated weld with the same energy of 300 J. Figure 6.9(b) shows the relative motion (i.e. velocity difference) between parts. The maximum velocity profiles are discerned into four stages: a slip stage, slip-stick transition stage, stick stage, and over-welding stage, which are labelled as Stage 1 to Stage 4 in Figure 6.9, respectively. These stages are divided based on the relative motion of the top and bottom foils. In the following discussion, the three pairs of interfaces are abbreviated as: S/T for sonotrode/top foil interface, T/B for top foil/bottom foil interface, and B/A for bottom foil/anvil interface.

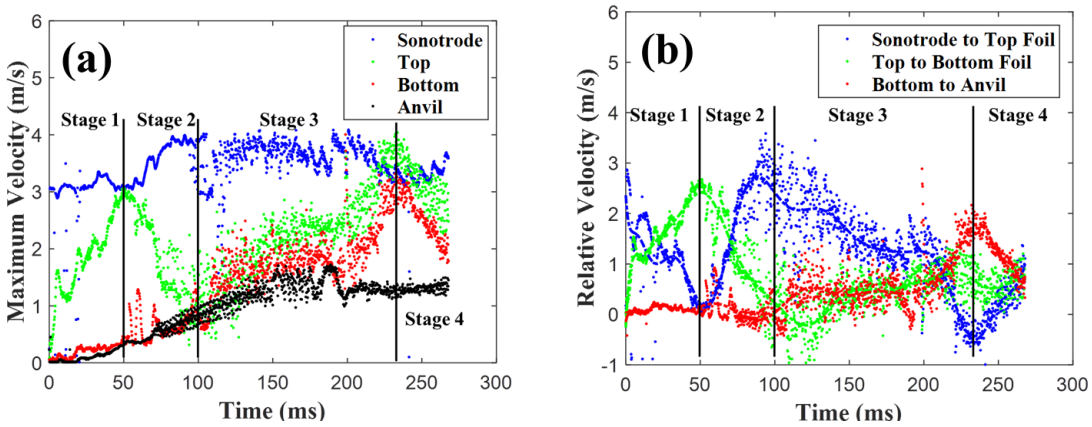

Figure 6.9 (a) Maximum velocity profiles of the sonotrode, two foils, and anvil for an over-welded sample with a welding energy of 300 J, and (b) the relative motion

In Stage 1 (slip stage, t <= 50 ms), the top foil is firmly gripped by the sonotrode tip and its velocity increases quickly to almost the same velocity as the sonotrode tip. At the same time, the bottom foil velocity increases much more slowly than the top foil. As a result, there is a large relative motion at the T/B interface, which is conducive to

removing contaminants, fracturing the oxide layer, and forming nascent metal surfaces. Scratch is the dominant feature at the T/B interface (see fracture surface of 10 J in Figure 6.5), which may evolve into a partially bonded region with increasing welding energy [172].

Stage 2 (slip-stick transition stage, 50 ms < t <= 100 ms) is characterized by a decrease in top foil velocity and an increase in bottom foil velocity until they reach the same value (which is lower than sonotrode velocity). At the beginning of this stage, local bonding is expected to form at a few asperities at the T/B interface; however, due to the short welding time and low temperature, it is insufficient for the vibration to disperse many of the oxides and contaminants, and collapse the asperities [173]. Moreover, it is likely the previously formed local bond could be torn apart by the relative motion at the T/B interface in one cycle but recovered at the next cycle. As a result, the majority of the faying surfaces is not bonded at this stage and thus no macroscopic bond forms. Nevertheless, the bonded region expands with increasing welding energy due to the collapse of more asperities which are softened by the frictional heat generated by the large relative motion at the T/B interface. As a result, the bond strength, albeit very low, gradually increases.

As the bond strength continues to rise, vibration transferred from the top foil to the bottom foil and anvil tip increases. Stronger coupling of the top foil, bottom foil, and anvil tip results in larger mass/inertia and higher elastic shear deformation that must be driven by the sonotrode. As gripping of the top foil by the sonotrode tip becomes

insufficient to maintain vibration at the sonotrode velocity, the top foil velocity thus drops and the relative motion at the S/T interface increases. The quick increase in relative motion between the sonotrode and top foil at this stage is also observed by other researchers using high speed cameras [161]. As shown in Figure 6.4, the exact end time for the slip-stick transition stage varies from 75 to 100 ms, indicating that a minimal energy of 20 J is necessary to fracture the surface oxides (predominantly Al_2O_3 and MgO in AA 6061 [155]) for bond initiation.

Stage 3 (stick stage, t > 100 ms) is the key stage during which a strong bond is formed. The beginning of this stage is marked by the increase in velocity for the two foils and anvil tip. This can be explained by the following reasons: the large relative motion between the sonotrode tip and top foil results in frictional heating at the S/T interface. Such heating is expected to cause a significant softening at the S/T interface region, which in turn leads to a deeper penetration of the sonotrode tip into the top foil and results in better gripping. As a result, the sonotrode tip is able to gradually increase the vibration velocity of the two foils and the anvil. At the same time, the relative motion at the T/B interface is low, largely preventing separation of the existing bonded regions. Furthermore, the temperature at the T/B interface continues to rise due to heat conduction from the S/T interface and deformation heating. The combined conditions of high temperature, plastic deformation, and low relative motion at the T/B interface are favorable for bond development and result in high bond quality.

The bond formation mechanism in Stage 3 (stick stage) is postulated to be DRX, the same mechanism suggested by other researchers [156]. DRX is evident due to the existence of a local recrystallized zone at the weld interface, which varies from a few isolated pockets at the initial period of the stick stage to a more continuous band by the end (see Figure 6.7 and Figure 6.8). As the area fraction of bonded region increases, the bond strength increases and the fracture mode changes from “interfacial fracture” to “nugget pull-out”. It is noted that DRX also occurs in other welding processes involving extensive thermo-mechanical deformation such as hot pressure welding and friction stir welding [174].

Finally, if the welding energy is further increased, over-welding can occur as marked by Stage 4 (over-welding stage, $t > 250$ ms) in Figure 6.9. Over-welding is likely caused by the following factors: first, due to its large mass, the anvil velocity levels off in the middle of Stage 3 at $t = 150$ ms. As a result, the relative motion at the B/A interface increases sharply, which in turn, leads to local heating, material softening, and more firm gripping of the bottom foil by the anvil tip. The better coupling by the anvil causes a rapid decrease in bottom foil velocity, thus the relative velocity of the two foils increases, indicating that the bonds formed in the previous stage may be broken. Second, heating at the S/T interface may lead to overheating and severe softening at the S/T interface, which may result in sonotrode tip sticking to top foil. Moreover, excessive thinning of the foils due to deeper penetration by the sonotrode and anvil results in reduced cross section area (load bearing capacity), and cracks may form at the edge of the nugget due to excess work hardening; both are commonly encountered when a high welding energy is used.

The aforementioned bond evolution is supported by the development of anvil tip imprints into the bottom foil as shown in Figure 6.10. For Stage 1 (slip stage), the small relative motion at the B/A interface leads to small indents with low penetration depth of approximately 18 μm by the anvil tip, as shown in Figure 6.10(a) and (d). As the bottom foil is heated and softened, the imprint gradually widens and deepens over the course of Stage 2 (slip-stick transition stage). In particular, during the transition from Stage 2 (slip-stick transition stage) to Stage 3 (stick stage), the penetration depth rises to ~ 50 μm as shown in Figure 6.10(b) and (d). As discussed previously, the anvil velocity levels off in the middle of Stage 3, resulting in a sharp rise in the relative motion and thus frictional heating at the B/A interface. Such heating and softening of the bottom foil lead to a significant increase in anvil penetration depth to ~ 160 μm at the end of Stage 3 as shown in Figure 6.10(c) and (d). As expected, the imprint on the bottom foil surface matches the knurl pattern of the anvil as shown in Figure 6.10(d), (e) and (f). In other words, the bottom foil is fully penetrated by the anvil at the end of Stage 3 for the welding energy of 250 J.

In summary, the contributions of the four different stages to the bond formation in USW of aluminum are the following: first, although there is no appreciable bond formed in the first two stages (slip stage and slip-stick transition stage) at low welding energy (10 to 20 J), they play an important role in removing contaminants, fracturing the oxide layer, and forming nascent metal surfaces at the T/B interface [173], all of which are essential to the start of Stage 3 (stick stage). The end of Stage 2 marks the moment of bond initiation. Second, the low relative motion at the T/B interface at Stage 3 (stick stage)

provides a favorable condition for bond development [162]. At this stage, the bond region expands as the temperature increases and the plastic deformation accumulates, contributing to higher DRX at the T/B interface region [157]. As the bond gets stronger, the fracture mode changes from “interfacial failure” at 150 J to “nugget pull-out” at 250 J. Finally, over-welding takes place if there is excess welding energy and has a detrimental effect on bond strength.

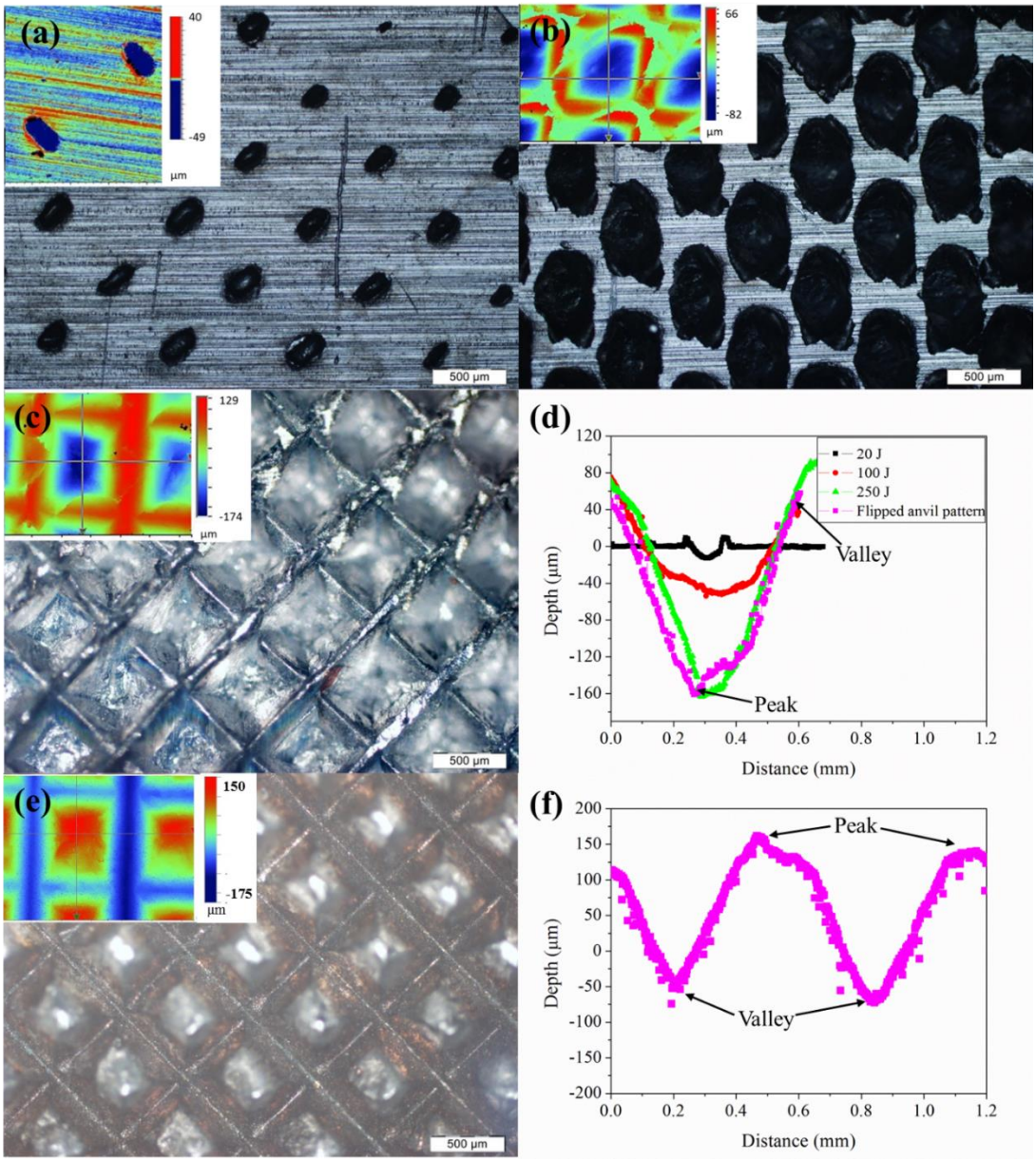

Figure 6.10 Optical images showing the imprint on the bottom foil by the anvil tip at welding energies of (a) 20 J, (b) 100 J and (c) 250 J with inset optical topographical images. (d) plots the typical depth profile across an indent at the three welding energies and the "tooth" profile of anvil. (e) is an optical image of the anvil knurl pattern with inset optical topographical image, and (f) the typical surface profile of the anvil knurl pattern

6.4.2 Peak temperature experienced at bond interface

DRX in Stage 3 (stick stage) can be used to imply the temperature condition at the T/B interface. Rajabi et al. [175] studied microstructure evolution during hot rolling of AA 6061 at three different temperatures (523 K (250 °C), 623 K (350 °C) and 723 K (450 °C)) and strain rates (7, 15 and 23 s^{-1}), and found that temperature had a significant effect on DRX. Particularly, dynamic recovery occurred instead of DRX at 523 K. On the other hand, DRX occurred at both 623 and 723 K, and resulted in formation of new precipitates at 723 K. Fan et al. [176] observed DRX in hot compression of AA 6061 at temperatures from 673 K (400 °C) to 773 K (500 °C) and strain rates from 0.01 to 1 s^{-1}, finding that deformation at higher strain rates led to finer subgrains.

In the present study, the precipitates in the recrystallized region at the interface, shown as white particles in Figure 6.7, resemble those in the bulk, albeit the precipitates in the recrystallized region have a smaller size distribution. In other words, the temperature at the interface is likely to be sufficiently high for DRX to occur while insufficiently high for new precipitates to form. Based on results of Rajabi et al. [175], it is estimated that the peak temperature at the T/B interface is about 623 K, which is consistent with the peak temperatures in USW reported by Sasaki et al. [161] . Finally, for USW of AA 6061, it has been estimated in the literature that the strain rate is on the order of 10^3 s^{-1} [158]. Such high deformation rate is expected to contribute to refined grains and improved local strength based on the results of Fan et al. [176].

The high temperature in USW results from several heat sources, including frictional heating at the interfaces, plastic deformation heating, and possible acoustic heating from the ultrasonic wave. The frictional heating originates by the large relative motion initially at the T/B interface in Stage 1 (slip stage) and Stage 2 (slip-stick transition stage), and later at the S/T interface in Stage 3 (stick stage). The temperature rise softens the materials locally, which in turn facilitates extensive plastic deformation at the faying surfaces under the combination of normal force and vibration shear force. The acoustic softening effect can reduce the apparent shear stress of the material either by superimposing an extra stress wave or by heat generation with selectively absorbed ultrasonic energy at the microstructural defects [177]. In particular, dislocations are activated with the absorbed energy and glide with enhanced mobility which causes severe plastic deformation to occur. Severe plastic deformation further contributes to a temperature increase due to dissipation of deformation heating.

6.4.3 Comparison with bonding mechanisms from literature

The four aforementioned bonding stages based on the relative motion of different parts during USW of aluminum are consistent with those reported in the literature. In particular, the slip stage, characterized by large relative motion at the T/B interface, was also observed by Sasaki and Hosokawa [178] using a high speed camera and DIC, and by de Vries [159] using a force sensor. The slip-stick transition stage has not been clearly reported in the literature. On the other hand, due to high relative motion at the T/B interface, frictional heating is expected to be the dominant heat source during the initial

two stages. This was indeed observed by Li et al. [160] based on heat flux measurements using thin-film microsensors.

The beginning of the stick stage in the present study is marked by the two foils vibrating together at a velocity lower than the sonotrode velocity. The velocity of the two foils then gradually increases to the sonotrode velocity over the course of the stick stage. This behavior was observed by Sasaki et al. [161], but was treated as two separate stages. In particular, they observed the two foils vibrating with similar amplitude while the large relative motion existed at the S/T interface, called the 2^{nd} stage. The 3^{rd} stage was then marked by an increase in the vibration amplitude of the two foils. Li et al. [160] described a plastic work stage and diffusion bonding stage, which is consistent to the expanded DRX region during the stick stage in the present study.

As mentioned previously, Sasaki et al. [161] did not observe a Stage 4 (over-welding stage) since the high speed camera was out of focus at longer welding time; however, using a medium speed camera with sampling frequency of 1000 Hz, de Vries [159] observed the extrusion of aluminum foils at longer welding times, an indication of over-welding. Moreover, based the data from a force sensor, they found that over-welding took place when the interface force exceeded the maximum sonotrode force, a situation that would lead to sliding of the top foil against the sonotrode. Such sliding of the top foil is consistent with the velocity decrease in the top foil as measured by the in-situ PDV in this study.

Finally, numerical modeling based on finite element analysis (FEA) has also been used to investigate the bonding process in ultrasonic welding. Kelly et al. [179] separated the ultrasonic consolidation process into a frictional heating dominated slip phase and plastic deformation heating dominated stick phase, which are consistent with the bond evolution found in the present study.

6.4.4 Effect of welding parameters

It is noted that only the welding energy is varied while all other welding parameters are held constant in the present study; other welding parameters include the vibration amplitude, normal clamping force, and vibration frequency. Additional variables include material properties (e.g., yield strength), material surface conditions (e.g., contaminants, oxides and surface roughness), geometry of the coupons, and geometry of the tools (e.g., the knurled patterns on the sonotrode and anvil). All of these variables can affect the vibration dynamics and the resulting weld quality. Despite the large number of variables, the fundamental mechanism of bond formation is likely to remain the same for USW of AAs. In the following section, the bonding mechanism observed in the present study is used to analyze the effect of several key welding parameters; the analysis results are compared to the published literature.

Vibration amplitude is an important parameter which significantly affects bond quality. In general, the weld strength increases with increasing amplitude. As the vibration frequency is typically set at 20 kHz by the spot welder, an increase in amplitude results in an increase in velocity. As discussed previously, the large relative motion at the

T/B interface in the first two welding stages (slip stage and slip-stick transition stage) is essential to disperse the surface contaminants and oxides to form nascent metal surfaces. In other words, the high relative motion at the T/B interface in the initial stages is crucial for subsequent bond formation. If the vibration amplitude (thus velocity) is too low, surface contaminants and oxides may be insufficiently cleaned, which in turn can limit bond development. To obtain such a large relative motion at the T/B interface, it is important that the top and bottom foils can be firmly gripped by the sonotrode and anvil tips, respectively. A coarse patterned anvil is found to be more effective in gripping the bottom coupon compared to a fine patterned anvil [162], which can improve the bond formation. On the other hand, a worn sonotrode or anvil tip and a low clamping force will likely reduce the gripping efficiency and therefore have a detrimental effect on bond formation.

As welding proceeds to Stage 3 (stick stage), the large relative motion shifts from the T/B interface to the S/T interface; higher vibration amplitude can lead to more heating at the S/T interface. As aluminum has high thermal conductivity, the heat can quickly diffuse to the T/B interface, facilitating DRX and thus bond development; however, as mentioned previously, over-welding can take place if the welding energy is too high. In Stage 4 (over-welding stage), the higher vibration amplitude can have a detrimental effect as it adds excess frictional heating to the joint. Al-Sarraf and Lucas [180] utilized a stepped amplitude where the vibration amplitude decreased from 40 to 17 μm toward the end of the welding process. It was found that the stepped amplitude resulted in a stronger

bond between 100 µm thick aluminum foils than was produced with a constant amplitude of either 40 or 17 µm.

Finally, thicker foils are more difficult to weld with USW because the increased rigidity can make gripping more difficult. Moreover, the ultrasonic energy decreases sharply across the thickness [181]. If the two coupons have different thickness, placing the thinner coupon on the sonotrode side is expected to yield better bond strength. Such stack-up arrangements will facilitate the large relative motion at the T/B interface in Stages 1 and 2 followed by diffusion of heat to that interface from the frictional heating at the S/T interface in Stage 3.

6.5 Summary and Conclusions

In summary, vibration kinetics at multiple locations were measured simultaneously in-situ during USW of AA 6061-T6. From the measured velocity profiles, the relative motion between sonotrode tip, aluminum specimens, and anvil was studied. The welding energy was systematically varied from low to high to observe bond formation. The lap-shear tensile strength, weld microstructure, and indentation profiles on the bottom foil by the anvil tip were correlated to the relative motion to understand the bonding mechanism.

Four different welding stages can be discerned from the velocity profiles: Stage 1 (slip stage), Stage 2 (slip-stick transition stage), Stage 3 (stick stage), and Stage 4 (over-welding stage). The first two stages (slip stage and slip-stick transition stage) are characterized by a large relative motion at the top and bottom foil interface, which is essential to disperse contaminants and oxides to form nascent metal surfaces. The relative

motion at the T/B interface diminishes toward the end of Stage 2 (slip-stick transition stage), marking bond initiation. Stage 3 (stick stage) is the key stage for bond development. Particularly, DRX occurs in the locally bonded regions due to the large plastic deformation and high temperature. DRX is expected to further strengthen the local bond by creating new, refined grains across the original bond line. As welding energy increases, the fraction of recrystallized regions also expands, resulting in an increase in bond strength and a change of failure mode from interfacial failure to button pull-out. The peak bond strength is obtained when the sonotrode and the two foils vibrate with a similar velocity. Finally, if the welding energy is too high, over-welding takes place, marked by a quick drop in bottom and top foil velocities. In this stage, the bond formed in Stage 3 (stick stage) can be broken and tool sticking can take place; both have a detrimental effect on the final bond strength.

Chapter 7 Conclusions and future work

7.1 Conclusions

AHSS and aluminum alloys have been widely used in automotive industries for light weighting and crash resistance of vehicles. The steep temperature gradient in resistance spot welding leads to the formation of complex microstructures in resistance spot welded AHSS, especially SCHAZ and CGHAZ, two locations prone to premature failure. Resistance spot welding of complex stack-ups is challenging due to the heat balance issue especially in those with large thickness ratio. For further light-weighting of vehicle, multi-materials structure involving AHSS and aluminum alloys have been increasingly used. A cost-effective and high-quality process to join aluminum to steel in mass production remains a long-standing challenge.

To address the above challenges, this research investigated the fundamentals of resistance spot welding of 2T and complex stack-ups of AHSS. In addition, a novel joining method was developed for Al to steel welding to reduce IMCs and improve mechanical properties. The key conclusions are summarized as follows.

7.1.1 Resistance spot welding of 2T stack-ups of Usibor 1500

- Microstructure

- SCHAZ consists of tempered martensite with hardness reduction of approximately 40% compared to base metal. The severe tempered region is 0 – 300 μm away from A_{C1} line.

- Process and microhardness modeling
  - The weld nugget size and electrode indentation calculated are consistent with those measured experimentally over a wide range of welding currents, validating the process model incorporating the existing electrical contact resistance formula.
  - The two current-off cycles at the end of each impulse lead to oscillation in thermal profiles for the region close to the centre (e.g., weld nugget and CGHAZ), while such effect on temperature profile is diminished for the SCHAZ, which is located furthest from the centre.
  - Isothermal tempering tests for simulated SCHAZ show that the extent of martensite tempering depends more strongly upon temperature than time. From the isothermal tempering data, the activation energy Q and the exponent n are determined to be 531.3 kJ/mol and 0.0658, respectively. By inputting these kinetic parameters into the non-isothermal JMAK equation, the predicted local hardness of SCHAZ is found to be consistent with that measured experimentally.

- Local constitutive behaviour for post-weld simulation
  - CGHAZ and SCHAZ microstructures are successfully recreated by Gleeble® 3800 in gauge section of tensile bars for measurement of local

constitutive behaviour by quasi-static tensile testing aided by DIC for strain mapping. CGHAZ with fully martensitic microstructure has a high UTS of 1800 MPa but a low fracture strain of 20%. On the other hand, SCHAZ with tempered martensite has a low UTS of 1100 MPa but a high fracture strain close to 60%. Such local constitutive behaviour of SCHAZ and CGHAZ is essential to accurately predict the deformation and failure behaviour of spot weld.

7.1.2 Resistance spot welding of complex stack-ups

- RSW of 3T stack-ups of 0.75mm JAC270/1.4mm JSC980/1.4mm JSC590 is investigated. Nugget size at thick/thick sheet interface and geometrical centre are increasing almost linearly with welding current. However, the nugget size at thin/thick sheet interface is rapidly increasing initially and saturates to be 5 mm as welding current is higher than 9 kA. The effect of welding current on nugget penetration into the thin sheet is similar to nugget size. It increases rapidly at low welding current and saturates to be 32% when the welding current is higher than 9 kA.

- With increasing electrode force from 3.4 kN to 4.4 kN, the current for nugget formation at interface A is 2 kA higher while the nugget formation at interface B is not significantly affected. Once the nugget penetrates into the thin sheet, the effect of electrode force on nugget size and penetration at both interfaces is negligible. However, the electrode indentation on thin sheet side with a higher electrode force

(4.4 kN) is about 12.5% larger compared to that with a lower electrode force of 3.4 kN at welding current of 9.5 kA.

- With Class 3 electrode on thin sheet side, nugget penetration can be 53%, which is approximately 20% higher than the one welded with traditional electrodes. Therefore, electrode materials/geometry has the most significant effect on nugget formation and penetration into thin sheet.

- 3D fully coupled electro-thermo-mechanical model is developed for resistance spot welding of complex 3T stack-ups. Heat generation at interface A is high at the initial stage of the welding process. Nugget initiation location can be dependent on the welding current. Nugget initiation at the geometrical centre of the stack-up when the welding current is lower than 8 kA. As welding current increases, the nugget initiation location shifts from geometrical centre to interface B and the middle sheet.

- RSW of 4T stack-ups of 0.75mm JAC270/1.4mm JSC980/1.4mm JSC590/1.5mm Usibor 1500 is also investigated. More than 30% of penetration into thin sheet can be achieved with nugget diameter saturating to 5 mm at thin/thick sheet interface. Based on process simulation and nugget formation kinetics study, nugget initiates at the JSC590/Usibor 1500 interface and grows in both lateral and through-thickness direction as welding time progresses.

7.1.3 U+RSW of Al to steel

- Al/steel joints created by U+RSW show a brazing feature with liquid aluminum wetting and spreading on solid steel surface.
- Baseline weld with the following parameters - Insert: 0.4 mm AA6061, electrode on Al side: dome-shaped electrode with surface diameter of 6 mm, electrode on steel: flat electrode, and machine: AC spot welder
    - No expulsion at Al/insert and insert/steel interface up to a high welding current of 16.5 kA
    - Less than 2 μm-thick IMCs are observed at weld center which does not deteriorate the bond strength of the joints welded by U+RSW method.
    - At the maximum welding current of 16.5 kA, a peak load of 3.2 kN can be obtained which is comparable to resistance spot welding of 1 mm-thick A6068 aluminum alloy.
    - Four different types of failure modes can be observed, and they are significantly affected by welding current. As the welding current is less than 13.6 kA, a shear fracture occurs at Al/insert interface (Type 1 failure mode). With welding current between 13.6 kA and 15.2 kA, the crack initiates at Al/insert interface, deviates into the insert and propagates through insert/steel interface (Type 2 failure mode). As the welding current is higher than 15.2 kA, Type 3 (nugget pull-out from aluminum sheet), Type 2 and Type 4 (interfacial fracture) failure modes at insert/steel interface can be observed.

- The quality of the intermediate joint affects the strength of the primary weld. Particularly, at a low ultrasonic spot welding energy of 50 J, a strong metallurgical bonding was not formed at insert/steel interface. Consequently, the tensile shear strength of primary joint is low. The tensile shear strength increases with the ultrasonic welding energy and does not depend the ultrasonic welding energy used as long as it is higher than 150 J.

- Improved weld with the following parameters - Insert: 0.3 mm-thick 3003, electrode geometry: F-type electrode on Al side, and machine: AC/MFDC
  - A consistent nugget pull-out failure mode can be observed as welding current is at/above 19 kA and the welding time of 83 ms in lap-shear tensile testing. The nugget size and peak load for the spot-welded joints with AC versus MFDC machines are comparable, which indicates that the results are not sensitive to the power supply. Similar to AA 6061 insert, the tensile shear strength is not adversely affected by the intermediate joint quality as the ultrasonic welding energy is higher than the threshold energy, i.e. 125 J, when AA3003 is used as an insert. 83 ms is found to be the optimum welding time in this study since although there is a 0.5 kN increase in peak joint strength with welding

time of 200 ms, severe electrode wear can be observed at the electrode on Al side, especially at high welding current.

- Wedge test is successfully applied in Al/steel U+RSW welds for in-situ observation of deformation and failure. At welding current of 17 kA, two competing mechanisms exist with the final failure at insert/steel interface. At high welding current of 19 kA, necking occurs at Al sheet with the final failure mode of button pull-out. The load displacement curve can be divided into two stages for Al/steel U+RSW welds, with relatively low opening force of 0.123 kN at Stage I and rapid increasing of opening force at Stage II.
- The failure modes of full weld at welding current of 17 kA and 19 kA are comparable to that of the half weld. However, inconsistency of failure modes of full weld and half weld can be observed at welding current of 20 kA, which could be due to occasionally-occurred expulsion at high welding current of 20 kA. The insertion force at Stage I of the full weld is about twice that of the half weld. However, the ratio of the peak insertion force of the full weld to the half weld at Stage II is about 1.73. The maximum peak joint strength of the full weld is approximately 1.6 kN, which is comparable to the maximum peak

strength in cross-tension test of AA6022/low carbon steel reported in literature.

7.1.4 In-situ relative motion measurement in USW

- Four different welding stages can be discerned from the velocity profiles: Stage 1 (slip stage), Stage 2 (slip-stick transition stage), Stage 3 (stick stage), and Stage 4 (over-welding stage).
- The first two stages (slip stage and slip-stick transition stage) are characterized by a large relative motion at the top and bottom foil interface, which is essential to disperse contaminants and oxides to form nascent metal surfaces. The relative motion at the T/B interface diminishes toward the end of Stage 2 (slip-stick transition stage), marking bond initiation. Stage 3 (stick stage) is the key stage for bond development. Particularly, DRX occurs in the locally bonded regions due to the large plastic deformation and high temperature. DRX is expected to further strengthen the local bond by creating new, refined grains across the original bond line. As welding energy increases, the fraction of recrystallized regions also expands, resulting in an increase in bond strength and a change of failure mode from interfacial failure to button pull-out. The peak bond strength is obtained when the sonotrode and the two foils vibrate with a similar velocity. Finally, if the welding energy is too high, over-welding takes place, marked by a quick drop in bottom and top foil velocities. In this

stage, the bond formed in Stage 3 (stick stage) can be broken and tool sticking can take place; both have a detrimental effect on the final bond strength.

- In addition to understanding bond formation, the characteristics of the relative motion obtained by in-situ PDV during USW can potentially be useful for improving bond quality by minimizing over-welding and sonotrode sticking. Moreover, the velocity profiles can provide quantitative experimental data for validation and calibration of numerical USW models.

7.2 Future work

7.2.1 Resistance spot welding of 4T stack-ups

A 3D fully coupled thermo-electro-mechanical model has been generated for process modeling of 4T stack-ups of JAC270/1.4mm JSC980/1.4mm JSC590/1.5mm Usibor 1500 for a better understanding of temperature evolution and nugget formation. However, an accurate prediction of the nugget formation in the 4T stack-ups is challenging due to the complicated contact resistance at each interface from different coatings. Besides validation by nugget size at each interface, further validation of 4T process model is required using the following two proposed methods. One is the thermal profile measurement by micro sensors at HAZs of each sheet for validation of 4T process model. Micro sensors can be deposited near to the weld metal and HAZs to measure the thermal history of each location with high accuracy. The other way is to investigate the nugget formation by using high speed video. In this case, half of the electrode and half of the welding current and electrode force need to be used, which might be deviate from the

actual welding condition. However, it will be an effective method for model validation since nugget formation at the cross-section of the weld can be observed directly. The nugget penetration into thin sheet can be increased by electrode force variation combined with pulsation to facilitate nugget formation at the thin/thick sheet interface

7.2.2 U+RSW of Al to steel

Aluminum alloy 6061 to uncoated low carbon steel has been successfully welded by U+RSW. However, multi-material structure with high joint quality of stronger aluminum alloys with coated AHSS has been a long-standing challenge. To obtained a high-quality joint of strong AA with coated AHSS by U+RSW, the fundamental knowledges of the relation of process-microstructure-properties of AA/AHSS welds need to be investigated.

The feasibility of wedge test of Al/steel U+RSW welds for full welds and half welds has been conducted and the relation of the strength of full welds and half welds have been investigated. However, a better understanding of the effect of the restrain for full weld and half weld on the failure modes during wedge testing by simulation.

Bibliography

[1] S. Keeler, M. Kimchi, P. Mooney, eds., Advanced High-Strength Steels Application Guidelines Version 6.0, 6th Edition., 2017.

[2] O.L. Ighodaro, E. Biro, Y.N. Zhou, Comparative effects of Al-Si and galvannealed coatings on the properties of resistance spot welded hot stamping steel joints, J. Mater. Process. Technol. 236 (2016) 64–72.

[3] S. Burget, S. Sommer, Modeling of deformation and failure behavior of dissimilar resistance spot welded joints under shear, axial and combined loading conditions, Icf13. (2013) 1–12.

[4] S. Sommer, S. Burget, F.W. Iwm, Characterization and modeling of the fracture behavior of spot welded joints in press hardened steels for crash simulation Contact data Summary Key Words Spot welds in ultra-high strength steels, (2015) 15–19.

[5] Z. Feng, S. Babu, M. Santella, B. Riemer, J. Gould, An incrementally coupled electrical-thermal-mechanical model for resistance spot welding, in: 5th Int. Conf. Trends Weld. Res., 1998: pp. 599–604.

[6] S. Dancette, V. Massardier-Jourdan, HAZ microstructures and local mechanical properties of high strength steels resistance spot welds, ISIJ Int. 51 (2011) 99–107.

[7] J. Gould, W. Peterson, J. Cruz, An examination of electric servo-guns for the

resistance spot welding of complex stack-ups, Weld. World. 57 (2013) 243–256.

[8] J. Yu, Effect of cover sheet on dissimilar three-steel sheets resistance spot welding, Int. J. Adv. Manuf. Technol. 89 (2017) 483–491.

[9] T. Sakayama, G. Murayma, Y. Naito, K. Saita, Y. Miyazakki, H. Oikawa, T. Nose, Dissimilar metal joining technologies for steel sheet and aluminum alloy sheet in auto body, Nippon STEEL Tech. Rep. (2013) 91–98.

[10] W. Zhang, D. Sun, L. Han, Y. Li, Optimised design of electrode morphology for novel dissimilar resistance spot welding of aluminium alloy and galvanised high strength steel, Mater. Des. 85 (2015) 461–470.

[11] D. Sun, Y. Zhang, Y. Liu, X. Gu, H. Li, Microstructures and mechanical properties of resistance spot welded joints of 16Mn steel and 6063-T6 aluminum alloy with different electrodes, Mater. Des. 109 (2016) 596–608.

[12] N. Chen, H.P. Wang, B.E. Carlson, D.R. Sigler, M. Wang, Fracture mechanisms of Al/steel resistance spot welds in lap shear test, J. Mater. Process. Technol. 243 (2017) 347–354.

[13] K. Miyamoto, S. Nakagawa, C. Sugi, H. Sakurai, A. Hirose, Dissimilar Joining of Aluminum Alloy and Steel by Resistance Spot Welding, SAE Int. J. Mater. Manuf. 2 (2009) 58–67.

[14] H. Oikawa, S. Ohmiya, T. Yoshimura, T. Saitoh, Resistance spot welding of steel and aluminium sheet using insert metal sheet, Sci. Technol. Weld. Join. 4 (1999) 80–88.

[15] M.R. Arghavani, M. Movahedi, A.H. Kokabi, Role of zinc layer in resistance spot

welding of aluminium to steel, Mater. Des. 102 (2016) 106–114.

[16] I. Ibrahim, R. Ito, T. Kakiuchi, Y. Uematsu, K. Yun, C. Matsuda, Fatigue behaviour of Al/steel dissimilar resistance spot welds fabricated using Al–Mg interlayer, Sci. Technol. Weld. Join. 21 (2016) 223–233.

[17] Z. Ling, Y. Li, Z. Luo, S. Ao, Z. Yin, Y. Gu, Q. Chen, Microstructure and fatigue behavior of resistance element welded dissimilar joints of DP780 dual-phase steel to 6061-T6 aluminum alloy, Int. J. Adv. Manuf. Technol. (2017).

[18] R. Qiu, N. Wang, H. Shi, L. Cui, L. Hou, K. Zhang, Joining steel to aluminum alloy by resistance spot welding with a rivet, Int. J. Mater. Res. 106 (2015) 60–65.

[19] R.G. Davies, Influence of martensite composition and content on the properties of dual phase steels, Metall. Trans. A. 9 (1978) 671–679.

[20] H.C. Chen, G.H. Cheng, Effect of martensite strength on the tensile strength of dual phase steels, J. Mater. Sci. 24 (1989) 1991–1994. doi:10.1007/BF02385411.

[21] H. Karbasian, a. E. Tekkaya, A review on hot stamping, J. Mater. Process. Technol. 210 (2010) 2103–2118.

[22] J. Bian, H. Mohrbacher, Novel alloying design for press hardening steels with better crash performance, in: Proc. AIST Int. Symp. New Dev. AHSS, 2013: p. 251.

[23] D.W. Fan, B.C. De Cooman, State-of-the-Knowledge on Coating Systems for Hot Stamped Parts, Steel Res. Int. 83 (2012) 412–433.

[24] ArcelorMittal, Steels for hot stamping -Usibor ®, (2014).

[25] M. Naderi, Hot stamping of ultra high strength steels, PhD Thesis. RWTH,

Aachen. (2008).

[26] T.G. Digges, C.R. Irish, N.L. Carwile, Effect of boron on the hardenability of high-purity alloys and commercial steels, J. Res. Natl. Bur. Stand. (1934). 41 (1948) 545.

[27] R.W. Richards, R.D. Jones, P.D. Clements, H. Clarke, Metallurgy of continuous hot dip aluminising, Int. Mater. Rev. 39 (1994) 191–212.

[28] J.H. Yoo, K.S. Yun, R.S. Kalubarme, C.N. Park, C.J. Park, Hydrogen generation using the corrosion of Al-Sn and Al-Si alloys in an alkaline solution, Met. Mater. Int. 20 (2014) 619–627.

[29] K. Easterling, Introduction to the Physical Metallurgy of Welding, Butterworths & Co., London, 1983.

[30] W.F.Smith, Structure and Properties of Engineering Alloys, 2nd edition, McGraw-Hill Science/Engineering/Math, New York, 1993.

[31] G.R. Speich, W.C. Leslie, Tempering of steel, Metall. Trans. 3 (1972) 1043–1054.

[32] D. Gaude-Fugarolas, Modelling of transformations during induction hardening and tempering, 2002.

[33] M. Jung, S.J. Lee, Y.K. Lee, Microstructural and dilatational changes during tempering and tempering kinetics in martensitic medium-carbon steel, Metall. Mater. Trans. A Phys. Metall. Mater. Sci. 40 (2009) 551–559.

[34] H. Bhadeshia, R. Honeycombe, Steels: microstructure and properties, 3rd ed., Amsterdam;Boston:Elsevier,Butterworth-Heinemann, 2006.

[35] T. Furuhara, K. Kobayashi, T. Maki, Control of cementite precipitation in lath

martensite by rapid heating and tempering, ISIJ Int. 44 (2004) 1937–1944.

[36] S.T. Ahn, D.S. Kim, W.J. Nam, Microstructural evolution and mechanical properties of low alloy steel tempered by induction heating, J. Mater. Process. Technol. 160 (2005) 54–58.

[37] V.H. Baltazar Hernandez, S.S. Nayak, Y. Zhou, Tempering of Martensite in Dual-Phase Steels and Its Effects on Softening Behavior, Metall. Mater. Trans. A. 42 (2011) 3115–3129.

[38] L.D. Jaffe, B. Swartz, Time-temperature relations in tempering steel, Watertown, Mass., 1944.

[39] M. Avrami, Kinetics of Phase Change. II Transformation-Time Relations for Random Distribution of Nuclei, J. Chemcial Phys. 8 (1940).

[40] M. Avrami, Kinetics of Phase Change. I General Theory, J. Chemcial Phys. 7 (1939).

[41] E. Biro, Haz softening kinetics in dual-phase and martensitic steels, McMaster University, 2013.

[42] W. Zhang, Probing heat transfer, fluid flow and microstructural evolution during fusion welding of alloys, The Pennsylvania State University, 2004.

[43] S.K. Jadav, J. Gandhi, Experimental Investigation of Resistance Spot welding: A Literature Review, Int. J. Eng. Res. Technol. 3 (2014) 1503–1506.

[44] Menachem Kimichi, Resistance spot welding lectures, Columbus, 2015.

[45] K. Hofman, M. Soter, C. Orsette, S. Villaire, M. Prokator, AC or DC for resistance welding dual-phase 600?, Weld. J. 84 (2005) 46–48.

[46] W. Li, E. Feng, D. Cerjanec, G.A. Grzadzinski, ENERGY CONSUMPTION IN AC AND MFDC RESISTANCE SPOT WELDING, Sheet Met. Weld. Conf. XI. (2004) 1–12.

[47] B. Niu, Y. Chi, H. Zhang, Electrode clamping force regulation of servo gun mounted on resistance spot welding robot, IEEE/ASME Int. Conf. Adv. Intell. Mechatronics, AIM. (2008) 576–582.

[48] M. Muneo, T. Koichi, O. Kenji, Development of Next Generation Resistance Spot Welding Technologies Contributing to Auto Body Weight Reduction, 2013.

[49] H. Zhang, J. Senkara, Resistance Welding: Fundamentals and Applications, CRC Press Taylor & Francis Group, 2006.

[50] S.A. Gedeon, T.W. Eagar, Resistance spot welding of galvanized steel: Part II. Mechanisms of spot weld nugget formation, Metall. Trans. B. 17 (1986) 887–901.

[51] S.A. Gedeon, C.D. Sorensen, K.T. Ulrich, T.W. Eagar, Measurement of Dynamic Electrical and Mechanical Properties of Resistance Spot Welds Displacement curves and dynamic resistance provide significant data for evaluating nugget quality, Weld. J. 66 (1987) 378s–385s.

[52] O.L.R. Ighodaro, E. Biro, Y.N. Zhou, Study and Applications of Dynamic Resistance Profiles During Resistance Spot Welding of Coated Hot-Stamping Steels, Metall. Mater. Trans. A Phys. Metall. Mater. Sci. 48 (2017) 745–758.

[53] Y.-S. Jong, Y.-K. Lee, D.-C. Kim, M.-J. Kang, I.-S. Hwang, W.-B. Lee, Microstructural Evolution and Mechanical Properties of Resistance Spot Welded Ultra High Strength Steel Containing Boron, Mater. Trans. 52 (2011) 1330–1333.

[54] Y. Yu, C. Wang, S.J. Chen, Z.Y. Lu, Study on Intermediate Frequency Spot Welding Process of Hot Stamping High Strength Steel, Adv. Mater. Res. 339 (2011) 375–378.

[55] C.-W. Ji, I. Jo, H. Lee, I.-D. Choi, Y. do Kim, Y.-D. Park, Effects of surface coating on weld growth of resistance spot-welded hot-stamped boron steels, J. Mech. Sci. Technol. 28 (2015) 4761–4769.

[56] D.C. Saha, C.W. Ji, Y.D. Park, Coating behaviour and nugget formation during resistance welding of hot forming steels, Sci. Technol. Weld. Join. 20 (2015) 708–720.

[57] J.A. Greenwood, Temperature in spot welding, Br. Weld. J. 6 (1961) 316–322.

[58] J.E. Gould, An Examination of Nugget Development during Spot Welding, Using Both Experimental and Analytical Techniques., Weld. J. 66 (1987) 1s–10s.

[59] H.A. Nied, The Finite Element Modeling of the Resistance Spot Welding Process, Weld. J. (1984) 123–132.

[60] C.-L. Tsai, O. Jammal, J.C. Papritan, D.W. Dickinson, Modeling of Resistance Spot Weld Nugget Growth -Applications for the Automotive Industry, Weld. J. (1990) 47–54.

[61] Z. Hou, I.-S. Kim, Y. Wang, C. Li, C. Chen, Finite element analysis for the mechanical features of resistance spot welding process, J. Mater. Process. Technol. 185 (2007) 160–165.

[62] I.R. Nodeh, S. Serajzadeh, A.H. Kokabi, Simulation of welding residual stresses in resistance spot welding, FE modeling and X-ray verification, J. Mater. Process.

Technol. 205 (2008) 60–69.

[63] H. Eisazadeh, M. Hamedi, A. Halvaee, New parametric study of nugget size in resistance spot welding process using finite element method, Mater. Des. 31 (2010) 149–157.

[64] H. Moshayedi, I. Sattari-Far, Numerical and experimental study of nugget size growth in resistance spot welding of austenitic stainless steels, J. Mater. Process. Technol. 212 (2012) 347–354.

[65] J. Wang, H.-P. Wang, F. Lu, B.E. Carlson, D.R. Sigler, Analysis of Al-steel resistance spot welding process by developing a fully coupled multi-physics simulation model, Int. J. Heat Mass Transf. 89 (2015) 1061–1072.

[66] Z. Wan, H.P. Wang, M. Wang, B.E. Carlson, D.R. Sigler, Numerical simulation of resistance spot welding of Al to zinc-coated steel with improved representation of contact interactions, Int. J. Heat Mass Transf. 101 (2016) 749–763.

[67] S. Babu, M. Santella, Empirical model of effects of pressure and temperature on electrical contact resistance of metals, Sci. Technol. Weld. Join. 6 (2001).

[68] P. Rogeon, P. Carre, J. Costa, G. Sibilia, G. Saindrenan, Characterization of electrical contact conditions in spot welding assemblies, J. Mater. Process. Technol. 195 (2008) 117–124.

[69] J. Kaars, P. Mayr, K. Koppe, Generalized dynamic transition resistance in spot welding of aluminized 22MnB5, Mater. Des. 106 (2016) 139–145.

[70] A. Peer, Y. Lu, T. Abke, M. Kimchi, Deformation Behaviors of Subcritical Heat-affected Zone of Ultra-high Strength Steel Resistance Spot Welds, in: 9th Int.

Semin. Conf. Adv. Resist. Weld., Miami, FL, 2016: pp. 1–15.

[71] Y. Lu, A. Peer, T. Abke, M. Kimchi, W. Zhang, Heat-Affected Zone Microstructure and Local Constitutive Behaviors of Resistance Spot Welded Hot-Stamped Steel, in: Sheet Met. Weld. Conf. XVII, Livonia, MI, 2016: pp. 1–17.

[72] S. Burget, S. Sommer, Modeling of deformation and failure behavior of dissimilar resistance spot welded joints under shear, axial and combined loading conditions, in: 13th Int. Conf. Fract., 2013: pp. 1–12.

[73] M. Pouranvari, S.P.H. Marashi, Critical review of automotive steels spot welding: process, structure and properties, Sci. Technol. Weld. Join. 18 (2013) 361–403.

[74] S.S. Babu, B.W. Riemer, M.L. Santella, Z. Feng, Integrated Thermal-Microstructure Model to Predict the Property Gradients in Resistance Spot Steel Welds, in: Proc. Sheet Met. Weld. Conf. VIII, Detroit, 1998.

[75] M. Pouranvari, S.P.H. Marashi, Critical review of automotive steels spot welding: process, structure and properties, Sci. Technol. Weld. Join. 18 (2013) 361–403.

[76] M. Pouranvari, S.P.H. Marashi, Failure of resistance spot welds: tensile shear versus coach peel loading conditions, Ironmak. Steelmak. 39 (2012) 104–111.

[77] AWS Standards, AWS D8.1M, “Specification for automotive weld quality - resistance spot welding of Steel,” 2007.

[78] G.R. Payen, H. Klöcker, A. Lens, D.S. Wilkinson, J.D. Embury, Design of an in situ mechanical test for spot-welded joints, Eng. Fract. Mech. 96 (2012) 528–538.

[79] R. Lacroix, J. Monatte, A. Lens, G. Kermouche, J.-M. Bergheau, H. Klöcker, Spot weld strength determination using the wedge test: in-situ observations and coupled

simulations, Appl. Mech. Mater. 24–25 (2010) 299–304.

[80] A. Peer, Performance Testing and Modeling of UltraHigh Strength Steel and Complex Stack-Up Resistance Spot Welds, The Ohio State University, 2017.

[81] S. Dancette, D. Fabrègue, V. Massardier, J. Merlin, T. Dupuy, M. Bouzekri, Experimental and modeling investigation of the failure resistance of Advanced High Strength Steels spot welds, Eng. Fract. Mech. 78 (2011) 2259–2272.

[82] M. Pouranvari, S.P.H. Marashi, Failure mode transition in AHSS resistance spot welds. Part I. Controlling factors, Mater. Sci. Eng. A. 528 (2011) 8337–8343.

[83] M. Pouranvari, S.P.H. Marashi, D.S. Safanama, Failure mode transition in AHSS resistance spot welds. Part II: Experimental investigation and model validation, Mater. Sci. Eng. A. 528 (2011) 8344–8352.

[84] H.Y. Zhang, Resistance Welding: Fundamentals and Applications, Taylor & Francis CRC Press, 2005.

[85] D. Radakovic, M. Tumuluru, Predicting resistance spot weld failure modes in shear tension tests of advanced high-strength automotive steels, Weld. J. 87 (2008) 96-s - 105-s.

[86] Y.J. Chao, Ultimate Strength and Failure Mechanism of Resistance Spot Weld Subjected to Tensile, Shear, or Combined Tensile/Shear Loads, J. Eng. Mater. Technol. 125 (2003) 125.

[87] C. Ullner, S. Brauser, A. Subaric-Leitis, G. Weber, M. Rethmeier, Determination of local stress-strain properties of resistance spot-welded joints of advanced high-strength steels using the instrumented indentation test, J. Mater. Sci. 47 (2012)

1504–1513.

[88] T. Coon, A. Elliott, A. Joaquin, R. Koganti, A. Wexler, R. Bhatnagar, S. Lalam, Resistance Spot Weldability of Three Metal Stack Dual Phase 600 Hot-dipped Galvanized Steel, in: SAE, Detroit, MI, USA, 2007.

[89] C. V Nielsen, K.S. Friis, W. Zhang, N. Bay, Three-Sheet Spot Welding of Advanced High-Strength Steels, Weld. J. 90 (2011) 32s–40s.

[90] X. Wan, Y. Wang, P. Zhang, Modelling the effect of welding current on resistance spot welding of DP600 steel, J. Mater. Process. Technol. 214 (2014) 2723–2729.

[91] N. Ma, H. Murakawa, Numerical and experimental study on nugget formation in resistance spot welding for three pieces of high strength steel sheets, J. Mater. Process. Technol. 210 (2010) 2045–2052.

[92] J. Shen, Y. Zhang, X. Lai, P.C. Wang, Modeling of resistance spot welding of multiple stacks of steel sheets, Mater. Des. 32 (2011) 550–560.

[93] H. Eizadi, S.P.H. Marash, On the resistance spot welding of four-sheet stack of unequal sheet thickness, Sci. Technol. Weld. Join. 21 (2016) 632–637.

[94] F. Haddadi, Rapid intermetallic growth under high strain rate deformation during high power ultrasonic spot welding of aluminium to steel, Mater. Des. 66 (2015) 459–472.

[95] D. Sun, Y. Zhang, Y. Liu, X. Gu, H. Li, Microstructures and mechanical properties of resistance spot welded joints of 16Mn steel and 6063-T6 aluminum alloy with different electrodes, Mater. Des. 109 (2016) 596–608.

[96] A. Macwan, A. Kumar, D.L. Chen, Ultrasonic spot welded 6111-T4 aluminum

alloy to galvanized high-strength low-alloy steel : Microstructure and mechanical properties, JMADE. 113 (2017) 284–296.

[97] X. Liu, S. Lan, J. Ni, Analysis of process parameters effects on friction stir welding of dissimilar aluminum alloy to advanced high strength steel, Mater. Des. 59 (2014) 50–62.

[98] S. Chen, G.S. Daehn, A. Vivek, B. Liu, S.R. Hansen, J. Huang, S. Lin, Interfacial microstructures and mechanical property of vaporizing foil actuator welding of aluminum alloy to steel, Mater. Sci. Eng. A. 659 (2016) 12–21.

[99] H. Yu, Z. Xu, Z. Fan, Z. Zhao, C. Li, Mechanical property and microstructure of aluminum alloy-steel tubes joint by magnetic pulse welding, Mater. Sci. Eng. A. 561 (2013) 259–265.

[100] Y. Abe, T. Kato, K. Mori, Joinability of aluminium alloy and mild steel sheets by self piercing rivet, J. Mater. Process. Technol. 177 (2006) 417–421.

[101] W.H. Zhang, X.M. Qiu, D.Q. Sun, L.J. Han, Effects of resistance spot welding parameters on microstructures and mechanical properties of dissimilar material joints of galvanised high strength steel and aluminium alloy, Sci. Technol. Weld. Join. 16 (2011) 153–161.

[102] W. Zhang, D. Sun, L. Han, W. Gao, X. Qiu, Characterization of Intermetallic Compounds in Dissimilar Material Resistance Spot Welded Joint of High Strength Steel and Aluminum Alloy, ISIJ Int. 51 (2011) 1870–1877.

[103] S. Satonaka, C. Iwamoto, R. Qui, T. Fujioka, Trends and new applications of spot welding for aluminium alloy sheets, Weld. Int. 20 (2006) 858–864.

[104] R.F. Qiu, C. Iwamoto, S. Satonaka, Interfacial reaction layer in resistance spot welded joint between aluminium alloy and austenitic stainless steel, Mater. Sci. Technol. 26 (2010) 243–246.

[105] R. Qiu, C. Iwamoto, S. Satonaka, The influence of reaction layer on the strength of aluminum/steel joint welded by resistance spot welding, Mater. Charact. 60 (2009) 156–159.

[106] R. Qiu, C. Iwamoto, S. Satonaka, Interfacial microstructure and strength of steel/aluminum alloy joints welded by resistance spot welding with cover plate, J. Mater. Process. Technol. 209 (2009) 4186–4193.

[107] R. Qiu, S. Satonaka, C. Iwamoto, Effect of interfacial reaction layer continuity on the tensile strength of resistance spot welded joints between aluminum alloy and steels, Mater. Des. 30 (2009) 3686–3689.

[108] R. Qiu, H. Shi, K. Zhang, Y. Tu, C. Iwamoto, S. Satonaka, Interfacial characterization of joint between mild steel and aluminum alloy welded by resistance spot welding, Mater. Charact. 61 (2010) 684–688.

[109] X. Sun, E. V Stephens, M.A. Khaleel, H. Shao, M. Kimchi, Resistance Spot Welding of Aluminum Alloy to Steel with Transition Material - From Process to Performance - Part 1: Experimental Study - Weld Strength, Failure Mode, and Fatigue Life were Compared with Self-Piercing Rivets of the same Dissimilar Metals Co, Weld. J. 83 (2004) 188S–195S.

[110] W. Zhang, D. Sun, L. Han, D. Liu, Interfacial microstructure and mechanical property of resistance spot welded joint of high strength steel and aluminium alloy

with 4047 AlSi12 interlayer, Mater. Des. 57 (2014) 186–194.

[111] Honda R&D, Hot stamped boron steel composition, Unpublished. (2017).

[112] ISO 18278-2, Resistance welding - weldability, part 2 : alternative procedures for the assessment of sheet steels for spot welding, 2004.

[113] M.S. Xia, E. Biro, Z.L. Tian, Y.N. Zhou, Effects of Heat Input and Martensite on HAZ Softening in Laser Welding of Dual Phase Steels, ISIJ Int. 48 (2008) 809–814.

[114] E. Biro, J.R. McDermid, S. Vignier, Y. Norman Zhou, Decoupling of the softening processes during rapid tempering of a martensitic steel, Mater. Sci. Eng. A. 615 (2014) 395–404.

[115] E. Biro, J.R. McDermid, J.D. Embury, Y. Zhou, Softening kinetics in the subcritical heat-affected zone of dual-phase steel welds, Metall. Mater. Trans. A Phys. Metall. Mater. Sci. 41 (2010) 2348–2356.

[116] W. Zhang, J.W. Elmer, T. DebRoy, Kinetics of ferrite to austenite transformation during welding of 1005 steel, Scr. Mater. 46 (2002) 753–757.

[117] J.W. Elmer, T.A. Palmer, W. Zhang, T. DebRoy, Time resolved X-ray diffraction observations of phase transformations in transient arc welds, Sci. Technol. Weld. Join. 13 (2008) 265–277.

[118] J.A. Goldak, M. Akhlaghi, Computational Welding Mechanics, Springer US, 2005.

[119] T. Mukherjee, J.S. Zuback, W. Zhang, T. DebRoy, Residual stresses and distortion in additively manufactured compositionally graded and dissimilar joints, Comput.

Mater. Sci. 143 (2018) 325–337.

[120] D. LÖVEBORN, 3D FE Simulations of Resistance Spot Welding, KTH, 2016.

[121] W. Li, D. Cerjanec, G.A. Grzadzinski, A Comparative Study of Single-Phase AC and Multiphase DC Resistance Spot Welding, J. Manuf. Sci. Eng. 127 (2005) 583.

[122] J. Blaber, B. Adair, A. Antoniou, Ncorr: Open-Source 2D Digital Image Correlation Matlab Software, Exp. Mech. (2015) 1105–1122.

[123] G.Z. Voyiadjis, R. Peters, Size effects in nanoindentation: An experimental and analytical study, Acta Mech. 211 (2010) 131–153.

[124] MTS Nanoindenter XP Manual, MTS Systems Corporation, 2002.

[125] M. Dao, N. Chollacoop, K.J.V.A.N. Vliet, T.A. Venkatesh, Computational modeling of the forward and reverse problems in instrumented sharp indentation, Acta Mater. 49 (2001) 3899–3918.

[126] AWS D8.1 M:2007 Specification for Automotive Weld Quality-Resistance Spot Welding of Steel, 1st Edition, 2007.

[127] C. Kim, M.J. Kang, Y.D. Park, Laser welding of Al-Si coated hot stamping steel, Procedia Eng. 10 (2011) 2226–2231.

[128] D.C. Saha, E. Biro, A.P. Gerlich, N.Y. Zhou, Fusion zone microstructure evolution of fiber laser welded press-hardened steels, Scr. Mater. 121 (2016) 18–22.

[129] M.S.O. Sherepenko, M.S.N. Holtschke, P. Ing, S. Jüttner, Microstructural Imperfections in the HAZ of Resistance Spot Welded Ultra High Strength Steel 22MnB5 and Their Impact on Joint Fracture, in: 70th IIW Annu. Assem. Int. Conf., 2017.

[130] V.H. Baltazar Hernandez, S.K. Panda, Y. Okita, N.Y. Zhou, A study on heat affected zone softening in resistance spot welded dual phase steel by nanoindentation, J. Mater. Sci. 45 (2009) 1638–1647.

[131] J. Nemecek, ed., Application of nanoindentation technique in martensitic Structures, in: Nanoindentation Mater. Sci., InTech, 2012: p. 114.

[132] H. Bhadeshia, S.R. Honeycombe, Steels: Microstructure and Properties, 3rd ed., Cambridge, 2006.

[133] J.W. Christian, The Theory of Transformations in Metals and Alloys, 3rd ed., Pergamon Press, Oxford, 2002.

[134] Y. Lu, A. Peer, T. Abke, M. Kimchi, W. Zheng, Subcritical Heat Affected Zone Softening in Hot-stamped Boron Steel during Resistance Spot Welding, Mater. Des. 155 (2018) 170–184.

[135] E. Biro, S. Vignier, C. Kaczynski, J.R. McDermid, E. Lucas, J.D. Embury, Y.N. Zhou, Predicting Transient Softening in the Sub-Critical Heat-Affected Zone of Dual-Phase and Martensitic Steel Welds, ISIJ Int. 53 (2013) 110–118.

[136] D. Dickinson, J. Franklin, A. Stanya, Characterization of spot welding behavior by dynamic electrical parameter monitoring, Weld. Reseach Suppl. 6 (1980) 170–176.

[137] M. Pouranvari, S.P.H. Marashi, Weld nugget formation and mechanical properties of three-sheet resistance spot welded low carbon steel, Can. Metall. Q. 51 (2012) 105–110.

[138] D.C. Saha, Kinetics of Carbide Precipitation during Laser Beam Welding of Dual-Phase and Martensitic Steels by, University of Waterloo, 2016.

[139] O. Sherepenko, S. Jüttner, Transient softening at the fusion boundary in resistance spot welded ultra high strengths steel 22MnB5 and its impact on fracture processes, in: IIW CIII-1791-17, 2017: pp. 1–32.

[140] Y. Lu, H. Song, G.A. Taber, D.R. Foster, G.S. Daehn, W. Zhang, In-situ measurement of relative motion during ultrasonic spot welding of aluminum alloy using Photonic Doppler Velocimetry, J. Mater. Process. Technol. 231 (2016) 431–440.

[141] L. Xu, L. Wang, Y.C. Chen, J.D. Robson, P.B. Prangnell, Effect of Interfacial Reaction on the Mechanical Performance of Steel to Aluminum Dissimilar Ultrasonic Spot Welds, Metall. Mater. Trans. A Phys. Metall. Mater. Sci. 47 (2015) 334–346.

[142] A.M. Pereira, J.M. Ferreira, A. Loureiro, J.D.M. Costa, P.J. Bártolo, Effect of process parameters on the strength of resistance spot welds in 6082-T6 aluminium alloy, Mater. Des. 31 (2010) 2454–2463.

[143] R.S. Florea, K.N. Solanki, D.J. Bammann, J.C. Baird, J.B. Jordon, M.P. Castanier, Resistance spot welding of 6061-T6 aluminum: Failure loads and deformation, Mater. Des. 34 (2012) 624–630.

[144] K.W. Zhang, W. Zhang, Unpublished work on wedge testing, (2018).

[145] N. Chen, H.P. Wang, B.E. Carlson, D.R. Sigler, M. Wang, Fracture mechanisms of Al/steel resistance spot welds in coach peel and cross tension testing, J. Mater. Process. Technol. 252 (2018) 348–361.

[146] F. Haddadi, F. Abu-Farha, Microstructural and mechanical performance of

aluminium to steel high power ultrasonic spot welding, J. Mater. Process. Technol. 225 (2015) 262–274.

[147] S.S. Lee, T.H. Kim, J.S. Hu, W.W. Cai, J. a. Abell, J. Li, Characterization of Joint Quality in Ultrasonic Welding of Battery Tabs, J. Manuf. Sci. Eng. 135 (2013) 21004.

[148] R. Jahn, R. Cooper, D. Wilkosz, The Effect of Anvil Geometry and Welding Energy on Microstructures in Ultrasonic Spot Welds of AA6111-T4, Metall. Mater. Trans. A. 38 (2007) 570–583.

[149] D. Bakavos, P.B. Prangnell, Effect of reduced or zero pin length and anvil insulation on friction stir spot welding thin gauge 6111 automotive sheet, Sci. Technol. Weld. Join. 14 (2009) 443–456.

[150] D. Bakavos, P.B. Prangnell, Mechanisms of joint and microstructure formation in high power ultrasonic spot welding 6111 aluminium automotive sheet, Mater. Sci. Eng. A. 527 (2010) 6320–6334.

[151] Y.-C. Chen, D. Bakavos, a. Gholinia, P.B. Prangnell, HAZ development and accelerated post-weld natural ageing in ultrasonic spot welding aluminium 6111-T4 automotive sheet, Acta Mater. 60 (2012) 2816–2828.

[152] D. Schick, S.S. Babu, D.R. Foster, M. Dapino, M. Short, J.C. Lippold, Transient thermal response in ultrasonic additive manufacturing of aluminum 3003, Rapid Prototyp. J. 17 (2011) 369–379.

[153] C.Y. Kong, R.C. Soar, P.M. Dickens, Optimum process parameters for ultrasonic consolidation of 3003 aluminium, J. Mater. Process. Technol. 146 (2004) 181–187.

[154] C. (Sam) Zhang, A. Deceuster, L. Li, A Method for Bond Strength Evaluation for Laminated Structures with Application to Ultrasonic Consolidation, J. Mater. Eng. Perform. 18 (2009) 1124–1132.

[155] C.Y. Kong, R.C. Soar, P.M. Dickens, Characterisation of aluminium alloy 6061 for the ultrasonic consolidation process, Mater. Sci. Eng. A. 363 (2003) 99–106.

[156] E. Mariani, E. Ghassemieh, Microstructure evolution of 6061 O Al alloy during ultrasonic consolidation: An insight from electron backscatter diffraction, Acta Mater. 58 (2010) 2492–2503.

[157] R.R. Dehoff, S.S. Babu, Characterization of interfacial microstructures in 3003 aluminum alloy blocks fabricated by ultrasonic additive manufacturing, Acta Mater. 58 (2010) 4305–4315.

[158] I. Gunduz, T. Ando, E. Shattuck, P. Wong, C. Doumanidis, Enhanced diffusion and phase transformations during ultrasonic welding of zinc and aluminum, Scr. Mater. 52 (2005) 939–943.

[159] E. de Vries, Mechanics and mechanisms of ultrasonic metal welding, The Ohio State Univeristy, 2004.

[160] H. Li, H. Choi, C. Ma, J. Zhao, H. Jiang, W. Cai, J. a. Abell, X. Li, Transient Temperature and Heat Flux Measurement in Ultrasonic Joining of Battery Tabs Using Thin-Film Microsensors, J. Manuf. Sci. Eng. 135 (2013) 51015.

[161] T. Sasaki, T. Watanabe, Y. Hosokawa, a Yanagisawa, Analysis for relative motion in ultrasonic welding of aluminium sheet, Sci. Technol. Weld. Join. 18 (2013) 19–24.

[162] S.S. Lee, T.H. Kim, J.S. Hu, W.W. Cai, J. a. Abell, Analysis of Weld Formation in Multilayer Ultrasonic Metal Welding Using High-Speed Images, J. Manuf. Sci. Eng. 137 (2015) 31016-1-31016–8.

[163] D. Balle, F., Wagner, G., Eifler, Characterization of the ultrasonic welding process through high-resolution laser-Doppler vibrometry, InFocus-Optical Meas. Solut. (2009) 1–4.

[164] J.R. Johnson, G. Taber, A. Vivek, Y. Zhang, S. Golowin, K. Banik, G.K. Fenton, G.S. Daehn, Coupling Experiment and Simulation in Electromagnetic Forming Using Photon Doppler Velocimetry, Steel Res. Int. 80 (2009) 359–365.

[165] H. Wang, D. Liu, G. Taber, Laser Impact Welding–Process Introduction and Key Variables, ICHSF2012. (2012) 255–264.

[166] D. Foster, G. Taber, Low Velocity PDV Measurements for Resonance Testing of Monolithic and Laminated Aluminum Components, 6th Annu. Photonic Doppler Velocim. Work. (2011).

[167] D.R. Foster, G. a. Taber, S.S. Babu, G.S. Daehn, In situ velocity measurements of very high power ultrasonic additive manufacturing using a photonic Doppler velocimeter, Sci. Technol. Weld. Join. 19 (2014) 157–163.

[168] S. Heinz, F. Balle, G. Wagner, D. Eifler, Analysis of fatigue properties and failure mechanisms of Ti6Al4V in the very high cycle fatigue regime using ultrasonic technology and 3D laser scanning vibrometry., Ultrasonics. 53 (2013) 1433–40.

[169] H. Wang, Laser Impact Welding and High Strain Rate Embossing, Disseration. The Ohio State University, 2013.

[170] D.R. Foster, Thermal and Mechanical Characterization of Ultrasonic Additive Manufacuturing, The Ohio State University, 2014.

[171] M.R. Sriraman, S.S. Babu, M. Short, Bonding characteristics during very high power ultrasonic additive manufacturing of copper, Scr. Mater. 62 (2010) 560–563.

[172] T. Watanabe, H. Sakuyama, A. Yanagisawa, Ultrasonic welding between mild steel sheet and Al–Mg alloy sheet, J. Mater. Process. Technol. 209 (2009) 5475–5480.

[173] C.Q. Zhang, J.D. Robson, O. Ciuca, P.B. Prangnell, Microstructural characterization and mechanical properties of high power ultrasonic spot welded aluminum alloy AA6111–TiAl6V4 dissimilar joints, Mater. Charact. 97 (2014) 83–91.

[174] L. Murr, G. Liu, J. McClure, Dynamic recrystallization in friction-stir welding of aluminium alloy 1100, J. Mater. Sci. Lett. 6 (1997) 1801–1803.

[175] F. Rajabi, a. Zarei-Hanzaki, M. Eskandari, S. Khoddam, The effects of rolling parameters on the mechanical behavior of 6061 aluminum alloy, Mater. Sci. Eng. A. 578 (2013) 90–95.

[176] X.H. Fan, M. Li, D.Y. Li, Y.C. Shao, S.R. Zhang, Y.H. Peng, Dynamic recrystallisation and dynamic precipitation in AA6061 aluminium alloy during hot deformation, Mater. Sci. Technol. 30 (2014) 1263–1272.

[177] B. Langenecker, Effects of ultrasound on deformation characteristics of metals, IEEE Trans. Sonics Ultrason. (1966) 1–8.

[178] T. Sasaki, Y. Hosokawa, Effect of Relative Motion between Weld Tool and Work Piece on Microstructure of Ultrasonically Welded Joint, Mater. Sci. Forum. 783–786 (2014) 1782–1787.

[179] G.S. Kelly, S.G. Advani, J.W. Gillespie, A model to describe stick–slip transition time during ultrasonic consolidation, Int. J. Adv. Manuf. Technol. (2015).

[180] Z. Al-Sarraf, M. Lucas, A study of weld quality in ultrasonic spot welding of similar and dissimilar metals, J. Phys. Conf. Ser. 382 (2012) 12013.

[181] A. Siddiq, E. Ghassemieh, Thermomechanical analyses of ultrasonic welding process using thermal and acoustic softening effects, Mech. Mater. 40 (2008) 982–1000.